Author:
Griffin, Daniel

Title:
Enabling data-driven research and development in composite product engineering

An over-braiding case study

Enabling data-driven research and development in composite product engineering: An over-braiding case study

Daniel Jack Griffin

A dissertation submitted to the University of Bristol in accordance with the requirements for award of the degree of Doctor of Engineering in the Faculty of Engineering.

University of Bristol
Faculty of Engineering
Department of Aerospace Engineering
July 2021

Word Count: 53,486

Abstract

The fibre reinforced polymer (FRP) composites manufacturing industry stands to benefit significantly from the exploitation of data-driven research and development practices. However, research organisations which are best placed to make advances in the associated engineering disciplines are often ill-equipped to generate and utilise the prerequisite consistent, contextualised data sets. The work herein seeks to address this issue by demonstrating a progressive approach to the generation of manufacturing data sets, in which emphasis is placed on maximising the potential research value, i.e. usefulness, of those data.

The approach is demonstrated via the development and implementation of a bespoke in-process measurement capability for the 2D axial over-braiding preforming process, with which to automate the measurement braid angle and preform thickness as informative quality metrics. Measurements were achieved using 2D Fourier transform image analysis and laser profilometry, respectively. System design prioritised contextualisation of measurement data and ensuring simplicity of operation. A method with which to evaluate the potential research value of additional process variable data sets, based on assessment of variable inter-dependencies, was developed to support the design process. Through it, a number of process parameters were identified that represent valuable, yet often overlooked, contextual information regarding process quality; the functionality to record these metadata via the user interface was thus included. Measurement system sensitivity to a range of material, process and procedural factors was assessed in order to optimise measurement performance and evaluate the associated uncertainty. Insights generated into the effect of yarn twist on preform thickness, factors influencing the stabilisation of the deposited braid architecture, and the relationship between braid angle and convergence cone geometry are presented. These illustrate some of the benefits that are enabled by ensuring the availability and re-useability of consistent data sets, as required to perform of data-driven research and development.

Acknowledgements

I would firstly like to acknowledge EPSRC, the National Physical Laboratory and the National Composites Centre for providing, in various forms, the funding which has made this project possible.

Next, my thanks goes to Professors Ivana Partridge and Ian Hamerton for their technical and pastoral support throughout the project in the role of academic supervisor.

The experience of this industrial doctorate has been particularly rewarding thanks to the efforts of my various industrial supervisors, Tim Young, Alper Aktas, Mike Gower, and, especially, Marcus Walls-Bruck. The opportunities that they have created have helped to shape this research as well as my personal development.

There are innumerable colleagues and peers who have also contributed significantly along the way, generously sharing their time and expertise on a whole range of topics. Worthy of particular mention are Maria Lodeiro, Simon Groves, Andrew Drane, Thibaut Buns and Pete Whitton, but there are many others besides.

Finally, I would like to thank my family and friends for their unwavering support and encouragement throughout, especially Lucy, who picked me up and helped me to press ahead when the walls were closing in.

Publications

Journal Articles

***Published*:**

- D. Griffin, S. Wood, and I. Hamerton. Measurement of the glass transition temperature of an epoxy resin using principal components of Raman spectra. *Composites Part B: Engineering*, 200:108210, November 2020. doi: 10.1016/j.compositesb.2020.108210.

Conference Papers

- D. Griffin, A. Aktas, M. Lodeiro, T. Young, I. Hamerton, and I. Partridge. A comparison of material state monitoring techniques applied to resin transfer moulding. In *21st International Conferences on Composite Materials*, Xi'an, China, August 2017.

Author's Declaration

I declare that the work in this dissertation was carried out in accordance with the requirements of the University's Regulations and Code of Practice for Research Degree Programmes and that it has not been submitted for any other academic award. Except where indicated by specific reference in the text, the work is the candidate's own work. Work done in collaboration with, or with the assistance of, others, is indicated as such. Any views expressed in the dissertation are those of the author.

Bristol, July 22, 2021

Daniel Jack Griffin

Contents

List of Figures

List of Tables

Glossary

Terms

Axial yarn	yarn deposited parallel to the braid ring central axis;
Bias yarn	yarn deposited by carrier-mounted spools around the braid ring central axis, a.k.a. helical;
Bobbin	see *spool*;
Braid pattern	repeating pattern created by interlaced yarns in braid structure;
Clip limit	upper threshold for pixel intensity applied to edge-filtered images;
Compaction	increase in fibre volume fraction of a preform due to application of pressure;
Convergence length	distance along the braiding axis between the guide ring (or braid ring) and converge plane;
Convergence plane	plane in which yarns converge upon the mandrel surface;
Convergence point	location at which yarns converge into a braid;
Convergence region	region between the guide ring (or braid ring) and converge plane;
Dark field	illumination with a high angle of incidence;
Data-driven	reliant on the collection and/or analysis of data;
Edge-filtered	having had an image processing filter applied to accentuate edge features;
Fell plane	see *convergence plane*;
Fell point	point at which a yarn contacts the mandrel surface;
Gelation	onset of large-scale, 3D cross-linking within a polymer network;
Guide ring	used to reduce the distance between braid ring and convergence plane;
Informational value	the potential for information to be derived from [data];
Kernel	matrix over which image processing operations are performed;
Mandrel	shaped tool over and onto which a braided textile is formed;
Parallax	apparent change in position (of an object) due to a change in observers point of view;
Permeability	measure of the ease with which resin can travel through a preform;
Polarising angle	angle of polarising filter relative to the braiding axis;
Specular reflection	mirror-like reflection from a surface;
Spool	cylindrical object from which yarns are unwound during braiding;
Spool carrier	hardware upon which a spool transported around the braid ring;
Tow	untwisted bundle of fibres;

Traverse mechanism	two-arm gantry mechanism used for control of mandrel position during over-braiding;
Yarn	bundle of (twisted) fibres, may comprise one or more tows;

Acronyms

AOI	area of interest;
AVS	APODIUS Vision System;
CAD	computer aided design;
CL	clip limit (i.e. upper threshold) for pixel intensity in edge image, as percentile;
D&M	design and manufacture;
DEA	dielectric analysis (a.k.a. dielectric spectroscopy);
DFT	discrete Fourier transform;
DMA	dynamic mechanical analysis;
DoF	degrees of freedom;
DSC	dynamic scanning calorimetry;
EC	eddy current;
FE	finite element;
FFT	fast Fourier transform;
FTIR	Fourier transform infra-red;
GAP	geometry, architecture, process;
IIoT	industrial internet of things;
ILSS	interlaminar shear strength;
ITA	Istitut für Textiltechnik, RWTH Aachen University;
LCM	liquid composite moulding;
LED	light emitting diode;
MAD	median absolute deviation from sample median;
MBSO	model-based self-optimisation;
MC	Monte Carlo;
MSA	measurement sensor assembly;
NCC	National Composites Centre;
NPL	National Physical Laboratory;
OD	outer diameter;
PES	potential energy surface;
PA	polarising angle (orientation of polarising filter relative to braider X axis;
PFMEA	process failure mode effects analysis;
PSD	power spectral density;
R&D	research and development;
RMSE	root mean squared error;
RSD	relative standard deviations;
RTM	resin transfer moulding;
RTO	Research and Technology Organisation;
TUM	Technical University of Munich;
UT	ultrasonic testing;
VARI	vacuum assisted resin infusion;
XCT	X-ray computed tomography;
XML	Extensible Markup Language;

Symbols

A	scale parameter;
α	circumferential angle;
$\Delta\theta_{fib}$	angular deviation between a yarn and fibres visible on the yarn surface;
$\Delta\theta_{layer}$	difference in braid angle between adjacent layers;
$\Delta\theta_{meas}$	difference between simulated and measured braid angle;
ΔYZ	length of surface normal between intersections with the fitted mandrel (i.e. baseline) surface and the corresponding fitted preform surface (i.e. point measurement of preform height in the plane of the profile);
$\overline{\Delta YZ}$	average of preform height measurements, using points with a surface normal gradient in excess of 10;
H_0	convergence region length;
K	median blur filter kernel size;
k	tuning constant for fitting operation;
κ	asymmetry of the peak fitting distribution;
λ	spread of the peak fitting distribution;
m	orientation of peak maxima;
μ	mean;
ω	orientation of bisecting line;
ϕ	maximum angular resolution of braid angle measurements);
R	residual from fitting operation;
r	radius;
r_{gr}	guide ring radius;
r_m	mandrel radius;
σ	standard deviation;
σ_{peak}	standard deviation error in peak centres during the braid angle angular intensity peak fitting routine;
$\sigma_{\theta,light}$	standard deviation of braid angle measurement results across all light offsets;
$\sigma_{\theta,light,X}$	standard deviation of braid angle measurement results across all light offsets and measurement locations;
T_{g}	glass transition temperature;
θ	braid angle;
$\widetilde{\theta}$	median braid angle;
θ_{nom}	nominal braid angle;
V_{f}	fibre volume fraction;
W	weights for fitting operation;

Chapter 1

Introduction

1.1 Research motivation

As with most aspects of life in the 21st century, the availability and re-usability of reliable data sets is becoming increasingly important to scientific and engineering endeavours. Within the scientific community, this is evidenced by efforts to realise the maximum value of research data through improved mechanisms for data management and sharing, especially where public funding bodies are involved. One such example is the development of the FAIR Guiding Principles for scientific data management and stewardship [1], first published in 2016, which provide a set of criteria against which to assess the *findability*, *accessability*, *interoperability* and *re-usability* of scientific research data, associated metadata and software tools; the principles themselves are presented in Figure 1.1. At the time of writing, there are a number of initiatives and committees seeking to support the implementation of these principles within research communities [2–6]. The COVID-19 pandemic has expedited this adoption process within the biomedical sciences, as efforts have been made to address this global public health crisis through collaborative, multi-national research. For instance, the European Commission has published guidance [7] to EU research grant recipients concerning the accessibility of publications and data relating to COVID-19 research activities, which is founded in the FAIR principles. Similarly, the European COVID-19 Data Platform [8] has been established to facilitate collaborative data sharing and analysis efforts, again via FAIR principle implementation.

Across engineering disciplines, and especially within manufacturing industries, the same underlying driver is responsible for the growth of technologies and practices labelled as 'Industry 4.0' and the Industrial Internet of Things (IIoT), i.e. value creation from the collection, analysis and exploitation of data. Whether to improve manufacturing productivity, or to develop more profitable or sustainable products and services, the availability of reliable, consistent data sets in a timely manner to inform decisions and drive processes is paramount. The fibre reinforced polymer (FRP) composites manufacturing industry is no exception. In fact, it stands to benefit a great deal from

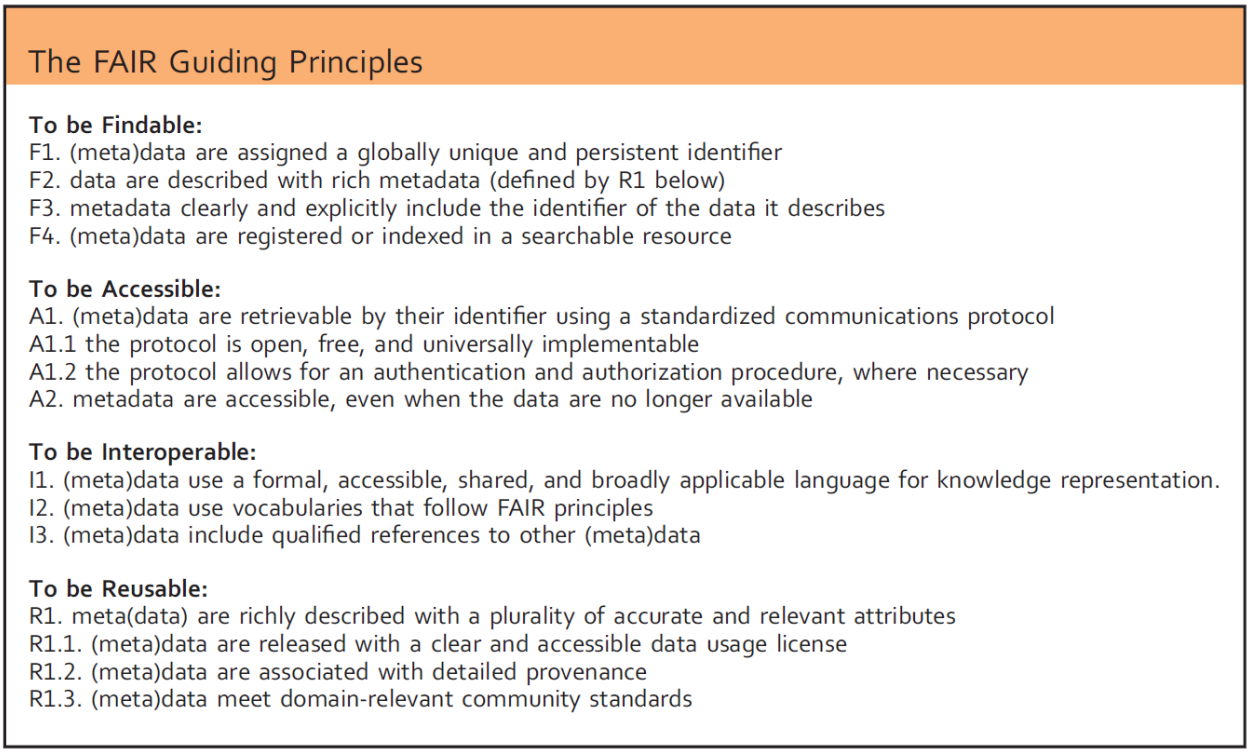

Figure 1.1: The FAIR Guiding Principles as published in [1].

the successful adoption of data-driven practices given:

- the challenges associated with optimisation of anisotropic material and structural properties whilst allowing for inherent material variability;
- the current reliance on labour intensive production processes;
- the need to develop more sustainable, environmentally friendly products.

The key enabler in this discussion is the ability to extract insight and generate value from data beyond that for which they were initially acquired. This, in turn, depends on the effective, efficient acquisition and management of consistent, contextualised data sets in order to maximise the usefulness of those data sets to other users and future applications, which can be thought of as maximising the *informational value* of data, i.e. the potential for information to be derived from data. This is the motivation behind the research presented herein, concerned with maximising the informational value of manufacturing data sets as required to realise the potential of data-driven research and development (R&D) activities in FRP composite product engineering.

The project was jointly sponsored by the National Physical Laboratory (NPL, Teddington), the UK's national measurement institute, and the National Composites Centre (NCC, Bristol), a member of the High Value Manufacturing Catapult specialising in the design and manufacture of composite structures. This combination of sponsors provided the ideal platform upon which to

investigate the benefit of high quality measurement data to the composites manufacturing research community.

1.2 Data-driven research and development in composite product engineering

Production of fibre reinforced polymer composite structures from primary constituents, i.e. dry fibre reinforcement and polymerising liquid resin as opposed to pre-impregnated fibre sheets or tapes, is becoming increasingly prevalent. This is largely due to the combination of lower material and processing costs, and increased design freedom. The high degrees of freedom (DoF) offered by the various dry fibre preforming and liquid composite moulding (LCM) manufacture processes presents both opportunities and challenges for product designers and manufacturing engineers alike, in their attempts to optimise product and process performance whilst meeting often stringent quality requirements. For instance, the design and manufacture (D&M) envelope from which to develop products that fully exploit the specific, multi-functional properties of composite materials is potentially vast, whilst the capacity to explore this envelope within any given project is often limited by budgetary constraints and the engineering expertise to hand.

This duality may be partly addressed by the development of tailored design methodologies for composites, such as the GAP (Geometry, Architecture, Process) methodology recently published by Neveu *et al.* [9]. However, the success of any chosen methodology will inevitably depend on the quantity and quality of supporting information upon which associated decisions are made. It therefore stands to reason that the likelihood of a successful composite product development cycle should be increased by increasing the breadth of reliable data sets that may be called upon during the cycle, e.g. material preparation, process configuration and product verification data from previous, relevant development or production activities. This premise underlies the chapters of this thesis, in which ways and means to increase the availability and re-usability, and investigate the potential research value, of data sets acquired during the manufacture of composite structures are investigated. Thus an exploration into the potential benefits of FAIR guiding principle implementation within composite product engineering is begun.

The particular manufacturing process chain selected as the subject of this work comprises dry fibre preform production via over-braiding, followed by preform impregnation with a liquid resin system via infusion or injection. For the most part, the focus is on the over-braiding preforming process, which entails the formation of a braided textile over a shaped tool (a.k.a. mandrel). As a general rule, the process is a suitable preforming method for structures with near-cylindrical or prismatic geometries, including those in which cross-sectional shape and/or size varies along its

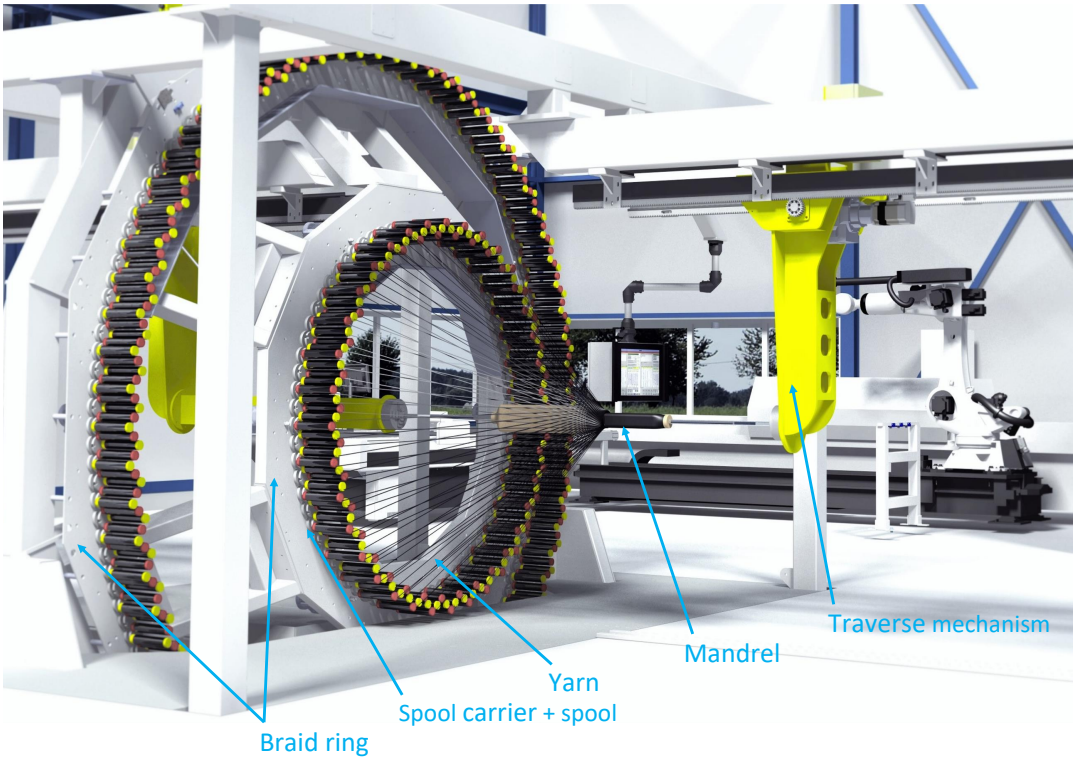

Figure 1.2: Illustration of the double-ring, axial over-braider, produced by Eurocarbon, that is installed at NCC.

primary axis, provided that the cross-sectional shape remains convex in nature. Typical components produced using over-braiding include propeller blades, drive shafts, roof support pillars and similar tubular structures.

Whilst a range of braiding processes exist, as introduced in "Handbook of advances in Braided Composite Materials" [10], this work relates to the production of laminar (i.e. two-dimensional) braided architectures using an axial braiding machine. The machine in question is a double-ring, axial over-braider, produced by Eurocarbon, which is installed at NCC; an illustration is provided in Figure 1.2 for reference. The 2D, axial over-braiding process consists of two mechanical stages:

- a *braid ring*, around which two sets of *spool carriers* rotate in opposing directions along sinusoidal paths[1];
- a mandrel *traverse mechanism*, onto which the *mandrel* is mounted and which controls the motion of the mandrel through the braid ring.

Carriers are positioned such that they travel around one face of the braid ring, oriented parallel to the braid ring axis. *Spools* (a.k.a. *bobbins*) wound with yarns of the chosen material are loaded

[1]The NCC over-braider has two braid rings of different diameters and number of spool carriers, only one of which is used for any given braiding operation.

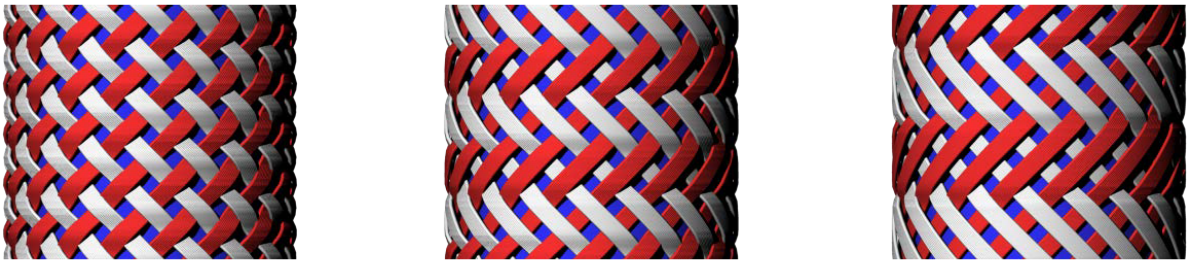

Figure 1.3: Braid pattern illustrations: 1/1 - diamond (left); 2/2 - regular (centre); 3/3 - hercules (right). Reproduced from [11].

onto the carriers and the yarn ends fastened to the mandrel prior to braid deposition. During the braiding operation, yarns are pulled from the spools under tension and are interlaced with other yarns as the carriers follow their counter-rotating sinusoidal paths around the braid ring and the mandrel is driven through the braid ring. The repeating pattern of the deposited braid is dependent on the loading arrangement of carriers around the braid ring, producing, for example, the diamond (1/1), regular (2/2) or hercules (3/3) braid patterns illustrated in Figure 1.3.

Braid geometry and dimensions are primarily determined by the relative speeds of the spool carriers and mandrel, the cross-sectional size and shape of the mandrel in the region of braid deposition, and the number and size of yarns being deposited. These independent variables are relatively few in number and simple to control individually, however, determining an acceptable combination to meet a specific set of design requirements can prove challenging. This is especially true when considering the full range of product design variables, as well as the numerous other aspects of process configuration and material preparation, many of which are not readily altered once selected; it is often necessary to conduct a significant amount of iterative manufacturing trials as a result. Hence, it has been written that "there remain challenges to manufacture braided composites that meet the stringent quality control requirements for the mass-market or high-end product industry. This is true in term of geometric accuracy and repeatability; preform impregnation quality and repeatability; and predictability and repeatability of end-product properties" [12].

A number of modelling tools are available to aid process definition, ranging from simplistic analytical equations [13–18], describing relationships between yarn and mandrel dimensions, process velocities, and deposited braid structure (i.e. unit cell dimensions), through to dynamic finite element (FE) models of the braiding process which can account for physical properties of the yarns, and yarn interactions along the process. Analytical and kinematic models tend to be computationally inexpensive, and inverse model solutions [15, 17, 18] enable prediction of machine controls and mandrel trajectories required to achieve target braid angles, making them attractive process design tools. However, their applicability is limited by various underlying assumptions, not least

the omission of physical yarn interactions. Where these assumptions are expected to have a significant detrimental effect on model accuracy, FE simulation methods may be used in order to more reliably predict the resultant braid architecture for a given process setup. These methods include representations for yarn-yarn, yarn-mandrel, and yarn-guide ring, as well as applied yarn tension [19], yarn stiffness [20] and yarn deformation [21–23]. However, they are computationally expensive, often requiring hours, if not days, of processing time to execute, which tends to limit the extent to which they are utilised.

The ability to augment experiential and simulation-based decisions throughout the design and manufacture workflow with insight gained through interrogation of pre-existing data sets is, therefore, expected to expedite arrival at an acceptable manufacturing outcome, thus reducing product development cycle timescales and costs.

1.3 Project aims and thesis structure

The work presented in this thesis was conducted with the aim of enhancing the capability for data-driven research and development within a Research and Technology Organisation (RTO), by improving the availability and re-usability of consistent, reliable data sets. In this regard, such an organisation may be considered to be resource-constrained, with limited scope for investment in a suitable data management infrastructure, hence the findings should translate to many other organisations who find themselves in a similar predicament. By way of a case study, enhancement was sought for a specific manufacturing process used in FRP composite product engineering at NCC, namely over-braiding of dry fibre preforms, through the development and implementation of an in-process measurement capability. The focus throughout was on the acquisition and application of data relating to manufacturing quality, since this is often the primary concern for product engineering activities, especially those involving braided components [24]. An overview of the constituent chapters and their content is as follows:

- **Chapter 2** reviews the predominant properties of FRP composite materials and structures that are used to assess the quality of a manufactured product, and the techniques by which they may be quantified during the manufacturing process; particular attention is paid to products of (over-)braiding and LCM processes.

- **Chapter 3** introduces a method that was developed as a means to assess the likely research value of variables identified along the engineering workflow that relate to the manufacturing quality for a given process. The assessment is based on the level of understanding and sensitivity ascribed to relationships between pairs of variables, with the output intended to

inform the implementation of data acquisition capability for the process in question. The method is demonstrated for the over-braiding facility which is the subject of this thesis.

- **Chapter 4** provides details of the in-process measurement capability that was developed for the over-braiding facility at NCC during the course of this project, based on the content of the Chapters 2 & 3. The primary aim was to automate the necessary data acquisition and analysis for measurement of key quality metrics for over-braided preforms, namely braid angle and preform thickness, in order to improve the consistency and reliability of these data sets across over-braiding R&D activities.

- **Chapter 5** presents the results of various measurement sensitivity analyses conducted during the development of the in-process measurement capability described in Chapter 4 in order to optimise measurement performance and characterise measurement uncertainty. The findings are vital to ascertaining the reliability of the generated measurements.

- **Chapter 6** reports results and findings from two over-braiding research projects in which the in-process measurement capability was deployed, demonstrating the added value of the measurement data to research activities in each case.

- **Chapter 7** presents an overall discussion regarding the relevance and potential impact of the concepts in this thesis to the composites manufacturing research community as a whole.

- **Chapter 8** summarises the conclusions and recommendations for future work drawn from the preceding chapters.

Chapter 2

Assessing quality of infused over-braided components

This chapter explores the available methods and techniques to enable assessment of quality throughout the production of FRP composite structures via LCM processes, with a view to informing the development of an in-process, quality-oriented measurement capability for the production of LCM over-braided structures.

Five themes are identified into which key quality metrics for FRP materials and components can typically be grouped. For each theme, the impact of associated quality metrics on material and product performance is reviewed, along with the available methods and techniques with which those metrics can be measured during the production process.

Research conducted and published by the author into a measurement technique for one of the themes, namely the properties of the cured polymer matrix, is introduced, which demonstrates the use of Raman spectroscopy coupled with multivariate spectral analysis for direct measurement of glass transition temperature, T_g.

2.1 Manufacturing quality themes

The quality of a manufactured component or product can be considered simply as the extent to which it fulfils the specification against which it has been produced; this could be considered as the performance of a complete product against its product requirements specification, or the conformance of a product, component or sub-component to its design specification. The discussions in this and subsequent chapters are concerned primarily with conformance of a manufactured component to the design specification, i.e. the manufacturing quality; the performance of a given product design will not be considered.

The manufacturing quality of FRP composite structures produced by LCM methods can be measured against a range of quality metrics, comprising both explicit (i.e. measured directly against design requirements) and implicit (i.e. necessary to meet design requirements) metrics, depending on the materials and processes involved. In general, these metrics can be grouped into five themes as follows:

1. the quantity and distribution of fibre in the structure;
2. the orientations of fibres relative to the component geometry;
3. the presence of voids throughout the structure;
4. the properties of the cured polymer matrix;
5. the presence of stress-induced distortions and defects throughout the structure.

Whilst these themes are relevant to the performance and quality of FRP materials in general, the survey and discussion in the following sections are tailored towards those metrics in each that have particular relevance to components produced via over-braiding.

2.1.1 Fibre content

In FRP composite materials, the desirable properties of specific strength and stiffness, as well as other mechanical and thermal properties, are invariably dependent upon the fibre content, or fibre volume fraction, V_f, of the material [25–27]. As such, V_f is typically specified as a material property requirement within the design specification [28–30] and is critical in determining aspects of the component geometry and performance. Fibre volume fraction has also been shown to indirectly influence material properties via its contribution to stress evolution within the polymer matrix and the resulting distortions and defects during and after the curing process [31, 32]; this effect is discussed further in Section 2.1.5.

Some examples of V_f sensitivity of braided composite materials reported in literature include in-plane elastic moduli variation for triaxial, 2D braided composite panels (8.3% increase between 55 % and 60 % V_f) [33], and reduction in creep compliance, i.e. rate of strain change under constant load, in 3D braided composites with increasing V_f, (reducing by approx 1/3 between 25 % and 40 % V_f) [34]. In other studies [35–38], strength and stiffness measurements are normalised against sample V_f for comparison, further demonstrating the dependence of these properties on fibre content.

The distribution of tows, or yarns, through a preform has also been shown to affect structural performance. For instance, an apparent increase in stiffness and decrease in tensile strength was reported for woven laminates with random stacking of tows between layers relative to those with regular stacking (i.e. no offset between layers) [39], whilst an increase in yarn spacing, i.e. reduced

cover factor, was reported to result in significant reduction of in-plane tensile properties in triaxial, 2D braided laminates [37].

The level of control over fibre content during the manufacture is dependent on the choice of processes. For instance, where resin transfer moulding (RTM) using matched, solid tooling is used for preform impregnation, V_f is primarily determined by the mould cavity design, and the quantity and distribution of fibre deposited in the preform; provided that the mould-preform fit is acceptable and the compaction behaviour of the preform is as expected, the intended V_f should be achieved. On the other hand, where flexible tooling is employed, the chosen impregnation strategy and control of variables within it can be crucial to achieving the laminate thickness necessary for a target V_f. In such processes, the range of achievable fibre volume fractions is dependent upon initial preform thickness and compaction behaviour, as well as the specifics of the chosen impregnation process. Thus, the laminate products of different variants of vacuum assisted resin infusion (VARI) processes have been shown to vary significantly in V_f and associated mechanical performance [40].

Aside from determining the material properties in the cured laminate, fibre distribution and V_f have also been shown to have a strong influence on processing characteristics of the preform such as compressibility and permeability [32, 36, 41, 42]. This has implications for the outcome of the impregnation process, which is particularly sensitive to preform permeability as discussed in Section 2.1.3.

Measurement options

Fibre content in FRP composite materials is typically quantified via destructive laboratory tests to determine the mass and density of constituent materials [43–47]. Visual analysis of fibre content is also commonly practised by means of optical microscopy [48, 49] or X-ray computed tomography (XCT) [50] for 2D and 3D analysis respectively, although in most instances this also requires samples to be cut from the composite structure.[1] Such methods are well established for offline material characterisation and enable fibre distribution variability to be analysed via sequential sampling through a structure, however, they are not viable for *in situ* assessment of V_f during the manufacturing process.

For *in situ* assessment, the quantity and density of preform material must be known as well as the laminate thickness, from which a generalised V_f can be calculated. This relationship has been utilised as a means of enabling in-process control of V_f during the manufacture of an aircraft wing component via an autoclave infusion process [51]. Low cost piezoelectric sensors were deployed in a through-transmission configuration in order to measure the ultrasonic signal time-of-flight through the laminate and mould upon complete preform impregnation. Hence, laminate thickness could be

[1] Whole structures may be analysed with XCT depending on the sample envelope of the machine, but scan duration and/or resolution are likely to be restrictive.

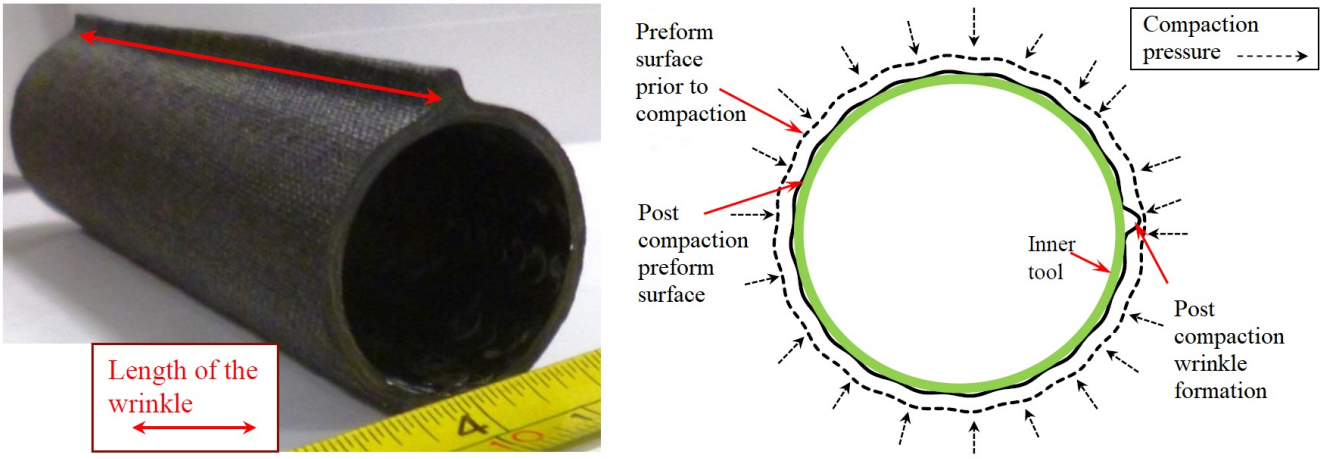

Figure 2.1: Wrinkle formation resulting from compaction of braided preform over rigid cylindrical tooling; adapted from [61].

inferred and pressure differential adjusted in order to achieve the desired laminate thickness prior to gelation of the resin, ensuring the necessary V_f in the cured component.

Other point thickness measurement techniques, using dial gauge [52], linear variable differential transformer (LDVT) [53, 54] and laser distance sensor [40, 55] arrays, have also been employed for indirect V_f measurement, often for preform compaction and permeability studies of flat preforms. As with destructive sampling methods, measurement coverage is determined by the number and positioning of sensors. Several methods for full-field thickness measurement during preform impregnation have also been demonstrated, using photogrammetry [56–58], digital image correlation (DIC) [59] and structured light scanning [60], again only for flat laminates produced via out-of-autoclave VARI and RTM Light processes. Although there is a scarcity of examples showing application of such techniques to more complex geometries, this should be achievable since they are established techniques for dimensional inspection activities.

Since the thickness, and resultant V_f, that is achieved during preform impregnation is dependent on the total preform thickness and its compaction behaviour, it may be beneficial in some instances to measure the evolution of preform thickness during the preforming process [62]. Take a multi-layer braided preform deposited over a rigid, cylindrical mandrel for example; when compacted, the reduced circumference will result in excess material in the outer layers which is likely to form into wrinkles (see Figure 2.1) or inhibit compaction to the required V_f, either of which will detrimentally affect the final product. Preform thickness measurements during deposition may provide information about the level of compaction achieved between each layer and hence the excess material length that is being generated. Laser profilometer sensors have been demonstrated for in-process measurement such as this [63–65], in which the sensor is scanned across the preform surface, layer-by-layer, to assess preform thickness as it is produced, although the properties of dry

carbon fibre textiles in particular do present challenges to these types of sensor.

2.1.2 Fibre orientation

Alongside fibre content, it is the orientations of fibres within an FRP material that determine many of its material and structural properties, as well as the anisotropy of those properties. In the case of 2D braiding and over-braiding, in-plane fibre orientation is primarily governed by the braid angle, θ, which is defined as the angle of bias yarns within the preform structure relative to the braiding axis, as well as the presence of axially aligned yarns in triaxial braided preforms. These yarn orientations will typically be defined in the design specification in order to achieve the required structural performance under expected load cases. Whilst the relative importance of fibre-dominated properties will be dependent on a given structure's intended application and associated performance requirements, numerous studies have investigated the sensitivity of typical properties of braided composites to braid angle.

One such study [33] reported significant braid angle sensitivity of in-plane properties for biaxial braided composites, as illustrated in Figure 2.2. Although these results relate to a specific set of material combination and design parameters, the trends in property behaviour are more widely applicable [36, 66, 67]. The effect on fatigue performance has also been investigated [68], reporting a reduction in endurance limit (i.e. the fatigue load required to produce a fatigue life of 1 million cycles) from 50% ultimate tensile strength at $\theta = 45^\circ$ to 40 % at $\theta = 30^\circ$. Further examples and details can be found in numerous published reviews of the mechanical properties of braided composites [62, 69, 70].

Operating regimes in which properties of interest exhibit especially high sensitivity to braid angle are of particular interest from a process measurement and control perspective, since relatively small deviations in θ may have a significant impact on product performance. This is exemplified in Figure 2.2 by elastic moduli, E_{xx} and E_{yy}, which exhibit increasingly steep response gradients for $\theta > 30^\circ$ and $\theta < 60^\circ$ respectively. A second example relating to a triaxial $0/\pm60^\circ$ braided laminate [71] outlined a 5 % change in longitudinal modulus, 6 % shear modulus, 9 % in-plane Poisson ratio for a corresponding 2° variation in θ.

In addition to continuous trends in properties as a function of θ, certain braid angle ranges may correspond to behavioural discontinuities, e.g. change in dominant failure mode. One such occurrence has been reported for glass fibre/epoxy braided tubes under tension [72], for which particular sensitivity of yield strength, strain to failure and specific energy absorption in the region 40° - 45° were reported, coincident with a transition in dominant failure mechanism from fibre failure to neck propagation. Another study [73] reported a transition in dominant failure mode for flat glass fibre/epoxy braided laminate samples at approximately 30° from tensile fibre failure

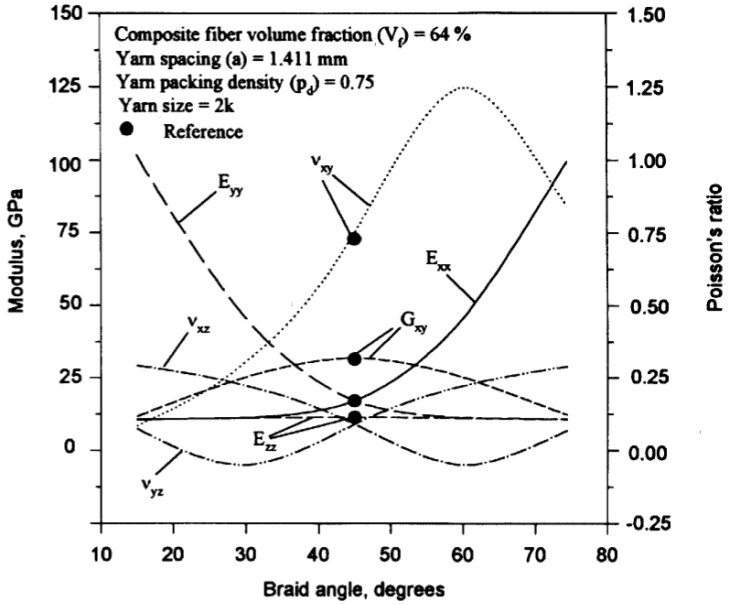

Figure 2.2: Variation in elastic moduli, E_{xx} and E_{yy}, shear modulus, G_{xy} and Poisson's ratios, ν_{xy}, ν_{xz} and ν_{yz}, with braid angle, for 2/2 carbon fibre/epoxy braided laminate; reproduced from [33].

($\theta \leq 30°$) to mixed fibre tensile and matrix shearing ($\theta > 30°$).

Secondary factors contributing to fibre orientation in braided preforms include yarn undulation, or crimp, produced by the interlacement of yarns, and yarn twist, introduced to yarns during the bobbin winding process with the intent to improve processing characteristics. These inevitably impact upon the mechanical characteristics of the yarns and the corresponding performance of the composite due to deviations of fibres within yarns from the in-plane yarn orientation [37, 74–77]. Following yarn deposition, fibre orientations may be affected by preform manipulations, for example during trimming operations, compaction during the impregnation process as discussed in Section 2.1.1, or as a result of cure-induced stress evolution reviewed in Section 2.1.5. The occurrence of out-of-plane wrinkles which can cause significant reductions in material performance and which are common in thick or curved geometries [78] is of particular concern.

Aside from mechanical performance of the composite laminate, processing characteristics of the preform such as formability and permeability are also influenced by tow/yarn orientations [32, 79]; as such, numerous studies have been published into the permeability sensitivity of braided preforms to yarn angle [36, 80, 81]. The relationship between preform permeability and quality of the composite product is dicussed further in Section 2.1.3.

Measurement options

Analysis of fibre orientations and misalignment in FRP composite materials is typically conducted via visual methods applied to cross-sectional images acquired by optical microscopy or XCT. Nu-

merous automated image analysis routines have been developed and demonstrated to improve the accuracy and repeatably of such measurements. Some enable determination of fibre orientation by elliptical modelling of visible fibres [82, 83] or structure tensor analysis [84–86]; others target quantification of out-of-plane fibre waviness relative to the sectioned plane based on individual fibre identification [87], pixel intensity correlation with a 'trial' fibre [88, 89] or 2D Fourier transform procedures [90].

The three-dimensional nature of XCT data also enables volumetric analysis of fibre orientations, several algorithms for which have been reviewed in the literature [91], although the sampling and data analysis requirements limit application to relatively small sample volumes in practice. Non-destructive assessment of in-plane fibre orientation and out-of-plane fibre waviness using ultrasonic inspection methods has also been demonstrated, using 2D fast Fourier (FFT) and Radon transforms [92, 93] and structure tensor analyses methods [94]. Whilst not requiring destructive sampling of the structure, data acquisition for these ultrasonic scanning methods is relatively slow and usually requires immersion of the structure in water; hence they are reserved for post-production inspection activities. The latter of these limitations is addressed by recent advances in laser ultrasound techniques, which enable non-contact ultrasonic inspection of FRP materials [95–97].

In order to determine fibre orientations prior to the impregnation process, more practical *in situ* inspection techniques are required. Radio frequency eddy current (EC) inspection is one such technique [98, 99], which has been shown to be suitable for inspection of dry fibre preforms [100] as well as impregnated and cured laminates [101]. As with ultrasonic techniques, EC inspection is conducted via probe scanning across the material surface, typically coupled with 2D FFT analysis, and enables limited through-thickness assessment of in-plane fibre orientations. This is particularly useful for processes which involve forming of multi-layered preform stacks.

Alternatively, optical imagery techniques have been developed for surface layer fibre orientation analysis. Some of these utilise analysis routines similar to those introduced for XCT and ultrasonic methods, including individual tow/yarn detection and measurement [102], and 2D FFT analysis [103–105], whilst others utilise the light-polarising properties of fibres themselves to determine per-pixel surface orientations [106, 107]. These vision-based approaches enable fast, areal data acquisition and are therefore well suited to relatively high rate preforming processes such as over-braiding, where individual layers are deposited and formed concurrently.

2.1.3 Void content

Void formation in composite laminates produced via LCM processes occurs during preform impregnation and resin curing. The resulting porosity, or void content, is typically quantified as a percentage of the total material volume. A range of mechanisms can be responsible, including air

entrapment during resin infiltration, release of volatile chemicals dissolved in the resin, production of gases from the polymerisation reaction, and shrinkage of the matrix during cure. Of these, air entrapment has received the most attention in scientific literature since it is a complex, multi-scale phenomenon which is dependent upon dynamic resin-reinforcement interactions and competing viscous (inter-tow) and capillary (intra-tow) preform permeabilities [32, 108]. A comprehensive review of void formation mechanisms and the impact on mechanical performance of FRP composites has recently been published by Mehdikhani *et al.* [109]. Although research relating specifically to braided laminates was found to be limited, a broad range of studies investigating woven carbon- and glass-fibre laminates were reviewed, for which the effect of voidage might reasonably be expected to be comparable in many instances.

In summary, the sensitivity of mechanical properties to void content was found to be stochastically driven. A reduction in interlaminar shear strength (ILSS) of between 5 % and 10 % was reported per 1 % increase in void content, depending on specific preform architecture, resin properties and void configuration; the effect on flexural strength was found to be comparable in magnitude. Sensitivity of compressive and tensile properties were also reported, albeit to a lesser extent than ILSS. A reduction in compressive strength of a few percent might typically be expected per 1 % of void content; reductions in tensile modulus and strength of 14 % and 2 % respectively were reported for woven laminates with a high proportion of $\pm$ 45° plies as void content increased from 0.4 % to 8 % [110]. Similar effects on tensile and shear moduli have been reported for 3D braided laminates [111, 112], with the sensitivity also dependent on braid angle and fibre volume fraction.

The impact of voidage becomes amplified in the presence of moisture and under fatigue loading, primarily due to increased crack initiation as a result of stress concentrations around voids [109].

Measurement options

Void content in cured laminate samples is typically quantified via destructive methods such as acid digestion [43], burn-off [113] and microscopy [40]. Non-destructive techniques such as ultrasonic testing (UT) [114–116] and XCT [50] are also commonly utilised for post-process inspection of composite structures; an example XCT analysis is shown in Figure 2.3. A thorough review of the development, application and performance of these techniques for void content analysis has been conducted by Mehdikhani *et al.* [109] and thus is not addressed here. The exploitation of techniques with which to detect and quantify the evolution of porosity during the manufacturing process itself is rather more limited. Although a greater variety of techniques have been demonstrated, their constraints tend to limit the scope of viable implementations.

XCT has been applied to *in situ* monitoring of void formation and transportation in experimental studies utilising miniaturised material processing equipment [118–122]. It enables 3D characterisation of individual voids, their immediate environment and the distribution of voids through the

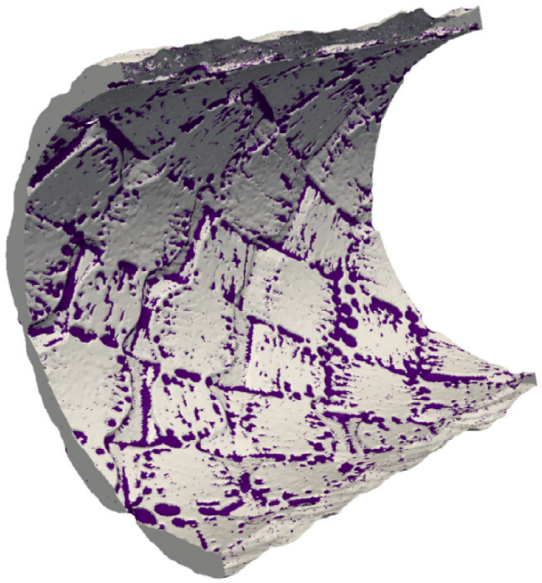

Figure 2.3: Cross-sectional view of braid geometry with voids (shown in purple) as detected using XCT; reproduced from [117].

material volume, providing a wealth of information on which to develop material and behavioural models. However, the technique is not practical for use with full-scale LCM setups given the typical sample size and scan rate constraints of XCT systems, not to mention hardware cost. Significant post-processing requirements for XCT data sets also pose difficulties for high sample throughput [123]. Similar limitations exist for magnetic resonance imaging which has been demonstrated for 3D inspection of void formation during preform impregnation [124, 125], not least the requirement for non-metallic tooling to prevent shielding of the electromagnetic signals.

Results generated via optical measurement techniques such as visible light transmission [126, 127] and reflection [128], and fluorescent dye penetration inspection [129–131] have been shown to correlate strongly with void content analyses. Such techniques, essentially comprising a light source and camera, offer a relatively simple, low cost route to *in situ* monitoring of void evolution during preform impregnation. However, the associated requirements and constraints placed upon the impregnation process itself, such as single- or double-sided transparent moulds, use of thin, flat preform samples and/or some manner of dye added to the resin, render these techniques better suited to preform characterisation studies and impractical for use in a production setting.

Various in-mould sensing methods have also been demonstrated, again primarily for the purpose of preform characterisation. These include electrical resistivity [132–134], heat transfer [135] and ultrasound [136–138] methods which can be used to quantify the extent of preform saturation at sensor locations under carefully controlled processing conditions. More commonly, systems based on dielectric analysis (DEA) [139–144], direct current resistivity [145, 146], electrical time-domain

reflectometry [147–149], ultrasound [150] and embedded fibre optics [151, 152] are used to monitor the position and velocity of resin flow front during impregnation, as reviewed in recent years by Konstantopoulos *et al.* [153] and Torres [154]. This is due to the fact that air entrapment is a predominant cause of porosity in LCM products and has been shown to be sensitive to relative intra- and inter-tow/yarn permeabilities [155, 156]. However, relatively few published examples of implementations in representative production scenarios exist [51, 157–160].

2.1.4 Cured matrix properties

In LCM processes, once saturation of the preform with the liquid resin has been achieved, the resin is converted to a 3D cross-linked polymeric matrix via chemical reaction. This polymerisation occurs at some combination of temperature, pressure and time and is crucial to the development of the desired functional characteristics in the composites structure. Whilst tensile and flexural properties in the direction of fibre reinforcement are typically governed by those of the fibre constituent, compressive, shear and off-axis (e.g. through-thickness) tensile properties are largely determined by the thermo-mechanical properties of the matrix constituent and the matrix-fibre interface [161, 162]. The strength, stiffness and fracture toughness of the cured matrix are therefore important in determining the overall material performance [163–166]. However, the relationship between the degree of cure and mechanical performance is rarely isolated from other contributing factors such as void content, matrix-fibre interface strength and cure-induced defects, since these are all sensitive to changes in the applied processing conditions [167].

The evolution of these matrix properties is governed by the rate and extent of polymerisation, otherwise known as the degree of cure. Values are generally expected to increase as the cross-linking density of the polymer network increases [168–170], although absolute values will be dependent upon the chemical composition of the chosen polymer [171–173]. The rate of reaction and resultant rate of modulus development in the matrix also impact upon the evolution of stresses within the laminate due to competing effects of thermal expansion and cure-induced shrinkage and the viscoelastic nature of the material, which can result in matrix cracking and geometrical distortions in the laminate [31, 174]; the impact of these defects is addressed in section 2.1.5.

The temperature above which matrix viscoelastic properties change dramatically, as the polymer transitions between glassy and rubbery states, is closely related to the degree of cure [171, 175, 176]. This glass transition temperature, T_g, is important for mechanical performance of composite laminates since it determines the upper bound of possible operating temperatures in which structural performance of the composite can be maintained and is often used as an indicator of material state.

Measurement options

Mechanical properties of the cured polymer matrix tend to be assessed by means of laboratory tests, either directly from neat polymer samples, or by inference from the composite material itself, using tests such as interlaminar (short beam) shear [177] and in-plane compression [178]. Another commonly used indicator of matrix cure state is the glass transition temperature, which again is measured by means of laboratory tests, typically using dynamic scanning calorimetry (DSC) [179] or dynamic mechanical analysis (DMA) [180]. These destructive test methods are conducted on samples which either have to be manufactured specifically for the purpose of testing or cut from a composite structure, therefore precluding them from *in situ* monitoring of matrix property evolution during a production process.

In order to determine matrix properties *in situ* during the curing process, techniques that monitor the progress of the polymerisation reaction can be used. These techniques typically monitor the extent of the reaction itself or the corresponding change in a physical property, such as those exploited by the in-mould sensing methods for resin arrival monitoring introduced in Section 2.1.3. Vibration spectroscopy techniques such as Fourier transform infra-red (FTIR) [181, 182] and Raman spectroscopy [183, 184] enable quantification of changes in chemical composition of polymer resin, and hence direct measurement of the extent of polymerisation, over the course of the reaction. Others, such as electrical resistivity [185–187] and dielectric analysis (DEA) [188–191], ultrasound [192–194], and optical-fibre Fresnel reflectometry [160, 195–197], monitor the evolution of a physical property, i.e. electrical impedance, acoustic impedance and refractive index respectively, as a result of polymerisation. The degree of cure can be determined relative to the known value for the fully cured state at a given sample temperature. Thermo-mechanical properties of the matrix can then be determined as a function of the degree of cure and T_{g} via material models generated by a series of laboratory characterisation experiments [198–201].

For the most part, these *in situ* techniques rely on physical contact between the sensor and the material under test, i.e. the composite product, and hence require the use of embedded or tool-mounted sensors. Embedded sensors, such as fibre optics or shielded cables, facilitate through-thickness measurements but their integration can add complexity to the preforming and impregnation processes, with the potential to compromise the mechanical performance of the product [202–204]. Tool-mounted sensors are typically limited to surface measurements but can be integrated into the process with minimal impact on production timescales, provided that the tooling strategy and component geometry allow.

An assessment of the outputs, relative performance and practical considerations of electrical resistivity, DEA and ultrasound cure monitoring methods was conducted by the author and presented at a conference during the course of this project [205]. From this work, the reliance on contact

with the component being manufactured and need for concurrent temperature measurements to account for the thermal dependence of the measurand were highlighted as potential limitations to the assessed methods. It was proposed by the author that these two limitations might be addressed by the use of Raman spectroscopy coupled with multivariate spectral analysis to isolate cure-dependent, thermally-stable components of the resin spectra to provide a non-contact, temperature independent method for cure monitoring of thermosetting resin systems.

Consequently, a study was conducted [206] in which a principal components regression (PCR) model was generated for a common, low temperature curing epoxy-amine resin system, in which spectral components were regressed against sample T_g over a range of cure states and sample temperatures. The model was shown to enable direct, *in situ* measurement of sample T_g for neat resin samples cured under controlled laboratory conditions, with negligible sensitivity to sample temperature; see Appendix A for details. It is expected that this technique could provide a versatile, in-process or post process option for resin state monitoring in FRP composite structures, although the impact of the fibre reinforcement constituent on spectrum acquisition, model generation and measurement performance has yet to be assessed.

2.1.5 Stress-induced defects

Internal stresses are developed within an FRP composite structure during the curing process as a result of numerous, complex, often competing thermal, chemical and mechanical interactions between the anisotropic fibre architecture, the polymerising matrix and the mould tooling. These stresses typically manifest as geometrical distortions of the structure or remain locked in the material in the case of highly constrained (e.g. tubular) geometries [207, 208]. Numerous reviews of the factors which contribute to the build-up of residual stresses [31, 209, 210] and the means to predict and mitigate the corresponding geometrical distortions and defects [211–213] have been published and will not be covered in any greater detail here.

For over-braided components, stress evolution is more likely to result in micro-cracking, delamination and wrinkles than significant distortions given the geometrical constraints of typical product designs. As for all FRP composites, higher stresses and increased risk of delaminations are generated in thick sections [174, 207, 214] where non-uniform heat distribution through the cure cycle leads to varying rates of cure evolution and associated thermo-mechanical properties [31]. Through-thickness cure-shrinkage is expected to exacerbate wrinkles resulting from excess length generation during compaction of the preform, while more open braid architectures, i.e. those with limited nesting between layers, are likely to exhibit micro-cracking in resin pockets formed between yarns [208, 215].

The quality implications of process-induced distortions and defects are application-dependent,

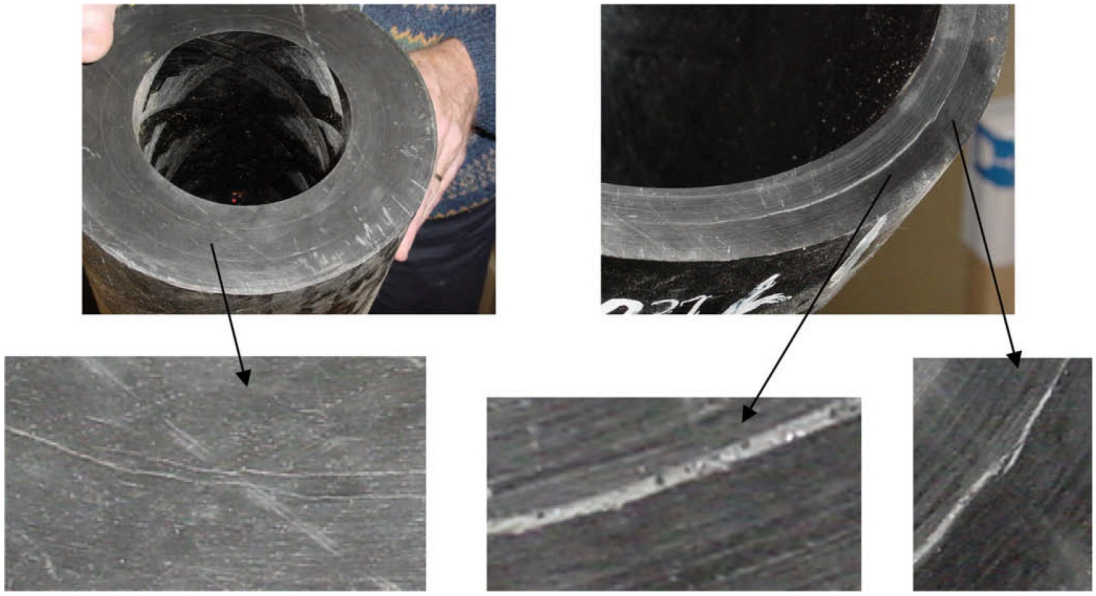

Figure 2.4: Stress-induced defects in thick, tubular, FRP composite structure; reproduced from [214]

but costly and/or labour-intensive actions are invariably required to manage their occurrence, especially where composite components are to form part of assembled structures with tight geometrical tolerances. Iterative mould cavity geometry alterations may be required in order to compensate for distortions present in the cured component; otherwise, additive and/or subtractive manufacturing methods may be used to correct the distorted geometry. Aside from any geometric implication, out-of-plane wrinkles have been shown to dramatically reduce both compressive and tensile strength of laminates, primarily as a result of interlaminar shear stresses developed under load [216–218].

Matrix cracking and delaminations constitute failure modes that can introduce significant inelastic strain to the material [219], which, in the case of braided FRP, would otherwise be considered resistant to such defects [68]. A reduction in compressive strength would be expected in the presence of delaminations [220], as well as off-axis tensile failure due to the coalescence of delaminations with transverse, intra-yarn cracks [221]. Micro-cracking also provides a pathway for moisture ingress into the material, which can cause a range of issues from matrix swelling and plasticisation to matrix-fibre interface failure as reviewed by Naebe *et al.* [222].

Measurement options

In most instances, the defects introduced to FRP structures during the curing process can only be assessed once the process has completed and the component removed from the tooling, not least because of the continual evolution of material properties as a function of reaction progress and process temperature. Resultant geometric distortions and external out-of-plane wrinkles are typically measured using industry-standard metrology techniques and systems (e.g. co-ordinate

measurement machines, laser tracking and scanning, stereo-photogrammetry), which can be used to measure specific dimensions or generate point cloud surface reconstructions as required. Inspection of internal distortions to the reinforcement structure require through-thickness sampling, either physically or using a technique such as XCT; refer to Section 2.1.2 for more detail.

The presence of micro-cracking can be assessed using microscopy techniques, often with the aid of a dye penetrant to enhance visibility [222], whilst a range of non-destructive inspection methods such as ultrasonic C-scan, thermography and radiography are suitable for the detection of larger cracks and delaminations [223, 224] depending on component dimensions, rate and resolution requirements.

Other non-destructive techniques that are available to characterise the residual stresses in polymer composites have been reviewed by Maxwell *et al.* [225, 226] and Parlevliet *et al.* [227]. These include Raman spectroscopy, which enables quantification of morphological changes in the matrix or fibre[2] as a result of residual strains at a point on the sample surface. Another is photo-elasticity [228, 229], which measures the polarisation of light transmitted through the composite material as a result of the stress fields present. However, these methods suffer from low sensitivity and complex, 3D field analysis respectively, besides the material constraints of each.

Where the tooling strategy and component design requirements allow, the development of stress-induced distortions may be monitored *in situ* using embedded fibre optic sensors. Localised strain measurements at discrete locations can be achieved with fibre Bragg gratings (FBGs) [230–232], with the option of multiple gratings, i.e. sensors, per optical fibre and multiplexing of multiple fibres [160, 233]. Alternatively, distributed strain measurement along the length of a fibre optic cable can be implemented using optical backscattering reflectometry, otherwise known as distributed optical fibre sensing [234, 235]. For more constrained scenarios, e.g. RTM, quantification of in-plane strains can provide valuable insight into the evolution of stresses within the laminate as a result of cure shrinkage, thermal expansion and part-tool interaction [211, 236–238]. This includes identification of the onset of gelation at which point there are significant changes in the viscoelastic properties of the resin [235, 236]. Longitudinal, transverse or through-thickness alignment of fibre optic sensors relative to the reinforcement enables measurement of the corresponding anisotropic strains [234, 239]. Such sensing systems can also be used to monitor the resin flow front during impregnation (as discussed in Section 2.1.3) as well as strains due to applied loads during testing or service, hence they are suitable for structural health monitoring applications in composite structures. However, the potential impacts upon the manufacturing process, i.e. to accommodate integration of optical fibres during layup, and/or the component performance tend to limit the viable applications of these embedded sensors.

[2]For carbon or Kevlar fibres only.

2.2 Opportunities to benefit from in-process measurement

This section summarises the opportunities for implementation of in-process, quality-oriented measurement capability through the over-braiding and LCM manufacture workflow as inferred from the literature surveyed in Section 2.1.

With regard to stress-induced distortions and defects, it is primarily matrix cracking and delaminations that are of concern for the constrained tubular geometries typically produced via over-braiding. Whilst sensing techniques have been demonstrated for quantification of stress evolution during resin cure, these tend to be suited to resin characterisation experiments rather than *in situ* measurement during the manufacturing process itself. Embedded fibre optic sensing techniques do provide a means to directly measure strains such as those arising from stress-induced distortions, as well as those due to applied loads, i.e. during testing or operational conditions. However, they are not considered practical for use in many instances given the complexity introduced to the manufacture process and disturbance of the material structure. The occurrence of stress-induced defects is also dependent on the stress distribution resulting from overall laminate thickness and fibre distribution throughout the matrix. Hence, monitoring of the fibre distribution and resultant preform thickness and compaction behaviour during the preforming process is likely to prove valuable in predicting and controlling such defects.

As for the determination of cured matrix properties, this capability is of interest to all FRP manufacture processes and accordingly there has been much research and development into techniques which can provide relevant information, usually via relation to the extent of reaction. Although there are inevitably opportunities to improve the performance or expand the capabilities of such techniques, as demonstrated by the author's study into measurement of T_{g} using Raman spectroscopy, it would seem that there are techniques available that would serve most requirements. The adoption of available techniques is, however, subject to the constraints of any given manufacturing process and tooling strategy; as a result, they are not commonly implemented.

Direct, *in situ* quantification of void content is no trivial thing to achieve, with most published examples requiring specific, controlled, even miniaturised material processing equipment, and intensive data processing routines. More commonly practised for LCM processes is resin flow monitoring, since the non-uniform, dual-scale liquid flow through the preform structure is often cited a major contributing mechanism to void formation. Numerous flow monitoring techniques have been demonstrated, some similar to those used for void monitoring, others based on embedded sensors similar to those used for cure state monitoring. Much work has also been conducted into the model-based prediction of preform permeability based on parameters describing its architecture. With predictive tools such as these, there is a need for *in situ* preform characterisation data, e.g. tow/yarn angles, geometries and spacings, in order to validate and parameterise models, much of

which is most readily acquired during the preforming process, although others are determined after preform compaction and hence less accessible.

The orientation of fibres in the composite structure is principally governed by the preforming process, provided that the preform does not require significant manipulation prior to the impregnation process and that it remains stable throughout it. Hence, the most obvious and accessible point at which to measure fibre or yarn angles is during the layered deposition process. Whilst such measurements can be achieved by a range of manual and image-based approaches, they are typically conducted manually. Greater utilisation of automated, image-based measurement presents an opportunity for increased measurement coverage and repeatability.

Fibre content and distribution is again determined by the preforming process, in combination with the chosen LCM strategy. For instance, where matched, solid tooling is used for preform impregnation, V_f is determined by the mould cavity design, and the amount and distribution of fibre deposited in the preform. Provided that the mould-preform fit is acceptable and the compaction behaviour of the preform is as expected, the intended V_f should be achieved. By contrast, where flexible tooling is employed, control of the impregnation process itself can be crucial to achieving the necessary V_f via control of the laminate thickness. In either scenario, thickness measurements of the preform prior to and/or during the impregnation process are vital to ensuring the design requirements for fibre content can be met, whilst data such as yarn widths and spacings, as well as relative spatial distribution of yarns between layers, provide information regarding fibre distribution. Understanding the preform consolidation achieved during deposition is particularly important for over-braided preforms, given the propensity for wrinkle formation during subsequent compaction due to excess material length and typical geometric constraints.

Based on this discussion, it would appear that the greatest opportunities to benefit from the development and implementation of in-process, quality-oriented measurement capability are presented within the preform production process itself. This follows from the observation that the arrangement and orientation of fibres comprising the preform are directly relevant to two of the five themes reviewed in this chapter, whilst indirectly contributing to a further two. Despite this and the variability that is widely acknowledged as a characteristic of dry fibre preforms, it is not uncommon for assumptions to be made regarding the structure of a manufactured preform that impact upon the outcome of subsequent processing activities, without sufficient supporting evidence. Contributing factors to this are the reliance on destructive testing methods for offline characterisation, and the size, rate and cost limitations of available non-destructive, volumetric imaging techniques. Hence, any relevant measurements that can be made during the preforming process, which are informative about the actual state of the product and the variability of the process, are bound to increase the likelihood of a successful manufacturing outcome. That is, with the proviso that those data are managed in such that they can be reliably analysed alongside corresponding

information from across the design and manufacture workflow, e.g. design, material and process setup, product verification.

In the case of over-braiding, the orientation of fibres is primarily determined by the relative orientation of yarns as they are deposited onto the mandrel, i.e. the braid angle of bias yarns. Although largely dictated by the over-braiding speed controls and mandrel geometry, this also depends upon several other process and material factors. It is, therefore, necessary to attain a thorough understanding of these dependencies in order to exert the desired level of control over this quality-defining variable. This requires a means to acquire reliable, accurate measurements of the deposited braid angle. The greater the spatial resolution and immediacy of such measurements, the greater the level of control that may ultimately be achieved.

The fibre arrangement throughout the preform is also dependent upon factors such as the yarn weight, cross-sectional shape and spacing, and the number of, and alignment between, preform layers, all of which influence the level of compaction and fibre content of the preform that is being produced. It is particularly important when producing tubular braided preforms that the compaction achieved during the deposition process is managed in order to minimise the accumulation of excess material which may jeopardise subsequent processes. In-process thickness measurements acquired between, or during, layer depositions would provide valuable information to this end.

As such, deposited braid angle and preform thickness were identified as suitable, informative data sets to be targeted in the development of an in-process measurement capability for over-braiding, which should contribute to the characterisation of process dynamics, material behaviour and manufacturing quality. The development and optimisation of just such a capability for the over-braiding facility at NCC is presented in Chapters 4 and 5 of this thesis, whilst the prioritisation of other potential in-process measurands is the subject of Chapter 3.

Chapter 3

Process variable mapping for measurement prioritisation

The value of data relating directly to quality-critical aspects of a manufactured component, such as those discussed in Chapter 2, is easy to appreciate in a scenario where the target outcome is known, the predominant influencing factors are understood, and process bounds are well-defined. For instance, in a production environment such data may enable the implementation of quality control measures to identify and address excursions from acceptable product quality.

However, where the process boundaries and (relative contributions of) variables which determine the manufacturing outcome are not well understood, data relating to typical manufacturing quality metrics can be of limited value when viewed in isolation. This is often the case for design and manufacture (D&M) research activities, during which additional measurement data and/or process constraints are typically required in order to meet the particular research objectives. Any additional measurement capabilities deemed necessary, beyond the existing capabilities for the manufacturing process in question, will tend to be established on a temporary basis for the duration of the project, with the data produced providing context for any defined quality metrics and informing the findings of the project. Whilst the findings themselves may prove valuable to the broader D&M envelope, either directly or via extrapolation depending on the scope of the research, the data generated are rarely utilised beyond the life of the project and any value they might contain for subsequent research activities is squandered. This is especially true for data generated by temporary measurement setups, since there is no continuity between projects and hence no opportunity to generate consistent, cross-project data sets.

To realise the full value of data generated during project-based D&M research activities, the data itself should be made readily accessible to other research activities, along with contextual information relating to the materials and operating conditions for which they were collected and any additional data sets. This chapter introduces a research method that was developed to support the

prioritisation of potential measurands to be included in the development of an in-process measurement capability, alongside chosen product quality metrics, which would enable a more consistent approach to data acquisition between projects. The method was trialled for the over-braider facility at NCC, the main findings and recommendations from which are presented.

3.1 Motivation

The ideal trajectory for a design and manufacture research project is to progress from a comprehensive set of functional and design requirements, along a linear workflow, arriving at the successful production of an acceptable, if not optimal, solution. If this can be achieved, costs and delays associated with re-design or re-manufacture activities which would otherwise arise due to deviation from an acceptable solution can be avoided. In reality, such deviations are often inevitable due to incomplete requirements, novel material and process combinations, or complexities of product design.

The need for re-work typically stems from a decision, or series thereof, made earlier in the workflow which has directed the workflow towards an outcome that is unlikely or unable to meet the specified product requirements. An analogy which is relevant to this discussion, illustrated in Figure 3.1, is that of a potential energy surface (PES), which represents the entire design and manufacture envelope for a (set of) manufacturing process. Upon the PES, a number of local minima exists which represent possible outcomes; some of these may be acceptable to the project, others may not. Decisions made during the workflow are intended to direct the project across the PES towards an acceptable minima, i.e. outcome, whilst inevitably reducing the remaining degrees of freedom (DoF). If the destination minima is subsequently determined to be unacceptable, energy input (i.e. cost of some description, whether that be capital expenditure, labour, time delay) is required to move back up the PES in order to transition to an alternative minima. There is, therefore, an inherent risk associated with each decision point in the workflow corresponding to the reduction in the degrees of freedom, and the breadth and accuracy of relevant information upon which the decision is made. The less comprehensive the available information, the greater the risk of incurring additional costs further along the workflow, whilst the greater the reduction in DoF, the greater any incurred costs are likely to be.

For projects for which there is a wealth of relevant knowledge or experience available to the project team, i.e. due to familiarity with materials or design requirements/component geometries, decision risks might be considered negligible. By the same reasoning, however, if projects are governed by the potential risk of an unacceptable outcome, they will likely be guided by precedent, thus minimising exploration of the wider D&M envelope and disregarding potential solutions therein. If the full potential of advanced composite materials, structures and manufacturing processes is to

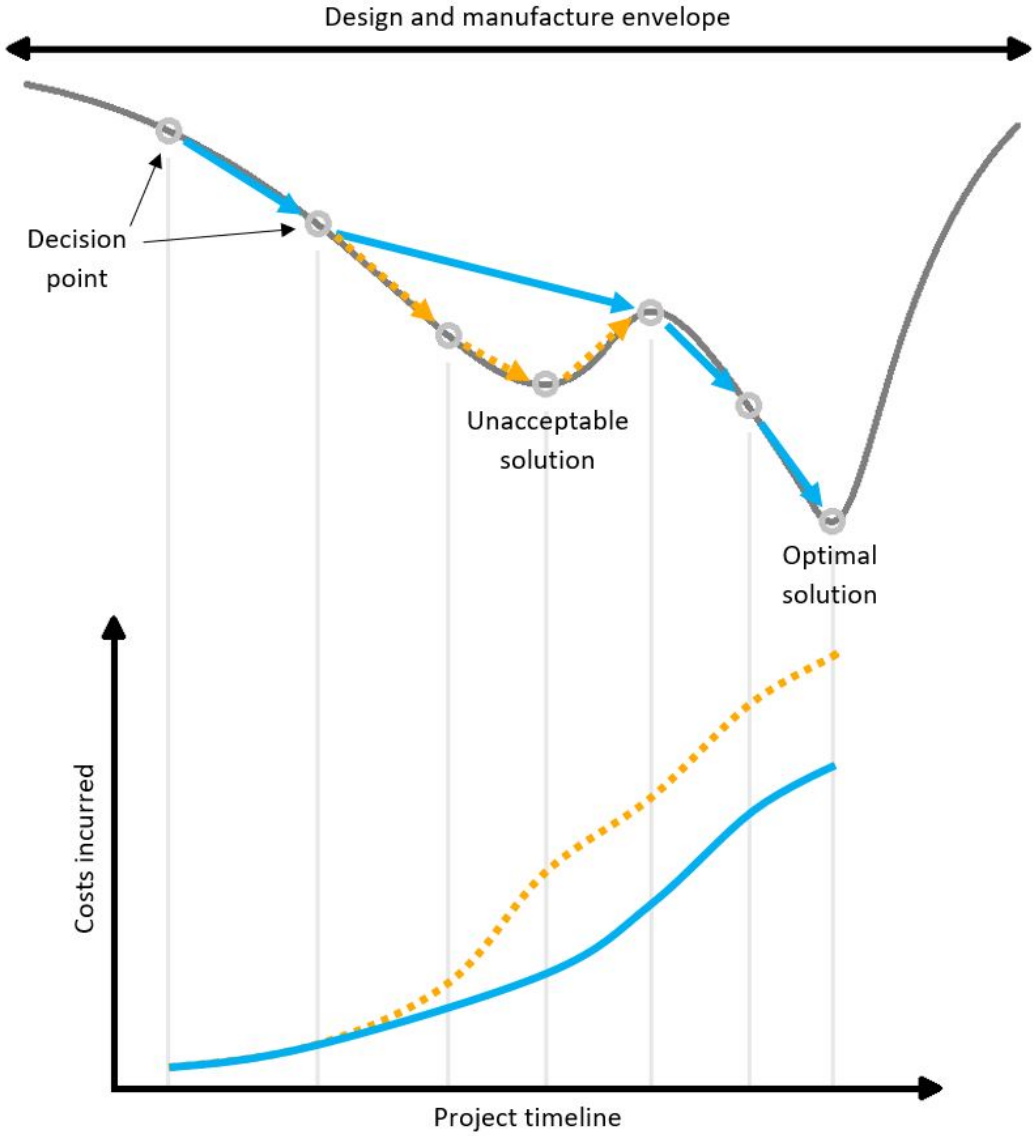

Figure 3.1: (Top) 2D potential energy surface representation of a design and manufacture envelope, on which a series of decision points resulting in both an unacceptable (i.e. local minima) and optimal (i.e. global minima) project outcome; note the divergence at the 2nd decision point, whereby one decision results in arrival at an unacceptable outcome, with subsequent additional work required in order to reach the optimal solution.
(Bottom) Illustrative profile of costs incurred during the project as a consequence of the 2nd decision point.

be realised, steps need to be taken to mitigate the risks associated with exploring unknown regions of D&M envelopes. Thus, design optimisations which exploit the advantageous material properties, and manufacturing developments which enable efficient production of those designs, may be exploited more readily.

One approach that would go some way towards achieving this decision risk mitigation is the standardised collection and management of material, process and product verification data across any and all D&M research activities for a given process; data that may or may not otherwise be acquired and managed on a per-project basis according to specific project requirements. Automation and integration of this data collection into business-as-usual activities would enable the development of consistent, comparable data sets with which to conduct data-driven research activities. Project-specific findings could then be supplemented with additional material- or process-specific insights by leveraging inherent project-to-project variability, thus expediting exploration of the D&M envelope for a manufacturing capability.

In order to implement such an approach, it is first necessary to determine the design, material, process and product variables that are relevant to the process in question. Once these have been established, the development and integration of suitable data logging and acquisition systems can commence. Whilst it might seem intuitive to implement a solution to capture every identified variable, this is rarely a practical approach to adopt, not least due to the capital investment required to do so. Aside from financial constraints, some of the variables identified may be inaccessible without disruption to the process or destruction of the product, requiring a compelling justification for their acquisition. Development of such arguments can be challenging, particularly in a research setting where the intended outcome is rarely directly related to a financial benefit, rendering typical methods such as cost-benefit analysis inapplicable without significant assumptions; i.e. what is the anticipated financial return for exploration of uncharted regions of a D&M envelope. A framework which considers the full range of workflow variables (i.e. material, process, product) and attempts to assign a non-financial value to data, based on the expected impact of data upon future research development activities, is therefore likely to prove beneficial when attempting to prioritise and justify selection of potential measurement targets. This chapter is concerned with the development of such a framework, intended to inform the strategy for implementation of process monitoring capabilities on a range of FRP composites manufacturing research facilities (at the National Composites Centre).

3.2 Research methodology

Since it is people, i.e. researchers, who are typically responsible for making decisions throughout a D&M workflow, it is pertinent that the framework should enable assessment of material, process

and product variable interdependencies based on the knowledge amongst those decision makers. This amounts to an assessment of the extent to which relationships between variables, and the sensitivity of those relationships, are understood, whether that be via the availability and use of quantitative physical models or on the basis of accumulated qualitative experience. The output would then be expected to reflect the potential value of data to those researchers.

The knowledge-based approach favoured in this work is consistent with recent published research by Thombansen *et al.* [240], which presents a framework for the development of model-based self-optimisation (MBSO) manufacturing systems. The MBSO concept aims to enable online process optimisation and quality control via embedded process knowledge, i.e. control models, and integrated sensing capability, thus increasing the autonomy of a manufacturing system to adapt to variations and disturbances. The framework relies upon a thorough, if qualitative, understanding of principal influencing process variables on product quality criteria, focusing on the translation of this knowledge into MBSO systems via the following five stages:

1. requirements analysis;
2. development of models;
3. design of sub-systems;
4. sensing;
5. actuation.

The contents of this chapter falls within the first element of the framework proposed in [240], but considers a broad process envelope as opposed to a specific production activity, and therefore assuming greater uncertainty in the understanding of variable relationships with product quality. Following the same logical consideration of process parameters, in-process and output variables, subsets of the resultant knowledge repository would be expected to contribute to the 'requirements analysis' and 'model development' stages of the MBSO framework.

Hartmann *et al.* [241] discuss the role of models in capturing domain knowledge in a format that enables model-driven data analytics, i.e. analytics that is structured by current, often detailed understanding of the domain. In doing so, they identified the importance of ensuring common data structures between models and other knowledge structures such that advances in either are mutually beneficial. To that end, this work recognises models as valuable relationship descriptors and considers how the output might be utilised alongside, and to the benefit of, existing and future modelling capabilities.

Alternative approaches by which an assessment of variable relationships for a given manufacturing capability might be implemented were considered, including literature surveys and process failure mode effects analysis (PFMEA). Whilst both are established tools in their own right, neither

was determined to meet the scope of a research capability knowledge repository; rather, they are seen as complementary to the process described here.

Literature surveys are appropriate for establishing the state-of-the-art for a particular subject matter, identifying research outcomes which may be relevant and/or applicable, and determining where opportunities for impactful research activities exists. However, findings are not always directly applicable to a specific research or manufacturing capability, nor do they necessarily reflect the knowledge base of a given research or manufacturing group; there is a distinction between findings that have been read/reviewed and those which have been implemented and/or validated. The availability of information in published literature is also likely to be limited by the desire of groups and organisations to protect intellectual property which may be embedded within a particular process or research outcome.

PFMEAs are widely used across many industries, deployed as part of risk management strategies to identify and address likely or common causes of failure, thus minimising the impact of such failures on the process performance. Implementation is reliant on historical experience to establish the severity and likelihood of occurrence in order to prioritise possible mitigation responses, with the implication that the process is already defined and parameterised. In many ways, the process presented here mirrors stages of a PFMEA, drawing on experience of a particular manufacturing process from a team of personnel comprising a range of relevant expertise, in an effort to identify causal dependencies between process variables. However, whereas a PFMEA is often concerned with the occurrence of particular events which are detrimental to process output under a given set of operating conditions, this process aims to collate knowledge relating to the underlying process behaviour which contribute to quality-critical outputs, without considering specific criteria for acceptance. Thus it may be viewed as a precursor to, or contributory resource for, project specific PFMEA activities.

3.3 Aims and objectives

The primary aim of this work was to develop a method with which to evaluate the potential research value of data relating to variables present along the design and manufacture workflow for a given manufacturing process. This value, i.e. the usefulness of data to current and future research activities, was to be derived from the interdependencies between workflow variables, particularly those pertaining to the quality of the manufactured component. The output was to be used to support the prioritisation and down-selection of potential data acquisition targets, i.e measurands, for the manufacturing process in question.

It was decided that the means of assessment should reflect the state of knowledge within a particular organisation, capability or research community. In doing so, the proposed method should

enable assessment of novel or bespoke manufacturing processes, for which the available literature or production data required to employ established research tools such as literature surveys and PFMEAs may be sparse. Hence, the assessment was to be conducted by people within that capability or community, based on their current level of understanding and perceived sensitivity[1] of the dependencies between pairs of workflow variables.

Furthermore, the output, in the form of a matrix containing the inter-variable dependency ratings, was designed with a view to functioning as a live knowledge repository, to be used, updated and expanded by future research activities. Initial development was to be conducted using a readily accessible software tool, i.e. Microsoft Excel, acknowledging that a more tailored software solution would be required to effectively implement and maintain the output as a live knowledge repository.

3.4 Method and data collection

A workshop was held in which members of the team responsible for the over-braiding research capability at NCC were asked to generate a comprehensive list of variables relating to the over-braiding manufacturing process. It was conducted by the author, leading discussions on each stage of the process workflow and collating the agreed variables. Workshop attendees comprised engineers with experience in activities encompassing customer requirements capture, material and process down selection, process and tooling design, process simulation, and manufacturing operations. As part of the activity, participants were prompted to consider the following list of variable sources:

- material selection;
- material setup;
- process setup;
- in-process;
- process output;
- environmental.

Recognising that the over-braiding process is not a stand-alone manufacturing process, but is a precursor to a resin impregnation and curing process, participants were also prompted to consider process output variables relevant to subsequent manufacturing processes as well as final product quality. Following variable identification, variables were categorised according to the following definitions, in order determine their expected behaviour during the manufacturing process:

[1] Assessment of relationship sensitivity may be expected change as the level of understanding increases and can therefore be viewed as a current perception, or awareness, of sensitivity.

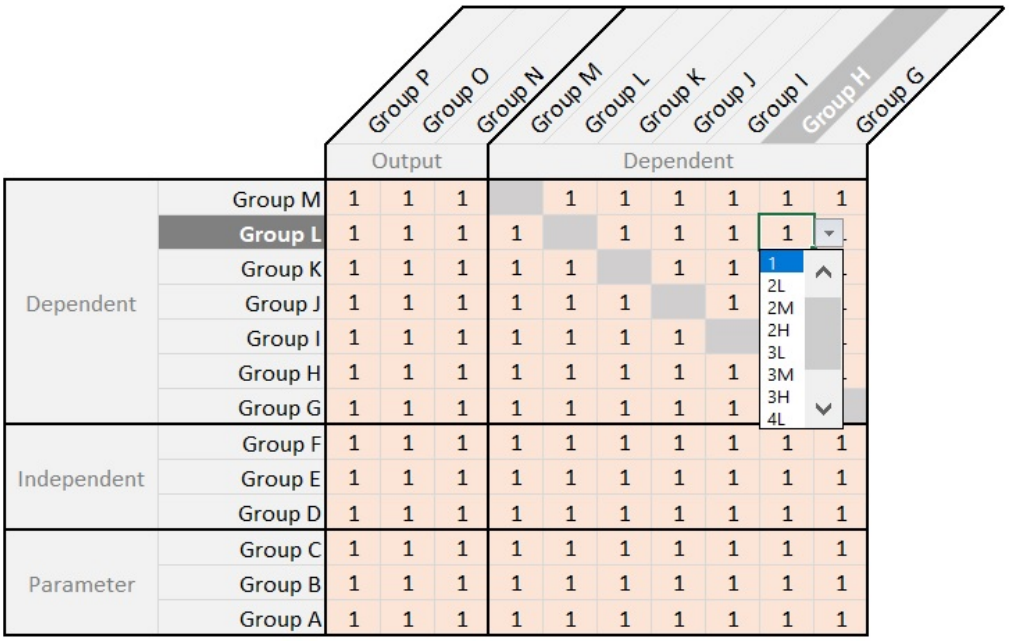

Figure 3.2: Example dependency matrix generated from a categorised and grouped list of variables, prior to population; ratings assigned to variable group pairings (i.e. at the intersection between a row and column) correspond to the dependency of the column item on the row item; ratings are assigned from a drop-down menu for each dependency, with the default value *1*, 'relationship plausible but unconfirmed'.

Parameter: - defined and fixed prior to commencing the process; i.e. a scalar value;
Independent variable: - may change during the course of the process but not dependent on the process, e.g. controlled or programmed;
Dependent variable: - dependent on process parameters and/or independent variables;
Output: - subset of dependent variables which describe the product/output of the process.

The intention was then to assess the relationship between each pairwise set of variables. However, for the 55 variables identified, the workload involved in providing a rating for each variable pairing was deemed excessive and likely to produce erroneous results, since it would have required upwards of 1100 individual assessments. The decision was therefore taken to group the variable list, where appropriate, to enable collection of fewer points of lower resolution data from a greater number of participants. Grouping was conducted only on variables within each of the 4 categories, and on items between which there was an obvious association. After grouping variables where possible, the variable list was reduced from 55 to 24.

From the categorised and grouped variable list, a matrix was generated comprising a row for each list item categorised as *parameter*, *independent variable* or *dependent variable*, and a column for

each item categorised as *dependent variable* or *output*. This ensured that only those variable groups expected *to affect* another variable group were included in the column down the left-hand side of the matrix, and only those groups expected *to be affected by* other groups were included along the top. The rating entered in the cell at the intersection between a row, α, and a column, β, therefore represented the influence of α over β, or the dependency of β on α. *Output* rows were omitted since they were not anticipated to have any dependents in the context of this activity, whilst conversely, *parameter* and *independent variable* columns were omitted since they are inherently not dependent on other items. An example matrix is provided in Figure 3.2, in which there are 3 *parameter*, 3 *independent variable*, 7 *dependent variable* and 3 *output* groups. Here, the rating being entered is between the row containing Group L and the column containing Group H and therefore relates to the dependency of Group H on Group L. The resulting dependency matrix for the over-braider consisted of 232 individual pairwise comparisons.

Three participants from the initial variable identification workshop were each asked to populate a copy of the dependency matrix, providing a rating for each intersection, i.e. what is the dependency of each column on each row, based on their knowledge and experience. The participants were selected to cover the broadest possible range of expertise relevant to the over-braiding manufacturing process:

- a process specialist, with experience in the design and manufacture of over-braided components and other textile-derived manufacturing processes;
- a simulation specialist, with experience of a range of process simulation capabilities for over-braiding, as well as other composite manufacture;
- a materials and process selection specialist, with experience of concept design, material selection and resin impregnation manufacturing processes.

The rating system developed for this activity differentiated between the level of understanding and the sensitivity of a pair-wise relationship. Understanding, i.e. the extent to which a relationship between variables can be described, was rated on the scale *0 - 4*, where:

0 = No plausible / significant relationship;
1 = Relationship plausible but unconfirmed;
2 = Relationship confirmed but unvalidated;
3 = Partially validated relationship / model available;
4 = Fully validated relationship / model available.

The analogy to the existence of a mathematical model in these definitions was made to exemplify the description of a relationship. In order to generate a mathematical model of a physical process,

some equation (or set thereof) is required with which to represent the observed dependency between model variables. Generally speaking, the greater the fidelity or validated range of the model, the greater the understanding of the underlying physical relationship. The default rating for all relationships was set to 1, i.e 'plausible but unconfirmed', in order to avoid the dismissal of relationships which are as yet unexplored but physically plausible; participants were instructed only to enter a rating of 0 if the absence of a relationship has been confirmed or is physically implausible.

Sensitivity of relationship was rated as low, medium or high, according to the following guidance:

$$\begin{aligned} \textit{Low} &= \textit{change in Column } \alpha \textit{ (\%)} < \textit{change in Row } \gamma \textit{ (\%)} \\ \textit{Medium} &= \textit{change in Column } \alpha \textit{ (\%)} \approx \textit{change in Row } \gamma \textit{ (\%)} \\ \textit{High} &= \textit{change in Column } \alpha \textit{ (\%)} > \textit{change in Row } \gamma \textit{ (\%)} \end{aligned}$$

Where a percentage change in certain variables is not realistic, e.g. changing yarn material type from carbon to glass, participants were instructed to interpret these definitions as:

$$\begin{aligned} \textit{Low} &= \textit{little to no change in the dependent;} \\ \textit{Medium} &= \textit{similar behaviours exhibited to a significantly lesser or greater extent;} \\ \textit{High} &= \textit{change in the types of behaviour exhibited by the dependent.} \end{aligned}$$

Sensitivity ratings were only applicable where an understanding rating of 2 or more was assigned by the participant, since the notion of sensitivity implies the existence of a level of understanding sufficient to provide some description of the relationship.

Once the participants had each completed a copy of the dependency matrix, their responses were collated and compared to assess the level of agreement between them. A review session was then conducted with the participants in which significant disagreements between ratings, e.g. low vs high sensitivity, were discussed to determine the source of the discrepancy. Only in instances where a discrepancy was caused by misinterpretation of variables or variable groupings, or ambiguity resulting from the rating system, were participants asked to amend their rating accordingly; otherwise ratings remained unchanged.

Finally, a single matrix was compiled from the responses, to represent the aggregated viewpoint. This was achieved by taking the most common (i.e. modal) ratings for understanding and sensitivity for each variable pairing where possible. Where no modal value existed, the rounded average value of ratings greater than 1 was used, since a rating of 1 could indicate a personal lack of understanding, thus skewing the calculated average.

Upon completion of this process, the resultant matrix was available for use in the as-populated form (i.e. with grouped variables), or in an extrapolated full matrix form using the complete, ungrouped variable list, in which the rating for each variable group pairing was applied to all dependencies between the constituent variables. Findings presented in Section 3.5.1 are concerned

only with the grouped variable matrix form, whilst a discussion pertaining to applications of the expanded form is made in Section 3.6.

3.5 Results and discussion

3.5.1 Initial findings

The results presented and discussed in this section are those generated for the over-braiding capability at NCC. The dependency matrix presented in Figure 3.3 was compiled from the responses of three subject experts; variables within each variable group are provided. The full list of variables identified as part of this process, along with variable categorisations, groupings and definitions, is included in Appendix B. Whilst there may be a number of ways to analyse the information contained within the dependency ratings matrix, this initial discussion is focused on the number of *medium* or *high* sensitivity ratings assigned to each variable group based on the dependency of other variables. This should serve as an indication of the influence those variables exert over the outcome of the manufacturing process and, hence, of how informative the corresponding data sets are likely to be.

Parameters

All groups categorised as *parameter* (i.e. those determined prior to, and remaining constant during, the process), with the exception of *material preparation*, received 9 or more *medium* and *high* sensitivity ratings out of a possible 12. This is unsurprising given that these groups are comprised of design and setup variables, which one would expect to influence the process. The lower number of *medium* and *high* ratings for *material preparation* is perhaps a reflection that the primary purpose of items in this group is to facilitate processing of the yarns with minimal process-induced damage, and hence their impact on other process variables may not be well understood. *Material preparation* also has the highest number of ratings equal to *1* for understanding, i.e. 'relationship plausible but unconfirmed', which supports the previous statement.

Items in this category will necessarily have been determined prior to execution of the over-braiding process, i.e. during product and process design, or process setup activities. The corresponding data should be recorded elsewhere in the workflow for example, technical drawings, computer aided design (CAD) models, or a manufacturing instruction sheet. The challenge, therefore, is not how to measure these variables but how to ensure that the corresponding data can be readily accessed alongside in-process measurement and quality data as and when required. Ideally, there would be a single source of truth for each of these *parameter* variables, with which other variable data can be linked. However, this is rarely achieved due to the variety of tools and processes

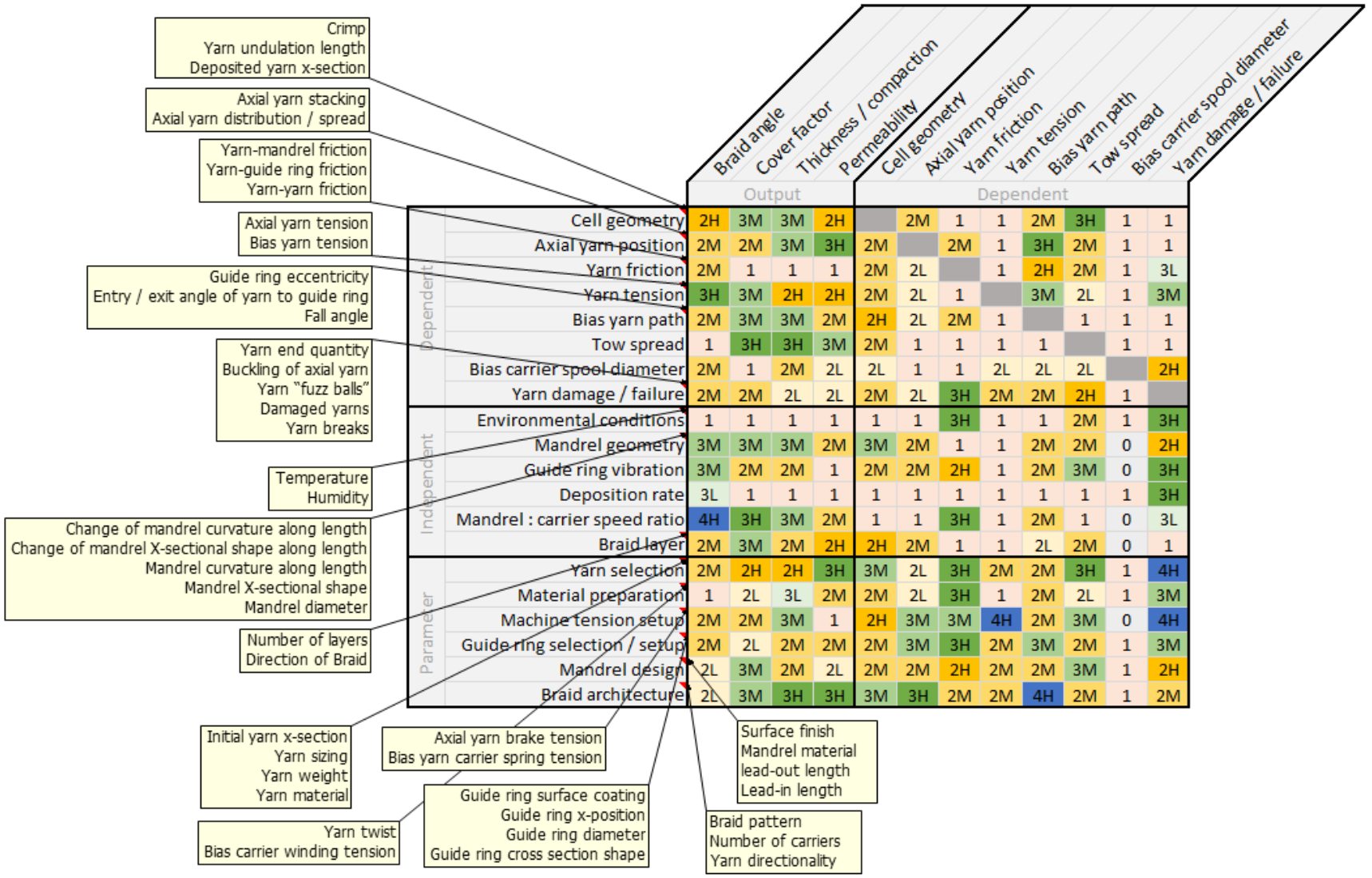

Figure 3.3: Variable dependency matrix for the over-braiding process compiled from the responses of three subject matter experts. Each cell with a rating relates to the dependency of the column variable group on the row variable group; variables within each variable group are provided in the boxes outside of the matrix itself. Ratings are colour coded based on the level of understanding assigned (i.e. 0 - 4), with shading indicating the sensitivity (i.e. *L, M, H*).

involved in a design and manufacture workflow and the general lack of interoperability between them, meaning that considerable effort can be required to find and access the various data sets when they are needed.

Independent variables

In the *independent variable* category (i.e. those which are determined prior to, but may vary during, the process), two groups received 9 M or H sensitivity ratings, namely *mandrel geometry*[2] and *guide ring vibration*; these groups may be considered as high(er) priority targets, whereas *deposition rate* and *environmental conditions* received just 1 and 3 M/H ratings for sensitivity, respectively, and hence might be considered low priority. Again these low sensitivity counts coincide with a high proportion of 'relationship plausible but unconfirmed' ratings for understanding in each case.

Generally speaking, the *independent variables* are more involved to capture than *parameters* since they are dynamic in nature, relating to control of the braiding machine, i.e. vibration motor frequency and amplitude, and mandrel traverse co-ordinates, as well as the machine setup. For example, in the case of *mandrel geometry*, the distance between braid and guide rings would be required as well as the mounting position of the mandrel relative to the traverse mechanism and the position of the traverse mechanism during the process in order determine the instantaneous geometry at the point of yarn deposition. This information may be defined in a process simulation and used to generate the machine program, although it is possible that the relative positions of mandrel and machine components differ from the simulation in reality. Capturing the associated data for these *independent variable* groups during the process is, therefore, necessary to verify process performance. For dynamic variables relating to machine control, these would realistically be acquired from the machine control system, in which case a large range of variables are likely to be accessible without the need for prioritisation. The exception are those relating to braid layer, since the number of deposited layers is not explicitly captured within the control system, unless each layer has an individual control program. This information could be provided via a manufacturing execution system if it exists, otherwise some other approach to demarcate the transition between layer depositions would be required.

Although seemingly low priority based on process sensitivity, *environmental conditions* in the manufacturing cell could be measured inexpensively with a standalone device or via existing facilities management infrastructure, enabling an increase in the current low level of understanding about the affect of these commonly overlooked variables on the process.

[2]This group refers to the instantaneous mandrel geometry and cross-section at the point of yarn deposition, as opposed to the overall mandrel geometry which is determined during the design phase and remains constant during the over-braiding process.

Table 3.1: *Dependent variable* priority based on sensitivity *of* other groups

	# of M and H sensitivity ratings
Variable group	*Total (Output)*
Axial yarn position	8 (4)
Yarn tension	7 (4)
Cell geometry	7 (4)
Yarn damage / failure	7 (2)
Bias yarn path	6 (4)

Dependent variables

The final category to consider is *dependent variable* (i.e. those which vary during the process as a result of design, setup and control variables), for which the number of M/H sensitivity ratings received varied between 3 and 8 of a possible 11. Of these, *axial yarn position* received the highest number, followed jointly by *cell geometry*, *yarn tension* and *yarn damage / failure*, as shown in Table 3.1. With the exception of *yarn damage / failure*, these high sensitivity ratings were driven by the sensitivity of the defined *output* variables.

There is a distinction to be made between variable groups which describe the process and those that describe the product, which has implications for accessibility of associated measurements. For instance, *cell geometry* is concerned with the 3D structure of the deposited braid[3] which is not trivial to acquire during the braiding process itself. Whilst systems exist which are capable of performing the necessary data acquisition, process integration is likely to require a trade-off between resolution, preform areal coverage and process rate, and therefore not necessarily practical in all instances. *Axial yarn position* information could be acquired more readily than cell geometry, e.g. using visual means; however, this variable group is only relevant for triaxial braiding operations and therefore may be of limited value.

On the other hand, *yarn tension*, i.e. the tension along each yarn during the process, describes the effect of the process on the material. Potential measurement solutions need to consider the large number of individual yarns, the variability in tension along a single yarn and the motion of bias yarn carriers around the braid ring. Therefore, whilst the measurement itself may not be challenging, sensor integration with the process to achieve per-yarn measurement is likely to require a complex acquisition system. The *bias yarn path* group is also concerned with the process itself, and as for *yarn tension*, monitoring the trajectory of individual yarns as the carriers move around the braid ring is not a trivial operation. However, since yarn trajectory is predominantly determined by the carrier location, it may be more feasible to infer from the shape of the interlaced web of yarns formed between carriers and mandrel at certain target locations around the braid ring. Either way,

[3] Aside from the braid angle which was identified as an *output* variable in its own right.

Table 3.2: *Dependent variable* priority based on sensitivity *to* other groups

	# of M and H sensitivity ratings
Variable group	*Total (Dependent)*
Cell geometry	15 (6)
Yarn spread	15 (5)
Bias yarn path	14 (5)
Yarn friction	13 (4)
Yarn damage / failure	13 (3)

if implemented, measurements relating to these two variable groups are likely to provide relevant data for the vast majority of braiding operations.

Yarn damage / failure straddles both product and process description, since damage and failure occur during the process and may be evident in the deposited braid. Accumulation of damage along the yarn path from spool to mandrel might also be expected to affect the processing characteristics of the material; this is consistent with the relatively high dependency of other *dependent* variables indicated by these results. Given its cumulative nature and the potentially large number of individual yarns used in the process, per-yarn quantification of yarn damage during the process is likely to be difficult to implement, not least because it typically requires destructive, off-line test methods. A qualitative, visual-based measurement similar to that made by process operators may be possible, although implementation of such a capability would require a machine learning approach with a suitably large training data set, whilst a broken yarn count would be trivial to implement but much less informative.

Given the complexities and compromises identified for each, it may be not be appropriate to prioritise variable groups in the *dependent variable* category on the basis of sensitivity *of* other variable groups alone. For this category, it is also possible to consider the sensitivity of a given variable group *to* other groups as an indication of how informative the acquired data are likely to be. From this perspective, the findings are the same whether we consider sensitivity to all other variable groups, or only to other *dependent variable* groups, as shown in Table 3.2.

Cell geometry again features highly, which is not surprising given that it relates directly to the product structure, and would therefore be expected to be sensitive to other variable groups. *Yarn spread* received the second most ratings, despite not featuring in the top five based on the sensitivity *of* other variable groups, as was the case for *yarn friction*. A meaningful in-process measure of yarn spread could perhaps be made at the point where yarns pass over the guide ring[4] via contact or visual means, although this would be complicated by the density and motion of the yarns at that location; it may be also be inferred from *cell geometry* measurements, i.e deposited

[4]Provided that a guide ring is used in the braiding setup.

yarn widths on the mandrel, and thus not a priority in itself. Meanwhile *yarn friction* covers yarn-yarn interactions, of which there are many, as well as yarn-guide ring and yarn-mandrel interactions; whilst coefficients of friction may be measured off-line for a particular braiding setup, variations may be expected during the process due to yarn variability and process-induced yarn damage. It would be more feasible to monitor the effect of such variations in other variables, such as yarn tension or fell angle of yarns, than via direct in-process measurement.

The third highest number of ratings was received by *bias yarn path* which also appeared in the top five for sensitivity *of* other variable groups. With medium or high sensitivity to five other *dependent variable* groups, this group is likely to provide information relating to other variable groups that are challenging to measure directly, e.g. *yarn tension* and *yarn friction*, as well as its relevance to the specified *outputs*.

The third group to appear in the top five for both sensitivity *of* and sensitivity *to* other variable groups is *yarn damage / failure*. However, the indication is that it is less informative with regards to other *dependent variables* and less relevant to *outputs* than *bias yarn path*, coupled with the challenges of in-process quantification already identified.

Recommendations

Based on a sensitivity-based assessment of the dependency ratings presented in Figure 3.3, and a brief consideration of measurement accessibility, the following recommendations for implementation of logging or measurement systems in support of the over-braiding research facility might be made:

- Prioritise *cell geometry*, *bias yarn path* and *yarn damage / failure* measurements from the *dependent variable* category as these are expected to be informative with regards to the specified *outputs*, as well as other, less accessible *dependent variables*;
- Gain access to the braider control system to enable the recording of a large range of temporal *independent variable* data sets, since these may be used to describe the state of the process at any point in time, e.g. mandrel location, and thus help to explain behaviours in *dependent variable* measurements;
- Enable the recording of all *parameter* variables in a manner such that the values are accessible alongside in-process data, as this will provide the context to ensure the re-usability of manufacturing data sets.

3.5.2 Observations and limitations

As conducted in this research, the variable dependency assessment method is reliant on the knowledge, experience and engagement of participants. Ensuring a common understanding of objectives,

requirements and definitions among the participants is therefore essential during its implementation. This knowledge-based approach to data collection was a conscious decision during method development as it allows for application to bespoke or novel processes, about which there may not be a wealth of documented research. For more established processes, however, it does risk neglecting published research findings that may be relevant, and should therefore be supported by literature surveys as appropriate.

The assessment method also presents a number of challenges, not least of which is ensuring consistent application of the rating system by different participants. The scales and corresponding definitions for assessing understanding and sensitivity were devised to be applicable to the broadest possible range of relationship types, whilst providing sufficient differentiation to enable meaningful analysis of the results. However, this flexibility inevitably allows for a level of subjectivity in responses, particularly in the case of non-linear or discontinuous relationships such as those relating to *yarn selection* or *mandrel geometry*. When comparing the ratings assigned by the three participants in this study, a general trend was observed whereby the responses of each participant exhibited a varying degree of optimism or pessimism. For instance, the ratings assigned by the simulation expert tended towards lower levels of understanding and also sensitivity of relationships, whilst those of the materials expert tended towards greater levels of both understanding and sensitivity; the responses of the process expert tended towards the middle ground for both ratings. A spread of responses is to be expected in such an exercise given its subjective nature, thus it is necessary to obtain input from experts with a range of backgrounds and experiences to minimise the impact of bias on the outcome. Three participants is, arguably, an insufficient number to produce a reliable, repeatable outcome upon which to base decisions. The study presented here would have been improved by incorporating responses from, for example, the machine manufacturer and process operators. Nonetheless there is value in testing the approach to understand its pitfalls and limitations in order to develop it further.

Responses might also have been weighted based on the level of confidence in each assigned rating. However, this was not allowed for directly in the method, since the concept of confidence is closely aligned with the 'understanding' aspect of the rating system. For very low, or no, confidence in the existence of an inter-variable dependency, the default value of *1* would be expected, whilst a rating of *4* implies an amount of supporting evidence and thus greater confidence in the associated sensitivity.

A further challenge is ensuring a common understanding of the terminology used in identifying the variables and variable groups. Despite agreeing a terminology for use in the over-braiding case study as part of the initial workshop, failure to provide a glossary of terms to participants for reference during matrix population resulted in a number of anomalies between responses. These were addressed in a review session with all of the respondents, the purpose of which was to identify

and rectify any discrepancies owing to misinterpretation of terms rather than seek common ground for all dependency ratings. This additional session would ideally be avoided as, in this case, it took 3 hours to conduct and would be both costly and impractical with a larger number of participants. It was, however, valuable to highlight the misunderstanding that can occur when conducting a knowledge capture exercise such as this, the majority of which arose from unfamiliar or ambiguous terminology. This issue is particularly relevant to over-braiding and other processes originating from the textile industry that are now practised within composites manufacture, for which the textile-based terms are inconsistent with those used by, or unfamiliar to, the composites industry. Some examples include the use of 'yarn' or 'tow' for the material format used in braiding, and the use of 'bobbin' or 'spool' for the item onto which the material is wound and then unwound during the process. Resolving issues around terminology is critical to avoid ambiguity during population of the dependency matrix and hence ensure consistency between participant's ratings.

Besides the output of the method, i.e. the variable dependency matrix, the value to be gained from the initial variable identification workshop also became evident during method development. This was observed during the over-braiding case study presented here, as well as during another study relating to a bespoke, multi-stage dry fibre preform deposition process recently commissioned at NCC which is not presented in this work. Discussions between a host of stakeholders and subject-matter experts, i.e. designers, operators, structural analysts, etc., on topics relating to the manufacture process itself yielded much constructive debate regarding variables arising throughout the D&M workflow and their perceived relevance to manufacturing quality. Their discussions were key to compiling a comprehensive list of relevant variables required to implement this kind of dependency assessment method, but also highlighted some fundamental assumptions that should be challenged and opportunities to benefit from increased knowledge sharing between research capabilities.

3.6 General discussion and recommendations for implementation

The requirement for data acquisition within any given project will vary depending on the specific aims and objectives of that project. Some may look to exploit known, defined dependencies in order to realise particularly challenging tolerance criteria for one of the *output* quality variables, for example braid angle. In such a scenario, variable groups might be prioritised on the basis of the sensitivity of their relationships with that particular *output*, either directly or indirectly. For instance, where preform permeability was of particular concern, resources might be focused on monitoring and controlling the deposited cell geometry, axial yarn positioning and yarn tension due

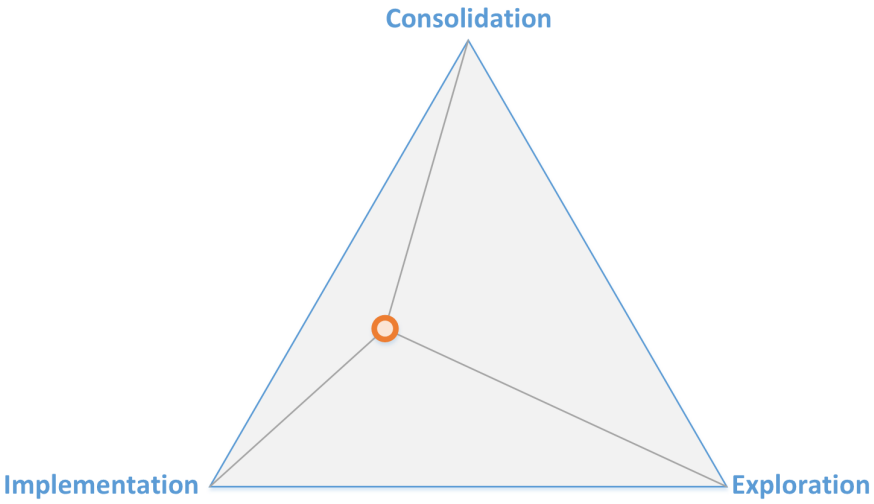

Figure 3.4: Research projects will seek to implement, consolidate and explore variable relationships to differing degrees.

to the indicated high sensitivity of permeability to these dependent variables. The chosen braid architecture, including the number and direction of deposition of individual layers, and the tension setup of the machine would consequently be highlighted as variables of interest. Thus, it would be possible to target project resources towards implementing, or improving, measurement capability for material and process variables expected to provide most value to the project.

Another project may strive to consolidate or advance the understanding of relationships between certain variables that are suspected to be highly influential but as yet poorly understood. In this case, the prioritisation of measurement targets might be focused around variable groups which received a greater number of *2H* or *3H* ratings, for instance *yarn tension*. Alternatively, those variable groups with a large number of *1* ratings, i.e. 'relationship plausible but unconfirmed', might be prioritised in order to explore those less well understood relationships and hence determine their potential to influence the process. In reality, there is likely to be some combination of these requirements for implementation, consolidation and exploration of variable dependencies, as illustrated in Figure 3.4.

The initial assessment of results presented in Section 3.5.1 demonstrates one way in which the information collated and presented within the variable dependency matrix might be interpreted, i.e. to inform a decision making process regarding instrumentation of a manufacturing process, based on relative sensitivity of, and to, variables. The project requirements in this instance were more heavily focused towards implementation and consolidation of known relationships. Whatever the chosen approach, it would be advisable to use the matrix alongside, rather than in place of, other available resources.

Whilst offering a means to evaluate the expected value of data relating to variables within a

process in a semi-quantitative manner, this will only be advantageous if care is taken during the matrix population and maintenance to ensure accuracy and consistency of ratings. One way to do this would be to substantiate ratings with evidence, e.g. references to project reports, model documentation, etc. where possible, which would serve as validation and enhance the value of the matrix as a knowledge and reference repository. Ideally, this would have been performed for the over-braiding case study presented, however the request for participants to provide supporting references was not wholly adhered to; this should be prioritised in any future implementations.

Despite the relative simplicity of the over-braiding manufacturing process, at least in terms of the number of process stages and controls, the scale and complexity of the resulting variable dependency matrix illustrates the challenge facing research teams attempting to explore the potential design and operational envelope of the process. However, the increasing prevalence of digital technologies within the product engineering arena offers the composites manufacturing industry an opportunity to do just that. Until recent years, the management of data arising throughout a design and manufacture workflow has been a labour intensive and predominantly paper-based activity, both in regards to collation and storage, as well as access and utilisation. The tools and technologies are now becoming available to automate this data management, enabling data acquisition, management and analysis to be conducted on a much more comprehensive scale, whilst freeing up resources to discover the value of the data itself. Whilst a potentially valuable tool for the management of knowledge acquired by conventional research projects, it is as a framework to manage the findings from digitally-enabled, data analytics research activities where a knowledge repository such as that presented here is anticipated to offer the greatest benefits.

The final paragraph of Section 3.4 raised the option of expanding the grouped variable matrix, as presented in Figure 3.3, to produce a full variable dependency matrix containing a row and/or column for each of the individual variables. The expanded matrix was deemed impractically large for the purpose of the knowledge capture method that was being developed due to the time, and associated cost, involved in multiple participants providing an assessment for over 1100 individual variable pairings. Additionally, it would be challenging for each participant to maintain focus and clarity of thought when presented with such a large number of individual but inter-related relationships, jeopardising the reliability of the results. For these reasons, variable grouping was undertaken to produce a more manageable, grouped variable matrix, containing 232 variable group pairing, i.e 1/5 of the number in the full matrix. However, it is envisaged that the resolution offered by the full matrix could be recovered as part of ongoing activities to maintain the dependency matrix as a live knowledge repository. Whilst all variable (child) pairings underlying a grouped variable (parent) pairing would initially be assigned the rating of the parent pairing, the child sub-matrices would be revised as and when greater detail was required. For example, when determining which elements of *bias yarn path* would be the most informative to monitor in relation to the the effects of

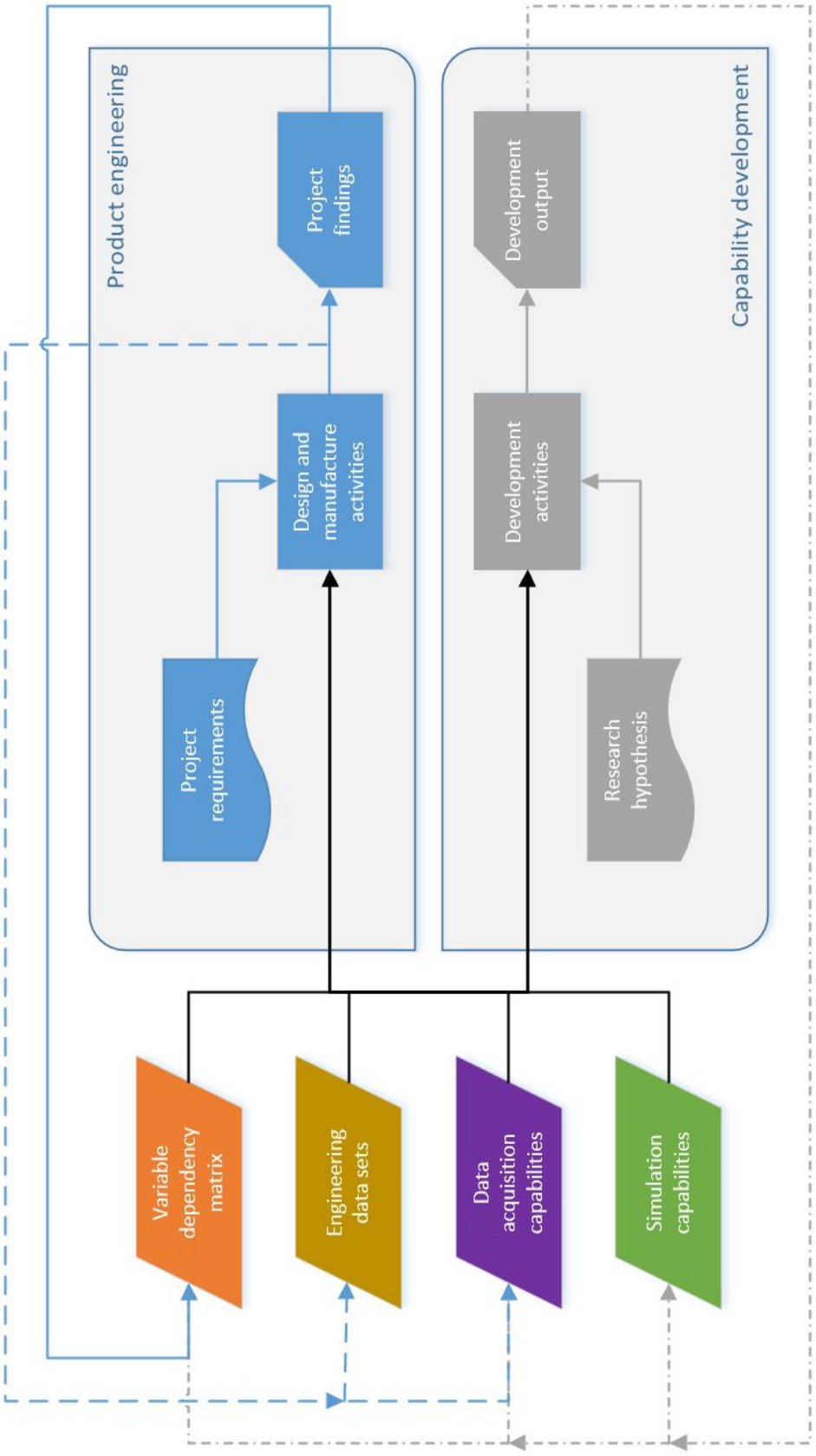

Figure 3.5: Illustration of the workflow by which a live knowledge repository in the form of a variable dependency matrix might be incorporated into regular project-based research activities and thus maintained and updated.

yarn friction. Similarly, upon completion of research activities, ratings would be updated to reflect the findings of the research.

The proposed workflow by which the matrix-based knowledge repository might be deployed and updated alongside other resources in a product engineering research and development scenario is outlined in Figure 3.5. The dependency matrix, historic engineering data sets, data acquisition and simulation capabilities may be called upon to deliver, either, project-driven product engineering activities, or capability development activities as necessary, depending on the specific project requirements or development objectives. Considering a product engineering project, additional data acquisition capabilities that may have been implemented, as well as any data sets generated from design and manufacture activities, will contribute to their respective resources; upon completion, specific project findings would be expected to provide evidence with which the update the dependency matrix. As for a capability development activity, the output would typically be expected to contribute to the data acquisition or simulation capabilities depending upon the objectives; in the case of a data-driven research activity, however, the output might yield might new insights into variable relationships and thus inform updates to ratings in the dependency matrix. If kept live and updated in this manner as a matter of course, reliable information at the full, expanded variable level could be developed iteratively over time, thus increasing the value of the repository.

Recommendations for future development and implementation include:

- The dependency matrix provides a means to perform some level of variable prioritisation based on expected research value, however, the method of analysis is open to interpretation based on project requirements.
- Where appropriate, ratings should be supported by evidence (e.g. project reports, model documentation) as a mean of validation.
- A comprehensive glossary of terms found in the defined list of variables should be supplied to all participants providing variable dependency assessments to mitigate ratings discrepancies arising from misinterpretations. This should include descriptions that state any alternative terms.
- A tailored software implementation for matrix population and management would be required to realise its potential as a live knowledge repository, which should supplement, or integrate with, existing reference and data management systems and procedures.

Chapter 4

Development of an in-process measurement capability for over-braiding research

In this chapter, the in-process measurement capability developed for the over-braider at NCC is presented, alongside a review of state-of-the-art process measurement systems for braiding technologies presented in scientific literature. The aims and objectives of the capability development are outlined, as well as the system design requirements and constraints. The system configuration is then described in detail, followed by the measurement procedures for the target quality metrics, namely braid angle and preform thickness.

4.1 Literature review of in-process measurement applications for (over-)braiding

Published scientific literature relating to the development, implementation and evaluation of in-process measurement systems for braiding and over-braiding processes is limited to a handful of institutions, each with varying approaches and motivations for system development.

A real-time image-based monitoring system was developed by researchers at Auburn University [242, 243], utilising low-cost webcams to track braid point position for tubular braids in two planes, i.e in the plane of the braid ring and perpendicular to it, as illustrated in Figure 4.1. This enabled detection of faults arising from yarn tension irregularities, as required in order to prevent subsequent yarn breakage. Braid formation angle was also measured from the angle made by yarns and the braid axis. A single computer system was used to operate image acquisition and analysis software, as well as the braid haul-off control program. Integration of the measurement system with the braiding

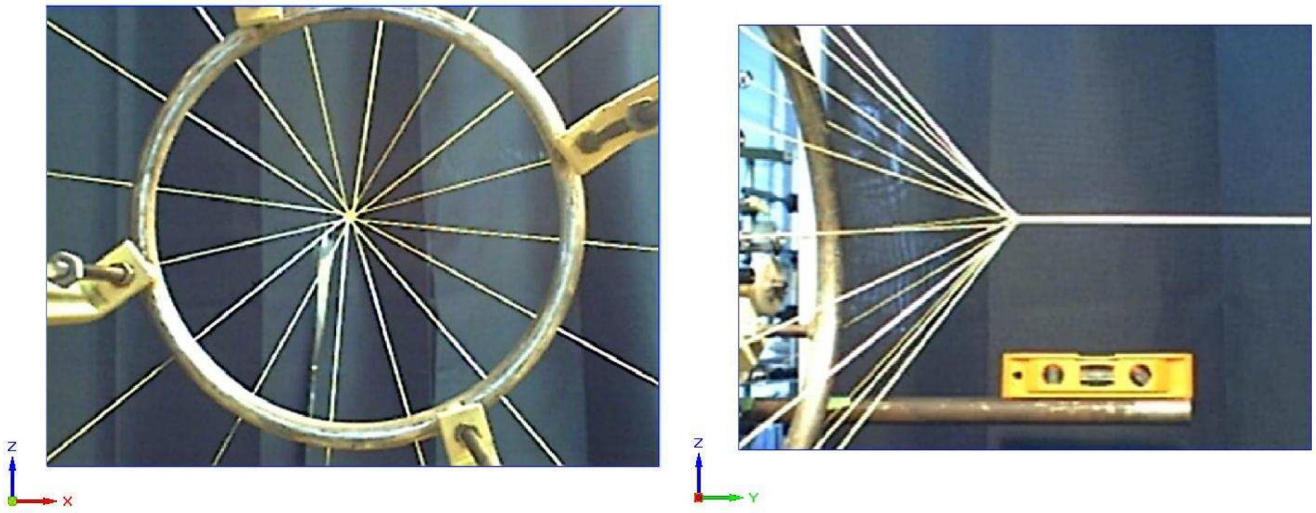

Figure 4.1: Braid point tracking in two planes as developed by researchers at Auburn University; reproduced from [242].

machine was implemented by way of event-triggered image acquisition based on machine travel intervals. Although the imaging techniques developed have limited applicability to over-braiding due to the small size of the braid machine and the absence of a mandrel, the setup resembles the basis of a control and monitoring platform upon which future system developments and research activities may be based.

An in-process braid angle measurement capability has been developed by Hunt and Carey for an axial over-braiding machine at the University of Alberta, Canada [105, 244]. The system is based on automated image analysis, via Fourier transform analysis, of high-resolution images acquired using a machine vision camera mounted perpendicular to the mandrel surface under diffuse light emitting diode (LED) lighting as illustrated in Figure 4.2. It was designed for use with straight, constant cross-section (i.e. tubular) mandrels, and able to account for the effects of mandrel curvature on the measurement output as determined *a priori*. The stated motivation was improved quality assurance relative to existing manual measurements. The measurement technique employed was found to be relevant to the aims of this project, and hence forms the basis of the braid angle measurement capability described herein.

Researchers at Istitut für Textiltechnik (ITA), RWTH Aachen University, have implemented in-process measurement of braid angle and cover factor for preforms produced over constant cross-section mandrels via radial over-braiding. Measurements have been achieved using the commercially available APODIUS Vision System (AVS) mounted at a fixed position relative to the braid ring, beyond the plane in which yarns converged on the mandrel, i.e. convergence plane. The AVS has been utilised in the development of a model-based self-optimisation (MBSO) feedback control

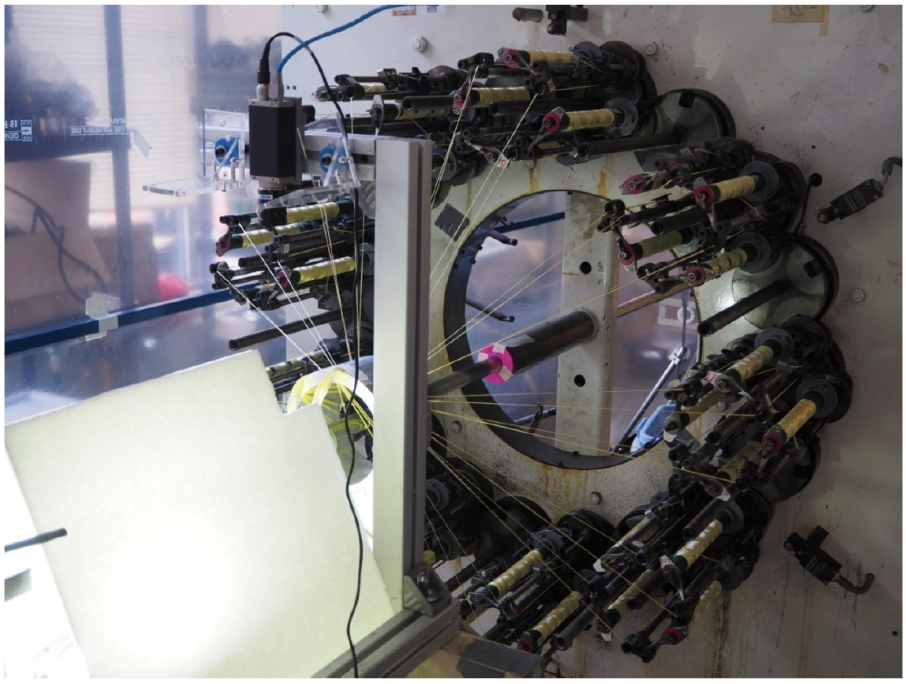

Figure 4.2: Camera and lighting setup installed on radial braider by Hunt and Carey for braid angle measurement system; reproduced from [244].

system for braid angle [245], in which haul-off (c.f. mandrel) speed is controlled for a constant carrier rotational speed, although only simulated results have been published to date. Integration of the measurement system and control software was required to achieve this outcome, whilst a limitation of post-deposition braid angle measurement for control applications was identified in the control system response lag due to the distance between the convergence plane and measurement system location.

The AVS, pictured in Figure 4.3, has also been utilised in cover factor measurements of glass-fibre "sleeves" in an investigation into the effect of guide ring vibration on yarn width [246]. Frequency and amplitude measurements of guide ring vibration were acquired by means of a piezoelectric sensor attached to the ring itself, with the amplified signal received by an oscilloscope. There is no indication as to whether the measurement systems in this study were integrated with the process or each other, but the findings suggest that this may be a worthwhile endeavour to enable some level of process control over deposited yarn widths.

In a separate development, an active carrier system incorporating a strain gauge and electric motor within each carrier (see Figure 4.4) has been implemented on a 144 carrier radial braider [247] to enable individual measurement and control of bias yarn tension during the process, above and beyond the control provided by the existing mechanical tensioning system. Whilst the performance and associated benefits of this system have yet to be evaluated, it is expected to enable reduction

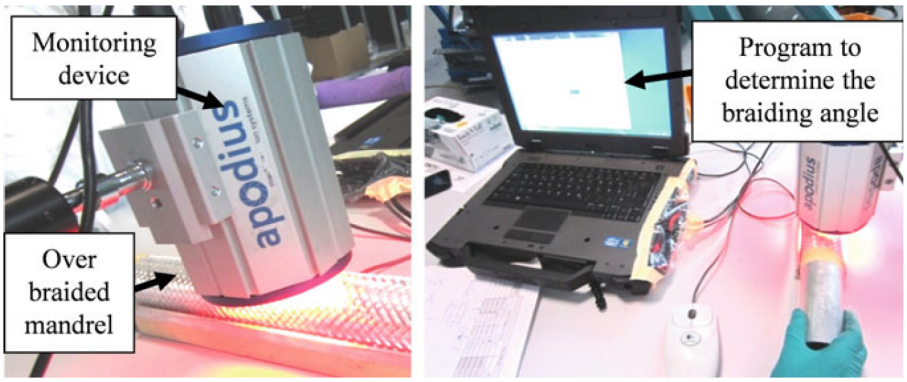

Figure 4.3: Apodius Vision System (AVS) used by Reimer *et al.* for braid angle and cover factor measurements; reproduced from [246].

of yarn damage and yarn path deviations due to tension fluctuations. Given the complex nature of the setup, i.e. wireless connectivity to each machine carrier, its value relative to a wider process measurement strategy would likely need to be established in order to justify its recreation elsewhere. This is especially true for larger braiding machines comprising a greater number of carriers, such as the over-braiding machine at NCC which has a total of 480 carriers over the two braid rings.

Alternative carrier-based systems for yarn tension measurement and control have been developed [248, 249] with varying configurations but similar operational principals and installation complexities. An inactive tension monitoring system, aimed at considerably reducing system complexity and cost, has been demonstrated by researchers at Technical University of Munich (TUM) [250, 251], motivated by quality assurance and increased productivity. The system relates the signal generated by a magnet mounted on the carrier yarn release mechanism, which varies as a function of mechanism position, to yarn tension. This occurs each time the carrier passes a stationary Hall sensor mounted on the braid ring, thus simplifying the carrier adaptation at the expense of measurement frequency. It aims to detect anomalies and enable operators to intervene prior to defect development in the preform or yarn breakage, although multiple sensors mounted around the braid ring may be required to enable intervention in a timely manner.

Moving away from per-yarn measurements, the same research group has since developed sensorised guide rings (see Figure 4.6) with embedded force sensing resistors [252], able to detect the presence of tension irregularities as yarns circumnavigate the guide ring. The approach enables continuous measurement of the effect of uneven tension across the yarns, but lacks the ability to directly identify offending yarns. Whilst a number of technical challenges exist to extend the measurement technique beyond the scenario for which it was developed, i.e. biaxial radial braiding over tubular mandrels, it potentially offers a more practical in-process yarn tension monitoring system for quality assurance and productivity applications.

An on-line inspection capability has been reported by the braided textile producer A&P Tech-

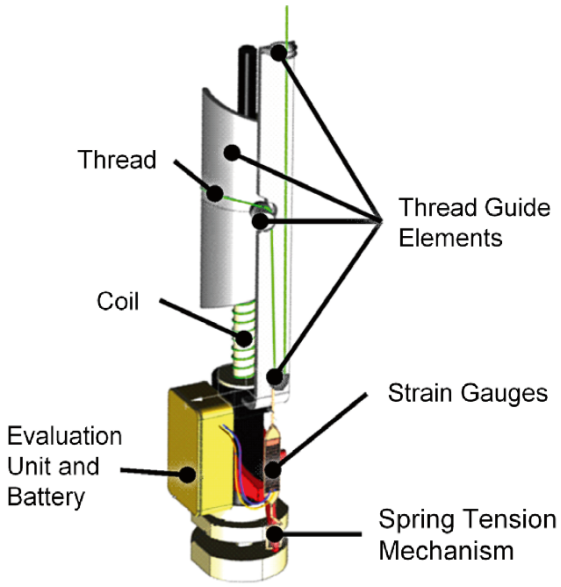

Figure 4.4: Active carrier from the system developed by researchers at ITA RWTH; reproduced from [247].

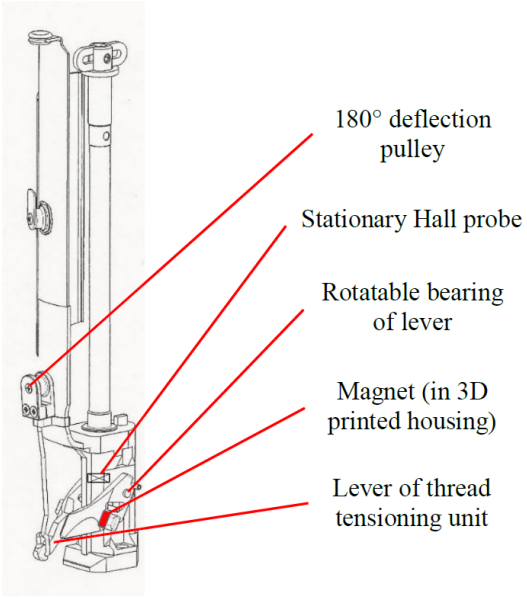

Figure 4.5: Carrier-based tension monitoring system developed by researchers at TUM; reproduced from [251].

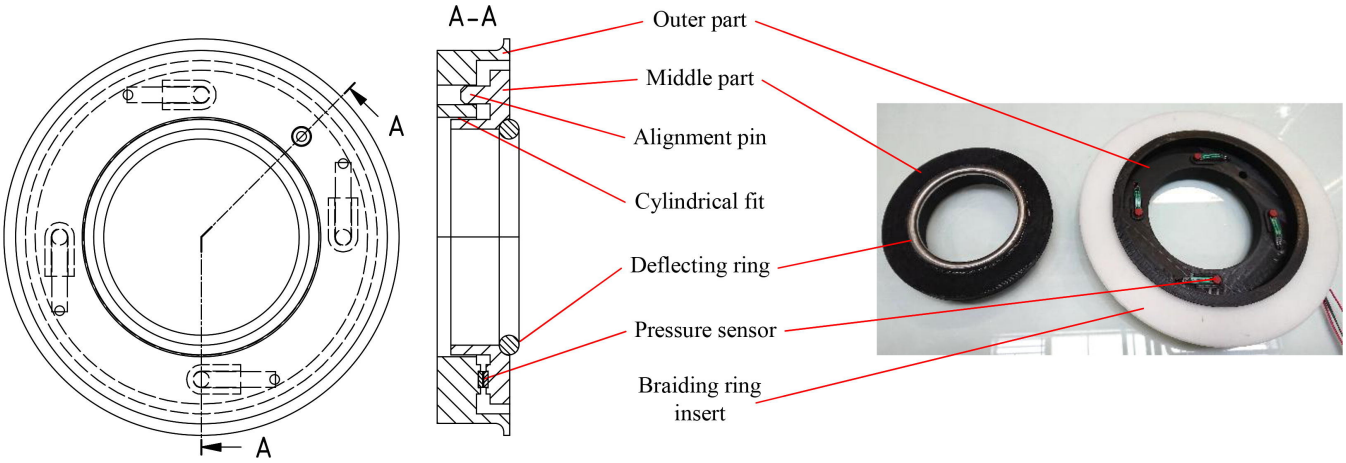

Figure 4.6: Sensorised guide ring developed by researchers at TUM; reproduced from [252].

nology [253], comprising braid angle and preform thickness measurements, and defect detection, although no details regarding configuration or performance are available. The primary drivers for the system would appear to be process setup validation and quality assurance, whilst the level of integration with the production process and workflow is unclear. It is anticipated that similar systems exists within the composites manufacturing supply chain which are not publicised; such systems are most likely to focus on quality assurance, and elements of process control.

The developments and applications of in-process measurement systems reviewed here range from research systems designed around specific process configurations, i.e. radial or axial, braiding or over-braiding, to sensorised process components which could be retrofitted to a whole range of braiding machines. Motivations for system development include product quality assurance and defect detection, process anomaly detection to reduce down-time and increase productivity, as well as the implementation of closed-loop process control systems. However, discussions regarding the value of the measurement data rarely extend beyond the specific scenarios for which they have been acquired; only the system at Auburn University [242, 243] was discussed in the context of a process measurement platform with which to facilitate future design and manufacture research activities. Failure to collect and store data from process measurement and inspection systems as a matter of course, in a structure, and with sufficient contextual information, to render them useful for future, data-led research activities, is a missed opportunity. In order to develop and benefit from digital engineering practices, it is necessary to ensure that measurement systems and their data are integrated with other aspects of the design and manufacture workflow.

The system described in the subsequent sections of this chapter has been designed as the foundation of a process measurement platform with which to support future research activities into over-braiding at NCC. It incorporates some of the measurement techniques and principles employed within the reviewed systems, such as event-triggered image acquisition and processing, into a platform that enables operators to capture relevant contextual, i.e. material and process setup, data alongside the acquired process measurement data. The system has also been developed with a view to facilitating increased in-process measurement integration into the over-braiding design and manufacture workflow in future developments, to ensure that it can become part of standard research activities, and therefore underpin future process-oriented capability and knowledge developments. Whilst this first stage is focused towards measurements pertaining to product quality, it is intended that the system will be expanded to incorporate additional sensing capability for in-process variables in future developments.

4.2 Aims and objectives for system development

For this initial stage of development, the measurement of two quality metrics for the produced braided preform was targeted, alongside the logging of material and process setup variables identified and discussed in Chapter 3. The two metrics chosen were braid angle and preform thickness, measurements of which are otherwise reliant on manual measurements made by the operator(s) during process stoppages. Definitions for these metrics are as follows:

- Braid angle - the angle of bias yarns in the braided preform structure relative to the braiding axis;
- Preform thickness - the greatest distance between, and normal to, the substrate (i.e. mandrel) surface and the uppermost surface of the preform.

Whilst the impact of process downtime required to make these manual measurements is less in a research setting than in a production environment, a compromise between the number of measurement locations, and therefore areal resolution, and time taken is inevitable in either scenario. Uncertainty associated with manual measurements is also undesirable, as it limits the value of the measurements in decision making. Consequently, the time and effort that is afforded to acquiring the measurements in the first instance may be limited. The system described in this chapter aims to increase spatial resolution and reduce uncertainty of these measurements through automation.

The objectives for the development of the system were to:

– automate the collection and storage of data required to make braid angle and preform thickness measurements at specified locations or intervals along the mandrel surface;
– automate the analysis of acquired data to generate measurement results;
– enable data acquisition and measurement for axisymmetric mandrels with varying cross-sectional geometry, i.e. non-tubular mandrels;
– enable measurements to be referenced against the corresponding mandrel locations;
– enable material and process setup information (i.e. metadata) to be recorded and stored alongside measurement data;
– provide a live readout of measurement results for the operator to use as appropriate during the process;
– minimise impact on the machine operators' working area.

4.3 System requirements and constraints

It was intended that the measurement system developed should be suitable for use with complex, i.e. non-tubular, mandrel geometries, with effective mandrel diameters ranging from 40 mm - 750

mm, and for multi-layer, bi- and triaxial braid architectures. It should also function at all machine speeds, i.e. up to the maximum traverse speed of 2000 mm/min (33.3 mm/s), in order not to impact upon the process operating envelope. Desired measurement accuracies to be achieved were specified by the process owner as:

- ◇ braid angle: ± 0.5°;
- ◇ preform thickness: ± 0.1 mm.

The primary system constraint for this stage of development was the lack of access to the braider control system, particularly information relating to mandrel traverse co-ordinates, and thus the mandrel location, during the braiding process. As a result, the system was limited to use with linear mandrel paths only (i.e. no motion in Y and Z axes of the traverse), with motion along the X axis to be measured as part of the system.

A second constraint was that the system would be developed for data collection from a single, fixed perspective, and therefore data would only be acquired along a single strip of the preform as determined by the orientation of the mandrel once mounted. This constraint could be removed in future developments by replication of the measurement hardware setup described in this chapter, or by the introduction of robotic control and positioning of the hardware assembly such that the orientation of the sensor assembly relative to the braider is no longer static.

Thirdly, the system was to be designed for use in a single braiding direction, i.e. forward braiding only, given the added complexity of mounting a sensor assembly on the reverse side of an axial braiding machine, i.e. inside the cone formed by yarns between the braid ring and guide ring. This constraint could also be addressed in future system developments in order to provide measurement capability for reverse braiding operations.

4.4 Review of measurement techniques

4.4.1 Braid angle

The baseline measurement device for *in situ* braid angle measurements by the machine operators is a protractor, which is a low cost solution that allows the operator to measure the angle between a pair of intersecting yarns at any accessible location along the produced braid (see Figure 4.7); braid angle is recorded as half of the measured value. Whilst simple to implement, measurement accuracy is dependent on the care, attention and skill of the user in order to minimise sources of error such as parallax, and is reliant on manual data entry and its associated pitfalls to record measurements. Achievable resolution will depend on the device but will typically be limited to 0.5°, i.e. 0.25° for braid angle, whilst measurement repeatability will be user-dependent.The braiding

Figure 4.7: Manual measurement of braid angle is typically performed by the operator using a protractor.

process will usually need to be stopped in order for measurements to be made, thus the number of measurement locations (to determine spatial resolution) and number of measurements per location (to reduce uncertainty) will impact upon the duration of the manufacturing process.

An alternative to physical protractor measurements is equivalent software-based angle measurements made from digital images of the braided preform, in which the user identifies and traces yarn edges between which angles are calculated. Depending on the camera setup and image acquisition rate, spatial resolution can be greatly increased relative to manual protractor measurements, although a slower response time is likely due to image transfer and software operation times. Measurement uncertainty arising from the manual yarn selection process for such a process is thought to be in the region of $\pm$ 2° [17], whilst image perspective distortion, caused by misalignment between image and subject (i.e. preform surface) planes, or lens distortion, can also cause systematic measurement errors.

In order to automate image-based measurements and thus enable faster measurement response times, a number of automated image analysis procedures have been presented in literature. Kysoev [102] proposed a yarn edge detection procedure, for high resolution greyscale images, which returns a histogram of detected edge orientations relative to the frame of the image, from which braid angle is calculated. The procedure, initially developed with image processing tools available in the Matlab programming environment, and subsequently implemented by Liu and Kysosev in Python

programming language [254], consists of the following steps:

- background detection and removal via morphological opening;
- edge filtering using the Canny method;
- line fitting to detected edges using the Hough transformation;
- line orientation calculation and binning.

Canny edge detection is employed as it is capable of detecting both strong and weak edges whilst exhibiting reduced sensitivity to noise. This is achieved via application of two threshold parameters, returning strong edges as those above the upper threshold and weak edge as those between the lower and upper but connected to strong edges. Whilst the Matlab implementation of the Canny method appears to automate the threshold parameterisation, other implementation such as those available for Python require user threshold specification, thus potentially limiting the robustness of the procedure to variations in image composition e.g. yarn colour, yarn reflectively, image brightness [254]. Additionally, the Hough transformation used for line fitting is subject to three parameters, for threshold, minimum line length, and maximum allowable gap, further increasing the number of parameters to be optimised for a given combination of imaging setup and subject composition. The measurement resolution is dependent on histogram bin width, with Kyosev reporting braid angle, θ, to the nearest 1°; a subsequent implementation by Monnot *et al.* [18] reported results to 0.1° by calculating the average line angle. Whilst Kyosev made no specific reference to optimal lighting arrangement for this method, Monnot utilised oriented lighting to accentuate yarns on opposing trajectories and thus aid edge detection. No indication of the analysis time or computational cost was given.

An alternative approach that has be implemented in numerous studies relating to braiding, and other composite and textile applications [90, 103–105, 255, 256] utilises the frequency domain of an image, accessed via 2D Fourier transform, to identify the predominant angular frequencies present. The sequence of steps involved in such a procedure are:

- edge filtering (using Canny or other method);
- Fourier transform of the image into the frequency domain;
- calculation of mean pixel intensity along angular frequency components of the resulting power spectral density (PSD);
- identification of peaks in the angular intensity distribution.

The most comprehensive assessment of this approach was published by Hunt [105, 244], in which θ measurements were reported to the nearest 0.1°, as dictated by the angular resolution utilised in calculation of the angular intensity distribution. An indication of measurement uncertainty was provided by presentation of results for 15 repeat images of the same preform section under static

conditions, showing a range in measured value of $\sim 0.5°$, with reported standard deviation of $0.11°$. This behaviour was attributed to pixel intensity fluctuations caused by image sensor noise, whilst sensitivity to lighting and reflections from yarn surfaces were cited as potential limitations of the technique. Unlike the Hough transformation used for line fitting in the spatial domain, the 2D Fourier transform can be conducted without user-defined parameters and is thus expected to be more robust approach with regards to variations in image composition.

A third automated image-analysis method, which is the basis of the AVS introduced in Section 4.1, enables assessment of fibre orientation at each pixel using structure tensor analysis. In this method, the intensity gradient within a specified window around each pixel is assessed in order to determine an orientation for that pixel which can subsequently be analysed to determine the distribution of fibre orientations across the image. Edge filtering is not performed as the image detail is required to perform the analysis. An assessment of fibre angle measurement performance for this method has been performed by Schmitt *et al.* [257, 258], with a reported uncertainty of $< \pm 0.3°$ (95 % confidence interval) over a range of scenarios.

Similar results can be obtained by exploiting the orientation-dependent reflective properties of fibres themselves to determine per-pixel orientations values. This is achieved by analysis of multiple images under varying optical conditions: either the incident angle of illumination (photometric stereo [106, 259]), or the orientation of a light polarising filter (polarisation [107]) can be varied. The former computes, amongst other components, an azimuth angle for each pixel, which corresponds to the in-plane angular component, i.e. fibre orientation. This is analogous to the phase angle, or angle of maximum polarisation, generated from the latter (provided that the degree of polarisation is sufficiently large). For dry fibre preforms, fibre angle measurement uncertainty of $\pm 0.8°$ (at 95 % coverage factor) has been reported for the photometric stereo technique [106], although the subject must remain stationary while the necessary image set is acquired, which may ultimately limit the methods suitability for in-process measurement applications. This limitation can be avoided for the polarisation technique by the use of polarised image sensor, for which each pixel is fitted with a polarising filter for one of four angles. This effectively enables four images to be captured simultaneously, at the expense of image resolution.

Of the image-based measurement procedures reviewed, only van Ravenhorst and Akkerman [17] implemented a perspective transformation to correct for misalignment between image and subject planes; all others assumed or ensured that the subject was imaged parallel to the image focal plane. This is an important consideration when the surface normal of the preform is likely to change, i.e. as a result of mandrel geometry, since such misalignment will introduce measurement errors. The effect of preform surface curvature also needs to be considered since braided preforms are most commonly produced as near-tubular geometries and hence images cannot necessarily be assumed planar during analysis routines. This effect was investigated by Hunt and Carey for the Fourier

transform analysis method but will inevitably affect all others discussed.

For this work, the 2D Fourier transform analysis method was chosen due to the simplicity of the data acquisition setup and minimal parameterisation of the analysis routine. The fidelity offered by the structure tensor, photometric stereo and polarisation approaches was deemed unnecessary for this implementation since the use of twisted yarns in some over-braiding operations means that the angle of individual fibres is not necessarily indicative of the yarn orientation used for braid angle measurement.

4.4.2 Preform thickness

In this discussion, preform thickness refers to the perpendicular distance between the preform substrate, e.g. the over-braiding mandrel and/or infusion tooling, and maxima formed by yarns across the upper surface of the preform. Whilst it is theoretically a point measurement, in reality a measurement it will represent an average value over a number of maxima, be they individual fibres on a yarn surface, or multiple yarn surface maxima in the measurement region. Such measurements are typically made prior to, or during, the impregnation process, once the preform is in its compacted state, in order to ascertain the level of compaction and hence the fibre volume fraction that has been achieved. However, the constraints imposed on over-braided preforms by their tubular structure (discussed in Section 2.1), plus the tendency to conduct preform impregnation *in situ* on the braiding mandrel, means that as-deposited thickness measurements are particularly valuable during the over-braiding process. By monitoring the layer-by-layer thickness evolution, it should be possible to determine, and even control, the level of *in situ* compaction that is achieved during the deposition process and hence the amount of excess yarn length that may need to be managed during the subsequent impregnation.

The baseline manual device for such measurements is a depth gauge or Vernier caliper depth rod, which can be used to make point measurements of the distance between the mandrel and outer preform surfaces. Being an absolute, contact-based method, contact with the mandrel surface is required. This may only be possible without disturbing the preform for more open (i.e. low cover factor) braid structures with a small number of layers; a hole must otherwise be created in the preform which may not be desirable and is likely to influence the measurement due to distortion of the preform. The method also requires contact with the outer surface of the preform, which again is likely to influence the measurement due to the deformable nature of dry fibre preforms. As for manual braid angle measurements, the braiding process will need to be stopped while measurements are collected, thus the number of measurement locations, and measurements per location will impact upon the duration of the manufacturing process.

For a more comprehensive, non-contact assessment of preform dimensions, a laser line scanner

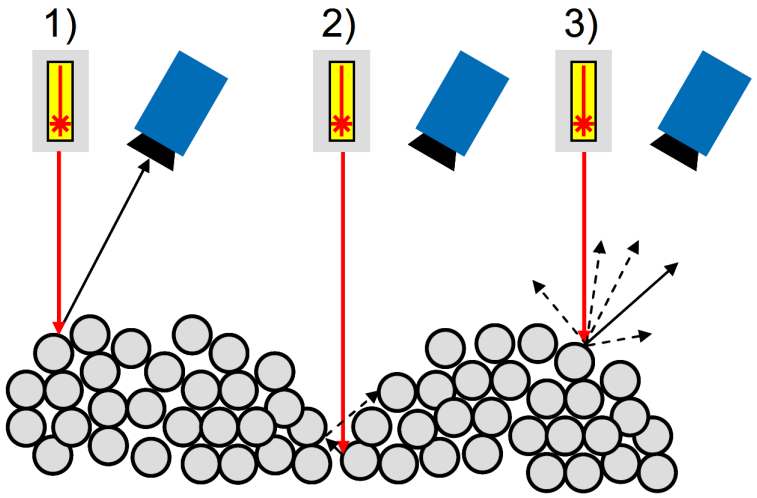

Figure 4.8: Effect of preform surface structure on laser line signal intensity, showing: 1) direct reflection and maximum intensity; 2) no reflection; 3) reduced intensity due to light scattering; reproduced from [262].

mounted on an articulated measuring arm may be employed, as commonly used for dimensional metrology activities. Such instruments generate a 3D point cloud of the inspection surface(s), from which measurements can be made. For *in situ* preform thickness measurements, a scan of the tool surface prior to preform deposition is required, which must be aligned with the preform scan data [260]. Measurements are then typically made between point cloud data and a fitted feature surface (i.e. fitted to a section of the mandrel surface point cloud), or between two fitted surfaces (i.e. a section of the preform surface and corresponding mandrel surface), meaning that they are sensitive to the fitting method used [261]. The acquisition may be automated by mounting the sensor on a robotic arm to reduce inspection time and increase repeatability [64]. However, data collection for full surface coverage cannot typically be performed during the braiding operation as these techniques rely on a known spatial relationship between the sensor and the inspection surface throughout acquisition. Also, the response time to generate measurements can be relatively slow due to the large number of data points that can be acquired and the use of analysis routines that are often conducted manually.

The use of laser line scanners for in process preform inspection activities has been demonstrated [63, 262], in which measurements are conducted on each surface profile as it is acquired. This reduces the data analysis to two dimensions on relatively small data sets (i.e. $\sim$ 1000 point co-ordinates per profile) and thus robust automation of the analysis routine can be more readily achieved. However, sensitivity to noise is increased relative to 3D point cloud analysis. This is a particular challenge when inspecting dry fibre preforms, since the structured surface created by the bundles of individual fibres causes scattering of the incident laser light, reducing the intensity

of light reflected back towards the sensor as illustrated in Figure 4.8. When combined with the strongly absorbing nature carbon fibres, relatively long exposure times are necessary to obtain a strong signal; analysis conducted by Schmitt *et al.* [262] determined an expose time of at least 5 ms per profile was necessary. In a subsequent investigation [63], a least-squares robust regression algorithm was employed to exclude outlier data points from profiles, before a linear function was fitted as an average measure of preform surface position. No attempt to identify the upper of the undulating surface was made, as necessary for thickness measurements relative to a smooth reference (i.e. tool) surface. Uncertainty in fitted surface position was assessed as a function of the angle between laser line and fibre orientation in unidirectional fabric samples, reporting maximum uncertainty at 0° of 241 μm at the 95 % confidence interval, reducing by approximately half to a minimum at 90°. Between 30° and 60°, i.e. the range of orientations to be expected for biaxial yarns in over-braiding,[1] reported uncertainty was in the range 180 μm - 200 μm.

The approach chosen for this work was to acquire discrete profile scans of the preform surface from a laser line scanner (a.k.a. profilometer) mounted in a fixed, known position, perpendicular to the braiding axis, as the mandrel moves through the braid ring. In this way, a thickness measurement for each acquired surface profile may be made relative to scan data for the corresponding mandrel surface location, obtained from a scan of the mandrel surface prior to preform deposition. The use of a single profilometer limits coverage to a section of the mandrel circumference, with measurement accuracy dependent upon alignment of mandrel and preform point cloud data as determined by the repeatability of mandrel positioning between scans.

4.5 Measurement system configuration

This section describes the measurement system that was designed and built as part of this project to meet the objectives and requirements outlined in the Sections 4.2 and 4.3. The hardware assembly described, referred to the measurement sensor assembly (MSA), is depicted in Figure 4.9, whilst the configuration of system hardware is provided in Figure 4.10.

Camera

High resolution, grayscale images of the deposited preform are acquired using the following hardware, assembled as shown in Figure 4.9:

- 12.3 MP monochromatic machine vision camera (Flir Blackfly S Mono BFS-PGE-122S6M-C: 4096 × 3000, 1.1" SONY IMX304 CMOS with global shutter);
- Low distortion, fixed focal length 50 mm lens (Kowa LM50SC) fitted with:

[1] Assuming the laser line is oriented parallel or perpendicular to the principal braiding axis.

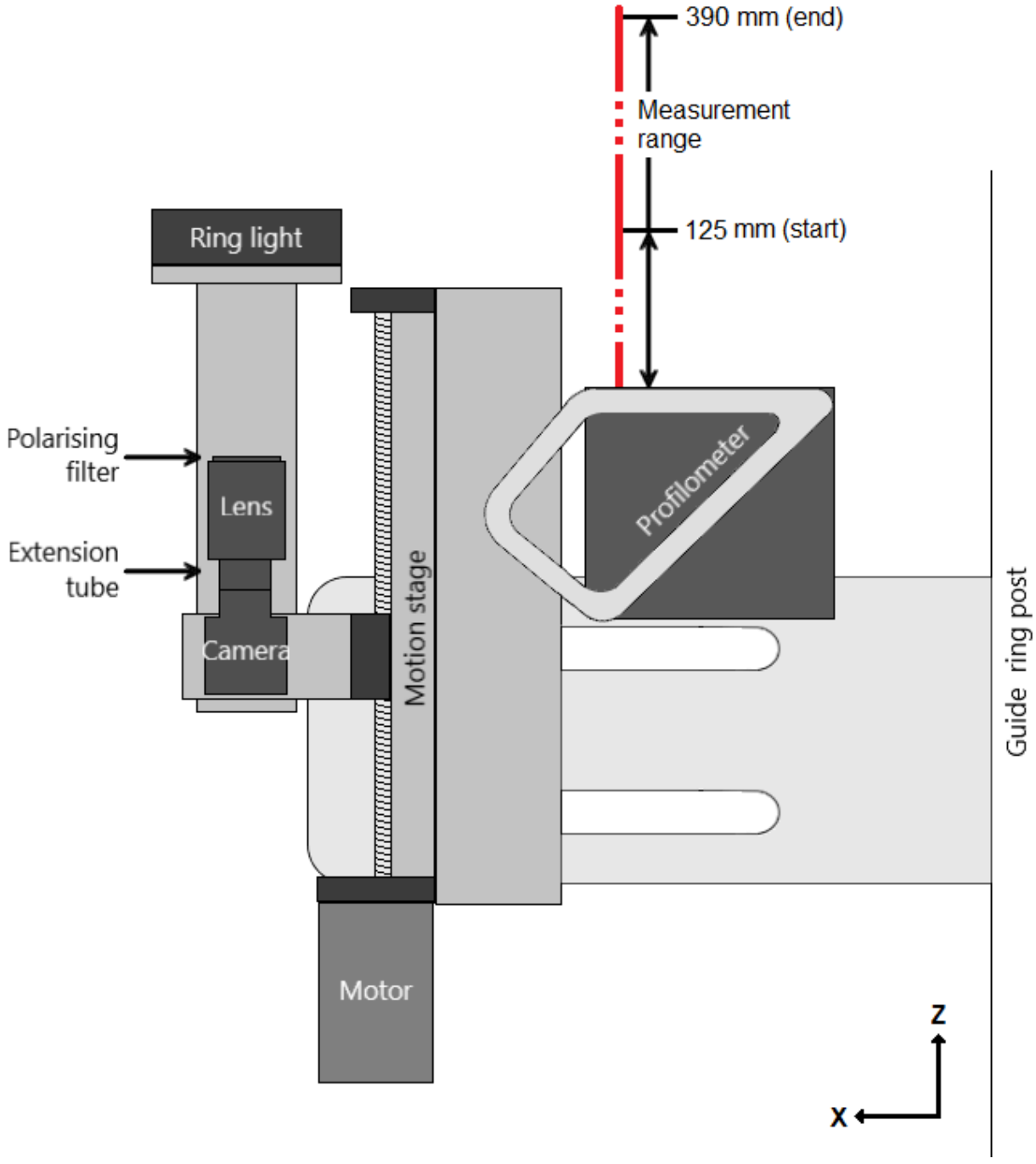

Figure 4.9: Measurement sensor assembly.

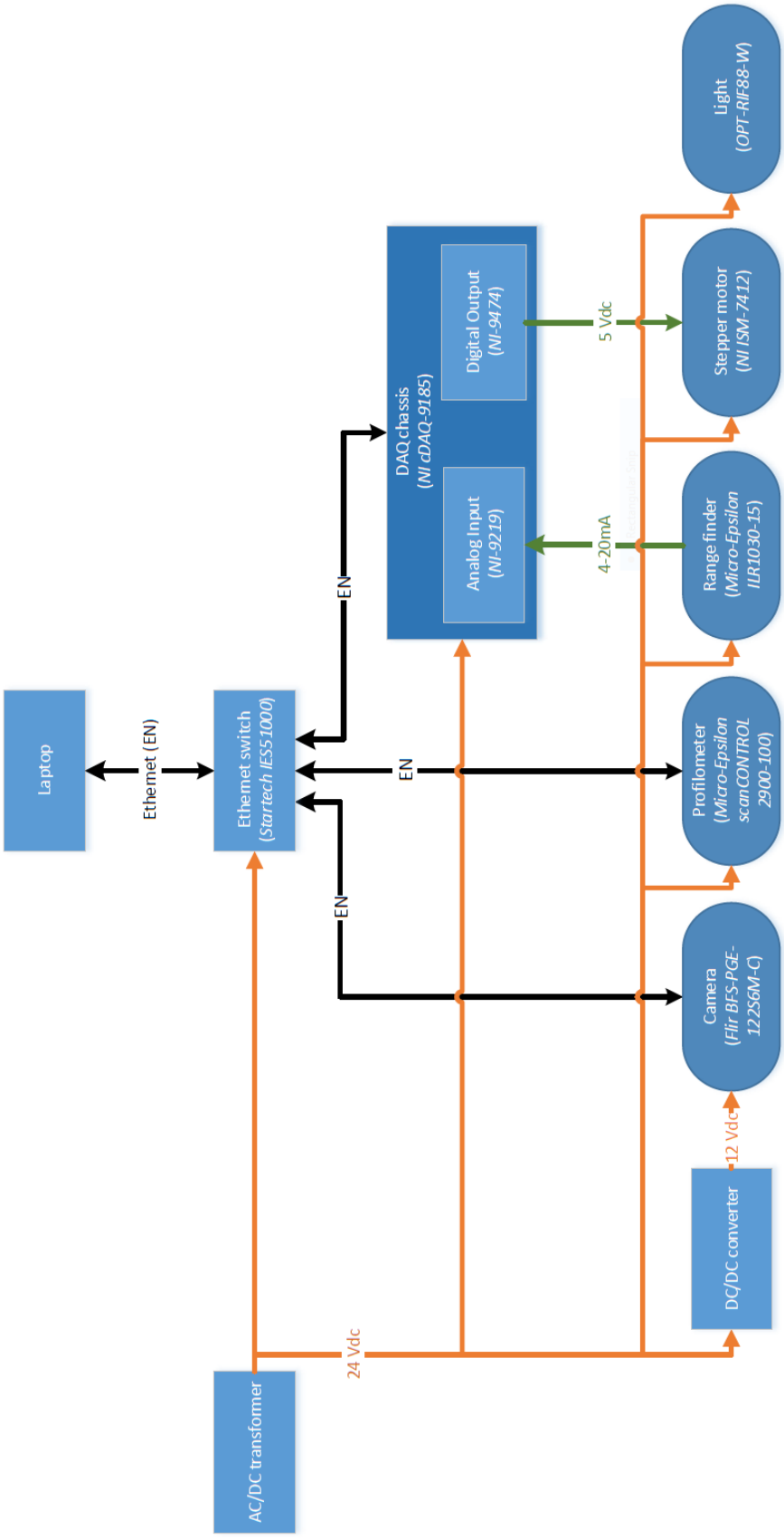

Figure 4.10: Measurement system hardware configuration.

  - 15 mm lens extension tube, fitted between lens and camera body;
  - adjustable, lens-mounted polarising filter (VS Technology SV-PL340-SS);
- 88 mm outer diameter diffuse, dark field LED ring light (OPT Machine Vision OPT-RIF88-W).

This arrangement captures images covering an area of 47 mm × 34 mm at an effective working distance of 185 mm, i.e. distance from the outer edge of the lens assembly to the subject with the lens focus set to ∞; the resultant image scale is 87.1 pixels/mm. Exposure time is limited to 5 ms maximum in order to minimise image blur due to motion of the subject. At such low exposures, it is necessary to limit the aperture to f/4 at most in order to achieve acceptable image brightness, resulting in a restricted depth of field of approximately 4 mm. The use of a dark field LED ring light, i.e. with a high incident angle of light, is intended to accentuate edge features in the acquired image, such as yarn edges, whilst the polarising filter reduces specular reflections from yarn surfaces, which is a particular issue for dry carbon fibre yarns.

In order to maintain focus on the preform surface via automated adjustment of the camera height during operation, the camera and lighting assembly is mounted to a linear motion stage assembly comprising:

- Thompson MS25 high precision screw drive liner motion stage (3 mm thread pitch, 250 mm travel, NEMA-23 motor mount);
- National Instruments ISM-7412 stepper motor.

Profilometer

Surface profiles of the deposited preform are acquired using a laser triangulation profilometer (Micro-epsilon scanCONTROL 2900-100, with red, 658 nm laser diode), which has a standard measurement range of 100 mm in Z (265 mm extended range). An exposure time of 5 ms per profile is used for profile acquisitions at full laser power ($\leq$ 8 mW) to ensure sufficient signal strength whilst minimising the motion of the subject during each acquisition (i.e. $\leq$ 0.167 mm movement in mandrel X position up to a maximum traverse speed of 33.3 mm/s).

Measurement sensor assembly

Both the camera motion stage and laser profilometer are mounted to a 400 mm length of 40 mm^2 aluminium extrusion, positioned and aligned on opposite sides of the extrusion, at a separation of 146 mm (profile to image centre line). This assembly constitutes the MSA seen in Figure 4.9. The MSA is mounted to the braider guide ring post via the extrusion, by means of a slotted aluminium mounting plate, such that the extrusion is parallel to the post, with camera assembly

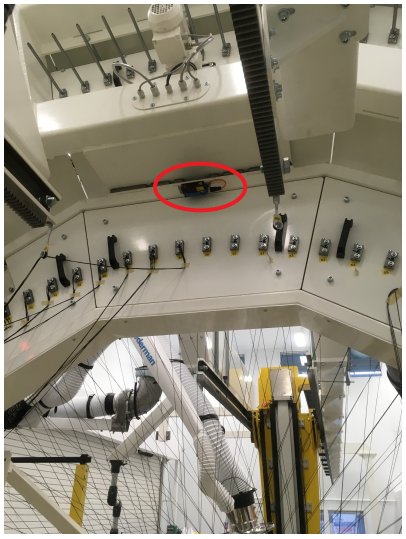

Figure 4.11: Distance sensor mounted on rear of the braid ring.

Figure 4.12: Laser path between distance sensor and master traverse target.

and profilometer aligned with the X axis of the braider. The slotted mounting plate allows for manual adjustment of the MSA position relative to the guide ring, along the X axis, to ensure that data are acquired beyond the convergence plane of the yarns, i.e. after the plane in which yarns are deposited onto the mandrel. The profilometer is positioned between the the guide ring and the camera, ensuring that laser profiles are acquired prior to images for the same location on the preform. This enables surface profile data to be used to adjust the camera motion stage position.

Trigger

A time-of-flight laser distance sensor (Micro-Epsilon optoNCDT ILR 1030) is used to measure changes in the position of the master mandrel traverse arm relative to the braid ring, in order to trigger data acquisition at user defined intervals along the mandrel. The distance sensor is mounted along the top edge of the braid ring, on the opposite face to the spool carriers, pointing at a metal plate on the rear (i.e. master) traverse (see Figures 4.11 and 4.12). Readings are acquired at 100 Hz, with position calculated as the average on 10 readings to reduce the noise. The response time of 0.1 s results in a positional lag of up to 3.3 mm at the maximum traverse speed, which is undesirable and which should be addressed in future developments by using positional data acquired from the braider control system. Once the guide ring post and MSA are fixed in position, measurement locations along the mandrel are determined relative to a datum feature on the mandrel, e.g. leading edge of the mandrel.

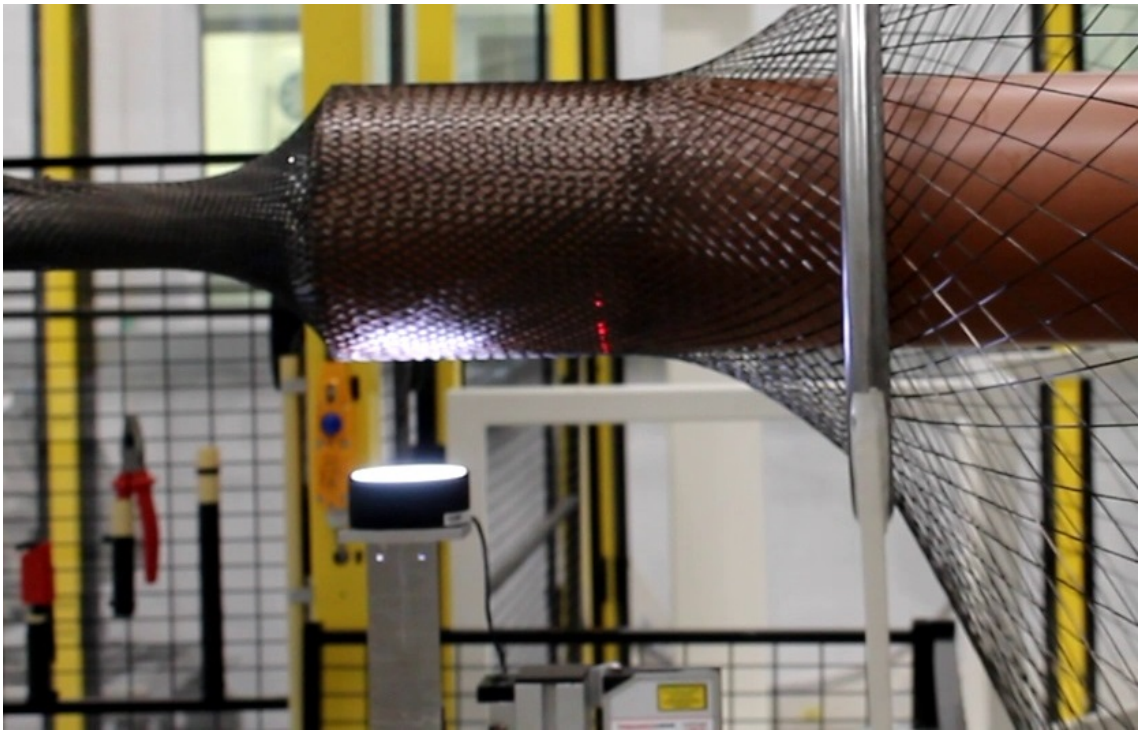

Figure 4.13: The MSA is positioned such that the projected laser line falls beyond the expected convergence plane of the yarns.

Control

Sensor operation, data acquisition, data processing and storage, and motor control are conducted via a custom-built LabVIEW [263] software programme that was developed by the author as part of this research project. The programme communicates with, and acquires data from, all sensors, displays sensor and measurement data for the operator to view, and stores sensor, measurement and user-defined setup data against a specified job ID.

4.6 Measurement system setup and operation

The MSA is mounted to the guide ring post, and its position with respect to the X axis is adjusted by the operator to ensure that the projected laser line falls beyond the expected convergence plane of the yarns (see Figure 4.13). This positioning must consider the maximum convergence length anticipated during the braiding operation. Z axis positioning of the MSA is adjusted by the operator such that the mandrel/preform surface remains within the measurement range of the profilometer and within the focal range of the camera assembly (see Figure 4.9).

Once powered on and connected to the control laptop, the MSA is operated and controlled

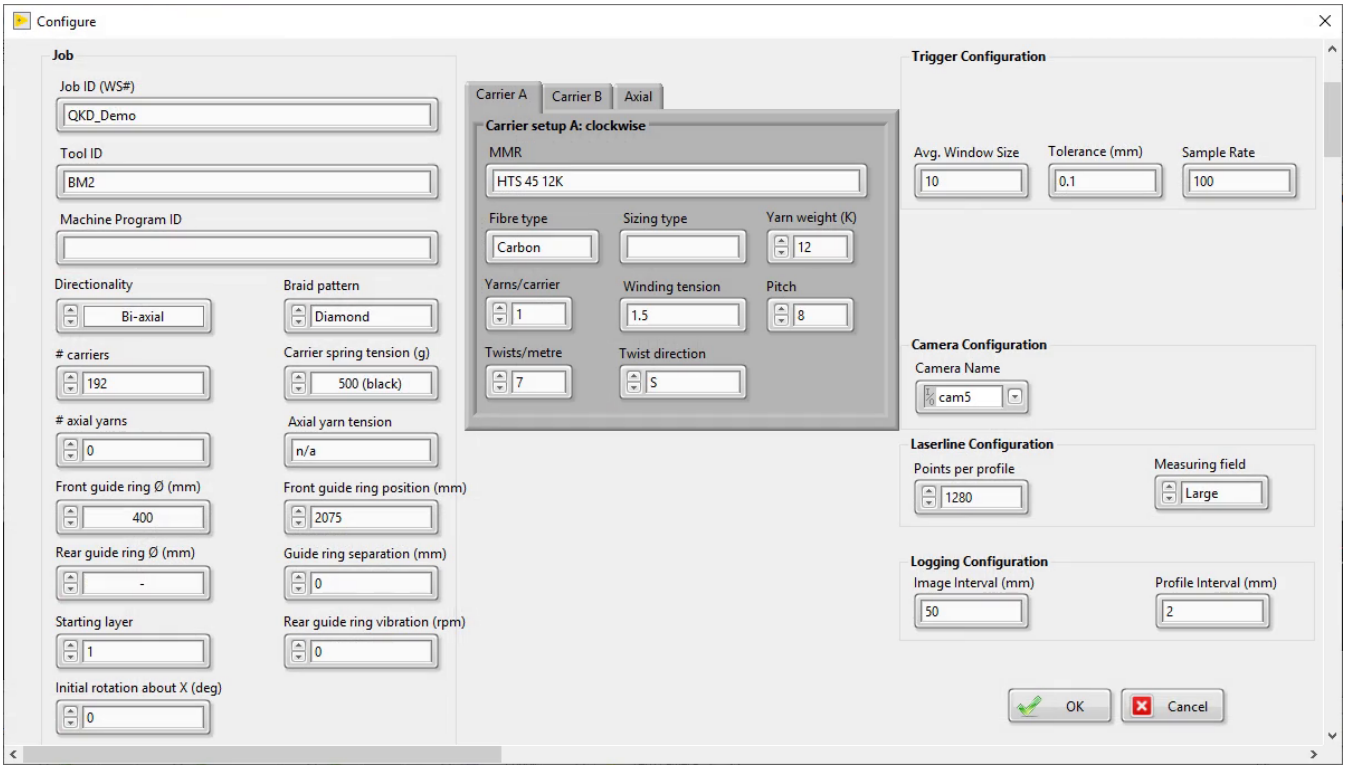

Figure 4.14: Measurement system 'Settings' screen.

from the LabVIEW program. From the 'Settings' screen shown in Figure 4.14, the operator enters an identifier for the braiding operation, a range of machine setup and material setup parameters, and measurement acquisition settings including X axis measurement intervals for image and profile acquisition; all of these details are saved to a pair of structured, machine-readable text files using the Extensible Markup Language (XML). The operator then selects 'Start' in order to begin acquiring sensor data (i.e. images, profiles and X axis position); these are displaying on screen, at which point the camera height can be adjusted in order to focus the camera images. If changes to sensor settings are required, this is conducted outside of the LabVIEW program using SpinVIEW software provide by the sensor manufacturer.

Once the mandrel has been loaded and positioned on the traverse mechanism, and the mandrel path programmed, the measurement system is referenced to a datum feature on the mandrel. To do this, the mandrel is driven to a location such that the specified datum feature is aligned with the centre of the camera image, as indicated by a cross-hair overlaid on the on-screen image. The X axis position as measured by the laser distance sensors (see Figures 4.11 and 4.12) is recorded as the 'zero' position; the position of all subsequent data acquisitions are measured relative to that 'zero' position.

Prior to commencing the braid deposition itself, a baseline scan of the mandrel is acquired. This consists of the mandrel being driven along its programmed path, i.e. at the same trajectory to be

used during the braiding operation, with profiles recorded at specified measurement intervals.

After the baseline scan has been completed, the braiding operation can begin. At the start of each layer, the operator indicates in the software that a new layer has begun; this enables data to be recorded as corresponding to that specific preform layer. The operator must ensure that the camera is in focus when the mandrel first enters the camera's field-of-view at the start of each new layer; the automated camera height adjustment feature can then be activated. This feature uses surface profiles acquired by the profilometer to calculate changes in the mandrel surface height (i.e. position in the Z axis) and adjust the vertical position of the accordingly to ensure the surface remains in focus. During the braiding operation, braid angle and preform thickness measurements based on the acquired images and profiles are displayed on screen for use by the operator as appropriate.

Software operations available to, and controlled by, the user can be summarised as follows:

- ◇ record job, process setup and material setup details, as shown in Figure 4.14;
- ◇ specify measurement acquisition intervals for laser profiles and images;
- ◇ set X axis reference position at a chosen datum feature on the mandrel;
- ◇ start/stop data acquisition;
- ◇ start/stop automated data logging and analysis;
- ◇ trigger manual data logging and analysis for single data point;
- ◇ activate/deactivate automatic camera height adjustment.

During operation, the following files are generated by the program:

- job, process and material setup details as entered by the user (.xml format);
- sensor configuration details and settings (.xml format);
- individual profiles at specified X axis intervals, for each layer (.csv format);
- individual images at specified X axis intervals, for each layer (.png format);
- measured braid angle vs position & layer (.txt format);
- preform thickness vs position & layer (.txt format).

The procedures by which the quality metrics of braid angle and preform thickness are extracted from acquired sensor data are outlined in Section 4.7.

4.7 Measurement and analysis methods

This section describes the data processing stages developed for the generation of braid angle and preform thickness measurements from image and profile data respectively. Processing parameters

defined here are the result of measurement performance optimisation work presented in detail in Chapter 5.

4.7.1 Braid angle

Automated braid angle measurement is achieved via an image processing and analysis software programme developed by the author as part of this research project. The programme is written in Python programming language and utilises the open-source OpenCV image processing [264] and SciPy scientific computing [265] libraries. The Python programme is called from within the LabVIEW acquisition software in order to generate braid angle measurements from images as they are acquired. Each high resolution monochromatic image captured by the system hardware is cropped to a square image, 2400 × 2400 pixels, in which the horizontal axis corresponds to the primary mandrel (X) axis, i.e. 0°. The cropped image is parsed to the script, along with the gradient of the imaged surface along the X axis relative to the image plane. This gradient value is calculated from the change in height of the mandrel surface between the for and aft edges of the image, as measured by the profilometer.

A perspective transformation is applied to the image (using the OpenCV *warpPerspective* function) as required to account for surface gradient along the X axis (a constant gradient across the image is assumed). This is a reasonable approximation in most instances given the relatively small width of the cropped images (covering ∼ 28 mm). No transformation for surface gradient along the secondary (Y) axis is applied, as the system has initially been designed for use with axisymmetric mandrels which are axially aligned with the camera; hence the average gradient relative to the Y axis is expected to be 0.

A median blur filter, of window size = 45, is then applied (using the OpenCV *medianBlur* function) to reduce the definition of yarn texture, i.e. individual fibres within yarns, as well as stray fibres, whilst maintaining that of yarn edges. This step, introduced to isolate yarn orientations from fibre orientations, is required due to the fact that a twist is often applied to yarns during the spool winding process to improve yarn processability, resulting in a difference between yarn orientation and the orientation of visible constituent fibres. Since braid angle is concerned with the angle of yarns, the measurement should disregard the orientation of individual fibres.[2]

Edge detection is subsequently performed using a 1st derivative Scharr operator (via a special case of the OpenCV *Sobel* function), with a 3 × 3 kernel, to emphasise step changes in pixel intensity that are primarily expected to correspond to yarn edges. The Scharr operator has been selected on the basis of its improved rotational invariance relative to the Sobel operator [266, 267],

[2]Quantifying the angular deviation of fibres from the orientation of their parent yarn may be an additional measurement of interest when determining the influence of processing conditions on the mechanical performance of a braided structure, since an effect on performance due to the introduction of yarn twist should be expected [77].

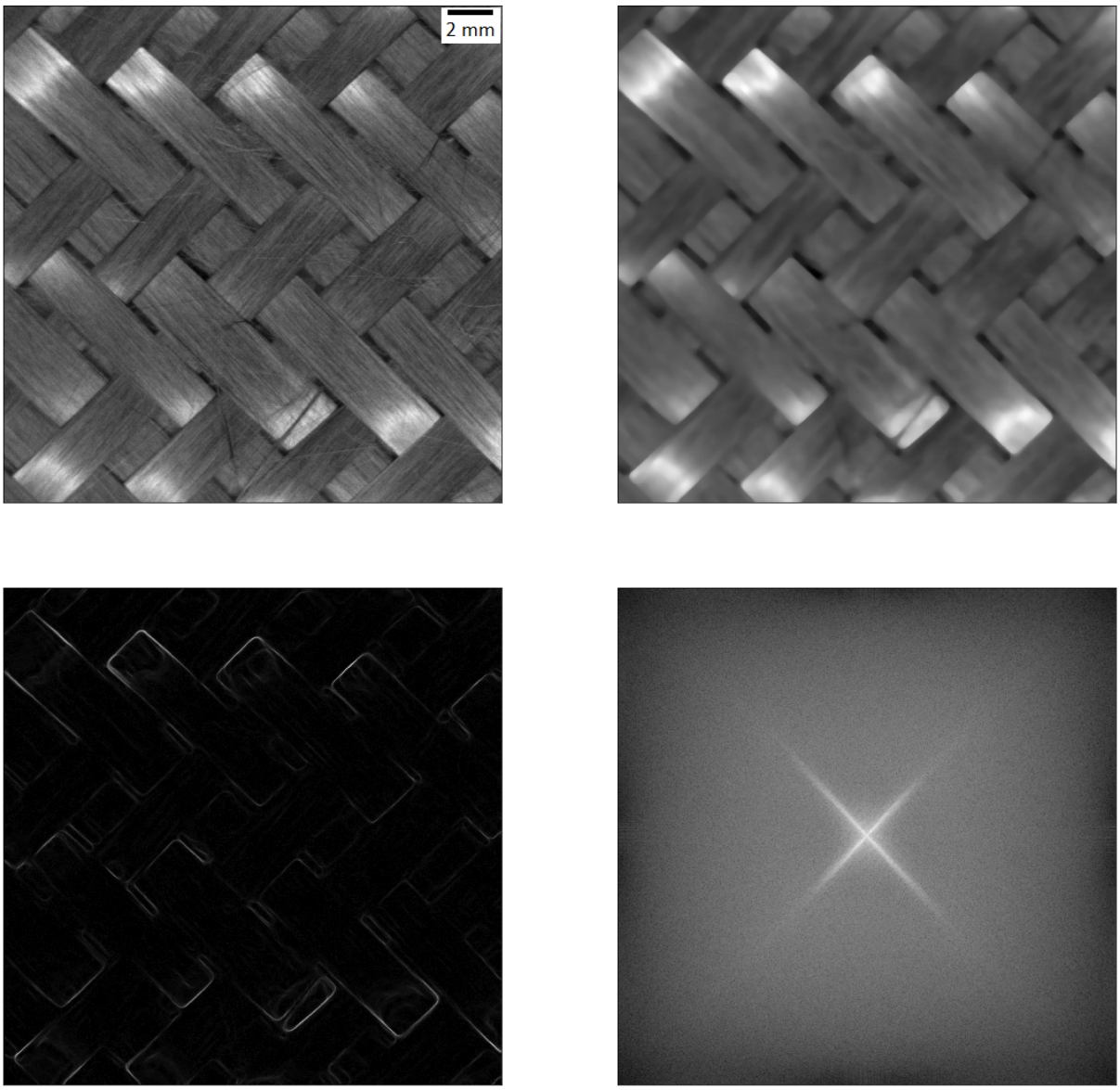

Figure 4.15: Output of image processing steps used during braid angle measurement routine: cropped image (top left); image blurred using median filter, size 45 (top right); edges detected using Scharr operator, kernel size = 3 (bottom left); logarithm of Fourier power spectral density (bottom right).

and preferred to the Canny operator utilised in [18, 102] due to the lack of input parameters, which is deemed advantageous in the development of a robust, versatile, automated measurement system.

Pixel values in the Scharr-filtered image correspond to the magnitude of the intensity changes across that pixel in the blurred image. Where there are specular reflections present on the surface of yarns, the edge intensities returned by the Scharr operator tend to be significantly larger than those returned across the rest of the image. In order to reduce the disparity between, and hence the visibility of, detected edges, an upper threshold is applied to intensity values in the Scharr-filtered image, in which intensity values are clipped at the 99^{th} %ile.

Discrete Fourier transform (DFT) of the clipped, Scharr-filtered image into the frequency domain is then performed (via the OpenCV *dft* function), in order to decompose the image into frequency contributions at different orientations. The resultant spectrum is translated in order to position lower frequencies towards the centre, prior to calculating the logarithm of the power spectral density (PSD), i.e. amplitude of the Fourier spectrum. Figure 4.15 illustrates the stages involved in generation of the logarithm of the power spectral density from the initial image.

From the PSD, peaks in mean pixel intensity versus orientation are identified to determine the predominant orientations present in the Scharr-filtered image. Firstly, a median blur filter (window size = 3) is applied to reduce speckle noise and smooth the PSD. Mean pixel intensities are then calculated along lines bisecting, and bounded by, a circle of radius r, projected onto the centre of the PSD at known orientations; this is illustrated in Figure 4.16.[3] The number of bisecting lines and their orientations are determined by the number and orientation of points on the circumference of the circle, for which r is calculated according to a specified maximum angular resolution, ϕ:

$$r = \frac{360/\phi}{\sqrt{2}\pi} \tag{4.1}$$

Co-ordinates of pixels along the bisecting line with orientation ω, terminated at each end on the circle circumference, are determined according to Bresenham's line-drawing algorithm [268]. For lines with ω between -90 and 90°, the mean intensity of line pixels is then calculated, producing mean pixel intensity versus orientation as shown in Figure 4.17.

From the mean pixel intensity versus orientation data, peak maxima are estimated (via the SciPy $signal.find\_peaks$ function) and used to initialise curve fitting operations at each peak location (via the SciPy $optimise.curve\_fit$ function). A scaled, asymmetric Laplace distribution is used to fit the peaks, as it bears a close resemblance to peak shape under idealised conditions, i.e. using simulated images with no fibre detail. The equation (Equation 4.2) comprises four fitting constants, of which m corresponds to the orientation of the peak maxima, λ and κ represent the spread and asymmetry of the distribution respectively, and A is the scale parameter; $s = sign(\omega - m)$.

[3]The vertical axis of the PSD corresponds with the horizontal axis, i.e. 0°, in the spatial representation.

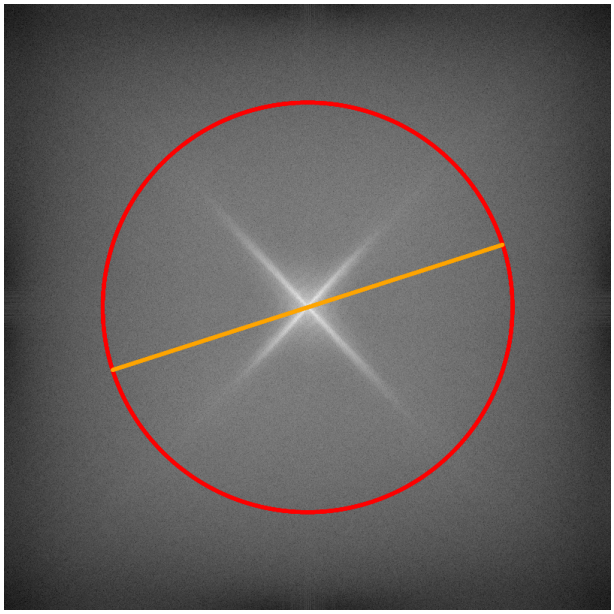

Figure 4.16: Logarithm of Fourier power spectral density, with projected circle of radius r and bisecting line at angle ω.

$$\frac{A\lambda}{\kappa + (1/\kappa)} e^{-(\omega - m)\lambda s\kappa^s} \tag{4.2}$$

Fitting is conducted using data points within a certain window centred on the initial peak position. For each peak, the window width is iterated over 6° - 30°, with the standard deviation error, i.e. square root of the diagonal of the covariance matrix, calculated for m at each window size. The value of m corresponding to the window size with the lowest standard deviation error is taken to represent a predominant angular component of the image.

This fitting procedure is conducted for the expected number of peaks, corresponding to the number of yarn orientations in the image, i.e. twice for a biaxial braid architecture, in order to obtain a value of m for each orientation. Figure 4.17 shows the result of peak fitting for the image in Figure 4.15, along with the value of m returned for each yarn orientation. An estimate of the mean braid angle, θ, is calculated as the average of the two largest absolute values of m; for the illustrated example, $\theta = \pm$ 43.1°. This calculation is applicable to both bi- and triaxial braids, since axial yarns present in triaxial braids, at, or close to, 0° are omitted.

4.7.2 Preform thickness

Preform thickness measurements are conducted via an analysis routine developed within the LabVIEW acquisition software by the author as part of this research project. A measurement of preform thickness at a given location along the length of the mandrel is calculated from a profile of

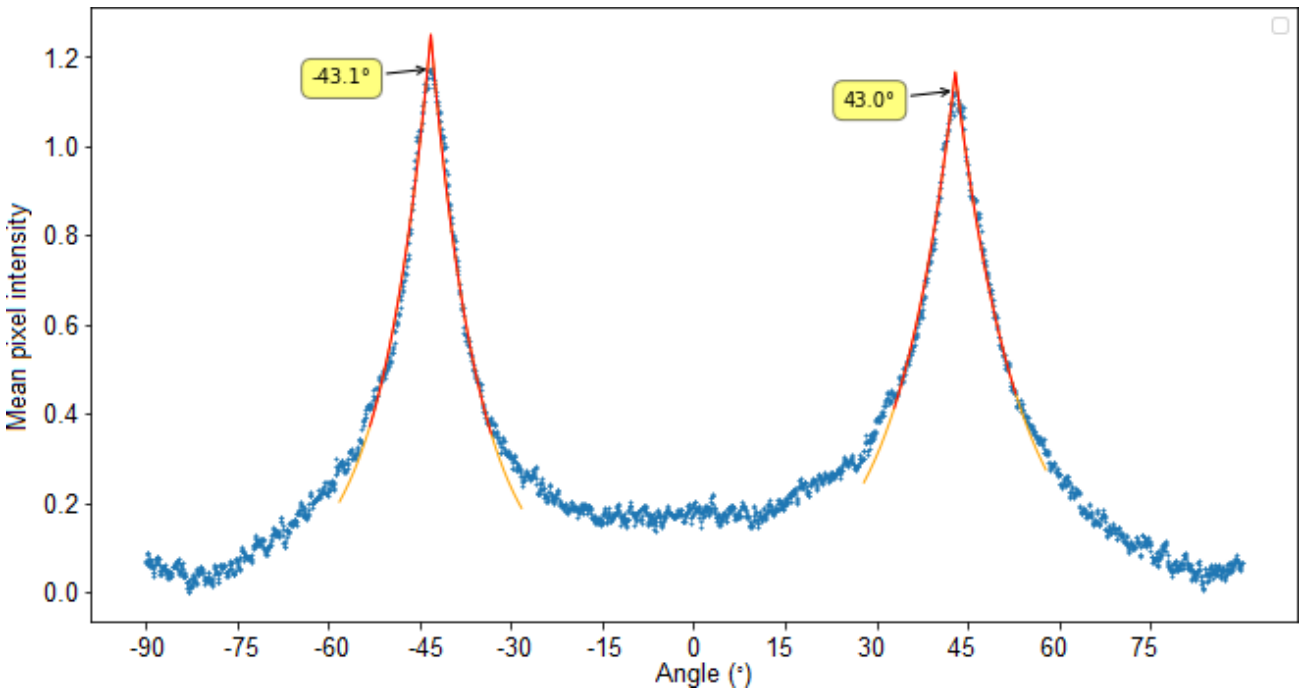

Figure 4.17: Mean pixel intensity plotted against line angle, ω; the fit for each peak over the selected fitting window is shown in red, along with the position of peak maxima, i.e. measured yarn angle.

the preform surface and a corresponding profile of the mandrel surface, i.e. acquired at the same location during a baseline scan of the mandrel.

The baseline scan of the mandrel is conducted prior to commencing preform deposition by driving the mandrel along its intended path, with profiles acquired at a user-specified interval in X (every 2 mm by default). A best-fit polynomial surface, typically 2$^{\text{nd}}$ order, is fitted to each baseline profile using the least-squares fitting method to approximate the mandrel surface. From this fitted polynomial, the equations of surface normals at specified intervals in Y, i.e. across the profile width, are calculated, typically every 0.1 mm. The coefficients of the fitted polynomial and each of the surface normals are then stored for use in subsequent preform thickness measurements.

During the deposition of each measured preform layer, profiles are acquired at the same mandrel locations and intervals used for the baseline scan. Two sequential polynomial fitting procedures, of the same order as used for the baseline fit, are performed for each profile, using the robust Tukey bisquare method. The bisquare method iteratively adjusts data point weights to minimise the least-squares residual of the fit, calculating weights, W, according to Equation 4.3:

$$W(R) = \begin{cases} \left(1 - \left(\dfrac{R}{k\sigma}\right)^2\right)^2 & \text{for } R \leq k\sigma \\ 0 & \text{for } R > k\sigma \end{cases} \tag{4.3}$$

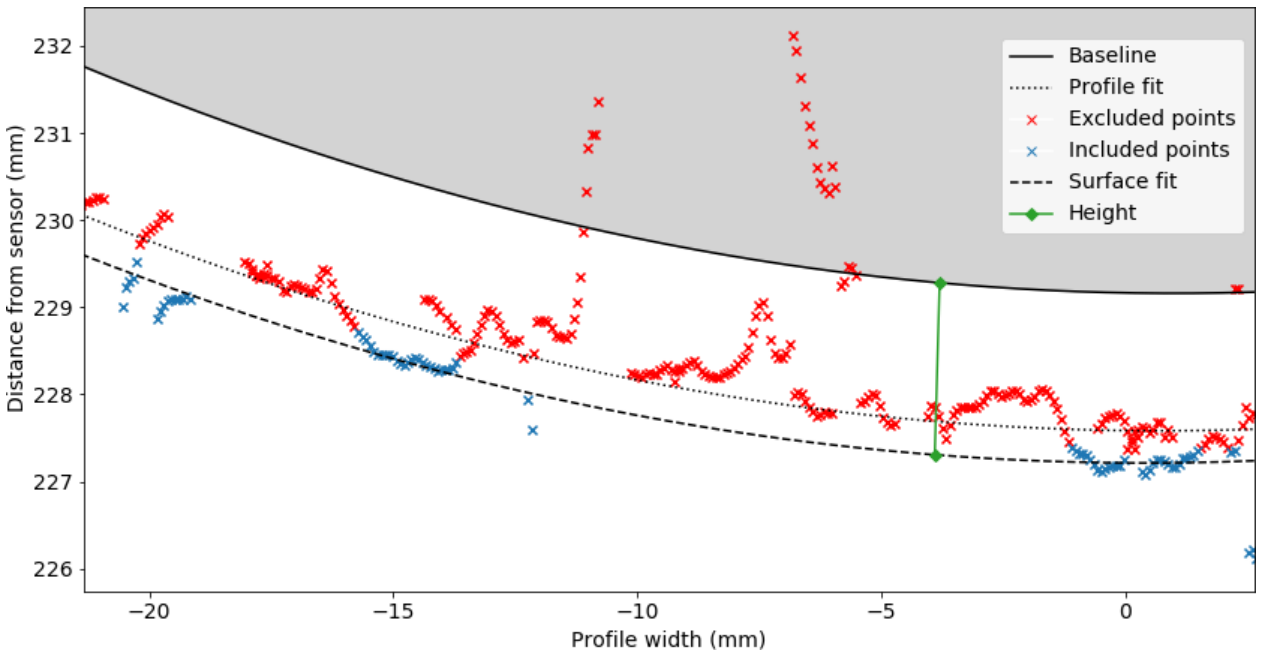

Figure 4.18: Output of thickness measurement procedure; lines correspond to fitted baseline (solid), profile midplane (dotted) and profile surface (dashed) respectively; data points included in the surface fit are shown in blue, and those excluded in red; the distance between intersections of a surface normal with the fitted baseline and preform surfaces, i.e. profile height, ΔYZ, is shown in green.

where R is the data point residual and k is a tuning constant; k is set to 4.685 as typically employed where normally distributed errors are assumed [269].

This method was used to reduce fitting sensitivity to outliers. It was preferred to a standard least-squares fit since the 2D point cloud profiles acquired using the laser triangulation measurement device were found to be prone to erroneous points, likely resulting from the scatter of the laser light by the undulating topology of interlocked yarns [262], as well as global curvature of the surface. Whilst the data scatter resulted in a relatively poor quality profile, sufficient information was obtained to enable an initial best-fit of the profile shape and position in space.

The first polynomial fit, using all profile data points, produces a best-fit polynomial that represents an 'average' surface between the peaks and troughs across the profile, i.e. the midplane of the profile. A second polynomial fit is conducted in order to estimate the position of the outermost surface of the profile, in which only data points with a residual from the first fit above a certain threshold value are included. The threshold is set equivalent to the 50^{th} %ile of R values greater than 0.

The length of each surface normal between intersections with the fitted mandrel (i.e. baseline) surface and the corresponding fitted preform surface is then calculated, yielding a measure of preform height in the plane of the profile, ΔYZ, at each defined point across mandrel surface. From these values, an average height, $\overline{\Delta YZ}$, is calculated using points with a low mandrel surface gradient

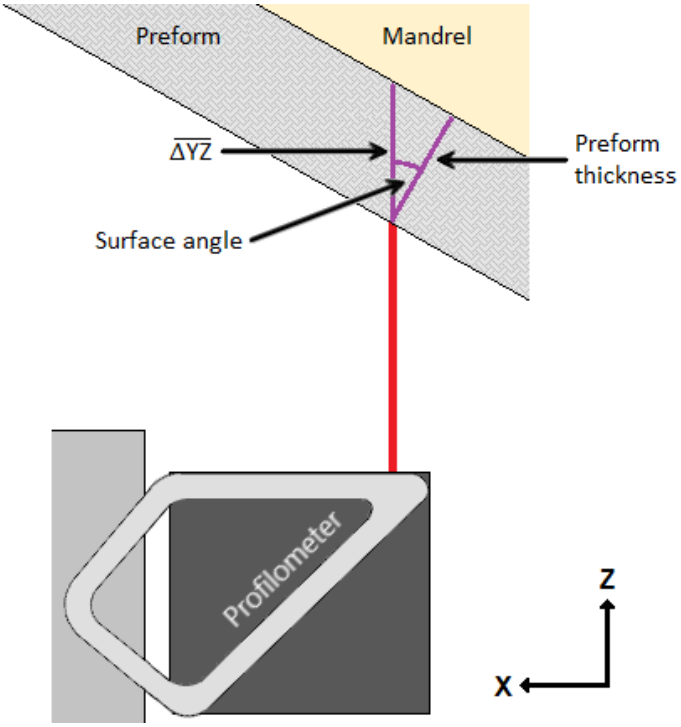

Figure 4.19: Relationship between height in YZ plane, $\overline{\Delta YZ}$, surface angle and preform thickness.

in relation to the incident laser line (i.e. surface normal gradient in excess of 10). This criteria is used to minimise sensitivity to higher order coefficients of the polynomial fitting process, since these become increasingly influential with increasing distance from polynomial extrema. Hence the

In instances where the surface being scanned is oriented perpendicular to the plane of the incident laser, i.e. when the mandrel surface gradient along the X axis, $\nabla_{surface}$, is equal to 0, the mean preform height is equivalent to the preform thickness at that scanned location. However, where $\nabla_{surface} \neq 0$, a correction is required in order to generate an estimate the thickness perpendicular to the surface, as illustrated in Figure 4.19. This is achieved by scaling $\overline{\Delta YZ}$ by the cosine of the angle between mandrel surface and X axis, which is equivalent to:

$$Thickness = \frac{\overline{\Delta YZ}}{\sqrt{1 + (\nabla_{surface})^2}} \tag{4.4}$$

For preform thickness measurements, surface gradient is calculated as the weighted average change in profile minima height over the preceding 10 profiles, weighted between 1 and 0 based on distance from current profile location.

Example preform profiles corresponding to circular mandrel cross-sections of diameter 100 mm - 400 mm are presented in Figure 4.20, along with 2nd order fitted polynomials corresponding to the profile midplane and estimated preform surface, to illustrate the performance of the surface estimation procedure with real data. The challenges associated with light scattering from the

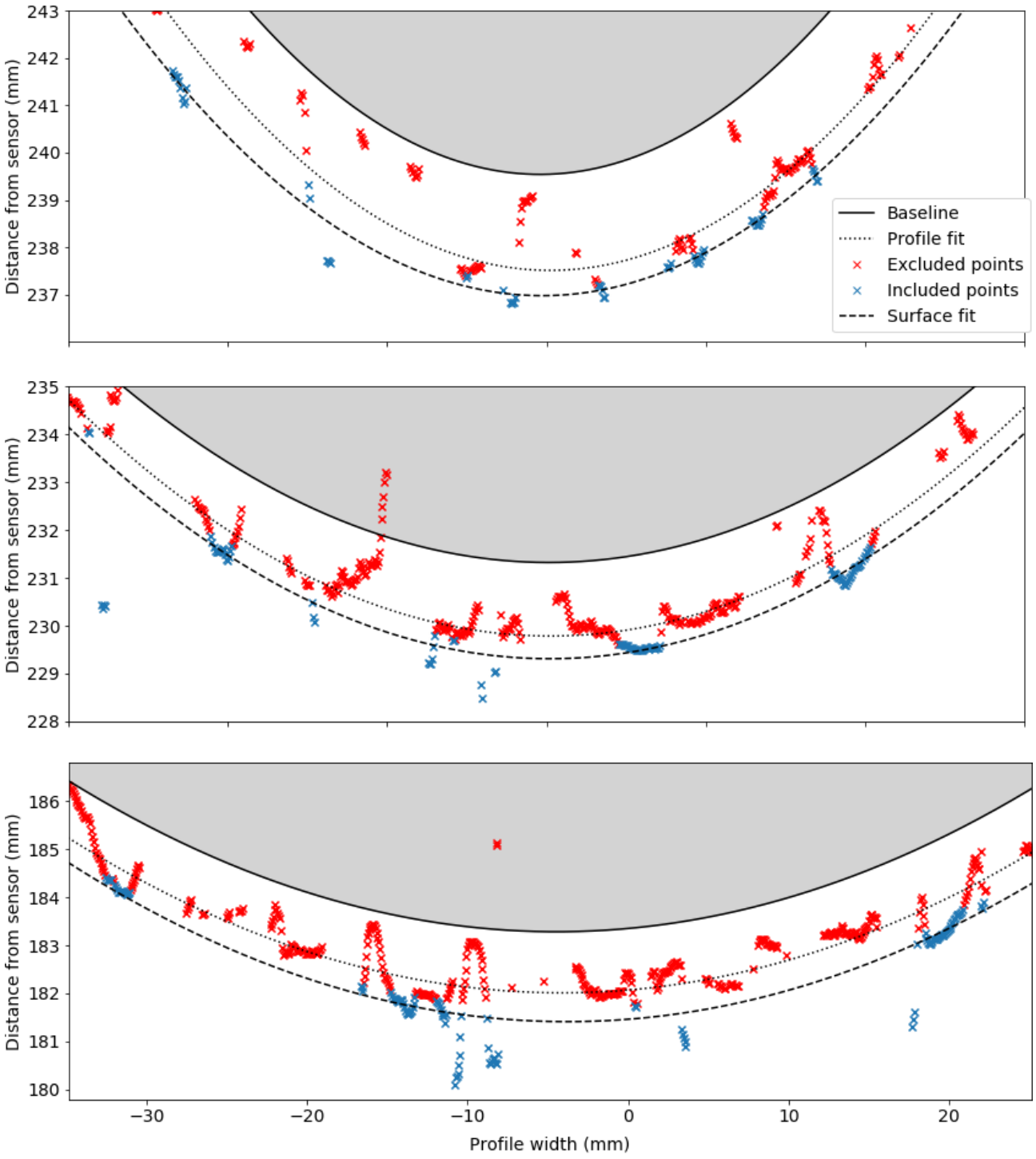

Figure 4.20: Example preform surface profiles acquired for cylindrical mandrels with diameter 100 mm (top), 200 mm (middle) and 400 mm (bottom); lines correspond to fitted baseline (solid), profile midplane (dotted) and profile (dashed) surfaces for each; data points included in the surface fit are shown in blue, and those excluded in red.

preform surface are evident in these profiles, with noisy, and in some case sparse, data points, whilst the positioning of the surface fit can be seen to align closely with many of the profile peaks. Despite the relatively low quality of the data, surface maxima can generally be identified every 10 mm - 15 mm across preform width, which is consistent with typical yarn spacing. However, it is evident from these profiles that a regular surface topology cannot be assumed for a braided preforms, due to the apparent variation in the distance of the peaks from the measured baseline surface. This is a result of irregularities within real braided textiles caused by variations in yarn cross-section, yarn spacing, relative yarn positioning between layers, etc. and highlights the challenges facing any thickness measurement procedure.

4.8 Summary of measurement system capability

This chapter describes the configuration and operation of the in-process measurement system that has been developed for the over-braiding facility at NCC as part of this research project. The system comprises a machine vision camera, laser profilometer, laser distance sensor and motorised linear motion stage, all operated via a bespoke LabVIEW software program. It has been designed for use with axisymmetric mandrel geometries which are over-braided along a linear mandrel path, i.e. mandrel motion in braider X axis only; it is suitable for use in the production of single- and multi-layer, bi- and triaxial preforms.

Braid angle measurements are made using image analysis techniques similar to those developed and evaluated by Hunt [244], adapted to enable use with multi-layered preforms, twisted yarns, and complex mandrel geometries, i.e. non-cylindrical. Non-contact preform thickness measurements are made from surface profiles acquired in a similar manner to that implemented by Schmidt *et al.* [63], with additional data fitting steps to enable in-process measurements relative to a baseline scan of the mandrel.

The LabVIEW operating program has been developed in accordance with the process variable mapping activity presented in Chapter 3, enabling the operator to log relevant job, material and process setup information (i.e. metadata) alongside the acquired measurement data to ensure that the data are suitably contextualised to hold value to future, data-led research activities. An assessment of measurement system performance, including associated measurement uncertainties, is presented in Chapter 5.

Chapter 5

Performance of in-process measurement research capability for over-braiding

This chapter is concerned with the performance of the braid angle and preform thickness measurement capabilities presented in Chapter 4. Results generated throughout development of the in-process measurement system, during which various aspects of the system design, configuration and parameterisation were investigated and optimised, are presented and discussed.

The chapter is separated into two main sections, the first focused on braid angle measurements, the second on preform thickness measurements. Each section covers the main factors that were found to impact upon measurement performance and how those factors were addressed. An assessment of overall measurement uncertainty is also presented for each, through which the main limitations of the current system capabilities are identified.

Results are presented throughout the chapter which were generated from data collected during a number of manufacturing trials. Relevant details of those trials are given in Table 5.1, along with mandrel geometry details in Figure 5.1.

Table 5.1: Details of the manufacturing trials during which data presented in Chapter 5 were acquired.

Manufacturing trial	A	B.1	B.2	C	D
Material	Toho Tenax -E HTS45 E23 12K 800tex				
Braid pattern	2/2	1/1		2/2	2/2
# carriers	288	144		288	288
Yarn twists per metre	10	7		7	10
Mandrel	M1	M2		M3	M2
# preform layers	3	3×2	1	1	8
Target braid angle (°)	40	45	30 - 60	n/a	30

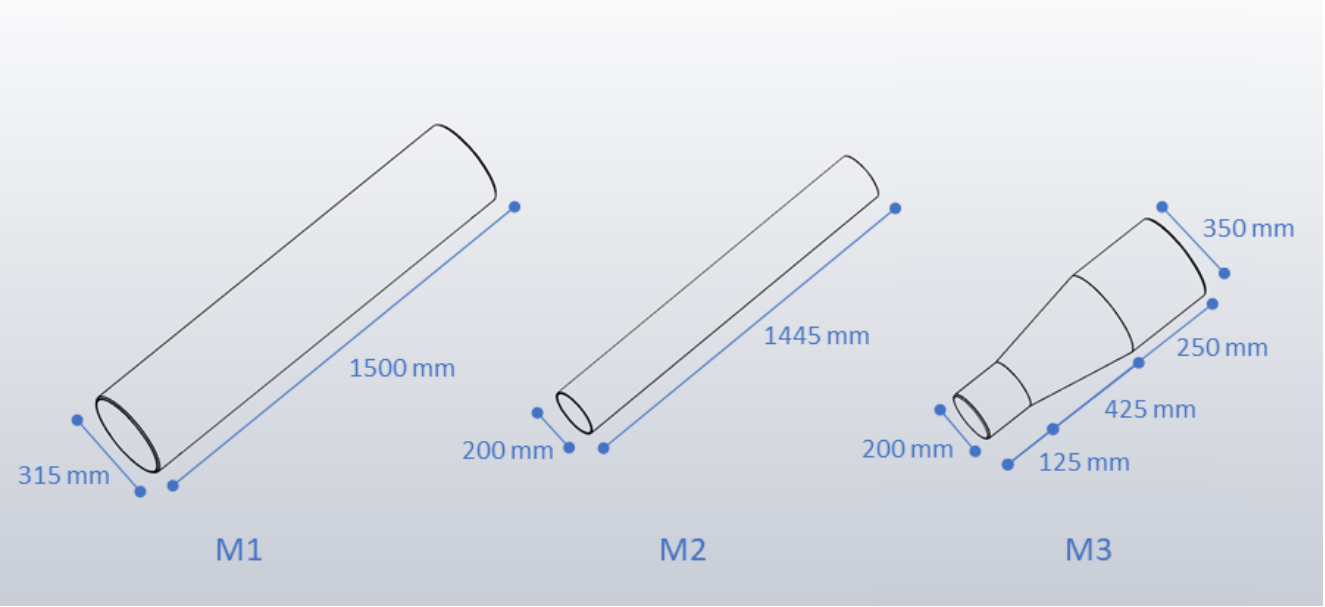

Figure 5.1: Mandrel geometry details relevant to the manufacturing trials presented in Chapter 5.

5.1 Braid angle

With regards to braid angle measurements, sensitivity of the image-based procedure detailed in Section 4.7.1 to the following sources of error and uncertainty was investigated:

- yarn twist;
- visibility of previously deposited (i.e. substrate) layers;
- light offset from the preform surface;
- orientation of the polarising filter;
- mandrel curvature;
- gradient of imaged surface relative to the camera focal plane.

The results of these investigations, including the optimisation of data processing steps implemented to minimise or mitigate measurement sensitivity, are presented and discussed in this section. This is followed by an assessment of overall measurement uncertainty, accounting for the aforementioned factors alongside anticipated sources of image variability, e.g. yarn width and spacing, brightness and focus.

5.1.1 Effect of yarn twist

Whilst generally acknowledging that braid angle, θ, is defined by the orientation of the yarns themselves, previous works which have developed and evaluated image analysis routines for braid angle measurement [102, 103, 105] have not explicitly considered the effect of fibre orientation due

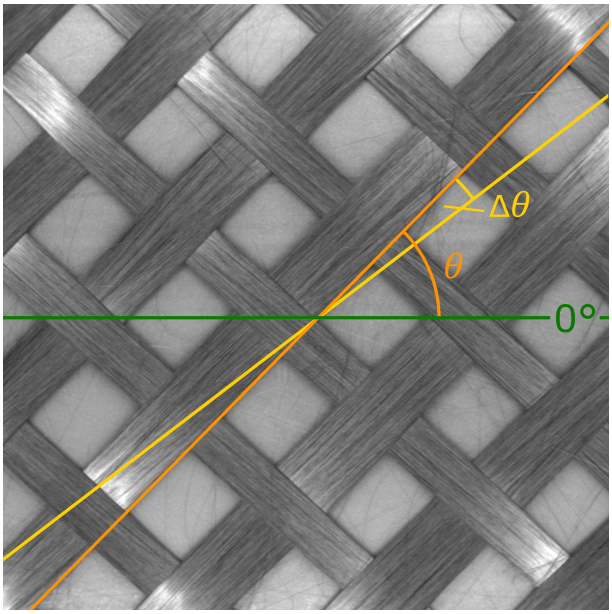

Figure 5.2: Difference, $\Delta\theta_{fib}$, between yarn-dominated braid angle measurement, θ, (orange), and fibre-dominated measurement (yellow); 0° corresponding to braider X axis is shown horizontally in green.

to yarn twist on the analysis output. This is an important distinction since twist is often introduced to yarns during bobbin winding, primarily to reduce process-induced damage [270, 271], although the effects on mechanical performance of the braided component may also be beneficial [77]. Twist direction is referred to as either Z or S such that fibres in the yarn, held vertically, align with the diagonal of the letters 'Z' and 'S', respectively. As a result, the orientation of fibres visible on the surface of a yarn deviate from the orientation of the yarn itself when deposited onto a mandrel surface. This difference between yarn and fibre orientation, $\Delta\theta_{fib}$, is illustrated in Figure 5.2. An image-based measurement technique should distinguish the orientation of yarns from that of individual fibres in order to return an accurate braid angle measurement.

In the method outlined in Section 4.7.1, this distinction is achieved by application of a median blur filter to the acquired image, which serves to reduce the definition of finer details such as those of individual fibres, whilst retaining definition of larger features, i.e. yarn structures. A median blur is performed by calculating the median pixel intensity over a square window (a.k.a. kernel) of size $K \times K$ pixels, where K is an odd integer. The median value is assigned to the pixel in the centre of the window.

By assigning a value that already exists within the window, the definition of edge features across which there is a step change in intensity is maintained. This has the effect of filtering out 'line' edges whilst retaining 'step' edges, the distinction between the two being governed by the kernel size, K. Hence K should be sufficiently large so as to treat fibre details as line edges and yarn edges as step edges, with the optimal size dependent on the scale of fibres and yarns in the image.

The relationship between kernel size and the resultant braid angle measurement was therefore investigated in order to establish an appropriate value of K for images acquired by the system described in Section 4.5, with image scale of 87 px/mm.

Method

Images acquired during deposition of the first preform layer in manufacturing trial B.1 were used for the initial investigation. Repeat braid angle measurements were conducted according to the method described in Section 4.7.1, with the exception that the kernel size of the median blur filter was varied between between 1 px, i.e. no blur, and 81 px, in 4 px intervals. The effect of kernel size variation on consecutive measurements across a 1 metre section of the preform was evaluated.

For this trial, yarns were wound onto bobbins with 7 twists per metre (t/m), with twist direction S for those loaded on carriers travelling around the braid ring in a clockwise direction and Z for those carriers travelling anticlockwise.[1] The result of this loading arrangement was that deviation of surface fibres from deposited yarn orientation was towards the braiding axis, which would cause an apparent reduction in measured braid angle. By calculating the helix angle for a helix of equivalent pitch and effective diameter as the yarns, it was possible to estimate the expected value of $\Delta\theta_{fib}$ [270]. Assuming an effective yarn diameter of 1.1 mm (12,000 filaments of 7 μm diameter at 50 % V_f), 7 twists per metre (or 143 mm pitch) equates to a helix angle of 1.4°; the angle of fibres visible on a yarn surface might be expected to deviate from the orientation of the yarn by a similar amount. The detection of a significant number of fibre edges during image analysis could therefore skew the braid angle measurements by as much as ± 1.4°.

In a second investigation, kernel size variation was conducted on a set of images collated from a range of manufacturing trials, all of biaxial preforms braided over cylindrical mandrels but with varying image compositions (e.g. mandrel surface material, visibility of previous preform layers, image brightness and focus). Again, K was varied between 1 px and 81 px, in 4 px intervals.

For each image, the change in measured braid angle between consecutive kernel sizes was calculated. From this, the average change in measured value across the set of images for each K interval was calculated, generating an *average gradient of change in measurement*. This value was used as an indication of the consistency of the effect of kernel size on measurements across all images; a positive (or negative) value would indicate a general increase (or decrease) in measured braid angle across the image set, whilst a value around 0 would indicate no common trend.[2] The average of the absolute change in measured value was also calculated across the set of images (a.k.a. the

[1] Directions as viewed from the front of the braid ring.

[2] Since the direction of yarn twist relative to the braiding axis was not consistent across the image set (due to the differing directions of travel of Z- and S-twisted spools around the braid ring), it was necessary to invert the direction of change in measurement results for some images, such that the expected change between fibre- and yarn-dominated measurements with increasing K was always positive.

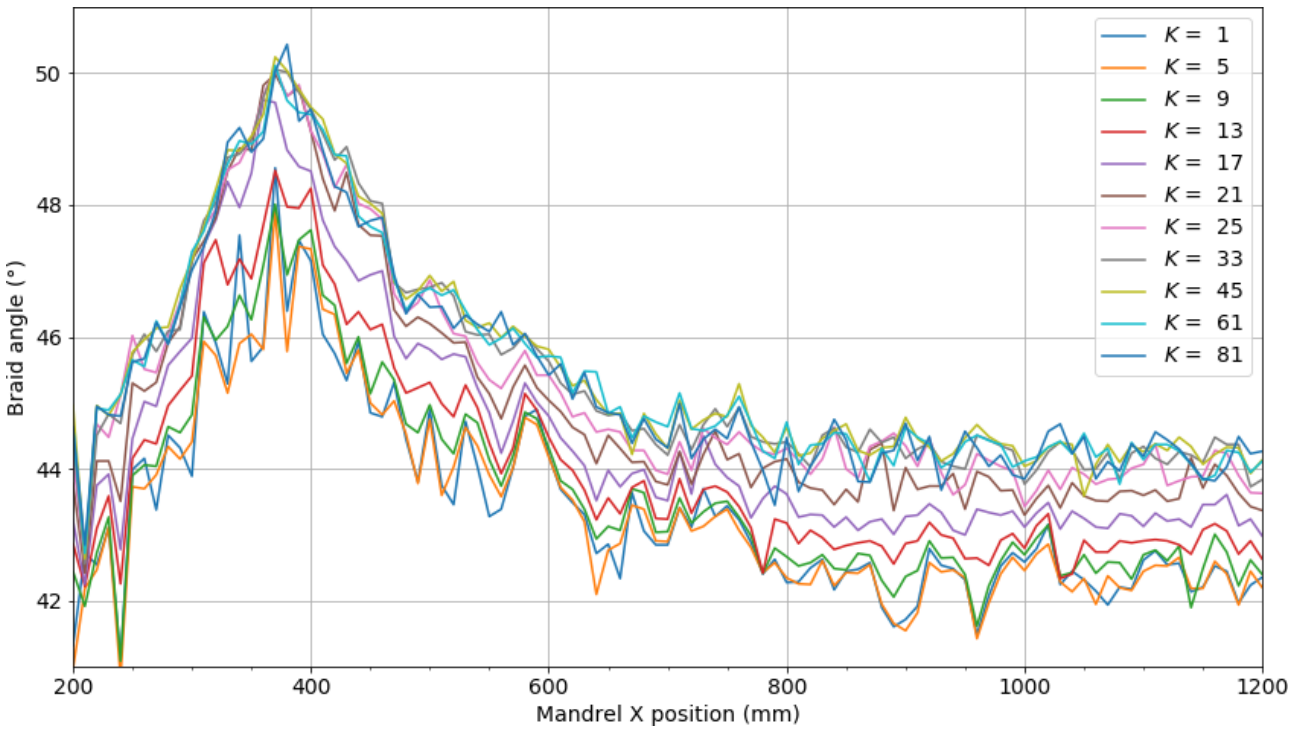

Figure 5.3: Braid angle measurements for a 1 metre section of the first deposited preform layer in trial B.1, obtained with a range of median blur filter sizes, K.

average absolute change in measurement), as an indication of the sensitivity of the analysis routine to changes in K.

Results and discussion

A series of measurement results corresponding to a 1 metre section of braided preform deposited during trial B.1, between which the the kernel size employed in the median blur filter was varied, are presented in Figure 5.3. These show an increase in measured braid angle of approximately 2° as K increased from 1 px to 33 px; above 33 px no further significant changes were evident. Given the yarn twist directions and estimated helix angle, this increase is consistent with the expected transition from fibre-dominated to yarn-dominated measurements. The underestimation of $\Delta\theta_{fib}$ by helix angle calculation can be explained by the associated circular approximation of deposited yarn cross-section, when in reality the cross-section geometry would have been closer to elliptical [21], resulting in an increase in helix angle when viewed from the broad side of the yarn. The evidence of a reduction in fluctuation between adjacent measurements along the mandrel length with increasing K is also consistent with a transition towards dominance of more stable yarn edges over fibre edges in the measurement procedure.

For the set of images collated from a range of different manufacturing trials, the average absolute

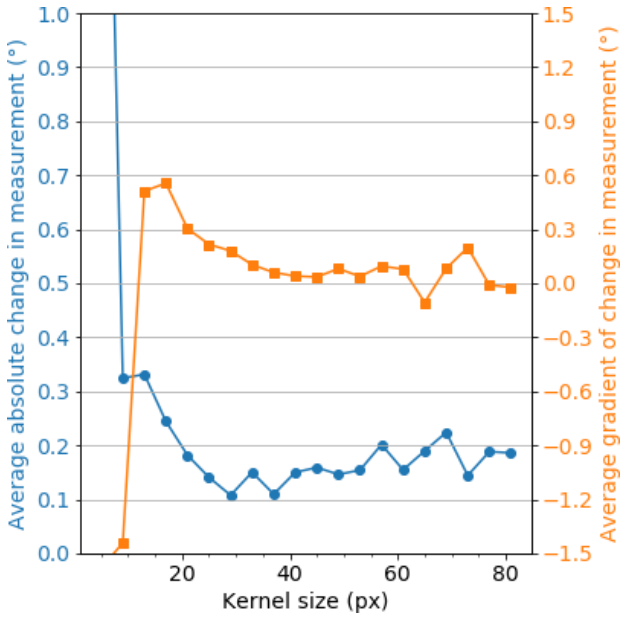

Figure 5.4: Average absolute change and average gradient of change in braid angle measurement with increasing values of K, calculated across a sample set of preform images.

change and average gradient of change in measured angles with increasing kernel size are presented in Figure 5.4. The *average absolute change* was found to reduce as kernel size increased, up until $K = 25$ px. This was in accordance with the anticipated effect of reduced fibre definition on measurements as a result of increased image blurring. Above $K = 25$ px, *average absolute change* per interval generally remained between 0.1° - 0.2°, with only a gradual increase evident across the remaining range of K values. This suggests negligible measurement sensitivity to kernel size at these higher values, although a slight reduction in measurement stability was apparent for $K > 50$ px.

In the case of *average gradient of change* between consecutive kernel size intervals, a large negative gradient was calculated for $K \leq 9$ px. This was not anticipated given the inversion of results for some images in order to ensure consistent direction of change between fibre and yarn orientations across the image set. It suggests that the effect of kernel size on the measurement procedure does not reliably follow the expected trend for these small values of K across all images. For K between 13 px and 45 px, however, a positive, gradually decreasing gradient of change was observed, which does conform to the expected trend as measurements generally transitioned towards higher, yarn-edge dominated values. The minimum absolute value was returned for $K = 45$ px, beyond which values fluctuated around 0, indicating an absence of any consistent trend in measurement changes above this value; i.e. changes in braid angle measurements as kernel size was increased further were likely due to random fluctuations.

The results presented in this section suggest that an optimal value for median blur filter kernel

size to ensure that any influence of fibre edges on measurements is mitigated, whilst also minimising measurement instabilities, is around 45 px for the described system configuration used with 12K yarns. This was as indicated by the negligible sensitivity to kernel size in this region, evident both visibly and analytically. As such, $K = 45$ px was specified in the procedure described Section 4.7.1. However, this value should be re-assessed if future system developments result in a change of scale for images used in the braid angle measurement procedure. It may also need to be adjust to optimise performance with thicker and thinner yarn materials, i.e. $\neq 12K$.

5.1.2 Effect of visibility of previous layers

Besides the sensitivity of measurements to individual fibre orientations, the image-based measurement procedure was also susceptible to yarn edges visible in substrate preform layers, i.e. those layers previously deposited during the preforming operation. However, since yarn edges in visible sub-layers are fragmented and partially obscured by yarns in the outermost layer, it was anticipated that their contribution to the Fourier power spectral density would not be significant. Thus the image analysis routine was expected to return a measurement corresponding to the outermost, unobscured layer.

Method

In order to test this hypothesis, braid angle measurements acquired during trial B.2 were analysed. In this trial, a step change in target braid angle from 26° to 60° was implemented by decreasing the mandrel traverse speed for a constant pick speed, generating a transition in deposited braid angle over a 600 mm length of the mandrel. This transient preform layer was braided over the top of the 3 layer preform produced in B.1 with a constant target $\theta = 45°$. The use off 144 bobbins resulted in an open preform architecture, ensuring high visibility of substrate yarns.

Where necessary, manual measurements were made with the image processing software ImageJ [272], using the angle tool to measure the angle of yarn edges relative to the horizontal X axis. The braid angle was calculated as the average of the median absolute angle from 10 yarn edge measurements per yarn direction. The median, rather than mean, value was used for each direction in order to reduce the influence of outliers, i.e. yarns with a significant difference in orientation compared to those around them, which can be caused by a number of material or process-induced factors. This approach mimics the tendency for humans to avoid such visible anomalies in favour of more representative regions when making manual measurements. For each manual braid angle measurement, the median absolute deviation from sample median (MAD) was calculated as a measure of sample (i.e. braid angle) dispersion.

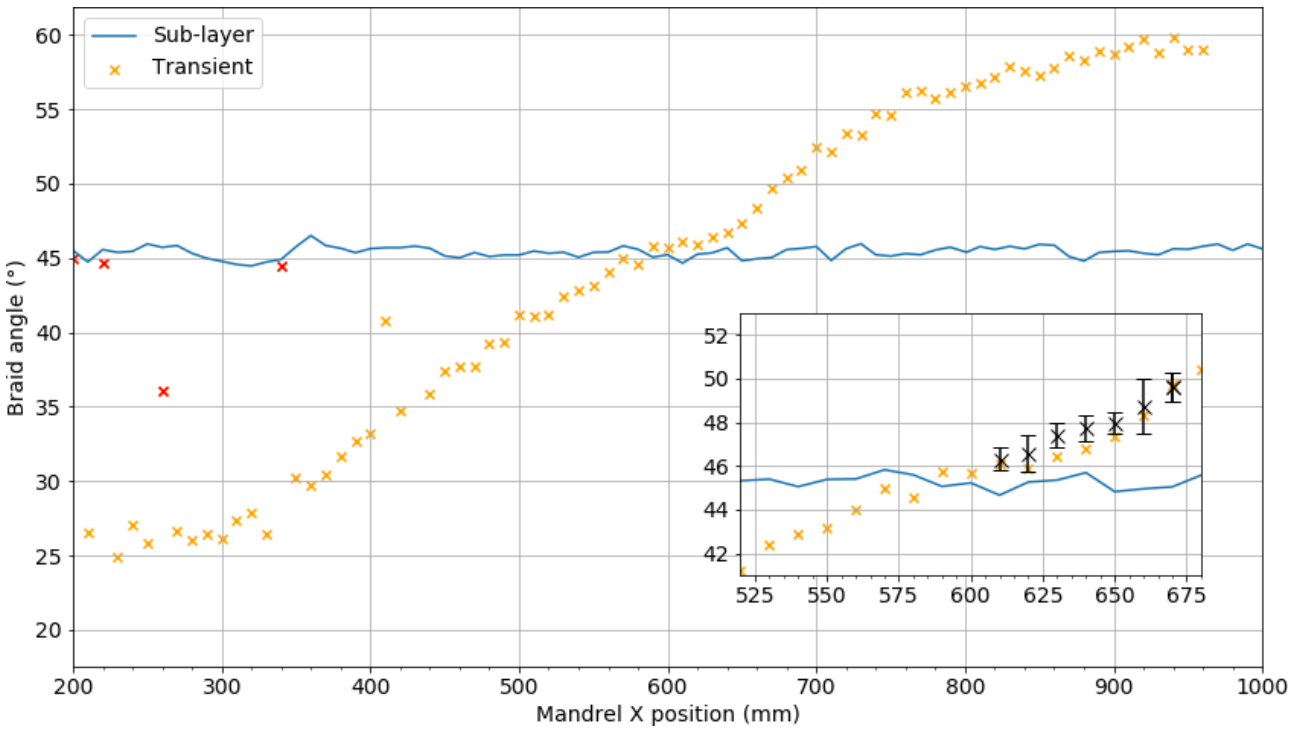

Figure 5.5: Braid angle measurements for the transient outer layer (orange) and the constant-angle substrate layer over which it was braided (blue) with target $\theta = 45°$; anomalous results due to oscillatory layer motion shown in red; manual measurements and associated MADs shown in inset (black).

Results and discussion

Braid angle measurements for the substrate (B.1, layer 3) and transient (B.2) layers are presented in Figure 5.5. On the whole, measured angles for the transient layer followed the expected behaviour, with a steady increase from $\sim 26°$ prior to the traverse speed step change at X $\approx$ 350 mm, up to $\sim 59°$ by X = 900 mm.

At lower mandrel locations, i.e. X $\leq$ 410 mm, a number of anomalous results were observed. Those marked in red were found to correspond to blurring of yarns in acquired images, due to oscillatory motion of the layer undergoing deposition caused by the dynamics of the braiding process. Consequently, the measurements were dominated by the sharper edges of yarns in the stationary substrate, for either one or both yarn directions. This behaviour ceased above X = 340 mm, as both braid angle and the amount of deposited material increased, creating sufficient friction to prevent further oscillatory motion. The result at X = 410 mm was not due to yarn blurring, but poor detection of yarn edges for one yarn direction relative to the substrate.

In the region 600 mm < X < 670 mm, measurement results were seen to deviate from the general trend, instead appearing to align with those for the substrate layer. Two possible explanations for this observation were explored: firstly, that the measurements were accurate, indicating alignment between the transient and substrate yarns (perhaps due to nesting effects); secondly, that the

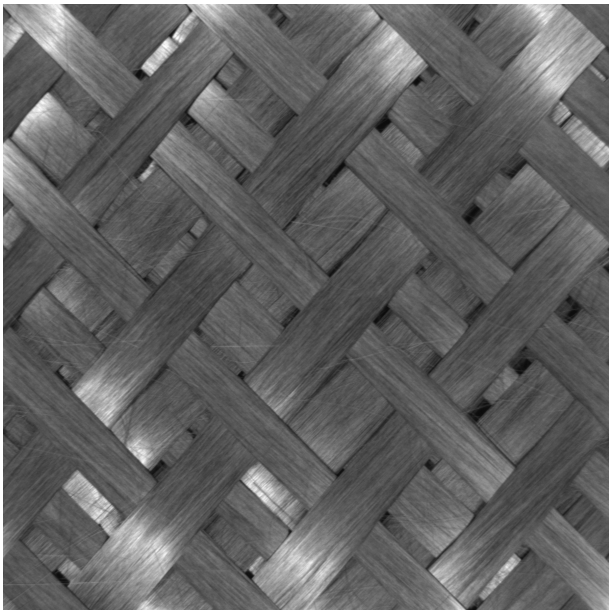

Figure 5.6: Image of the transient layer acquired at X = 640 mm, in which the alignment of inter-yarns gaps with yarns in the sub-layer can be seen.

system measurements were inaccurate, returning measurements of, or influences by, the substrate.

Manual measurements from images in this region were made, the results of which are presented in the inset of Figure 5.5. These were found to follow the expected general trend more closely than system measurements, suggesting that the system measurements were inaccurate in this region. Inspection of the corresponding images revealed high visibility of yarn edges in the substrate preform, due to alignment of inter-yarns gaps in the outer layer with yarns in the substrate, as can be seen in the image for X = 640 mm in Figure 5.6. In this scenario, neither set of yarn edges were found to dominate the image analysis routine, resulting in a broad peak in the plot of mean pixel intensity against angle (refer to Section 4.7.1 for details). The returned measurement value, i.e. peak centre, was therefore a combined measurement of the outer and substrate layers.

This finding is problematic for measurement of multi-layer preforms with relatively low cover factor, i.e. those for which inter-yarn spacing is greater than yarn width, and similar braid angles between layers. Further research into this performance issue is required to improve the identification and selective measurements of yarns in the outer, measurement target layer.

5.1.3 Effect of lighting

For the direct, dark field illumination lighting arrangement employed in this system, it was anticipated that minimising the distance between the light source and the preform surface would minimise specular reflections and maximise accentuation of edge details, thus producing the highest quality images. However, the system has been designed for use with complex mandrels with

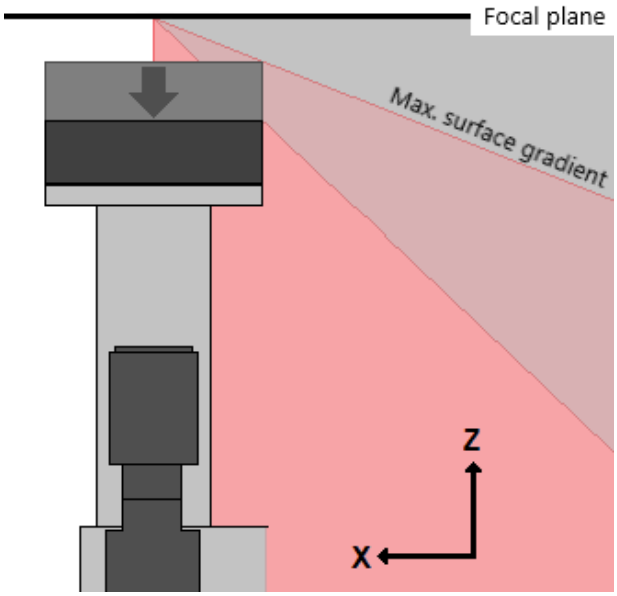

Figure 5.7: Effect of light offset on the maximum surface gradient that can be imaged within the focal plane of the camera assembly.

varying surface gradients, and will therefore be required to acquire images of surfaces which are not parallel to the focal plane of the camera setup. In such instances, the offset between light and surface restricts the maximum gradient of a surface that can be imaged, as illustrated in Figure 5.7; a greater distance between light and surface enables data acquisition for greater variety of mandrel designs and non-linear mandrel paths. The distance between the face of the light ring and the focal plane of the camera setup, from here on referred to as the light offset, is therefore a compromise between between image quality and measurement system flexibility. As such, the sensitivity of braid angle measurements to light offset was investigated.

Method

For this investigation, images acquired of the outer layer of the preform manufactured in trial A were used. Six sets of images were acquired over a 600 mm length of the preform, at 10 mm intervals. A different light offset was used for each set, varied between 10, 15, 20, 27, 35 and 50 mm. The camera exposure was set to automatic and the polarising filter removed.

To reduce the impact of any X axis positional uncertainty on the results , images within each set were stitched together using the photo stitching software Hugin [273], prior to conducting any braid angle measurements. Measurements were then conducted as per the method outlined in Section 4.7.1, on cropped, 2400 × 2400 pixel sections of the stitched image, taken centrally with regards to image height and at 5 mm (435 px) intervals along the length.

The image analysis routine is based on Fourier analysis of an edge-filtered image, in which the

intensity of edges is proportional to the change in intensity across pixels adjacent to the edge in the original, unfiltered image. Where there is a significant surface reflection from yarn sections in the original image (i.e. areas which have very high pixel intensities), this produces higher intensity edges in the edge-filtered image than those where there is no reflection. This was expected to adversely affect the resulting Fourier PSD, with edges adjacent to reflections contributing more strongly, and thus weighting the braid angle measurement towards those edges. In an attempt to minimise this source of measurement bias, an upper pixel intensity threshold, or clip limit (CL), is applied to the edge-filtered image prior to conducting the Fourier analysis, where the threshold is set equivalent to a %ile of all pixel intensities across the edge-filtered image. The effect of this clipping procedure and sensitivity of measurements to the value of CL was assessed as part of the investigation into the effect of light offset, in order to determine an optimal value for the mitigation of reflections.

Results are presented for each of the six light offset image sets in which the clip limit was varied between the 100^{th} and 95^{th} %iles of edge intensity values. Manual measurements, following the procedure previously outlined in Section 5.1.2, were made for images at 12 locations along the preform. Of these 12 locations, 6 were chosen due to relatively high apparent sensitivity to CL, the other 6 due to relatively low apparent sensitivity to CL.

Results and discussion

Figure 5.8 presents automated braid angle measurements along the length of the preform for each of the 6 light offsets with no threshold applied, i.e. CL = 100^{th} %ile, alongside the median manual measurements and their corresponding MADs. The sensitivity of automated image analysis measurements to light offset was found to vary along the preform length, from locations where all measurements were within 0.2° (e.g. X = 225 mm and 450 mm), to those where measurements varied by > 1° (e.g. X = 130 mm and 540 mm); the mean standard deviation of measurements at different light offsets, averaged across all measurement locations, was calculated to be 0.30°.

It can also be seen that, at a majority of the manual measurement locations, automated measurements fell within or close to the MAD for the manual measurement, regardless of light offset, demonstrating agreement between the underlying procedures. However, at X = 130 mm and 580 mm, automated measurements for half of the light offsets fell significantly outside of the MAD, suggesting the presence of a feature or features in the corresponding images that was accentuated at particular offsets. Edge-filtered images at each light offset for these two mandrel locations are presented in Appendix C. For X = 130 mm, these reveal a prominent yarn section towards the lower centre of the image, particularly for light offsets 15 mm - 35 mm, caused by strong reflection from the yarn surface at that location. The orientation of this section of yarn also happens to deviate considerably from that of adjacent yarns, and hence the Fourier PSD and resultant braid angle

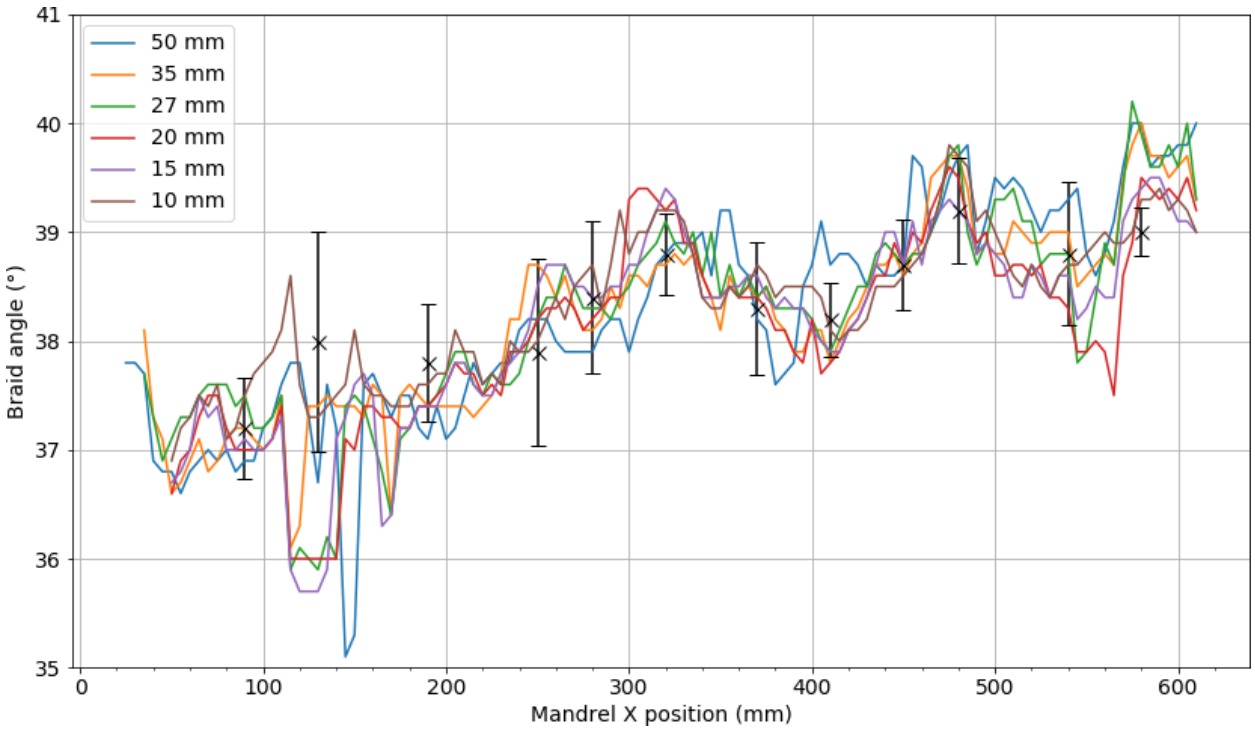

Figure 5.8: Braid angle measurements for each light offset; markers indicate manual measurements with error bars representing the corresponding median absolute deviation from sample median (MAD).

measurements were skewed towards the orientation of this particular, anomalous yarn section. In the case of X = 580 mm, the discrepancy coincided with high intensity edges along the upper edge of the image, particularly for light offsets $\geq$ 27 mm, due to reflections from a number of yarns. Again, these prominent edges resulted in measurement skew.

Given the intended use of the measurement system with complex mandrel geometries, for which specular reflections from highly reflective carbon fibre yarns are inevitable under direct lighting due to doubly curved and inclined surfaces, it is desirable to minimise sensitivity to lighting variations such as that evident in Figure 5.8. Hence the effect of clip limit was investigated on the same image sets.

The visible effect of clip limit on relative edge intensities in an edge-filtered image can be observed in Figure 5.9, where edge intensities are presented for each of the six thresholds applied to the image at X = 580 mm, light offset = 50 mm. In the case of CL = 100^{th} %ile, the majority of edge features across the image are barely visible due to relatively high intensity of a small number of edges towards the top and bottom of the image. These high intensity features coincide with regions of the image where the curvature of the preform surface caused an increase in reflections from yarn surfaces. It is expected that the resulting measurement was biased towards these small number of yarn edge sections coinciding with surface reflections.

The dominance of these high intensity regions was suppressed as the clip limit was lowered, with

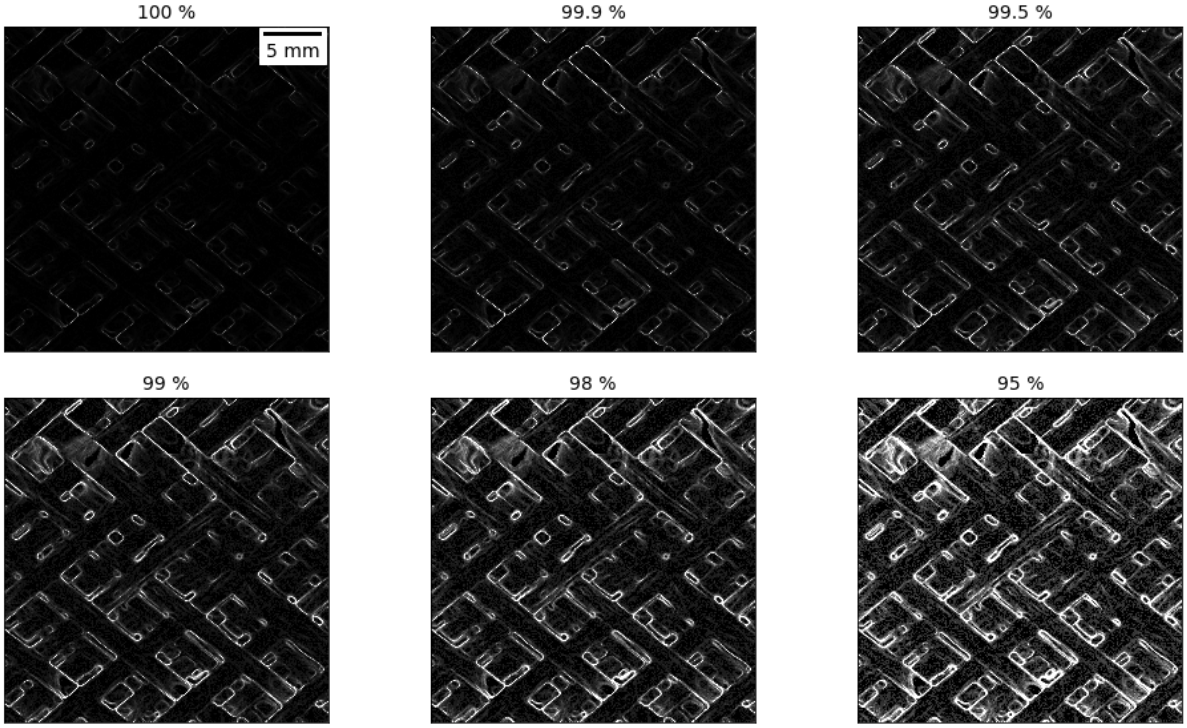

Figure 5.9: Edge intensities resulting from the application of each clip limit to the image at X = 580 mm, light offset 50 mm.

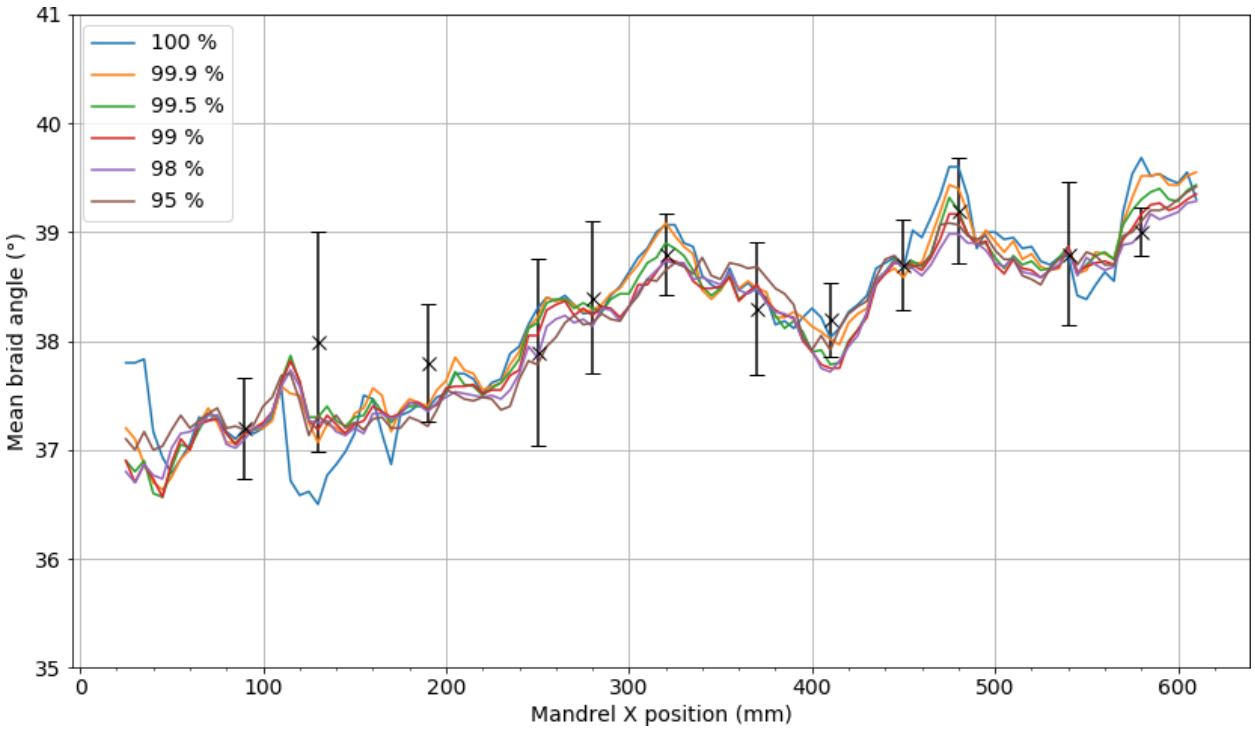

Figure 5.10: Braid angle measurements averaged across all light offsets, for each edge intensity upper limit; markers indicate manual measurements with error bars representing the corresponding MAD values.

greater uniformity of yarn edge intensities across the image visible for CL $\leq 99.5^{\text{th}}$ %ile, both in the upper preform layer and the visible sub-layer. This was expected to decrease the sensitivity of θ measurements to the orientation of such localised, high intensity edge sections. Indeed, results at X = 580 mm in Figure 5.10, which presents the automated measurement results averaged across all light offsets for clip limits between the 100^{th} and 95^{th} %iles, indicate that measurements converged to a value within the MAD of manual measurements for CL $\leq 99^{\text{th}}$ %ile. Similar trends are evident across many of the measurement locations, with θ appearing to stabilise at CL $\leq 99^{\text{th}}$ %ile.

It is worth noting, however, that edge features across the surface of yarns, corresponding to individual fibres, also become increasingly visible as the clip limit is reduced. This is particularly evident for CL = 95^{th} %ile in Figure 5.9, and is expected to adversely affect the measurement procedure as discussed in Section 5.1.1. Hence it was anticipated that an optimal threshold value or range exists in which the uniformity of yarn edge intensities is maximised whilst the level of fibre detail remains insignificant.

Table 5.2: Mean and standard deviation for $\sigma_{\theta,light,X}$ at each upper limit for edge intensity, i.e. clip limit.

Clip limit (%ile)	$\sigma_{\theta,light,X}$ μ (°)	σ (°)
100	0.30	0.195
99.9	0.19	0.094
99.5	0.15	0.069
99	0.15	0.065
98	0.15	0.065
95	0.19	0.071

Table 5.2 contains the mean and standard deviation for the standard deviation of measurements across all light offsets and measurement locations, $\sigma_{\theta,light,X}$, calculated for each clip limit. These results show a considerable reduction in the mean value upon the introduction of a clip limit (i.e. CL < 100 %ile), by as much as half for 99.5^{th} %ile $\geq$ CL $\geq 98^{\text{th}}$ %ile, They also show a concurrent reduction in the standard deviation, to a minimum for 99^{th} %ile $\geq$ CL $\geq 98^{\text{th}}$ %ile. This indicates that the spread of measurements generated under, and hence measurement sensitivity to, varying lighting conditions was minimised across all measurement locations for a clip limit in the range of 99^{th} - 98^{th} %iles.

The results presented in Table 5.2, supported by qualitative interpretation of the images in Figure 5.9, suggest that a clip limit set at the 99^{th} %ile minimises measurement sensitivity to varying illumination whilst not significantly increasing the susceptibility to non-yarn features, such as fibre edges. Hence CL = 99^{th} %ile was specified in the measurement procedure in Section 4.7.1.

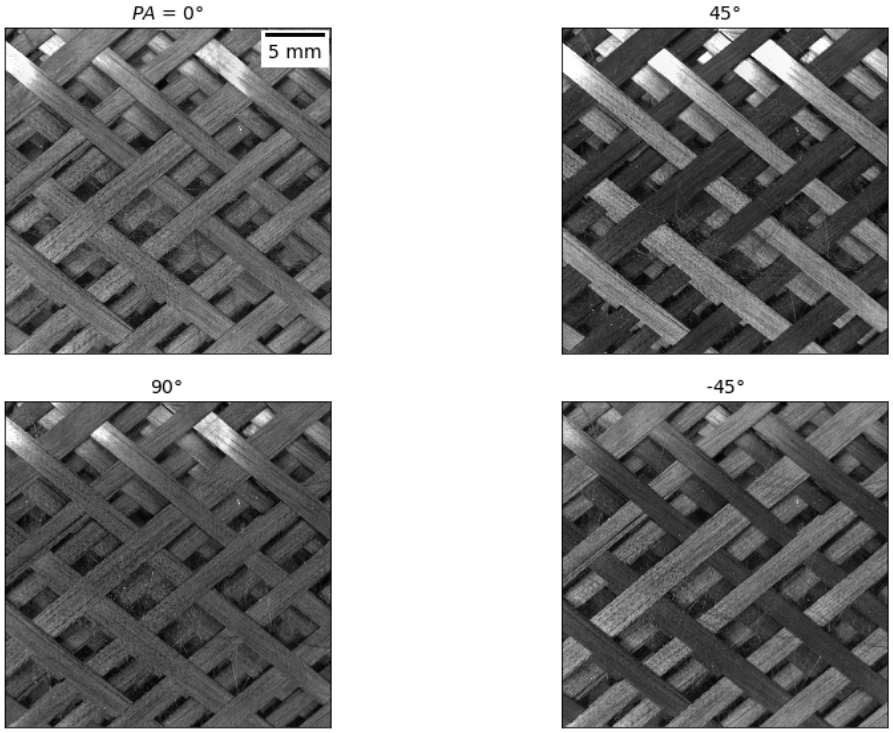

Figure 5.11: Images acquired with different polarising filter orientations, illustrating the accentuation of yarns aligned with the filter orientation.

5.1.4 Effect of polarisation

In an effort to reduce the occurrence of specular reflections in acquired images, an adjustable polarising filter was included in the camera assembly, mounted on the end of the lens. The effect of polarising filter orientation relative to the primary braiding axis, from here on referred to as polarising angle (PA), on the appearance of yarns in the acquired image and its subsequent impact on braid angle measurements was investigated.

Method

Four sets of images were acquired using the same mandrel, preform and image acquisition intervals as described for Section 5.1.3, between which the polarising angle was varied through 0°, 90°, 45° and -45°. The camera exposure was set to automatic and the light offset was set to 10 mm. As described in Section 5.1.3, images were stitched together prior to cropping 2400 × 2400 pixel sections of the stitched image at 5 mm (435 px) intervals along the length for image analysis.

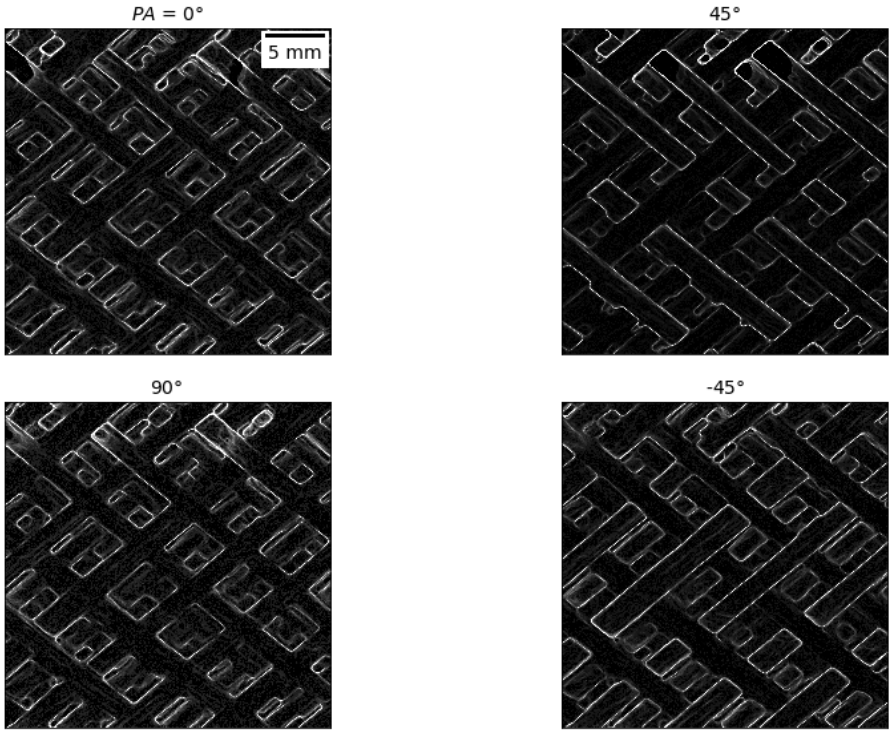

Figure 5.12: Edges detected in images acquired with different polarising filter orientations, illustrating the accentuation of yarns edges aligned with the filter orientation.

Results and discussion

Images of the same preform section acquired under the different polarising angles are presented in Figure 5.11. It can be seen for a polarising angle of ± 45° that yarns/fibres which were closely aligned with the polarising angle are accentuated, whereas an angle of 0° and 90° resulted in more uniform yarn intensities. The greater image brightness for PA = 0° relative to 90° was also likely due to closer alignment of yarns with the filter orientation, since the braid angle was < 45°. In the image analysis procedure, increasing yarn intensity relative to their surroundings, such as in the case of PA = ± 45°, is beneficial for yarn edge detection. This is demonstrated by the edge-filtered images in Figure 5.12, where the outlines of accentuated yarns are clearly defined.

Another observation is that the intensity of specular reflections visible towards the top of the original, unfiltered images in Figure 5.11 was maximised when the yarns were closely aligned with the polarising angle (i.e. for PA = 45°), and minimised when highly misaligned (i.e. for PA = - 45°). This demonstrates that optimal reflection suppression can be achieved by aligning the polarising filter orthogonal to the orientation of highly reflecting yarns.

Both with regards to accentuation of yarn edges and minimisation of reflections, it would appear that optimal performance is achieved when the filter is aligned with (yarn accentuation), or orthogonal to (reflection minimisation), each yarn direction being imaged. However, to take advantage of

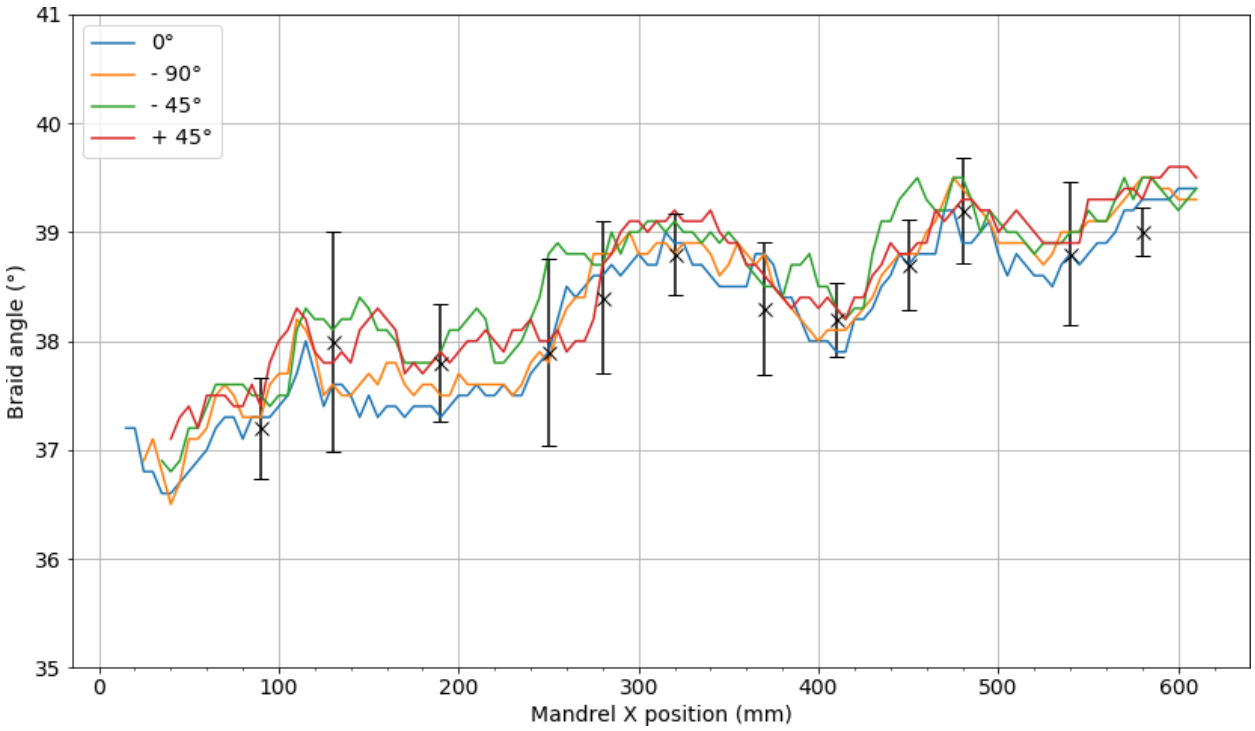

Figure 5.13: Braid angle measurements for each polarising angle; markers indicate manual measurements with error bars representing the corresponding MAD values.

this performance would require the ability to dynamically adjust filter orientation during preform manufacture at an appreciable rate. Whilst this would be possible to achieve with a motorised filter arrangement [274], or a novel polarised image sensor [107], neither option was pursued as part of this work due to the additional costs and complexity associated with either setup.

A compromise that does not require active filter adjustment whilst offering some reduction in reflection intensity was preferred for this stage of system development. This involves alignment of the filter either parallel with, or perpendicular to, the primary braiding axis, ensuring partial misalignment with both bias yarn directions, for all achievable braid angles (typically in the range 30° - 60°); i.e. for $\theta < 45°$, PA = 90°; for $\theta > 45$, PA = 0°. This setup achieves partial suppression of specular reflections on the surface of yarn, without biasing measurements towards either yarn direction. In the case of triaxial braiding, perpendicular filter alignment (PA = 90°) would likely be preferable to minimised reflections from axial yarns, although this has not been confirmed in this research.

5.1.5 Effect of surface curvature

The effect of surface curvature on the output of image-based braid angle measurement for cylindrical mandrels due to projection of helical yarn paths into a two dimensional image plane has been

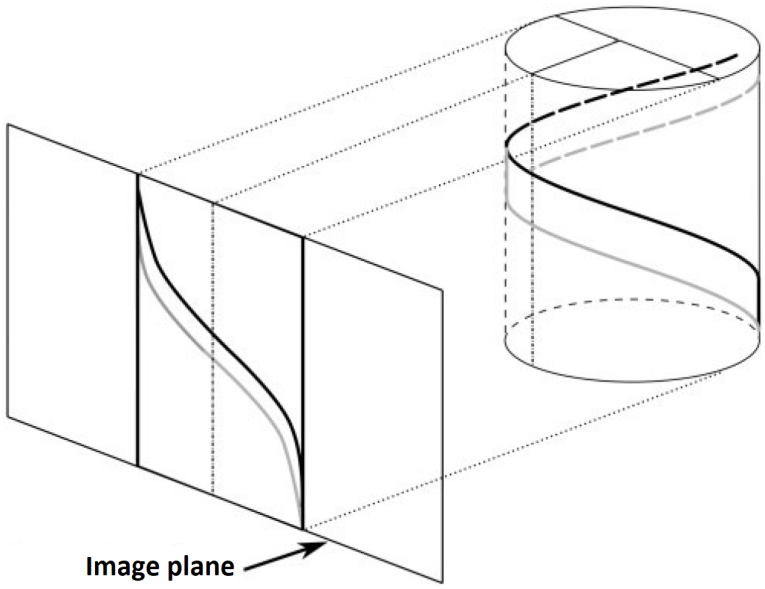

Figure 5.14: Apparent yarn path distortion resulting from projection of helical yarn path into image plane; recreated from [105].

investigated previously by Hunt and Carey [105]. The projection, illustrated in Figure 5.14, causes an apparent curvature of yarn path towards the axis of the cylinder and hence skews image-based θ measurements towards lower values.

To address this source of error, Hunt and Carey [105] compared the performance of image cropping and unwrapping procedures on the outcome of 2D Fourier transform-based braid angle measurements. For images of a 1" (25.4 mm) diameter tubular mandrel, the full width of which was captured in the field of view, an apparent broadening of peaks in the angular mean pixel intensity plot (see Figure 4.17 for example) was reported due to yarn path projections into the image plane. This broadening was found to reduce as the visible circumferential angle of surface, α, in images was reduced, by cropping, from 85° to 35°. However, negligible effect on the measured braid angle, taken as the position of the maximum mean pixel intensity value, was observed.

An alternative approach, in which images were 'unwrapped' onto the image plane based on *a priori* knowledge of the mandrel circumference, appeared to remove peak broadening. Statistically significant differences in measured braid angle between cropped and unwrapped images of approximately 0.7° were reported for expected braid angles of 45° and 55°, with the suggestion that the unwrapped results were closer to true value.

For the system developed in this work, images are cropped to a width of 2400 px as part of the image analysis procedure; no unwrapping is performed. With a scale of 87 px/mm, cropped images cover an area of 28 × 28 mm. Corresponding circumferential angles for the range of mandrel diameters that this system has been designed for use with are presented in Table 5.3. For mandrel

diameters greater than $\sim$ 50 mm, the visible circumferential angle is less that the smallest angle investigated in [105].

Table 5.3: Circumferential angle, α, visible in cropped images for various mandrel diameters.

Mandrel diameter (mm)	Circumferential angle, α (°)
40	44
50	33
80	20
200	7.9
315	5.0
500	3.2

Method

To investigate the presence, or otherwise, of a θ-dependent sensitivity to the visible circumferential angle, measurements were generated using images acquired during trial B.2, in which a preform layer with transient target braid angle was produced. Images corresponding to a 400 mm length of preform were used, over which θ varied from 33° to 57°. By varying the cropped image size between 1000 px and 3000 px, measurements for $3.3° \leq \alpha \leq 9.9°$ were generated.

Results and discussion

The results are presented in Figure 5.15 and appear to show a divergence in measurement values as mandrel X position increased, i.e. for higher values of θ, particularly evident for X > 600 mm ($\theta > 45°$). Linear regression analysis of measurements at each image location revealed a strong relationship between α and θ at locations where the median braid angle, $\tilde{\theta}$, was greater than 45°; the majority of locations where $46° \geq \tilde{\theta} \leq 54°$ produced a correlation coefficient > 0.8 (see Figure 5.16). Corresponding p-values for regression analysis are also presented, which indicate that the probability of correlations in the same θ range having been generated by a flat relationship (i.e. with correlation gradient = 0) is very low. However, the direction of the apparent correlation is opposite to what would be expected; rather than a decrease in measured θ as α increased, due to increasing contribution from distorted yarns paths away from the mandrel centreline, θ was found to increase with α. It was, therefore, concluded that this trend was not a result of mandrel curvature on the measurement procedure.

To further investigate the magnitude of curvature induced-measurement error, results were generated for images that had been unwrapped via orthographic projection, based on the known image scale and mandrel radius. The measurements were compared to those for the original image,

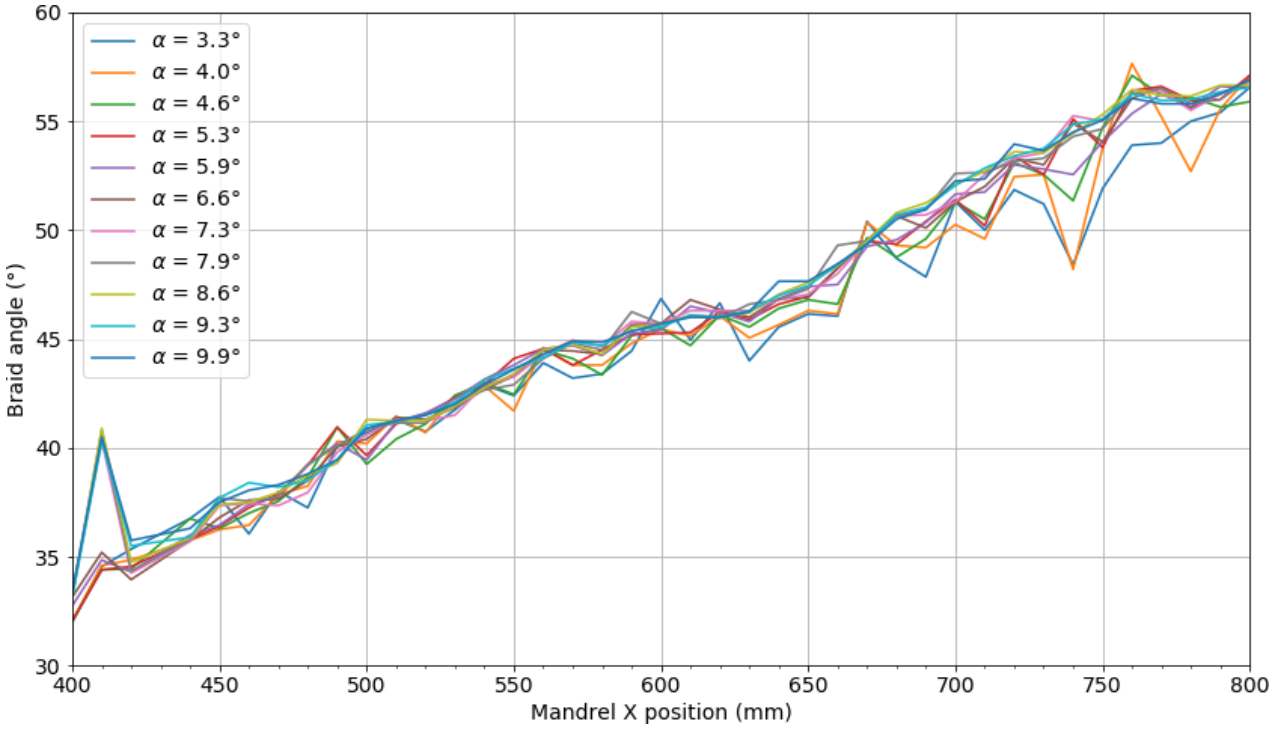

Figure 5.15: Braid angle measurements for varying circumferential angle, α.

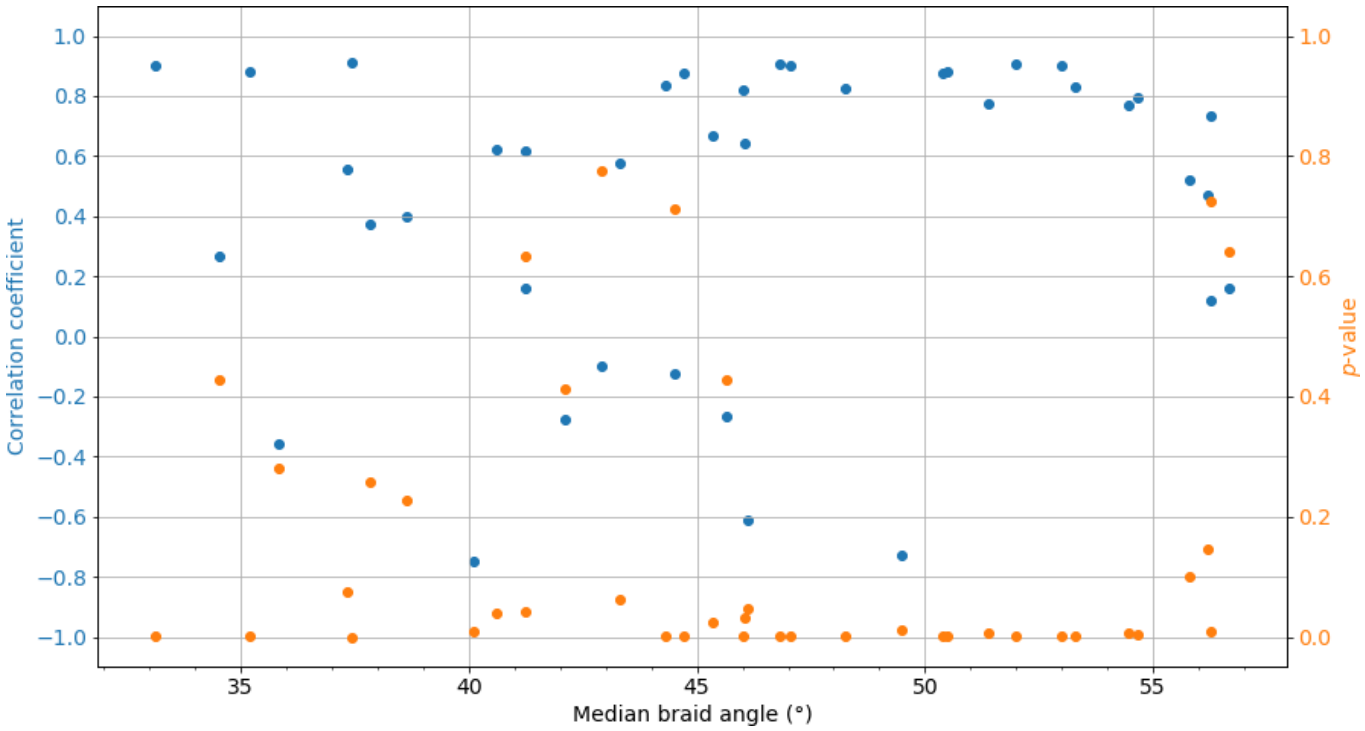

Figure 5.16: Correlation coefficient and corresponding p-values between circumferential angle and measured braid angle for each measurement location, plotted against median braid angle at each location.

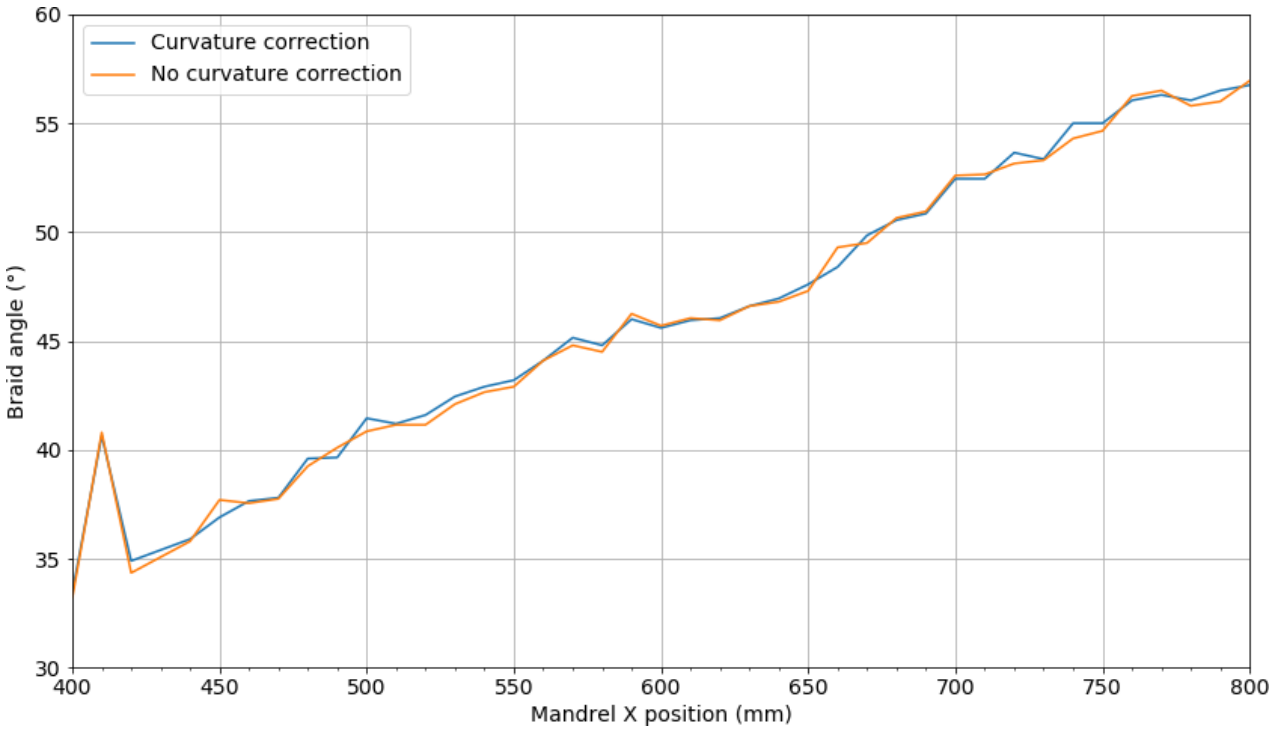

Figure 5.17: Braid angle measurements with and without correction for mandrel curvature.

obtained for a cropped image width = 2400 px ($\alpha = 7.9°$), as presented in Figure 5.17. The mean difference between the two sets of results was determined to be 0.09°, suggesting a slight increase in measurements for unwrapped images in accordance with expectation. However, with a standard deviation of 0.35° and sample size of 40, the mean difference between the two sets of results cannot be stated to be significant (at a 95 % confidence interval). It was also not possible to determine any θ dependence between the data sets.

Accordingly, measurement bias for the system configuration described in this work as a result of single surface curvature was proposed to be negligible, at least for mandrel diameters of $\geq$ 200 mm. Given the additional processing cost of incorporating surface curvature measurement and subsequent image transformation procedures, no correction for mandrel curvature was included in the image analysis procedure describes in Section 4.7.1.

Ideally, a more thorough assessment of perspective projection errors in images-based measurements due to mandrel form should be carried out to consider mandrel diameters smaller than 200 mm, down to 40 mm, as well as double curved surfaces found in more complex mandrel geometries. In the event that errors across this wider range of geometries cannot be disregarded, it may be preferable to determine necessary perspective corrections from the mandrel geometry in a virtual simulation of the process, and thus mitigate the impact of uncertainties in measurement of the surface itself.

5.1.6 Effect of surface gradient

In the measurement system configuration, image acquisition is constrained to the XY plane of the braiding machine. Accordingly, any image of a surface which is not parallel with the XY plane will incorporate a perspective projection which will result in erroneous measurement results if unaccounted for in the analysis routine. Since the system has initially been developed for use with axisymmetric mandrels, whose centrelines are expected to align with that of the camera during braiding operations,[3] the decision was made to apply perspective transformation along the X axis only, with no net gradient expected in Y. The surface gradient along X is calculated from surface profiles acquired by the profilometer (mounted in front of the camera in the MSA, between the camera and guide ring) and image transformation performed accordingly (refer to Section 4.7.1 for details).

Method

To evaluate the performance of the perspective correction procedure, braid angle measurements for images acquired trial C were used, in which a single layer preform was braided over a conical mandrel with cylindrical sections at either end. Measurement results were generated with: no perspective correction; correction based on surface profile gradient calculation; correction based on the design surface gradient (for the conical section) of 0.176.

Results and discussion

Measurements generated for the different gradient corrections are presented in Figure 5.18; results in the range 125 mm $<$ X $<$ 550 mm correspond to the conical mandrel section. For the chosen mandrel, with a relatively shallow surface gradient, a mean measurement error of approximately 0.42° (standard deviation 0.09°) was calculated for measurements where no image gradient transformation was performed relative to those where transformation was performed based on the known, design surface gradient of the conical mandrel section. This illustrates that measurement bias due to uncorrected perspective projection can be significant and highlights the importance of the image transformation step to negate gradient-based perspective error. The mean error was reduced to -0.02° for measurements corrected on the basis of in-process surface gradient measurements, although the spread of errors increased to 0.16° as a result of the uncertainty in surface gradient measurements.

The uncertainty in θ due to uncertainty in surface gradient cannot be expected to be constant for all scenarios, since the relationship between surface gradient and magnitude of image transformation is non-linear; for a given surface gradient uncertainty, braid angle measurement uncertainty is

[3] Assuming no eccentricity between mandrel and guide ring.

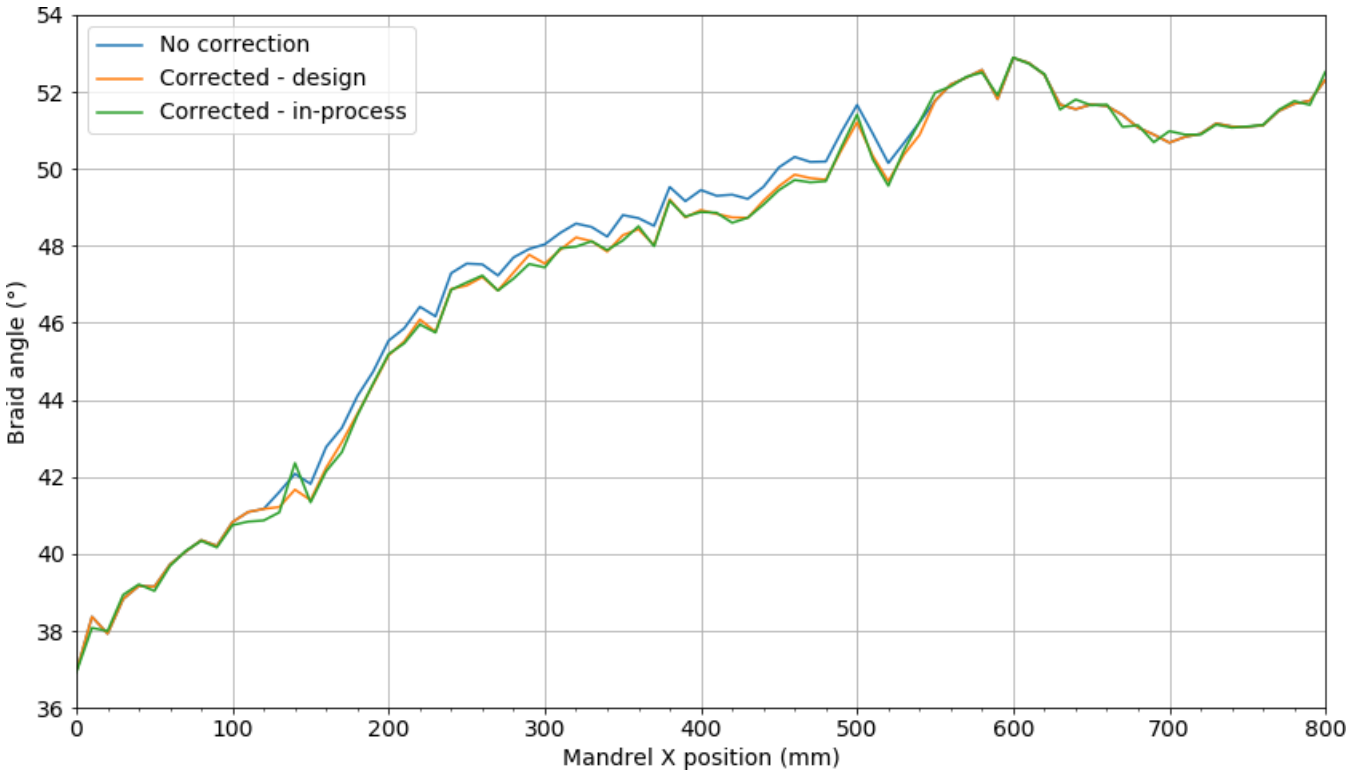

Figure 5.18: Braid angle measurements with: no perspective correction (blue); correction based on the as-designed surface gradient (orange); correction based on the measured surface gradient (green).

expected to increase with increasing gradient. This relationship is explored further in Section 5.1.7. However, the results presented here demonstrate that the in-process gradient-based perspective correction developed as part of the braid angle measurement setup successfully minimised the presence of systematic errors due to the surface gradient along the principal braiding axis.

Whilst there is room to improve the stability of in-process surface gradient measurements, and thus reduce perspective-based measurement uncertainty, this approach will ultimately be limited by the dynamics, i.e. oscillations and vibrations, of the manufacturing process itself. It would therefore be preferable in future system developments to determine perspective corrections from the mandrel geometry in a virtual simulation of the process, thus removing the reliance on in-process surface gradient measurements. Such a development would also enable curvature corrections (discussed in Section 5.1.5) to be made based on the model surface at each acquisition location.

5.1.7 Braid angle measurement uncertainty

In Sections 5.1.1 - 5.1.6, a number of sources of measurement variability and error, both random and systematic, relating to the developed braid angle measurement capability have been identified. An assessment of the combined contribution of these factors to braid angle measurement uncertainty

is presented here.

The following sources of variation in image composition were identified and discussed:

- fibre-yarn misalignment due to yarn twist;
- visibility of features below the preform layer being measured (e.g. yarns comprising previous braid layers);
- specular reflections from yarn surfaces due to lighting variations, mandrel form and material characteristics;
- accentuation of yarns as a function of polarising filter orientation;
- perspective projection due to mandrel surface curvature;
- perspective projection due to mandrel surface gradient (relative to camera focal plane).

Additional sources of variation not explicitly considered include:

- camera focus;
- braid angle;
- yarn width;
- yarn coverage (i.e. cover factor);
- yarn material;
- fibre fuzz or stray fibres due to yarn damage.

These manifest as variations in the images from which braid angle measurements are made that can be categorised as follows:

- image blur;
- image brightness;
- contrast between yarns on opposite trajectories;
- contrast between fibres within yarns;
- high intensity regions on yarns due to specular reflections;
- yarn orientation;
- yarn width;
- yarn spacing;
- angular deviation of fibres relative to yarns;
- contrast between foreground (yarns) and background (mandrel surface or substrate layers);
- background structure (e.g. visible yarns from preceding layer);
- stray fibres;
- yarn path distortion due to curvature;
- stretch due to image perspective.

Method

A Monte Carlo evaluation was conducted, in accordance with "Supplement 1 to the Guide to the expression of uncertainty in measurement – Propagation of distributions using a Monte Carlo method" [275], to assess the impact of the aforementioned variations on the uncertainty in braid angle measurements. The intention with such an assessment is to generate an estimate of the distribution of possible outcomes based on the known and/or specified distributions in the identified inputs, via stochastic sampling of those input distributions. In this case, that translates to an estimation of the distribution of errors from known braid angles in image-based braid angle measurements, based on a sample of images of braided preforms which exhibit some distribution of the identified sources of variability. This distribution should represent the uncertainty associated with the measurement procedure, whilst a non-zero mean difference between known and measured values would indicate a systematic measurement error causing measurement inaccuracy that would need to be corrected or accounted for.

Due to their stochastic nature, Monte Carlo methods require a very large number of input samples in order to yield a representative output distribution. This was achieved through the generation and use of simulated images, which provided the ability to control the actual angle between yarns present in each image (i.e. the known target value for braid angle measurements), as well as the variability in image composition. The simulated images were generated using the OpenCV [264], Random [276] and scikit-image [277] libraries in Python. They were constructed from graphical representations of a substrate (i.e. mandrel) surface, individual yarns, and fibres on the surface of each yarn. The stages of image construction and the probability distributions assigned to components at each stage in order to replicate the range of expected image features are outlined in Table D.1, Appendix D. These assignations were based on reasoned estimates as opposed to measured distributions; examples of resultant simulated images are provided in Figure D.1. Although surface curvature was identified as a potential source of systematic measurement error, this error was not considered to be significant. Any contribution to measurement uncertainty has therefore not been considered in the following assessments.

Two sets of results are presented and discussed:

- Firstly, results in which no surface gradient was applied during image generation, i.e. simulated images represented a flat, planar preform, imaged parallel to the focal plane - referred to as MC1;
- Secondly, results in which the contribution of surface gradient uncertainty as a function of surface gradient magnitude was incorporated - referred to as MC2.

In excess of 30,000 simulated images were generated for each set of results, with braid angle measurements generated according to the image analysis procedure described in Section 4.7.1

- MC1: Excluding surface gradient correction

For the first assessment, MC1, images were generated of either single or double layer preforms. For each simulated layer within an image, a nominal braid angle, θ_{nom}, was assigned from a uniform integer distribution between 25° and 65°. The orientation of each yarn within a layer was subsequently assigned according to $\mathcal{N}(\pm\theta_{nom}, 0.25)$, generating a known distribution of yarn orientations in the layer. The average braid angle for the layer was calculated as the mean of yarn orientations weighted by their relative lengths in the image. Braid angle measurements were conducted on the simulated images and the difference between the measured and simulated values, $\Delta\theta_{meas}$, calculated.

- MC2: Including surface gradient correction

For scenarios where the preform surface is not imaged parallel to the focal plane of the camera, an image transformation is required to correct for the perspective projection (discussed in Section 5.1.6. This transformation introduces additional uncertainty into the braid angle measurement due to uncertainty in the magnitude of the image perspective, i.e. the gradient of the imaged surface relative to the focal plane, $\nabla_{surface}$. An estimated standard uncertainty in surface gradient measurements of 0.012 was determined from a set of machine trials with a range of mandrel geometries; the value was assumed constant for the purpose of this assessment , i.e independent of the magnitude of the gradient. In order to assess the impact of this uncertainty on braid angle measurements as a function of surface gradient, a second Monte Carlo assessment was conducted, MC2.

For this scenario, only single layer images were simulated, in the same manner as outlined for MC1. A perspective transformation (i.e. reverse of the gradient correction transformation applied during the measurement procedure) was then applied to the image based on a surface gradient selected from a uniform distribution $\mathcal{U}(0, 1)$. The braid angle image analysis procedure was then applied, in which the image gradient used for perspective correction was assigned according to $\mathcal{N}(\nabla_{surface}, 0.012^2)$.

- Validation

In order to assess the uncertainty associated with repeat measurements, 10 image sets of the outer layer of the preform manufactured in trial A were acquired. Images were acquired over a 600 mm length, at 10 mm intervals, with the light offset set at 27 mm and polarising angle to 0°; camera exposure was set to 3 ms. Images within each set were stitched together prior to conducting any braid angle measurements, as described in Section 5.1.3. Image analysis was then conducted on cropped, 2400 × 2400 pixel sections of the stitched image, taken centrally with regards to image height and at 5 mm (435 px) intervals along the length. Measurements between $50 \leq X \leq 550$

mm were used in this assessment (see Figure 5.23), resulting in 10 measurements at each of 26 locations. The surface of the cylindrical mandrel was positioned parallel to the focal plane of the camera, therefore no surface gradient correction was applied to the images during the measurement routine.

Results and discussion

- MC1: Excluding surface gradient correction

Results presented and discussed here correspond to braid angle measurements of simulated, single and double layer braid images which are assumed to contain no perspective distortion due to a gradient between the braid surface and the image plane. The distributions of $\Delta\theta_{meas}$ for single and double layer images are presented in blue in Figure 5.19. For both types of image, the distribution appears to be centred around, and symmetrical about, 0° indicating a general agreement between known and measured values. Long tails are, however, evident in both distributions, suggesting heightened sensitivity of the measurement routine to one or more components of the simulated images. These tails are more prominent for double layer images, for which secondary peaks centred around ± 2°. This value corresponds to the offset between simulated fibre and yarn orientations assigned during image generation according to $\mathcal{N}(\pm 2, 1)$ and thus is likely due to a strong influence of fibre edges on the measurement result in certain instances. The greater prevalence in double layer images can be explained by yarn edge details in the uppermost layer being less well defined against lower layer yarns (which are constructed with the same pixel intensities, and thus poor contrast) than those from single layer images against a contrasting background, thus weakening the yarn contribution to the Fourier PSD; fibre edge details will be unaffected and therefore have a relatively stronger contribution to the PSD for double layer images, with a greater likelihood of influencing the measurement.

The results indicate that the chosen method to mitigation fibre detail sensitivity, i.e. image blurring using a median filter (Section 5.1.1) is not entirely robust. However, the effect in these results is believed to be exaggerated by the regular, linear nature of fibre edges in the simulated images, providing more homogeneous contribution to the PSD than would be expected for real fibres. This is coupled with the fact that parameterisation of the measurement procedure was optimised using real, as opposed to simulated, images. As such, the long tails of the results distributions are not expected to be representative of real measurements.

It was subsequently determined that the majority of values in the distribution tails corresponded to measurements for which the combined standard deviation error in peak centres, σ_{peak}, estimated during the peak fitting routine was particularly high. A low pass filter was, therefore, applied such that $\Delta\theta_{meas}$ values with a corresponding $\sigma_{peak} > 0.05$ were excluded, in order to negate the impact

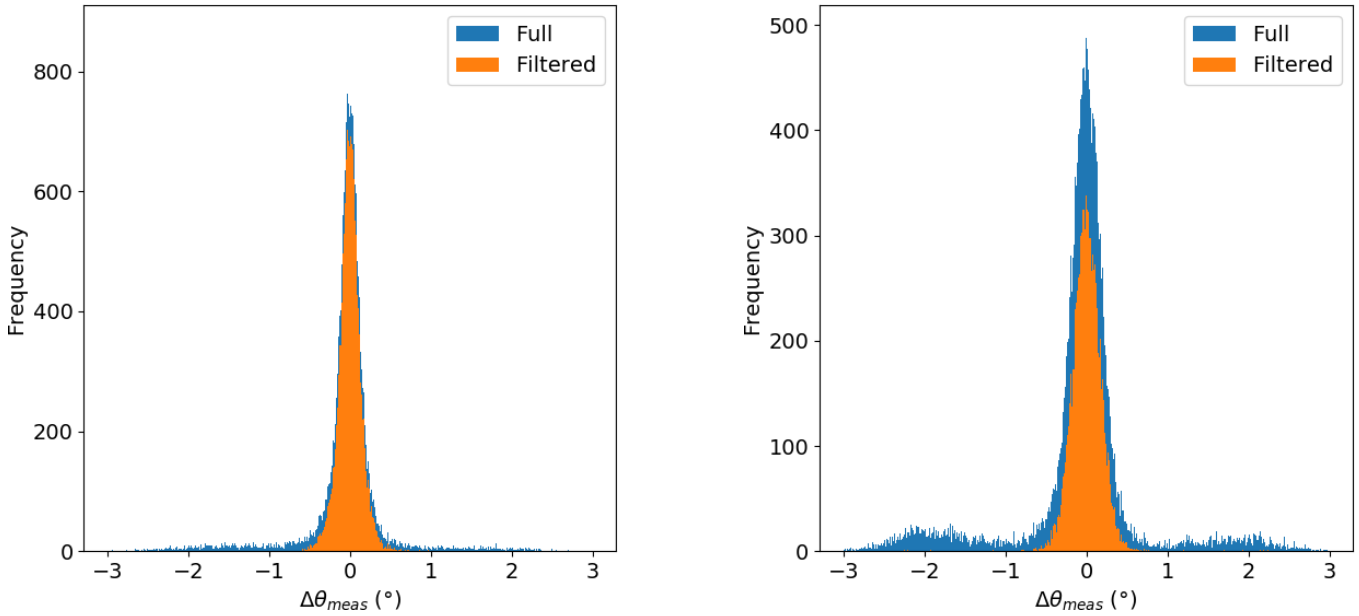

Figure 5.19: Filtered and unfiltered frequency distributions of the difference between the measured and simulated braid angle values, $\Delta\theta_{meas}$, for simulated single (left) and double (right) layer images.

of fibre edge effects from the uncertainty assessment. The resultant, filtered distributions of $\Delta\theta_{meas}$ for single and double layer preform images are presented in orange in Figure 5.19, and provide confidence that this filtering approach did not significantly affect the distribution of measurement results, beyond removing the tails. In future research, this approach could be explored as a means to indicate the uncertainty associated with an individual measurement.

Table 5.4: Mean and standard deviation of difference between actual and measured angle, $\Delta\theta_{meas}$, for simulated images containing 1 and 2 biaxial layers.

	# filtered	$\Delta\theta_{meas}$	
# layers	images	μ (°)	σ (°)
1	20015	-0.007	0.15
2	13118	-0.004	0.18

The mean and standard deviations for the filtered distributions are presented in Table 5.4. For both cases, the mean error was very close to 0°, providing no evidence for a systematic measurement bias. The standard deviation provides an estimate of the standard uncertainty of measurement error. These results indicate a standard measurement uncertainty for braid angle measurements of 0.15° for images which represent a single, planar preform layer parallel with the focal plane of the camera. This is increased to 0.18° for images containing a second, substrate preform layer, which is consistent with the findings from Section 5.1.2 where the measurement procedure was shown to be sensitive to visible yarn edges beneath the uppermost layer in some instances.

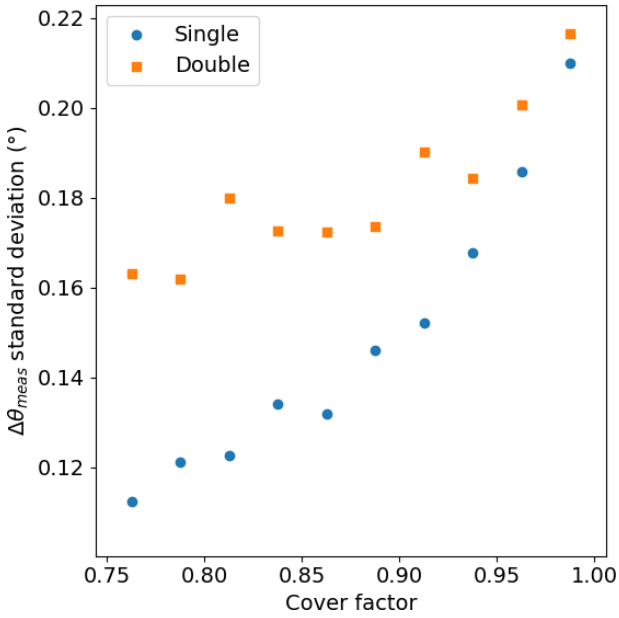

Figure 5.20: Standard deviation of $\Delta\theta_{meas}$ per cover factor interval for single and double layer images.

Upon further investigation, a dependence of measurement dispersion on yarn surface coverage, i.e. cover factor, was identified. During image generation, the cover factor, CF, of each simulated braid layer was approximated according to:

$$CF = CF_i + CF_j - CF_i CF_j \tag{5.1}$$

where CF_i and CF_j refer to the ratio of yarn pixels to image pixels for the two principal yarn directions, i.e. $\pm\theta$. Cover factors in simulated images ranged from 0.75 to 1.00. The standard deviation of measurements within 0.025 CF intervals was calculated and found to range from 0.11° (single layer) and 0.16° (double layer) for CF < 0.775, to 0.21° (single layer) and 0.22° (double layer) for CF ≥ 0.975. These trends are illustrated in Figure 5.20, which plots the standard deviation of $\Delta\theta_{meas}$ per cover factor interval for single and double layer images. Again, the greater uncertainty in double layer measurements relative to single layer at lower cover factors is consistent with findings from Section 5.1.2. The general trend of increasing uncertainty with increasing cover factor is to be expected given the corresponding reduction in length of visible yarn edge features on which the measurement procedure is founded.

Based on these results, it is proposed that braid angle measurements made in the absence of perspective projections due to surface gradient can be determined to between ± 0.22° for single layer, low cover factor preforms and ± 0.44° for multi-layer, high cover factor preforms, at a confidence interval of 95 %. It should be noted, however, that these values are, and can only be, estimates of the actual measurement uncertainty, since they themselves are dependent upon

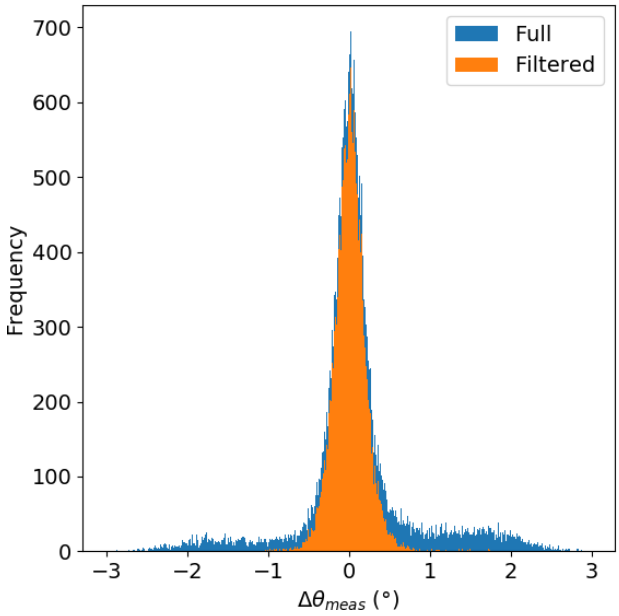

Figure 5.21: Filtered and unfiltered frequency distributions of the difference between the measured and simulated braid angle values, $\Delta\theta_{meas}$, for simulated single layer images with varying surface gradients.

estimates of distributions assigned to features of the simulated images on which this assessment has been conducted. They are also based on an assumption that measurement errors introduced by the presence of regularly structured, aligned fibre edge features in simulated images are unrealistic and that the exclusion of affected results from the uncertainty assessment was valid. Once a large and varied collection of real images has been acquired using the measurement system, subsequent assessments may seek to provide increased confidence in these distributions through analysis of the image data set, however, this was not possible at the time of this work.

- MC2: Including surface gradient correction

Results presented and discussed here correspond to braid angle measurements of simulated, single layer braid images incorporating a known perspective transformation to represent a gradient between the braid surface and the image plane. Prior to analysis, a low pass filter was applied to measurement results such that only $\Delta\theta_{meas}$ values with a corresponding $\sigma_{peak} \leq 0.05$ were considered, as was conducted for MC1. The distributions of both filtered and unfiltered results are presented in Figure 5.21. Filtered results were found to follow a near-normal distribution centred around 0.01°, providing no evidence for a systematic measurement bias. The corresponding standard deviation of 0.22° indicates an increase in the measurement uncertainty of approx. 50 % for single layer preforms as a result of the surface gradient uncertainty when compared against the output from MC1.

In order to determine any sensitivity to the magnitude of the surface gradient itself, the standard

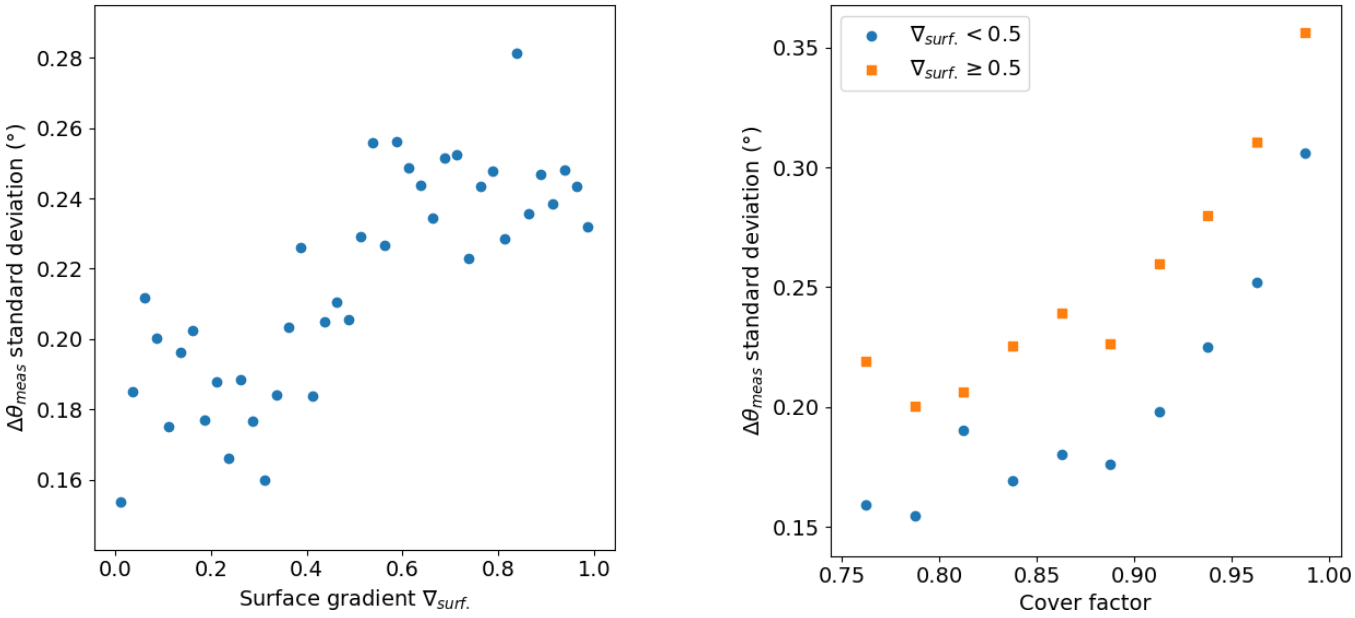

Figure 5.22: Standard deviation of $\Delta\theta_{meas}$: per surface gradient, $\nabla_{surface}$, interval (left); per cover factor interval for $\nabla_{surface} < 0.5$ and $\nabla_{surface} \geq 0.5$ (right).

deviation of $\Delta\theta_{meas}$ was calculated for measurements corresponding to surface gradient intervals of 0.025, between 0.0 and 1.0. Standard deviation, and hence measurement uncertainty, was found to increase from 0.15° for very low surface gradients, to 0.25° as $\nabla_{surface}$ approached 1.0 (see Figure 5.22, left). Whilst results for $\nabla_{surface} < 0.5$ exhibit quite significant scatter, a consistent increase is apparent above 0.5. These results indicate that a there is a detrimental impact on measurement uncertainty from both the uncertainty associated with the gradient itself, i.e. at lower surface gradients, and the magnitude of the gradient, i.e. at higher surface gradients. The combined effect equates to a significant increase of approximately 2/3 for higher gradient values compared to results from the first MC assessment, plateauing at around 0.25° for $\nabla_{surface} > 0.5$. In reality, however, most mandrel geometries are unlikely to incorporate gradients in excess of 0.33 and hence for the majority of scenarios this elevated uncertainty will not be applicable. Rather, a standard deviation ≤ 0.21 might be expected to apply, based on these result.

A cover factor dependence was evident, as in MC1, with the dispersion in $\Delta\theta_{meas}$ increasing from 0.16° to 0.31° for surface gradient less than 0.5, and from 0.22° to 0.36° for $\nabla_{surface} \geq 0.5$, over a cover factor range 0.75 to 1.0 (see Figure 5.22, right).

It is proposed that braid angle measurements including image transformation to account for measured surface gradient can be determined to between ± 0.32° for low cover factor, low surface gradient preforms and ± 0.72° for high cover factor preforms with surface gradient > 0.5, at a confidence interval of 95 %. Given that gradients in excess of 0.5 are expected to be unusual, it may be stated that measurement uncertainty within ± 0.5° can be expected in most scenarios

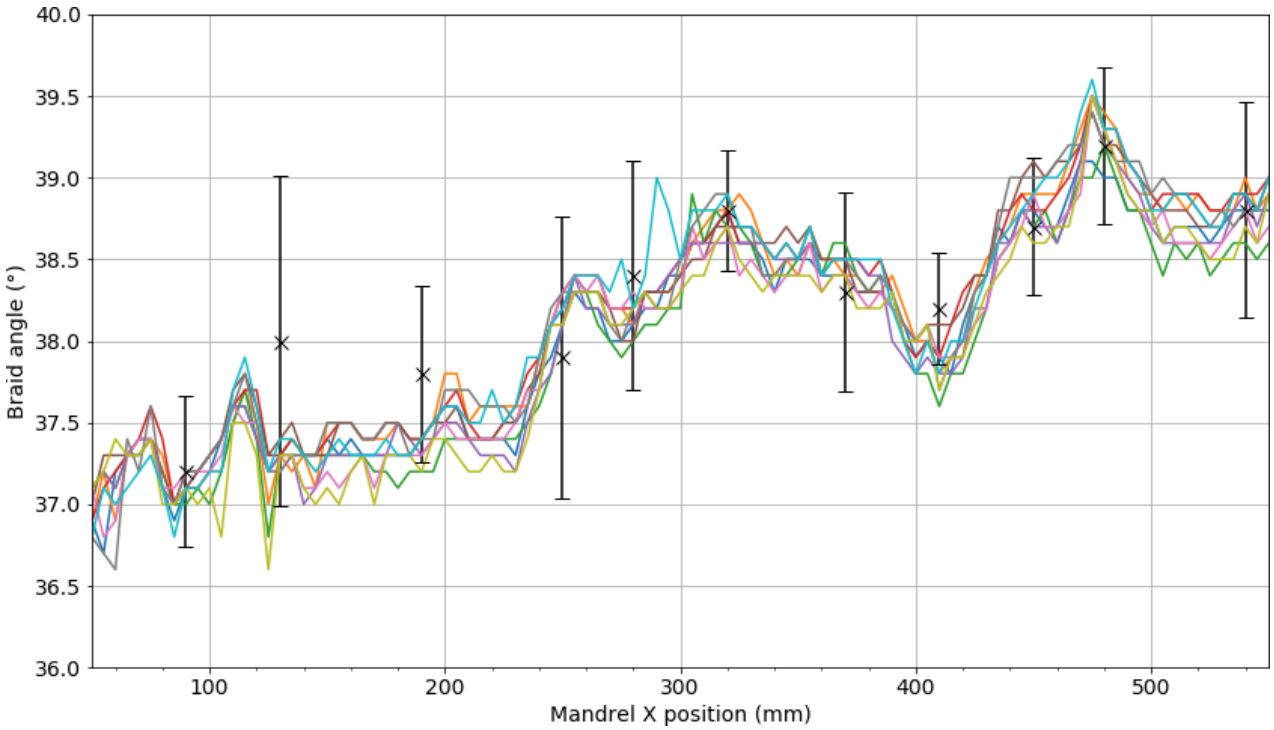

Figure 5.23: Repeat braid angle measurements used for validation of measurement uncertainty assessment; markers indicate manual measurements with error bars representing the corresponding MAD values.

where preform cover factor is < 0.95. However, the reported values are only valid for single layer preforms; uncertainties for multi-layer preforms are presumed to be greater, especially at lower cover factors, as per the findings of the first MC assessment. It should also be noted that these statements are based on the assumption that surface gradient standard uncertainty is independent of surface gradient magnitude. Further investigation is required in order to establish the validity of this assumption.

- Validation

Braid angle measurements for the length of preform used in this assessment are presented in Figure 5.23. The standard deviation of measurements at each location was calculated, with the average across all locations determined to be 0.12°. Assuming a normal distribution, this average standard deviation equates to an estimated uncertainty of 0.24° at a confidence interval of 95 %. This value is comparable to, although slightly lower than, the range determined in the first Monte Carlo uncertainty assessment relating to multi layer preforms of between 0.32° and 0.44° for braid cover factor in the range 0.75 - 1.0.

In order to incorporate the influence of surface gradient measurement uncertainty on this data set, measurements were repeated in which variable surface gradient correction was implemented,

according to a normal distribution $\mathcal{N}(0, 0.012)$, as per the second MC evaluation. This inclusion was found to have negligible impact on the uncertainty in braid angle measurements, with the mean standard deviation across measurement locations increasing to just 0.13°. Assuming a normal distribution, this average standard deviation equates to an estimated uncertainty of 0.26° at a confidence interval of 95 %. This value is comparable to, although slightly lower than, the range determined in MC2 for low surface gradient preforms, i.e. $\nabla_{surface} < 0.5$, from 0.32° to 0.62° for braid cover factor in the range 0.75 - 1.0.

Given that these results relate to only a subset of the scenarios covered by the uncertainty assessments presented in this section, the lesser estimates of uncertainty are to be expected and provide confidence that the MC assessments represent reasonable estimates of braid angle measurement uncertainty for the system and procedure outlined in Chapter 4. Further work is required to expand the range of validation for this assessment. Of particular interest are scenarios in which a surface gradient is present, since the assessment has indicated a significant risk of increased measurement uncertainty due to the perspective correction procedure required in these cases.

5.1.8 Summary of braid angle measurement performance

The findings of investigations presented and discussed in this section, relating to the performance of the braid angle measurement capability, can be summarised as follows:

Effect of yarn twist

Measurement sensitivity to fibre edge details was shown to result in erroneous braid angle measurements where yarn twist introduced misalignment between orientations of yarns and their constituent fibres. This sensitivity was mitigated by the introduction of a median blur filter at the beginning of the image analysis procedure to reduce the definition of fibre details visible in the image. An optimal value for the filter kernel size which mitigated any apparent influence of fibre edges whilst also minimising measurement instabilities, was found to be 45 px for the yarn material and system configuration in this work. This value is dependent on image scale and would need to be re-evaluated if system configuration were to be altered significantly in future developments, as well as for significantly different yarn sizes.

Effect of visibility of previously deposited layers

The visibility of previously deposited braid layers was found to impact upon measurements in the event that yarns in the outermost preform layer are not well defined in the acquired images, e.g. due to motion blur. This is a potential issue for open braid structures, i.e. those with low cover factors, where there is greater visibility of yarns comprising lower layers and may be inevitable at

the start of layer deposition if oscillatory motion of the braid due to dynamics of the process cannot be prevented. In such cases, images should be reviewed to identify any affected measurements.

It was also found that measurements may be influenced by substrate yarns in the event that inter-yarn gaps are greater than the deposited yarn width, coupled with close alignment of yarns between layers. Under these circumstances, there is minimal obscuration of substrate yarns edges and their contribution to the Fourier PSD can be significant. The resultant measurement then represents an average between the layers. This phenomenon was observed for a difference in braid angle between layers, $\Delta\theta_{nom}$, of less than 5°. Future research should endeavour to improve the identification and selective measurement of yarns in the upper layer to mitigate this source of error.

Effect of lighting

Lighting variations, produced by adjusting the offset between light ring and camera focal plane, and hence the imaged preform surface, highlighted the sensitivity of the measurement procedure to specular reflections from yarn surfaces. Measurements were found to be biased by high intensity yarn edges corresponding to sections of yarn from which surface reflections were visible. The implementation of an upper pixel intensity clip limit, CL, to the edge-filtered image as part of the image analysis procedure was demonstrated to minimise the sensitivity to surface reflections, with an optimal value of CL determined to be equivalent to the 99^{th} %ile of filtered edge intensities for the measurement system configuration described.

Effect of polarisation

The use of a polarising filter was shown to be effective at accentuating the edges of yarn with which the filter was aligned, whilst minimising the intensity of reflections from yarns to which it was perpendicular. Optimal measurements would therefore be achieved by enabling filter alignment with each of the yarn directions present in an image via an active filter adjustment system. To minimise system complexity, an alternative, passive approach was implemented, whereby the filter is aligned either parallel with, or perpendicular to, the primary braiding axis. This ensures partial misalignment with both bias yarn directions, for all feasible braid angles (typically in the range 30° - 60°), therefore providing partial suppression of surface reflections without biasing measurements towards either yarn direction.

Effect of surface curvature

No significant measurement bias was found to result from the uncorrected effect of yarn path distortion in images caused by projection from a curved mandrel surface for mandrel diameters $\geq$ 200 mm. This is due to the low circumferential angle visible in cropped images, with an imaged

area equating to 28 × 28 mm. Whilst the investigation did not cover the full range of mandrel diameters that the braiding machine is designed to accommodate, i.e. down to a minimum diameter of 40 mm where the presence curvature-induced measurement bias may become more pronounced, the decision was taken not to include curvature correction as part of the measurement procedure to avoid the additional complexities and associated uncertainties.

It is recommended that future system developments consider a suitable approach to incorporate correction for perspective projection if the bias caused by small mandrel diameters is determined to be significant. Ideally this approach would also enable correction for more complex surface geometries, i.e. doubly curved surfaces, as well as single curvature cylindrical geometries. For this, it may be preferable to determine necessary perspective corrections from the mandrel geometry in a virtual simulation of the process, and thus mitigate the impact of uncertainties in measurement of the surface itself.

Effect of surface gradient

Perspective projection due to surface gradient along the principal braiding axis was shown to introduce significant error into braid angle measurements; a mean error of 0.42° was determined over a conical mandrel section, relative to measurements corrected for the known gradient of 0.176. Correction based on in-process surface gradient measurements was shown to successfully minimise this systematic error, reducing mean error to just -0.02°, although the spread of errors was increased due to gradient measurement uncertainty. The significance of this uncertainty was explored further in the braid angle measurement uncertainty assessment.

Braid angle measurement uncertainty assessment

Monte Carlo assessments using simulated images were conducted in order to estimate the measurement uncertainty for the developed braid angle measurement capability. An assessment considering single and double layer preform images, in the absence of surface gradient variation, i.e. using planar images, determined measurement uncertainty to vary between ± 0.22° for single layer, low cover factor preforms and ± 0.44° for multi-layer, high cover factor preforms, at a confidence interval of 95 %. A second assessment, considering only single layer preform images in which surface gradient variation was included, determined measurement uncertainty to increase to between ± 0.32° for low cover factor, low surface gradient preforms and ± 0.72° for high cover factor preforms with surface gradient > 0.5, at a confidence interval of 95 %.

The inclusion of surface gradient uncertainty was found to have significant impact on braid angle measurement uncertainty, increasing the confidence interval by as much as 71 % at higher cover factors. Future work should focus on reducing surface gradient uncertainty in order to minimise its

effect braid measurements. This could be achieved by optimisation of the gradient measurement procedure outlined in Section 4.7, or by integration of the measurement system with a process simulation from which the orientation of the surface relative to the focal plane of the camera is determined for each image location.

5.2 Preform thickness

During the development of the in-process preform thickness measurement capability, the combination of high material reflectivity, structured yarn surface (due to bundled fibres), yarn undulation (i.e. crimp) and mandrel surface curvature, were found to result in a large amount of erroneous data points in acquired preform surface profiles due to scattering of the incident laser light, as reported by Schmitt *et al.* [262]. It was, therefore, necessary to develop a robust data processing procedure in order to reliably estimate the position of the preform surface and hence generate an accurate measurement of preform thickness.

As detailed in Section 4.7.2, preform thickness measurements generated by the system are dependent upon the acquisition, and subsequent processing, of laser line profiles at corresponding locations along the mandrel and preform layer being measured. For inclined surfaces, measurements are also dependent upon knowledge of the surface gradient at the measurement location in order to determine thickness normal to the surface. Results of the measurement procedure are therefore dependent upon:

- accurate estimation of the structured preform surface;
- sensitivity of surface estimation to light scattered by the preform surface;
- repeatability of mandrel surface position during braiding operations;
- accurate measurement of the surface gradient.

The impact of each of these dependencies on the measurement results is assessed and discussed in this section. The overall impact on thickness measurement uncertainty is also evaluated.

5.2.1 Effect of surface structure

The basis of the surface estimation procedure is a 2-stage polynomial fitting procedure, which can be summarised as follows:

- firstly, fitting to all profile data points in order to ascertain the midplane of the profile relative to the mandrel surface;
- secondly, fitting only to data points with a residual from the initial fit greater than some threshold value (those further above the mandrel surface having increasingly large, positive residuals).

The position of the estimated surface is therefore dependent on both the threshold value used and the form of the profile itself, as dictated by the structure and arrangement of the deposited

yarns. This relationship was investigated in order to assess the accuracy the surface estimation procedure and resultant thickness measurements.

Simulated mandrel and preform profiles were used in order to control the 'preform' thickness, with surface structure approximated to waveform variations. Baseline profiles (i.e. those representing the mandrel surface) were simulated with co-ordinates along the lower quadrant of a circle with known radius. Profile point co-ordinates were simulated according to Equations 5.2 and 5.3:

$$y = -(r + t - w)sin(\phi) \tag{5.2}$$

$$z = -(r + t - w)cos(\phi) \tag{5.3}$$

where r is the mandrel radius, t is the specified preform thickness, and ϕ is the angle of the data point relative to the centre point of the mandrel.

The wave component, w, specified by Equation 5.4, comprises the summation of two trigonometric terms to simulate the structural detail of the profile. This produces profiles with a distribution of peak heights, as expected along a preform surface profile due to variation in yarn thicknesses, stacking of yarns between layers, etc. 1 is added to the terms in the outer brackets to centre the wave component around 1, such that minima of the wave component correspond to peak heights in the simulated profile comparable to the nominal preform thickness, t.

$$w = \frac{A}{2}\left(\sqrt{\frac{1+b^2}{1+b^2cos\left(\frac{2\pi(r+t)}{d}\phi\right)^2}}cos\left(\frac{2\pi(r+t)}{d}\phi\right) + gsin\left(\frac{2\pi(r+t)h}{d}\phi\right) + 1\right) \tag{5.4}$$

A is the amplitude of the waveform, i.e. the distance between minima and maxima, b is a shape-determining constant which transitions the form of the first term between cosine and square wave, and d is the peak-to-peak distance. g and h are amplitude and peak frequency scalars respectively for the second, sine term, which is used to modify the symmetry, amplitude and regularity of the first term.

The effect of shape-constant b on the first term of the wave component, i.e. when g and/or $h = 0$, is illustrated in Figure 5.24, for values b in the range 1 - 16. It is proposed that a sinusoidal wave, i.e. $b = 1$, is only a reasonable approximation of the profile surface when the profile amplitude is low relative to the peak-to-peak distance. This is because deposited yarns typically exhibit a near-elliptical cross-section geometry [62], and bias yarns are not profiled orthogonally due to the relative orientations of the projected laser line and braiding axis. In other instances, the peak broadening observed as b increases is thought to improve the representation of the preform surface.

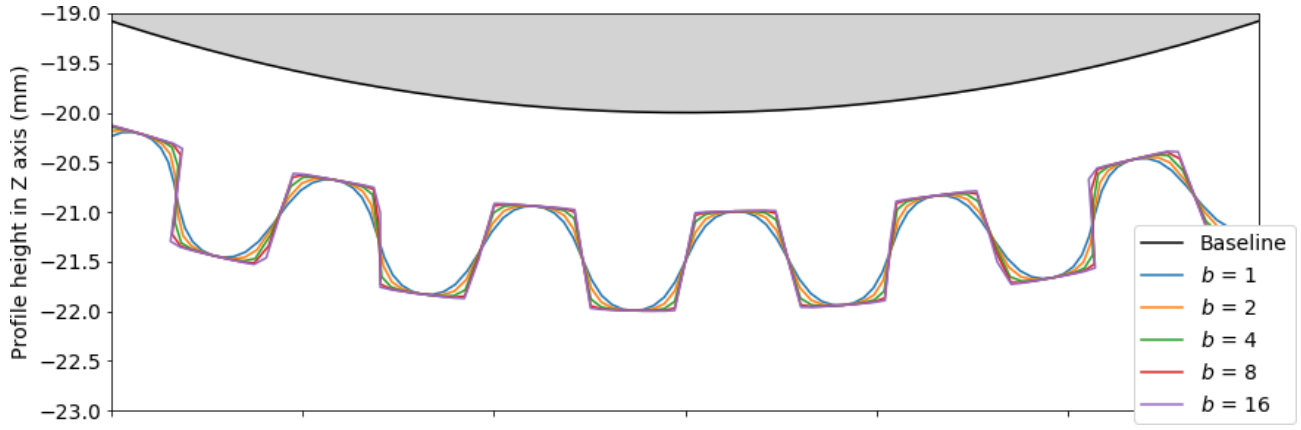

Figure 5.24: Change in simulated surface profile shape with varying shape constant, b; ($r = 20$ mm, $t = 2$ mm, $A = 1$ mm, $d = 2$ mm, $g = 0$, $h = 0$).

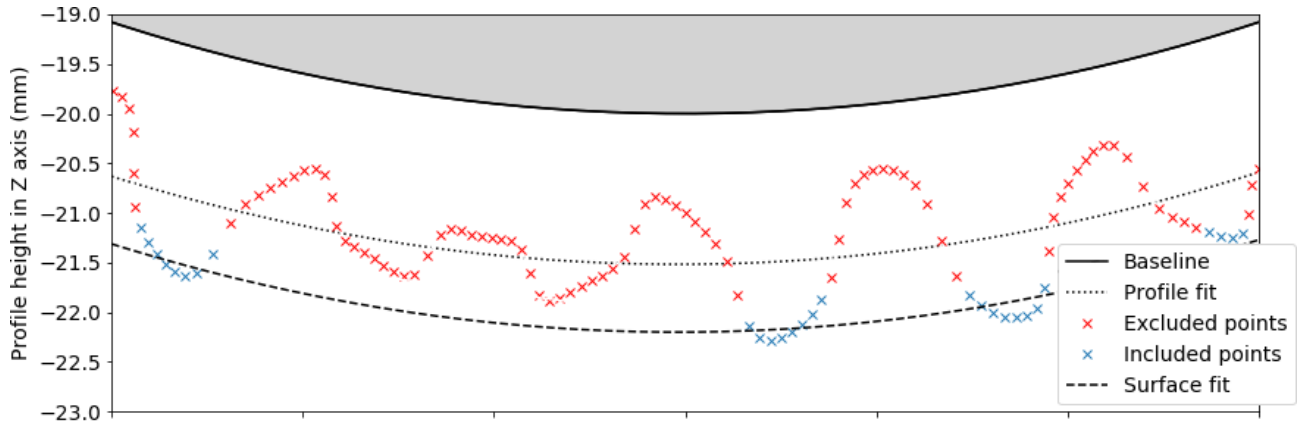

Figure 5.25: Simulated surface profile with midplane and surface fits; data points included in the surface fit using a residual threshold at the 50$^{\text{th}}$ %ile are shown in blue, those excluded are shown in red.

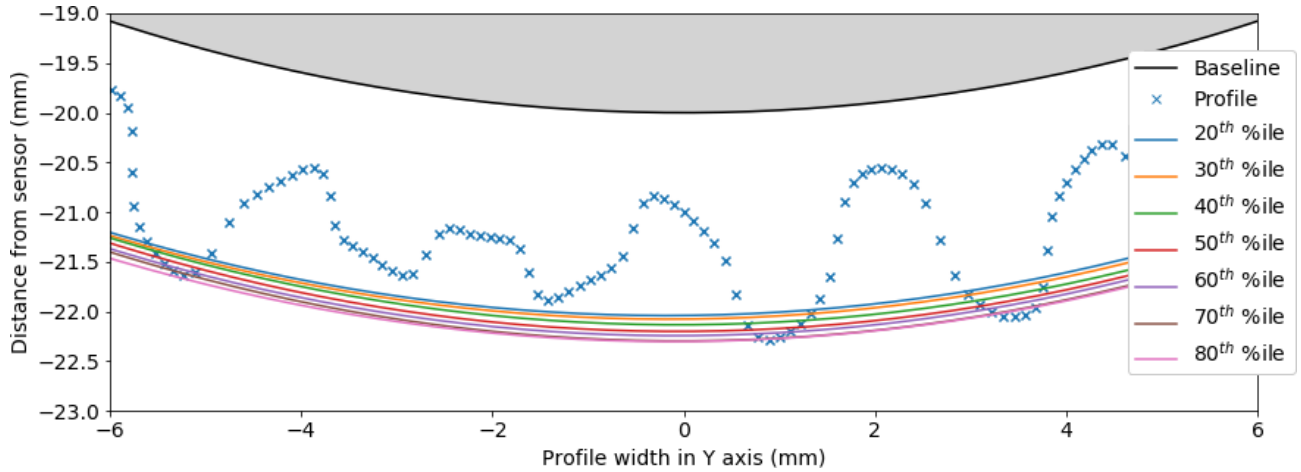

Figure 5.26: Change in fitted polynomial surface with varying residual threshold value.

An example of a simulated profile, illustrating the effect of the sine term, i.e. when g and h are greater than 0, is presented in Figure 5.25. Outputs from the thickness measurement procedure (detailed in Section 4.7.2) are included, namely the profile midplane resulting from the initial fit, and the estimated profile surface generated from the second fit using a threshold value equivalent to the 50^{th} %ile of residual values > 0. The effect of the threshold value on the estimated surface position is illustrated in Figure 5.26, for which the residual threshold was varied between the 20^{th} %ile and 80^{th} %ile of residual values > 0.

It is evident from Figures 5.25 and 5.26 that the surface generated using the 50^{th} %ile threshold lies above several of the peak minima, whilst increasing the threshold moves it towards those peaks. If the true preform thickness is taken to equal the maximum peak height in the surface profile (assuming that there are no erroneous data present), then the higher the threshold value, the closer the measured thickness should be to the true thickness. However, the higher the threshold value, the fewer data points will be included in the second, surface estimation fitting routine and hence, above a certain threshold, the goodness of the fit to the profile surface will begin to deteriorate.

Method

In order to investigate the sensitivity of the measurement procedure to the threshold value used for the surface fit, a Monte Carlo simulation was conducted in which a large number of simulated profiles with a broad range of forms were generated and measured. The approach was similar to that used for braid angle measurement uncertainty assessment in Section 5.1.7, using a stochastic approach to investigate the sensitivity of the measurement procedure to a combination of variables. Profiles were generated using the SciKit-learn [278] and Random [275] libraries in Python. 10,000 surface and corresponding baseline profiles were simulated using Equation 5.4, for which the profile variables were varied according to uniform distributions over the ranges outlined in Table 5.5. The use of uniform distributions was appropriate in this case for mandrel radius, preform thickness, profile amplitude and peak-to-peak distance since these variables are largely dependent on design choices and could realistically fall anywhere within the specified ranges. The remaining 3 variables do not have any physical meaning and were present solely to introduce irregularity to the simulated profiles; a uniform distribution is as appropriate as any other for this purpose. The true thickness value for each profile was determined as t minus the minimum value of the wave component w.

Surface fitting was conducted with the residual threshold varied between the 20^{th} and 80^{th} %iles; subsequent thickness measurements were made for each profile, at each threshold value. The coefficient and constant of linear regression between simulated and measured thickness was then calculated for each threshold value used, along with the root mean square error (RMSE). These values were used as indicators of the error and uncertainty associated with the measurement procedure. Regression constants can be interpreted as a measure of systematic measurement error

Table 5.5: Representative values investigated for each of the profile variables in Equation 5.4

Variable	Min.	Max.	Units
Mandrel radius, r	20	375	mm
Preform thickness, t	0.5	8	mm
Profile amplitude, A	0.1	2	mm
Peak-to-peak distance, d	1	16	mm
Shape constant, b	1	16	
Secondary amplitude scalar, g	0	1	
Secondary frequency scalar, h	0	1	

resulting from the measurement procedure. RMSE, on the other hand, provides a measure of dispersion of measured vs simulated values around the linear trend lines, hence representing the uncertainty associated with measured values due to random measurement error.

Results and discussion

Table 5.6: Results of linear regression between simulated and measured thickness values for simulated surface profiles, for which the threshold used in the surface fitting procedure was varied between the 20^{th} and 80^{th} %iles of residual values > 0.

Residual	Regression		
threshold (%ile)	coeff.	const.	RMSE
20^{th}	0.984	-0.13	0.175
30^{th}	0.987	-0.11	0.154
40^{th}	0.990	-0.08	0.137
50^{th}	0.992	-0.06	0.123
60^{th}	0.994	-0.03	0.119
70^{th}	0.996	-0.01	0.127
80^{th}	0.993	0.03	0.302

Measured preform thickness results are plotted against corresponding simulated thickness values in Figure 5.27 and exhibit a near-proportional relationship that is expected for an accurate measurement procedure. The strength of this relationship under the application of different residual thresholds in the measurement procedure is confirmed by regression results presented in Table 5.6, in which the lowest coefficient and constant of regression correspond to the lowest (i.e. 20^{th} %ile) threshold. These values are seen to improve, getting closer to 1 and 0, respectively, with increasing threshold due to increased selectivity of data points near to the profile maxima in the surface estimation fitting routine. Optimal values were obtained for the 70^{th} %ile, suggesting that the error between the simulated and measured thickness was minimised with this threshold value.

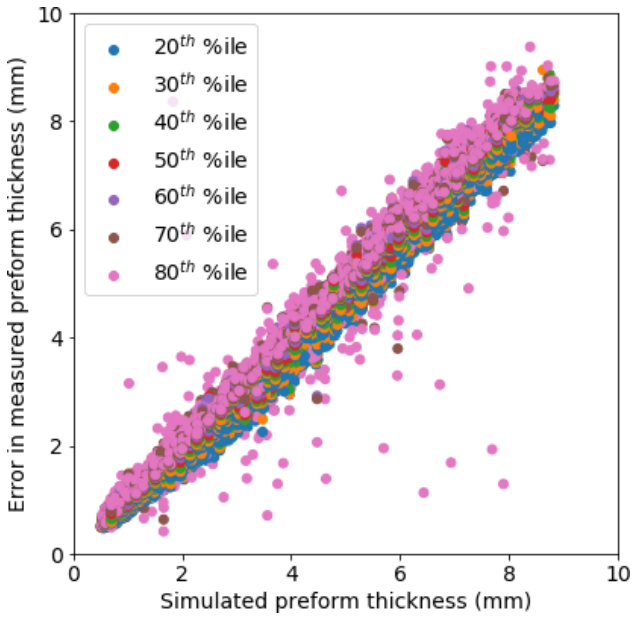

Figure 5.27: Simulated vs measured preform thickness resulting from 10,000 simulated profiles for which the threshold for data inclusion in the surface fit was varied between the 20$^{\text{th}}$ and 80$^{\text{th}}$ %iles of residual values > 0.

A decrease in the RMSE of measurements is also evident with increasing threshold, to a minimum value for the 60$^{\text{th}}$ %ile, indicating the optimal threshold to minimise measurement uncertainty. Above this value, RMSE can be seen to increase again, quite dramatically by the 80$^{\text{th}}$ %ile. This trend is consistent with a reduction in the goodness-of-fit of the surface estimation polynomial, probably due to insufficient data points included in the fitting procedure to accurately represent the general profile geometry. It corresponds with a positive regression constant for the 80$^{\text{th}}$ %ile, which also suggests a poor estimation of the preform surface.

These results indicate that the residual threshold used in the thickness measurement procedure should be set to the 70$^{\text{th}}$ %ile in order to maximise measurement accuracy, whilst the 60$^{\text{th}}$ %ile results in minimum measurement uncertainty for a small reduction in accuracy. However, these results do not account for the presence and effect of erroneous data often encountered in real surface profiles, due to the scattering of light; this is addressed in Section 5.2.2.

5.2.2 Effect of scatter

In addition to the challenges posed by the undulating structure of the preform surface, scattering of incident light from constituent yarns and fibres (as discussed in Section 4.4.2) tends to result in a number of erroneous data points along a given profile. This creates a further challenge for the surface estimation procedure, which should be insensitive to such occurrences in order to generate reliable thickness measurements. The impact of erroneous data arising from light scatter on measurement

results is investigated in this section via an extension of the Monte Carlo assessment conducted in Section 5.2.1.

Method

To investigate the sensitivity of the measurement procedure to such erroneous data, a Monte Carlo assessment using simulated preform surface profiles was conducted. For this assessment, profiles were generated in which the position of a proportion of surface points was altered by a random, arbitrary amount to mimic the effect of scatter on acquired preform surface profiles. 10,000 surface and corresponding baseline profiles were generated as per the method in Section 5.2.1), but with a randomly generated value in the range 1 - 5 added to the Z co-ordinate of a proportion of points in each profile. The proportion of altered points per profile was varied between 0 % and 50 %.

For each surface profile, a series of thickness measurements relative to the corresponding baseline profile were made in which the residual threshold employed for the second, surface fit was varied between the 20^{th} and 80^{th} %iles of residual values > 0. For each residual threshold value used, the constant of linear regression and associated RMSE between the simulated and measured thickness values were then calculated for profiles containing a percentage of erroneous data points within 5 % intervals (i.e. 0 - 5 %, 5 - 10 %). As per Section 5.2.1, these values were then used to evaluate the systematic and random error introduced to thickness measurements as a function of the proportion of erroneous data points and the residual threshold applied during surface estimation.

Results and discussion

Results are presented in Figure 5.28 for both the linear regression constant and RMSE calculated between simulated and measured thickness values over the range of erroneous data points and surface fitting residual thresholds investigated. The general trend evident in both plots is an increase in value with increasing percentage of erroneous data points after an initial steady state. These upward trends are indicative of increases in both systematic and random measurement error over this range, as discussion previously in Section 5.2.1, whilst initial steady state behaviour suggests low or negligible measurement sensitivity over the corresponding range of erroneous data points present.

The percentage above which the regression constant, and hence systematic measurement error, began to noticeably increase was found to vary from 25 % erroneous data using the 20^{th} %ile threshold to between 5 % and 10 % at the 80^{th} %ile threshold. Likewise, RMSE was found to increase significantly with just 5 % erroneous data using the 80^{th} %ile threshold, whilst an equivalent increase was not evident until the introduction of $\geq$ 20 % using the 20^{th} %ile threshold. The reduction in RMSE observed above 40 % erroneous data was likely due to the effect of these points

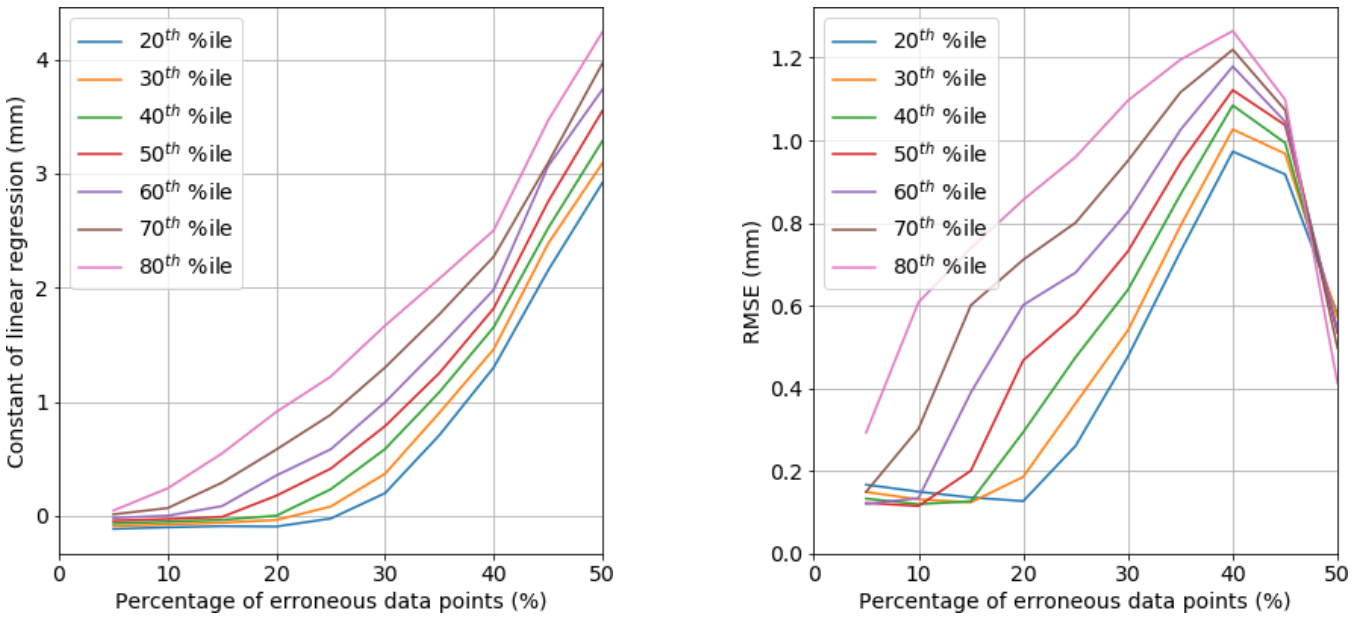

Figure 5.28: Regression constant (left) and RMSE (right), as determined by linear regression between simulated and measured thickness values, for simulated profiles containing varying proportions of erroneous data points. Results were calculated over 5 % intervals and presented for measurements in which the threshold for data inclusion in the surface fit was varied between the 20^{th} and 80^{th} %iles of residual values > 0.

on the fitting of the initial profile midplane, increasing the distance of the fitted midplane from the baseline surface and hence reducing the quantity of valid data points in the second, surface fit.

These results highlight the increased susceptibility of the measurement procedure to erroneous data points, such as those arising due scattered light or stray yarns and fibres protruding above the preform surface, as the surface fitting residual threshold is increased. The selection of an optimal residual threshold value for inclusion of data points in the surface fitting is therefore a compromise between minimisation of systematic and random measurement errors, and susceptibility of measurements to influence by erroneous data. The results presented in Section 5.2.1 suggest that, in the absence of erroneous data, a residual threshold for inclusion of data points in the surface fit set at the 70^{th} %ile of residuals > 0 produces the closest agreement between simulated and measured thickness values, therefore minimising systematic error in the measurement procedure. Reducing the threshold to the 60^{th} %ile increases the systematic error marginally whilst minimising the spread of errors, and hence the uncertainty in measured values. However, upon introduction of erroneous data points, a further reduction in threshold is required to prevent significant increase in both systematic measurement error and measurement uncertainty. A threshold at the 50^{th} %ile maintains the intercept and RMSE values below 0 mm and 0.2 mm, respectively, with up to 15 % erroneous data, whilst at the 30^{th} %ile, up to 20 % erroneous data can be accommodated. In light of these findings, the residual threshold value was set at the 50^{th} %ile, as specified in Chapter

4.7.2, in order to ensure robust, reliable, accurate surface estimation in the presence of up to 15 % erroneous data.

It should be noted that this assessment is based solely on the use of simulated profiles, with randomised waveform structures and uncorrelated erroneous, or anomalous, data points. Whilst it is expected to provide a reasonable evaluation of the performance of the measurement procedure over a wide range of scenarios (i.e. surface structures), it is possible that certain features present in real preform surface profiles may not have been represented, which may cause unexpected measurement errors. It is also possible that the measurement optimisation has been performed on too broad a range of surface profiles and therefore may not be as optimised as it could be for real preform measurements.

5.2.3 Effect of machine mechanics

Besides estimation of the position of the preform surface itself, each thickness measurement relies on an estimation of the position of the mandrel surface relative to the preform surface at the measurement location. This estimate is based on the position of the mandrel surface at the same location determined during a reference scan of the mandrel made prior to commencing the braid deposition, and the assumption that the mandrel surface will be in the same position when the preform surface profile is acquired, i.e. during deposition.

Method

To assess the validity of this assumption, the repeatability of mandrel positioning in the YZ plane of the braider as it traverses the X axis was investigated. For this, a stiff stainless steel tubular mandrel with outer diameter of 100 mm was used. Profiles were acquired at 2 mm intervals along a 1600 mm length of the mandrel. Mandrel position in the YZ plane was determined as the co-ordinates of the minima of the 2^{nd} order polynominal fitted to each acquired profile. Mandrel scans were conducted at three different traverse speeds, 500 mm/min, 1000 mm/min and 2000 mm/min, in both the forward (+X) and reverse (-X) braiding directions, with 5 sets of measurements made for each scenario.

The largest values of mean standard deviation for each co-ordinate were then used to perturb simulated surface and baseline profiles corresponding to cylindrical mandrels of varying diameters in order to assess the potential impact of variation in mandrel position on thickness measurements. Firstly, baseline profiles were generated with co-ordinates along the lower quadrant of a circle with known radius, as performed in Sections 5.2.1 and 5.2.2 previously. Idealised surface profiles (i.e corresponding to constant preform thickness, excluding any preform surface structure) were then generated from co-ordinates of an equivalent section of a concentric circles, with increased radii

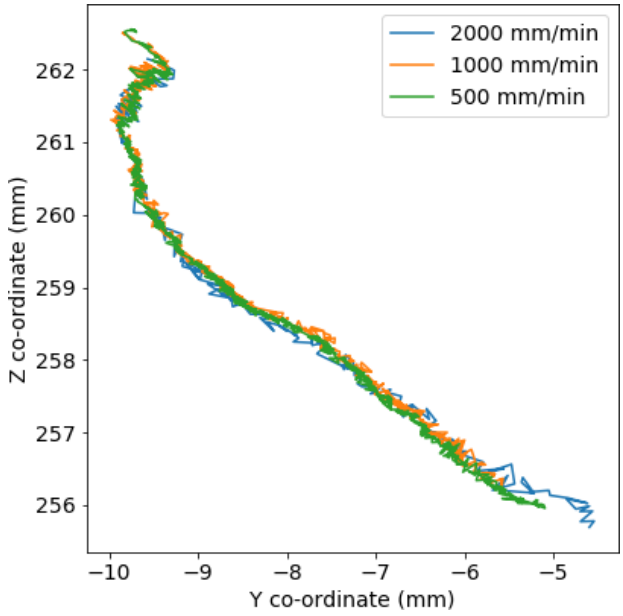

Figure 5.29: Variation in mandrel surface minima co-ordinates over the measured length of mandrel when driven in the forward braiding direction at three different speeds.

corresponding to the simulated preform thicknesses of 1 mm and 3 mm. This was repeated for baseline profiles corresponding to cylindrical mandrel cross-sections with diameter ranging from 40 mm - 750 mm, covering the range of mandrel diameters which the braider was designed to operate. Thickness measurements were then performed on the simulated profiles, during which the surface profiles were perturbed by the (assumed) equivalent standard deviations of both baseline and surface co-ordinates combined in quadrature, first in Y, and then in Z individually.

Results and discussion

Table 5.7: Average standard deviation between repeat surface position measurements at each measurement location along the mandrel length.

Traverse velocity (mm/min)	Mean standard deviation ± 1 σ Y (mm)	Z (mm)
+ 500	0.06 ± 0.028	0.08 ± 0.046
+ 1000	0.12 ± 0.061	0.14 ± 0.067
+ 2000	0.07 ± 0.054	0.09 ± 0.065
- 500	0.06 ± 0.028	0.04 ± 0.015
- 1000	0.07 ± 0.048	0.07 ± 0.037
- 2000	0.08 ± 0.053	0.07 ± 0.047

Example plots showing the change in surface minima co-ordinates along the mandrel length, for each traverse speed in the forward braiding direction, are presented in Figure 5.29. A low

frequency drift is evident at all three speeds, due to slight misalignment of the mandrel with the X axis; high frequency fluctuations in both Y and Z co-ordinates are also evident to varying extents. If such fluctuations, both high and low frequency, are systematic, and therefore repeatable between scans, then the influence on thickness measurement uncertainty (i.e. the spread in measurements corresponding to different profiles acquired at the same location) may be negligible. However, if they are not systematic then they will contribute to thickness measurement uncertainty.

The standard deviation in surface minima co-ordinates was calculated at each measurement location along the mandrel length, for each traverse velocity, in order to determine the repeatability of the fluctuations evident in Figure 5.29. The mean and standard deviation of these values across all 801 measurement locations are presented in Table 5.7.

From these results, it can be seen that the lowest mean value in both Y and Z co-ordinates occurred at the lowest traverse speed, ± 500 mm/min. For negative velocities, i.e. reverse braiding direction, there was a gradual increase in dispersion with speed, in both Y and Z co-ordinates. For positive velocities, dispersion at low speed (i.e. 500 mm/min) was greater than or equal to that for the equivalent negative velocity, increasing significantly by 1000 mm/min, before reducing again to comparable values by 2000 mm/min. This behaviour may be attributed to the fact that the master traverse arm is located on the rear of the braid ring, to which the front arm is slaved. Hence for positive traverse velocities the mandrel is effectively 'pushed', whilst for negative velocities it is 'pulled'. This arrangement may play some role in the increased uncertainty in surface minima co-ordinates evident at + 1000 mm/min.

In order to assess the potential impact of variation in mandrel position on thickness measurements, the largest values of mean standard deviation for each co-ordinate (i.e. those for a traverse velocity of + 1000 mm/min) were then used to perturb simulated surface and baseline profiles corresponding to cylindrical mandrels of varying diameters.The combined standard deviations applied were ± 0.17 mm and ± 0.20 mm for Y and Z co-ordinates respectively.

The resultant perturbation in thickness measurements was found to be directly proportional to Z co-ordinate perturbation at all mandrel diameters, whilst there was negligible effect of perturbation in the Y co-ordinate. This finding was expected, given that the procedure for average thickness calculation along each acquired profile, outlined in Section 4.7.2, only includes data points for which the surface normal gradient is greater than 10, in order to minimise sensitivity to higher order coefficients of the polynomial fitting process. It was, therefore, concluded that the influence of mandrel motion on subsequent thickness measurements is dominated by motion in the Z axis, i.e. that in which the laser profilometer is mounted; motion in the Y axis was subsequently disregarded.

Considering Z axis motion in more detail, the trend of the low frequency drift evident in Figure 5.29 was found to vary with traverse direction, as illustrated by the plot of mean Z co-ordinate

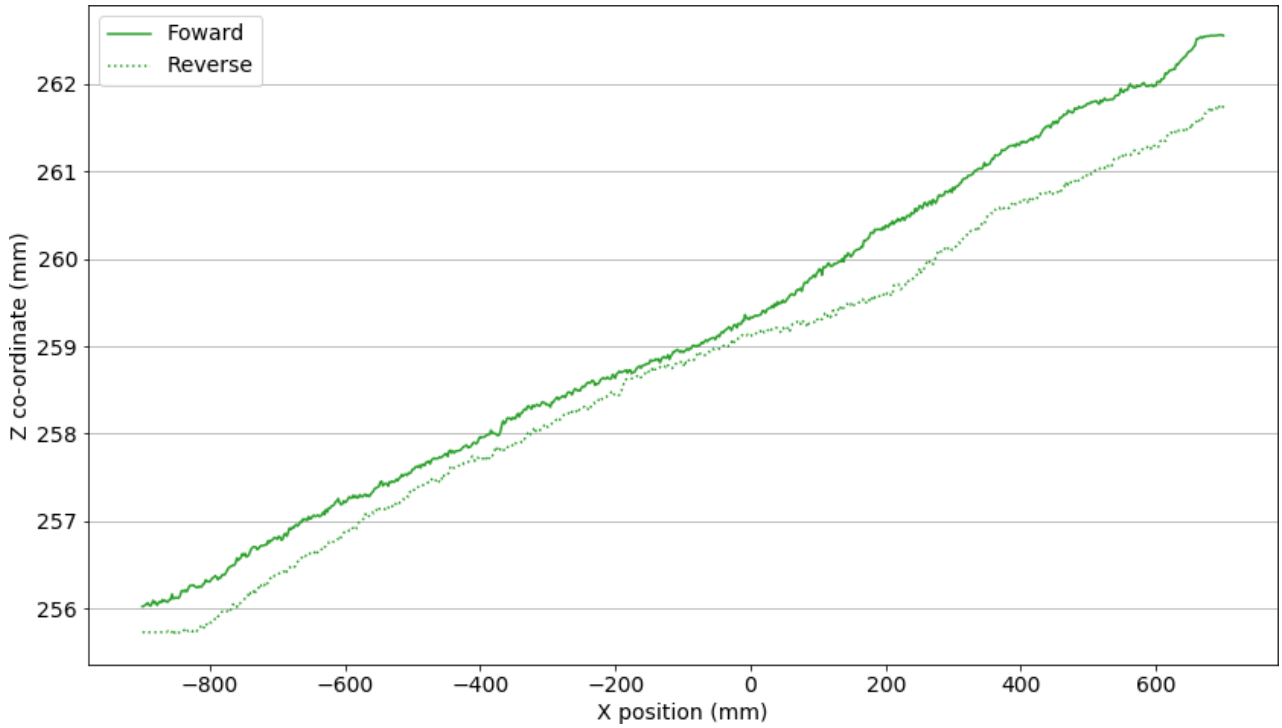

Figure 5.30: Mean Z co-ordinate of mandrel surface minima along mandrel length with mandrel driven at 500 mm/min in both the forward and reverse braiding directions.

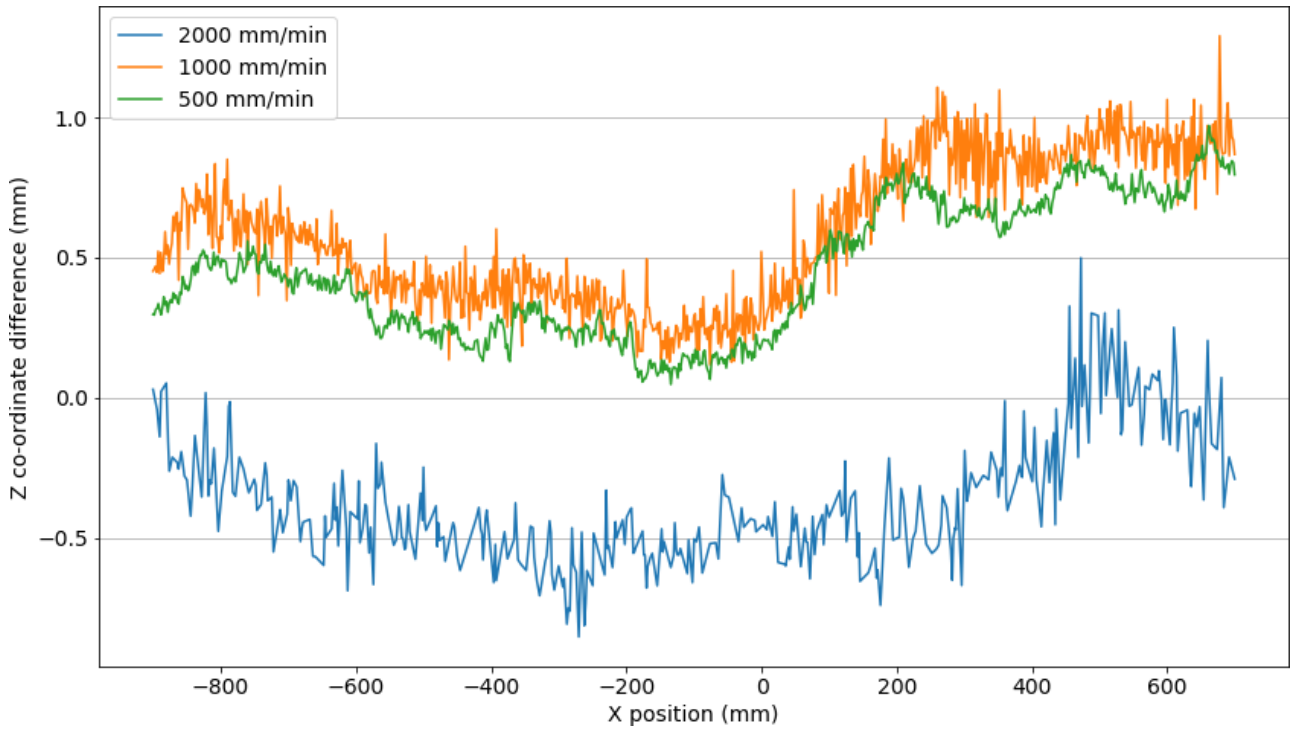

Figure 5.31: Difference between mean Z co-ordinate of mandrel surface minima along mandrel length with mandrel driven in the forward and reverse braiding directions, at three different speeds.

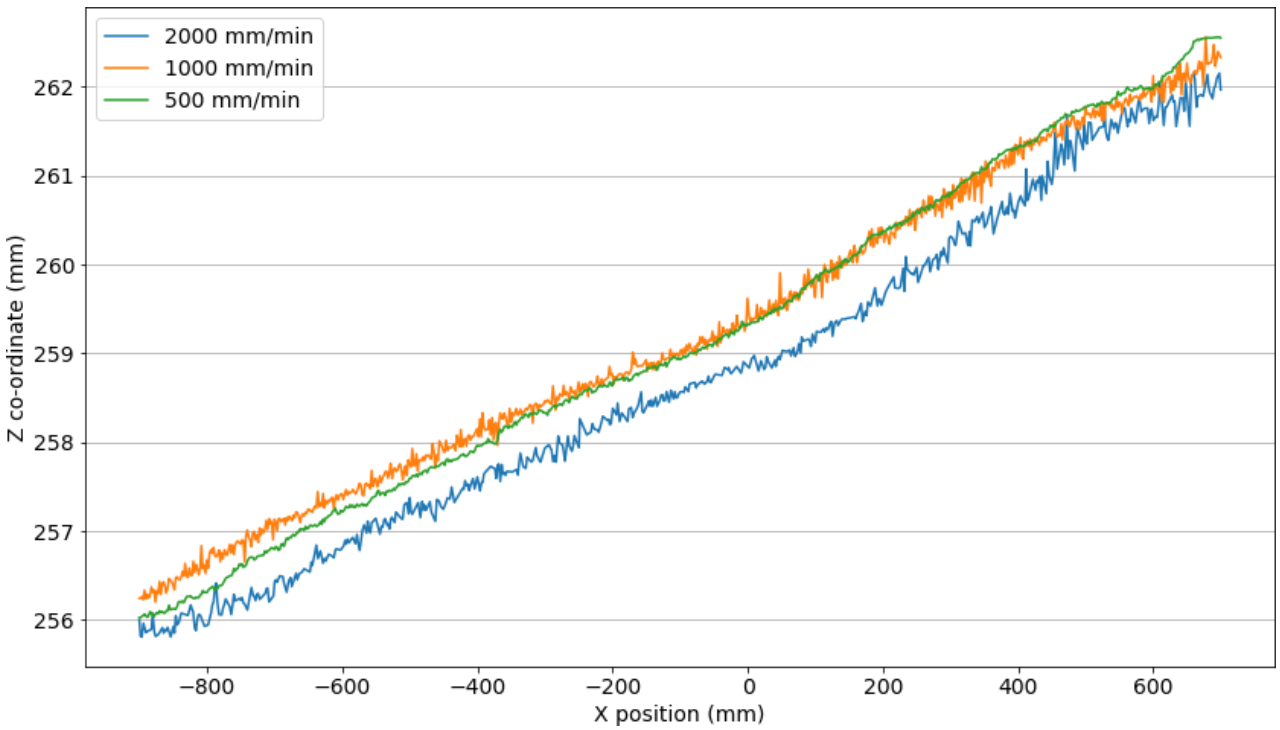

Figure 5.32: Mean Z co-ordinate of mandrel surface minima along mandrel length with mandrel driven in the forward braiding direction at three different speeds.

against mandrel X position for traverse velocities of ± 500 mm/min in Figure 5.30. The difference between traverse directions for each of the three speeds investigated is plotted in Figure 5.31, which shows a close agreement between the behaviour at 500 mm/min and 1000 mm/min over the mandrel length, albeit with greater stability at the lower speed. The magnitude of the difference, ranging from approximately 0.1 mm to 1.0 mm, is sufficiently large to represent a potentially significant source of systematic error in preform thickness measurements, considering that the thickness of a single braided layer itself is typically in the order of 1 mm. At the maximum traverse speed of 2000 mm/min, the difference between traverse directions inverted, indicating a possible change in the traverse mechanics which alters the relative position of the mandrel at higher speeds.

The trend of the low frequency drift evident in Figure 5.29 was also found to vary with traverse speed, as illustrated by the plot of mean Z co-ordinate against mandrel X location for the three positive traverse velocities in Figure 5.32. This was particularly noticeable for the increase from 1000 mm/min to 2000 mm/min, between which an offset of approximately 0.5 mm is evident. Again, this behaviour points towards some change in the traverse mechanics which alters the relative position of the mandrel at higher speeds. The magnitude of this offset is sufficiently large to represent a potentially significant source of systematic error in thickness measurements where the baseline and preform profiles are acquired at different traverse speeds.

These results indicate that baseline scans should be conducted at the same velocity, i.e. both direction and speed of motion, as the braiding operation during which measurements are to be acquired in order to mitigate the occurrence of systematic measurement errors introduced by the velocity-dependent mechanics of traverse and mandrel motion. For the current measurement system setup, measurements can only be conducted during forward braiding operations due to the positioning of the MSA. Therefore, it was concluded that baseline scans should also only be conducted in the forward direction, and at the traverse speed to be used during the braiding operation where possible. Under these conditions, measurement uncertainty due to uncertainty in mandrel position is expected to be equivalent to the combined standard deviation in Z co-ordinates of both mandrel and preform profiles, the maximum value of which was determined to be ± 0.20 mm at a velocity of + 1000 mm/min. This is equivalent to ± 0.39 mm at a 95 % confidence interval assuming a normal distribution of errors; the significance of this machine-induced uncertainty on thickness measurements will be discussed in Section 5.2.5.

It should be noted that these findings relate to the use of a constant traverse trajectory only; future investigations should seek to establish the repeatability of mandrel position under variable trajectories which are required when producing a variable braid angle for cylindrical mandrels or usually when braiding complex, i.e. non-tubular, mandrel geometries. Beyond that, if the system is developed to enable measurements for non-linear mandrel trajectories, where traverse motion in Y and Z axes is required, this assessment of mandrel position repeatability will need to be expanded to include traverse motion in these additional axes.

5.2.4 Effect of surface gradient

To this point in the assessment of preform thickness measurement performance, results have only been considered pertaining to tubular mandrels with no surface gradient, i.e. where the mandrel surface is parallel to the braider X axis.In such scenarios, the preform thickness is equivalent to the average height measured in the YZ plane, $\overline{\Delta YZ}$, as calculated between the fitted preform surface and that of the baseline mandrel surface at the measurement location. Where there is a gradient to the mandrel surface, i.e. $\nabla_{surface} \neq 0$, the average profile height in YZ must be scaled by the cosine of the angle between mandrel surface and X axis, as discussed in Section 4.7.2, in order to obtain the preform thickness normal to the mandrel surface. Accordingly, thickness measurements are subject to the accuracy and uncertainty of surface gradient measurements.

Method

To assess the accuracy and uncertainty of surface gradient measurements used for thickness measurements, surface gradient measurements made during trial C were analysed. The mean and

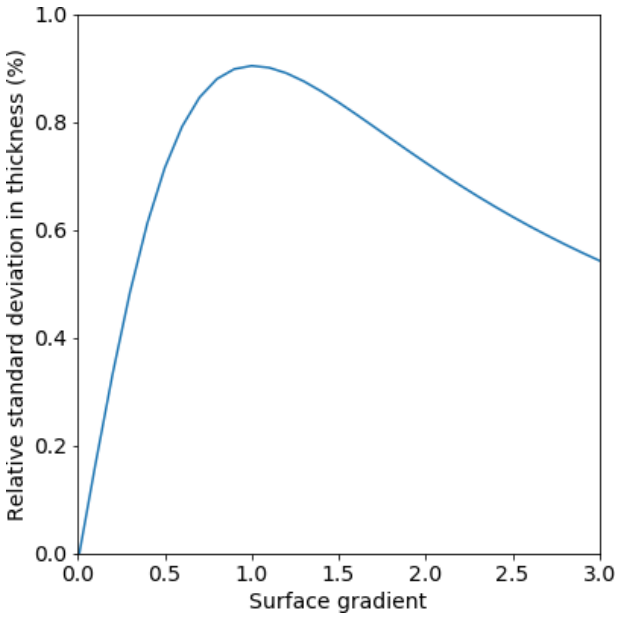

Figure 5.33: Relative standard deviation in thickness due to surface gradient uncertainty, plotted as functions of surface gradient.

standard deviation for in-process preform surface gradient measurements were calculated and compared to the known gradient for the mandrel, which was assumed to be mounted concentrically to the braid ring.

Results and discussion

The known gradient for the conical section of the mandrel used in the trial was 0.176. Corresponding in-process preform surface gradient measurements were determined to have a mean value of 0.178, with standard deviation 0.018. This result suggests that systematic surface gradient errors are negligible relative to the associated uncertainty, i.e. 1 % relative to ± 10 %, equating to an error in thickness measurement of just 0.04 mm for $\overline{\Delta YZ} = 10$ mm, $\nabla_{surface} = 1$. Accordingly, no systematic error correction was specified for surface gradient values used in thickness measurement procedure (Section 4.7.2).

The relative standard deviation (RSD) in thickness measurements resulting from a standard deviation in surface gradient of 0.018 was calculated for surface gradients in the range 0 - 3, as presented in Figure 5.33. As can be seen, RSD was determined to peak at 0.9 % for a gradient = 1.0; the significance of this uncertainty will be considered in the Section 5.2.5.

5.2.5 Preform thickness measurement uncertainty

In Sections 5.2.2 - 5.2.4, several sources of uncertainty in preform thickness measurements were investigated. These are presented in Table 5.8, along with the worst-case standard deviation values:

Table 5.8: Average standard deviation between repeat surface position measurements at each measurement location along the mandrel length.

Source	Standard deviation	Notes
Preform surface estimation	0.20 mm	Assuming 15 % erroneous profile data
Mandrel surface position relative to baseline scan	0.20 mm	For traverse trajectory = + 1000 mm/min
Mandrel surface gradient	0.9 %	For surface gradient = 1.0

Method

An assessment of the combined contribution of these factors to preform thickness measurement uncertainty is presented in this section. This assessment was performed by summation in quadrature of the uncertainties determined for each of the sources of variability, in accordance with the "Guide to the expression of uncertainty in measurement" [279]. Errors resulting from each source were assumed to follow a normal distribution, with no correlation assumed between the sources. Given the relative nature of uncertainty associated with mandrel surface gradient, two example scenarios are considered here:

- Firstly, for a mandrel with no surface gradient, or a thin preform thickness ($\sim$ 1 mm thick). In such instances, uncertainty in surface gradient can be neglected.
- Secondly, for a graduated mandrel surface with gradient = 1.0 and appreciable preform thickness (e.g. 15 mm), for which all three uncertainty sources must be considered.

Results and discussion

For a mandrel with no surface gradient, or a thin preform thickness ($\sim$ 1 mm thick), the combined standard uncertainty associated with the remaining two sources equates to 0.28 mm, or 0.55 mm at a 95 % confidence interval assuming a normal distribution. This value is reduced to 0.33 mm at a 95 % confidence interval in a realistic best case scenario, where the uncertainty associated with mandrel surface position drops to 0.08 mm (i.e. for + 500 mm/min), and with estimated preform surface position drops to 0.12 mm (i.e. corresponding to a low percentage of erroneous data points in the acquired profile).

For a graduated mandrel surface with gradient = 1.0 and appreciable preform thickness (e.g. 15 mm), the combined standard uncertainty equates to 0.31 mm, or 0.61 mm at a 95 % confidence interval assuming a normal distribution.

Considering the desired system performance for thickness measurements of ± 0.1 mm as stated in Section 4.3, the uncertainty arising from the first two sources alone means that no single thickness measurement can confidently be made with the desired level of accuracy. Whilst this may be improved by assuming, either, a lower level of uncertainty associated with mandrel surface position (i.e. as a result of a different traverse speed), or lower proportion of erroneous profile data points, it is only possible to achieve the required level of uncertainty by averaging over multiple measurements. For instance, in the scenario with no mandrel surface gradient, averaging over 11 - 30 measurements would be expected to produce a standard error of the mean of ± 0.1 mm at a 95 % confidence interval, and hence the desired level of accuracy may be achieved with a high level of confidence. However, where measurement averaging is not feasible or appropriate, then the higher level of uncertainty will remain. Further improvements in preform surface detection, either by improved performance of the laser profilometer or the fitting procedure, or machine modifications to reduce instabilities in the traverse drive mechanisms would be required to reduce the single measurement uncertainty further.

Validation results

Method

In order to validate the thickness measurement procedure, measurements acquired by the in-process measurement system were compared with those made using a Hexagon ROMER Absolute Arm 7751 SI with integrated scanner, mounted on a Brunson heavy duty stand. Measurements were acquired during manufacturing trial D, in which an 8 layer biaxial preform was braided over a cyclical mandrel (200 mm OD). The braider was configured to produce a regular braid pattern, with a target braid angle of 30°. Braiding was conducted in both forward and reverse directions, with measurements acquired for layers braided in the forward direction, i.e. layers 1, 3, 5 and 7, and the final layer, layer 8, after completion of the braiding operation. Profiles were acquired using the in-process measurement system at 2 mm intervals, at a resolution of 1280 points per profile.

To acquire the validation measurements, the scanning arm was setup alongside the mounted mandrel, positioned such that it would not interfere with traverse motion during the braiding operation whilst also able to reach the measurement region of the mandrel in its stationary position at the end of each forward braided layer. Care was taken not to alter the position of the scanning arm tripod during the braiding and measurement operations.

An area covering the lower half of the mandrel/preform surface, extending in excess of 800 mm

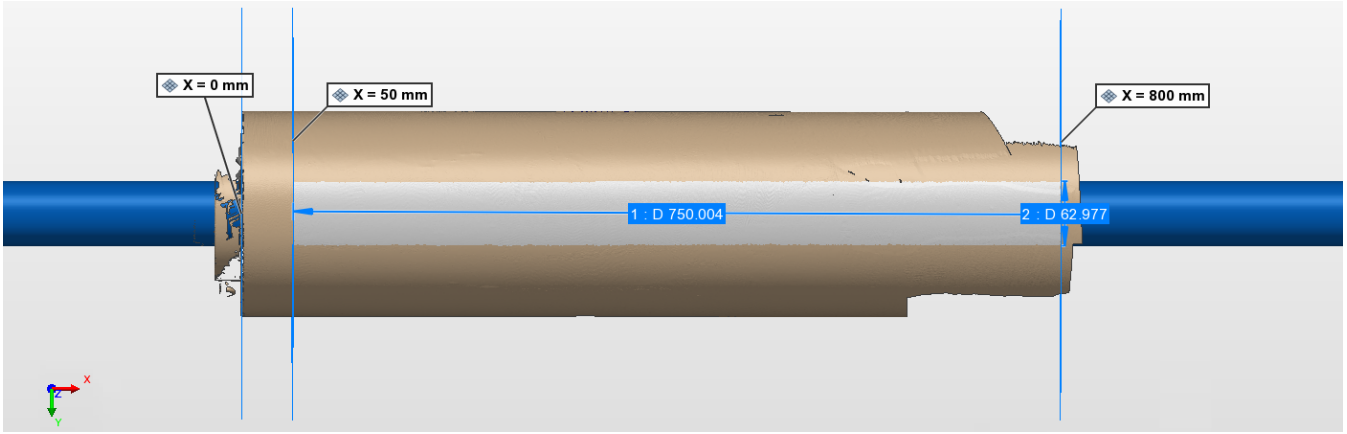

Figure 5.34: Scan data for the mandrel (beige), viewed from the underside, illustrating the 750 × 63 mm measurement region (silver), bounded by YZ planes at X = 50 mm and 800 mm; the leading face of the mandrel is indicated by the YZ plane at X = 0 mm.

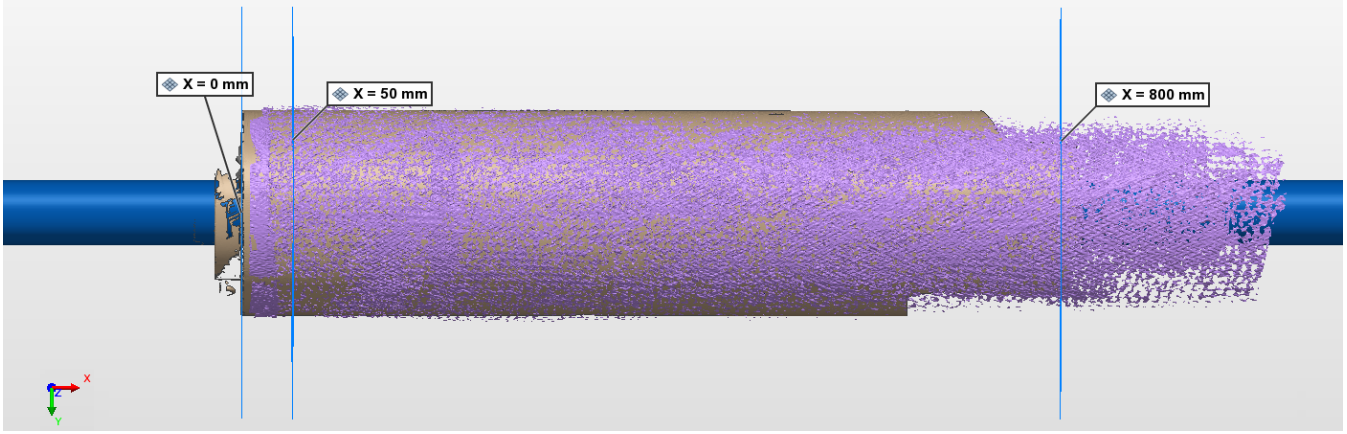

Figure 5.35: Scan data for layer 8 (purple) overlaid on the mandrel scan data.

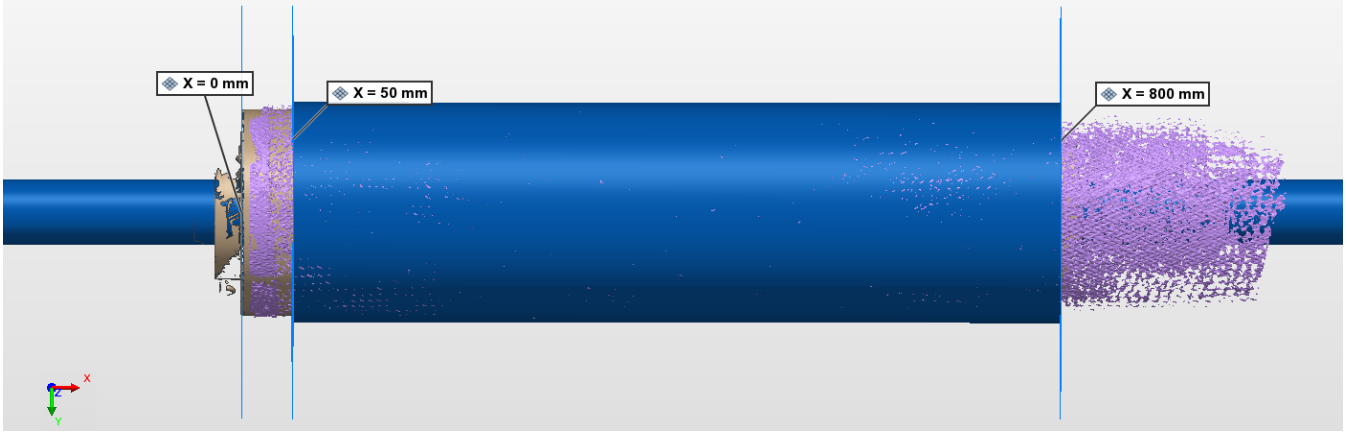

Figure 5.36: Cylinder (blue) fitted to layer 8 scan data over the length of the measurement region.

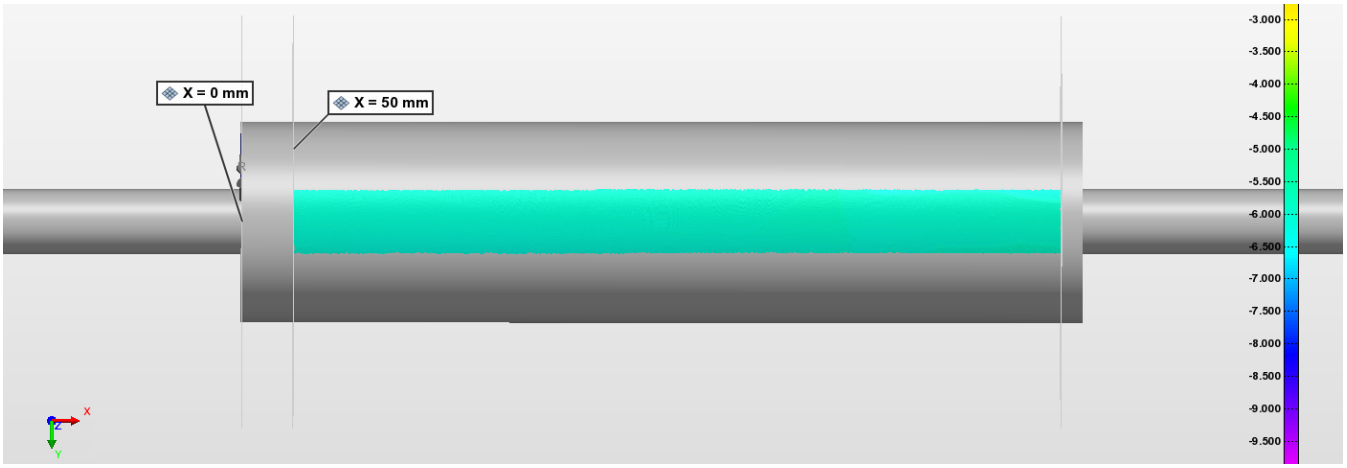

Figure 5.37: Colour map representing the deviation of the fitted cylinder for layer 8 from the measurement region on the mandrel surface; scale bar values are given as negative, in mm.

from the leading face of the mandrel (X = 0 mm) was scanned Data from a central strip ∼ 63 mm wide, taken between X = 50 and X = 800 mm, was used for thickness measurements, as illustrated in Figure 5.34. An average thickness for each layer was measured from the scan data as follows, using the PolyWorks Inspector Premium software package:

- scan data was cleaned to remove clearly anomalous data points (see Figure 5.35);
- a cylindrical feature was fitted to scan data between X = 50 and X = 800 mm, using the 'Max' fit type and rejecting outliers outside 2 standard deviations (see Figure 5.36);
- a colour map of deviations between mandrel scan data and the cylinder feature was generated for the area of interest (see Figure 5.37), from which the mean deviation, corresponding to the mean layer thickness, was calculated.

During the determination of preform thickness for layer 1, it became apparent that an offset of the mandrel position had occurred relative to the baseline scan, as indicated by a mean preform thickness measurement over the specified area of just 0.16 mm. This is believed to have occurred between the baseline mandrel scan and the start of the braiding operation, due to forces applied to the mandrel once the yarns had been attached and mobilised, causing the mandrel to re-seat in its mounts. Given the relatively open braid structure, much of the mandrel surface was present in the layer 1 scan data, making it possible to fit a cylindrical feature to the mandrel surface and measure the offset of this surface relative to that from the baseline scan. The offset, determined to be 1.07 mm, was added to the thickness measurement for each layer.

The resulting mean thickness values were compared with mean values calculated from in-process measurement data for the same region, as presented in Figure 5.38; error bars are included repre-

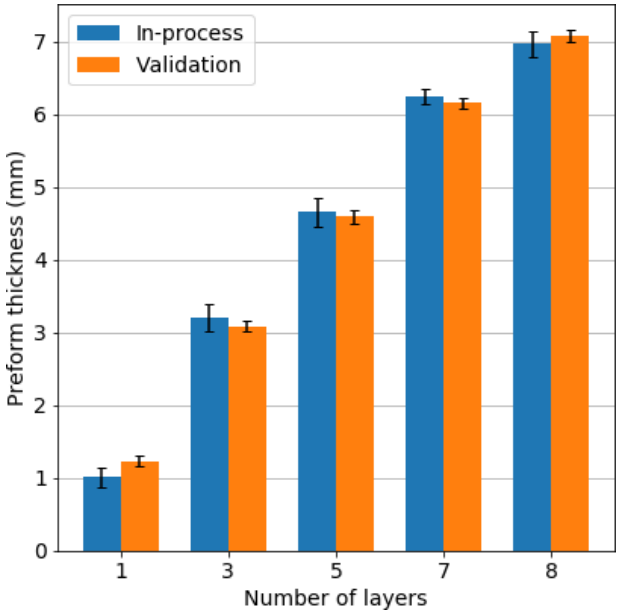

Figure 5.38: Comparison of in-process and validation measurements for mean preform thickness, measured after deposition of 1, 3, 5, 7 and 8 layers; error bars represent 1σ.

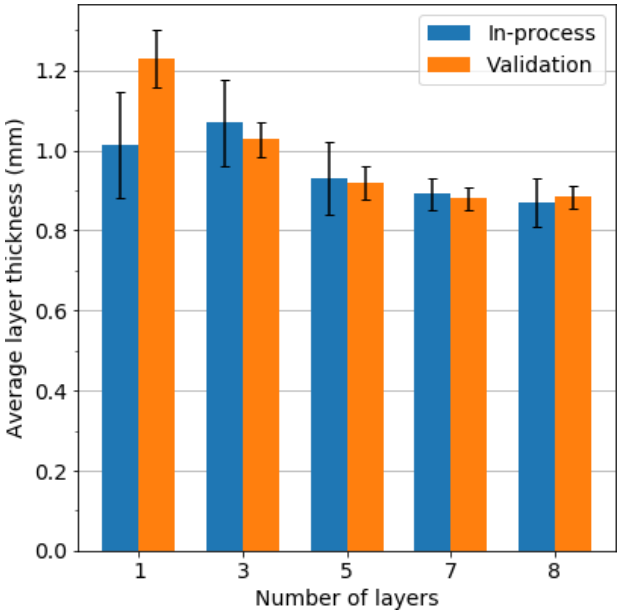

Figure 5.39: Comparison of in-process and validation measurements for mean layer thickness, calculated from preform thickness measurements; error bars represent 1σ.

senting 1 standard deviation. Average layer thickness values were also calculated for both data sets; these are presented in Figure 5.39, showing standard deviation error bars calculated in quadrature.

Deviation across in-process measurements was greater than that for validation measurements for all layers, as expected given the dynamic state of the measurement subject during in-process data acquisition. The greatest difference between in-process and validation measurements occurred for the first preform layer, with the mean in-process thickness 0.21 mm less than the validation measurement. For layers 3, 5 and 7, the in-process value exceeded the validation by between 0.13 and 0.06 mm, whilst for layer 8 the difference was -0.11 mm; this difference may be explained by a shift in mandrel mounting position resulting from the detachment of yarns spools prior to layer 8 measurement. Given the high number of samples averaged for both data sets, these differences in mean values are statistically significant and hence the in-process thickness measurement system can only be claimed to be accurate to approximately $\pm$ 0.2 mm based on these results.

5.2.6 Summary of preform thickness measurement performance

The fndings of investigations presented and discussed in this section, relating to the performance of the preform thickness measurement capability, can be summarised as follows:

Effect of surface structure

Estimation of preform surface from laser profilometer data, as required to enable preform thickness measurements, was found to present a challenge due to the structured nature of a preform surface, resulting from yarn geometry, yarn stacking, braid pattern, mandrel curvature. To address this challenge, a robust, 2-stage polynomial fitting procedure was developed, enabling determination of the midplane of a surface profile, followed by estimation of the outer preform surface by fitting only to data points above a certain residual threshold from the midplane fit. Using a Monte Carlo approach with simulated profiles to represent a broad range of preform surface structures with known maximum thickness values, systematic measurement errors were found to be minimised by setting the residual threshold value equivalent to the 70^{th} %ile of residuals > 0. This resulted in an estimated systematic measurement error of just -0.01 mm across the simulated profile set. Meanwhile, measurement spread due to random variation was shown to be minimised with the residual threshold value equivalent to the 60^{th} %ile, with an RMSE of 0.119; systematic measurement error remained low at -0.03 mm.

Effect of light scatter

Acknowledging the detrimental impact of scattered light from the preform surface on the quality of real profiles, erroneous data points were introduced into simulated profiles in a repeat of the Monte Carlo assessment performed for surface structure assessment. Errors were introduced to the Z co-ordinates of a random percentage of profile data points in the range 0 % - 50 % prior to surface estimation; correlations between measured and simulated thickness values were calculated for 5 % erroneous data point intervals. With a residual threshold at the 60^{th} %ile, both systematic and random errors were shown to increase significantly upon the introduction of 10 % - 15 % erroneous data; lowering the threshold to the 50^{th} %ile retained these values at below 0 mm and 0.2 mm respectively.

Effect of machine mechanics

The thickness measurement procedure utilises a baseline profile of the mandrel surface at each measurement location, with an assumption that the position of the mandrel surface is equivalent between the baseline and preform acquisitions. This assumption is dependent upon the stability and repeatability of braider traverse arm motion and was investigated in order to determine its validity and any associated uncertainty introduced to measurements. Speed- and direction-dependent variation in both Y and Z co-ordinates of surface profile minima was identified, although only Z co-ordinate uncertainty was shown to propagate to through to thickness measurements. Mean profile minima co-ordinates were found to vary significantly according to traverse speed and direction, by

as much as $\sim$ 1 mm between certain cases, hence it was proposed that the baseline scans should be acquired at the same traverse trajectory as to be used during the preform measurement scan, i.e. during the braiding operation.

Spread in Z co-ordinate values, as described by 1 standard deviation, was found to range from 0.04 mm at low, negative trajectories (i.e. reverse braiding at 500 mm/min traverse speed) to 0.14 mm at intermediate, positive trajectories (i.e. forward braiding at 1000 mm/min). Assuming equivalent uncertainties in both baseline and preform profile acquisitions, this is expected to translate to a standard deviation in thickness measurements resulting from traverse motion of as much as $\pm$ 0.39 mm.

Effect of surface gradient

In cases where surface profiles are not acquired perpendicular to the mandrel surface, i.e. when the lower mandrel surface is inclined due to a non-tubular mandrel geometry, the measurement procedure applies a trigonometric correction in order to estimate preform thickness perpendicular to the mandrel surface. The correction relies on a measurement of surface gradient determined from a number of preceding acquired profiles. The standard deviation in gradient measurements for a moderate mandrel gradient of 0.176 was found to be $\pm$ 10 %, equating to a maximum standard deviation in thickness measurements of 0.9 % at a gradient of 1.0.

Preform thickness measurement uncertainty

The combined uncertainty associated with thickness measurements arising from the effects investigated throughout Section 5.2 was evaluated by summation in quadrature of the contributing uncertainties, which were assumed to be additive and uncorrelated. The result was an expanded uncertainty ranging between 0.33 mm and 0.55 mm at a 95 % confidence interval for realistic best and worst case scenarios in the absence of mandrel surface gradient, with equivalent contributions assumed for surface estimation and mandrel position. Inclusion of surface gradient effects was determined to have negligible effect except in the case of thicker preforms, e.g. $>$ 10 mm thick, coupled with surface gradients approaching 1.0.

Even in the best case scenario, corresponding to low traverse speed and minimal profile noise, the combined measurement uncertainty means that the target accuracy for thickness measurements of $\pm$ 0.1 mm cannot be met without averaging over multiple measurements (where appropriate). A minimum of 11 samples would be required to produce an average measurement value with uncertainty equivalent to $\pm$ 0.1 mm at a 95 % confidence interval. Improvements in the surface detection and estimation capability, as well as machine modifications to reduce instabilities in the traverse drive mechanisms would likely be required to improve performance to the desired level.

Chapter 6

Advancing material and process understanding through in-process measurement

The motivation for development of the in-process measurement system outlined in Chapter 4 was to provide a capability for the acquisition of consistent, reliable, re-useable data sets, relating to, and informative of, the quality of over-braided preforms. In doing so, it was intended that data-driven research methods utilising the resultant, varied data sets acquired across numerous discrete over-braiding manufacturing research activities would be investigated. However, the timescale required to generate sufficiently large and varied data sets from upcoming projects was incompatible with that remaining for this research project once the measurement capability was operational.

This chapter, therefore, seeks to highlight the additional insights into material and process understanding that were generated during two initial over-braiding projects which made use of the measurement capability, as a means demonstrate the added value that might be brought to projects through the availability of such in-process data. It is hoped that this will encourage the standardised use of in-process measurement capabilities within future projects, as required to generate the aforementioned data sets suitable for data-driven research.

Findings from these two projects resulting from the available braid angle and thickness measurements are presented. Whilst aspects of the projects discussed were determined and conducted by other members of the research teams, the analysis of in-process measurement data and the associated advances in material and process understanding were the work of the author. Some of the data from these projects were used for measurement system development and optimisation and hence were presented in Chapter 5. These data are presented again in this chapter, in the context of the project in which they were generated. Manufacturing details are provided again in Table 6.1 for ease of reference, along with mandrel geometry details in Figure 6.1.

Table 6.1: Details of the manufacturing trials during which data presented in Chapter 6 were acquired.

Manufacturing Trial	B.1	B.2	D	E	F.1	F.2
Material	Toho Tenax -E HTS45 E23 12K 800tex					
Braid pattern	1/1		2/2		2/2	
# bobbins	144		288		288	
Mandrel	M2		M2		M4	
Yarn twists per metre	7		10		10	7
Guide ring diameter (mm)	400		400		400	
Target braid angle (°)	45	26 - 60	30	45	45	
Braiding direction	Fwd. only		Fwd. & rev.		Fwd. only	
# preform layers	3 × 2	1	8		4	

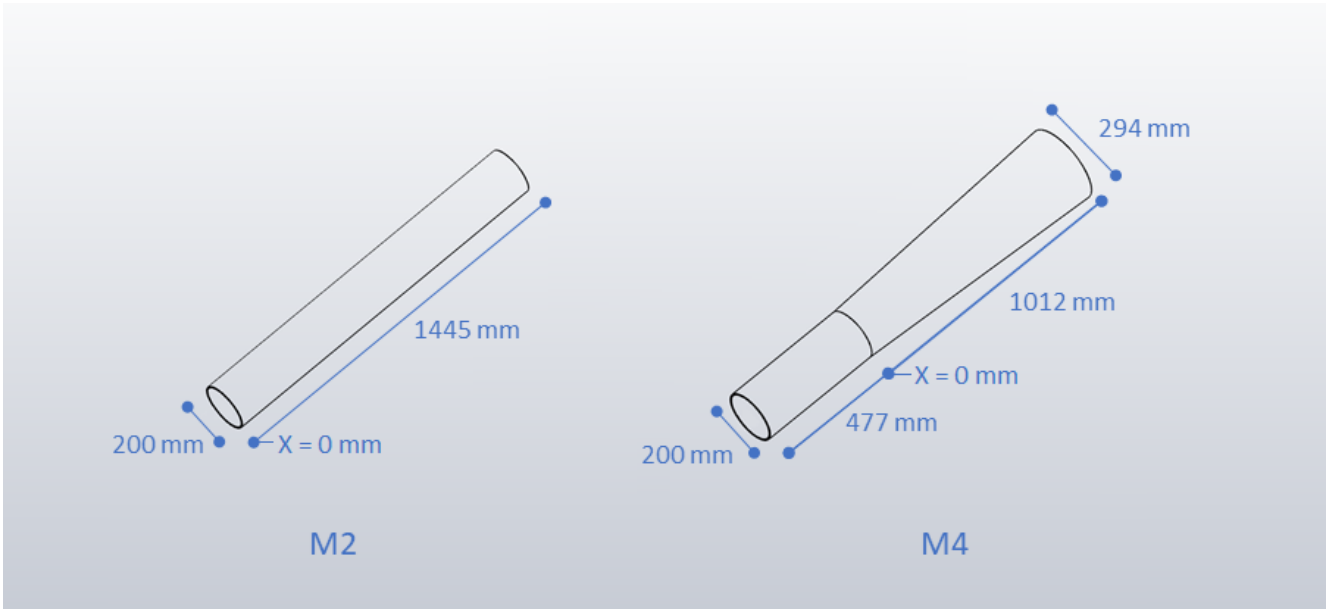

Figure 6.1: Mandrel geometry details relevant to the manufacturing trials presented in Chapter 6.

6.1 Preform manufacture for validation of braided preform permeability simulation

The in-process measurement capability introduced in Chapter 4 was utilised during a research project into the state-of-the-art for braided preform permeability prediction via simulation. The project was conducted collaboratively between researchers at NCC and the Bristol Composites Institute (ACCIS) at the University of Bristol, through NCC's Technology Pull-Through Programme. The aim of the project was to assess the accuracy of preform permeability predictions for multi-layer, biaxial braided preforms generated using the WiseTex [280] and FlowTex [281] software packages. These software are designed to enable virtual representation of the internal structure of textile materials and prediction of the corresponding permeability coefficients. Subsequent simulation of the liquid resin infusion process using the predicted permeability coefficients was conducted using PAM-RTM [282] to predict resin flow-front progression and infusion durations. The corresponding preforms were manufactured and infused under comparable conditions in order to validate the infusion simulations and hence the permeability coefficient predictions.

In-process measurement data for the as-manufactured preforms presented and discussed in this section were collected and analysed by the author during the course of the project; measurement values were not immediately available to the operator during preform manufacture. Modelling and simulation, preform manufacture and infusion, and cured sample preparation and analysis activities were conducted by other members of the project team. The findings from the project regarding the performance of the simulation capabilities are not discussed at length in this section; the focus is on the insights gained into the braiding process itself from data generated by the in-process measurement system.

6.1.1 Method

Braided preforms were produced using two mandrel designs shown in Figure 6.1, with six preforms produced in total over the course of the project. Measurement data acquired during the manufacture of four of these are presented in this section, the relevant manufacturing details for which are provided in Table 6.1.[1] Braid angle and preform thickness measurements were acquired at intervals of 20 mm and 2 mm, respectively, in all cases. The reference location, i.e. X = 0 mm, was set at the front face of the cylindrical mandrel, M2, for trials D and E, and the interface between cylindrical and conical mandrel sections of M4 for trials F.1 and F.2

As discussed in Section 4.5, the mounting position of the measurement sensor assembly limited

[1]Data acquired during the remaining two productions were invalidated by development issues with the measurement system.

data acquisition during the process to the forward braiding direction only. Hence, in the case of trials D and E, only layers 1, 3, 5 and 7 could be measured during deposition. The final layer, layer 8, was measured after preform deposition was completed, as the mandrel was driven back through the guide ring. For this project, the allowable braid angle deviation from the target angle, i.e. the braid angle tolerance, was specified as ± 3°.

6.1.2 Results

Braid angle

Braid angle measurements for preforms generated in trials D and E are presented in Figures 6.2 and 6.3, respectively. Dashed lines are included in the figures to illustrate the target angle (green), a ± 1° threshold (orange), and the ± 3° tolerance threshold (red). It is evident from these results that a significant length of braid was deposited before the measured braid angle was within tolerance for many of the odd-numbered layers. In most instances that length was around 200 mm, although for trial D, layers 3 & 5, it was around 600 mm, approximately 40 % the total preform length, despite starting within tolerance.[2]

For these trials, layer 8 was braided in the reverse direction, hence braid deposition started from the maximum X value of 1445 mm. In both sets of results, braid angle for layer 8 was seen to increase steadily until reaching a relatively stable value on or around a tolerance threshold. This transition occurred between the lower and upper tolerance thresholds for trial E, over a length of $\sim$ 600 mm, and was therefore deemed acceptable to the project. In the case of trial D however, the initial braid angle was shown to be significantly below the the lower tolerance threshold, only reaching an acceptable value by X = 550 mm, after deposition of $\sim$ 900 mm.

Since a preform length of 800 mm was required for the subsequent infusion process, and given the braid angle deviations recorded for trial D, layers 3 and 7, the decision was taken to discard layer 8 and proceed with the section of preform between X = 600 mm and X = 1400 mm. The corresponding braid architecture model, and permeability and infusion simulations were updated to match a 7 layer preform. This decision was made on the assumption that the final layer deposition of trial D was anomalous and not representative of the preceding reverse-braided layers. However, subsequent inspection of images from layers 3, 5 and 7 revealed that the substrate layer in each case, i.e. layer 2, 4 and 6, respectively, exhibited a similar trend to that seen for layer 8.

Manual braid angle measurements of the substrate layer were made from images acquired at X = 1150 mm using the line tool in the ImageJ software package [272]. Lines were drawn between

[2]Note that the total mandrel length for trials D and E was 1445 mm but the maximum X value for measurements was determined by the resting position of the mandrel after each layer deposition relative to the position of the measurement sensor assembly.

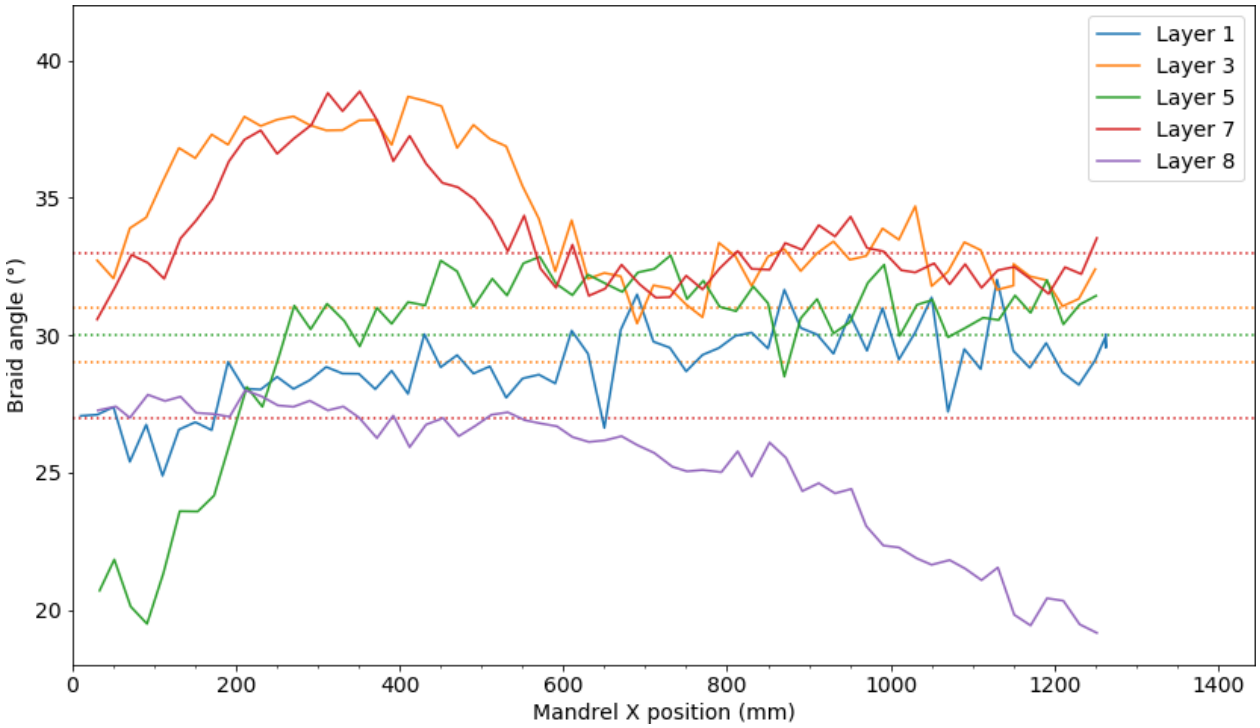

Figure 6.2: Braid angle measurements for 8 layer preform braided over cylindrical mandrel (trial D); target angle 30°.

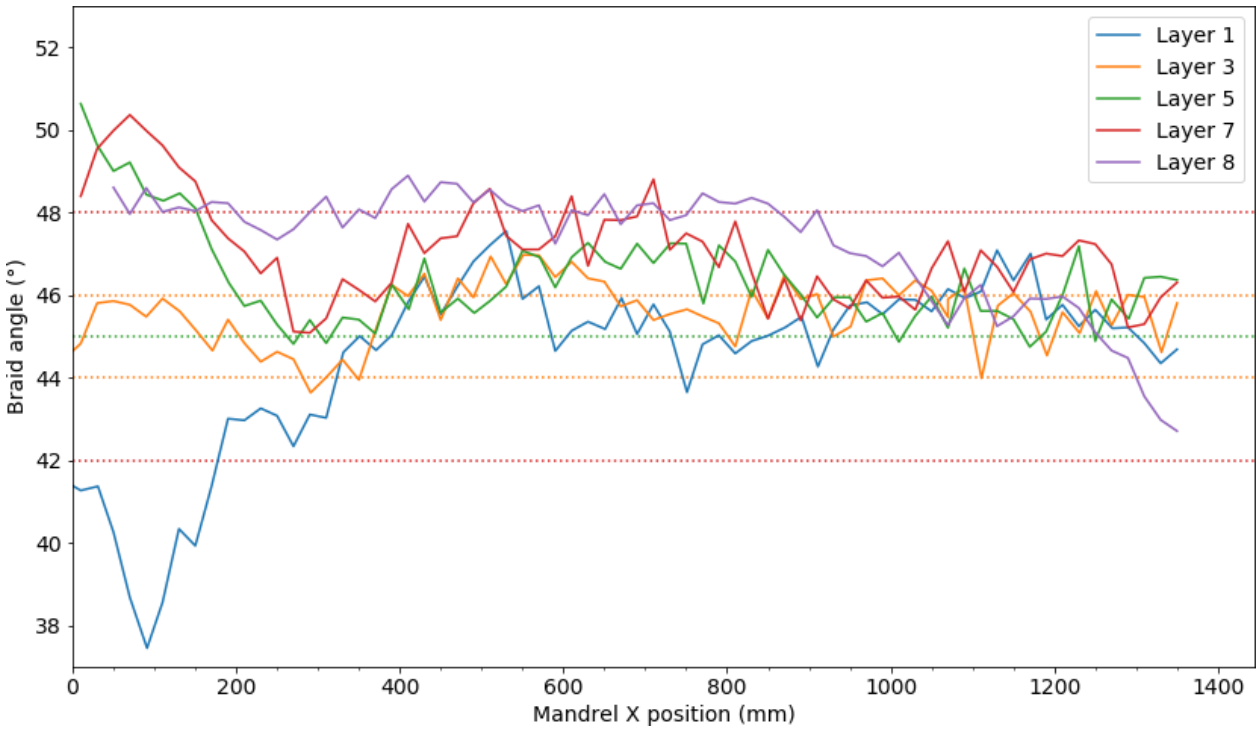

Figure 6.3: Braid angle measurements for 8 layer preform braided over cylindrical mandrel (trial E); target angle 45°.

visible sections of yarn edges in the substrate layer for 5 yarns in each yarn direction. The average absolute orientation of those lines relative to the frame of the image was then calculated. The resultant mean braid angle measurements for layers 2, 4, and 6 at X = 1150 mm were 20.2°, 20.8° and 17.7° respectively, suggesting a similar trend to that seen for layer 8, in which a significant length of braid was likely to have been out of tolerance for all reverse-braided layers in trial D. Due to the higher cover factor for trial E, estimated at 92 % relative to 83 %, it was not possible to conduct equivalent manual measurements in order to confirm the presence of similar trends.

The braid angle deviation confirmed for trial D will almost certainly have had an impact upon the preform infusion as a result of the irregularity introduced to the preform architecture and disruption to inter-layer nesting. Since the architecture models used to generate permeability coefficient predictions assumed a constant braid angle across all layers, this manufacturing deviation will inevitably have been a source of error in the corresponding infusion simulations. The availability of near real-time braid angle measurements during braid deposition would have aided the timely identification of these manufacturing deviations, thus enabling corrective action to be taken. As it happened, measurements for the layers braided in the forward direction were only available post-process due to the developmental stage of the measurement capability at the time, whilst measurements for the layers braided in the reverse direction are not currently within the capability of the system.

Preform thickness

Final preform thicknesses for manufacturing trials D and E, averaged across a 1000 mm length of the mandrel, are presented in Table 6.2. These results show an apparent lack of sensitivity to the change in preform braid angle between the trials, despite the associated change in cover factor. It is plausible that this observation is a consequence of the braid angle variability between layers seen for trial D, which would have limited the extent of inter-layer nesting. Given that the deposited yarn structure would have been expected to be equivalent between these manufacturing trials, these results suggest that there may have been some degree of inter-layer nesting achieved during trial E. Hence, measured permeability might have been expected to be lower than the maximum simulated value, corresponding to a fully stacked, un-nested architecture.

Table 6.2: Mean final preform thickness measurements for trials D and E calculated over a 1000 mm length of preform (200 mm $\leq X \leq$ 1200 mm).

Trial	Target θ (°)	Cover factor (%)	Thickness $\pm$ 1 σ (mm)
D	30	83	6.97 $\pm$ 0.23
E	45	92	6.86 $\pm$ 0.21

Aside from inter-layer braid angle variability, another potential factor determining deposited

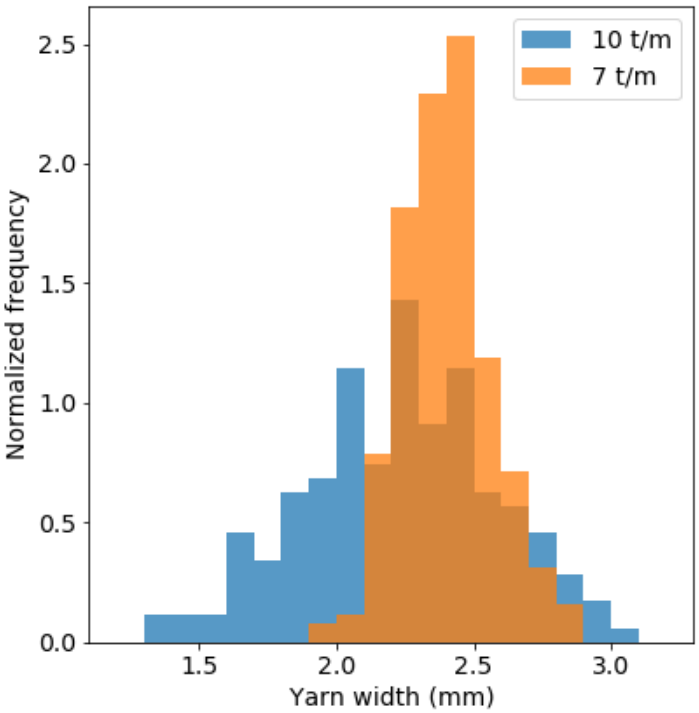

Figure 6.4: Comparison of yarn width distributions at 10 t/m (trial F.1) and 7 t/m (trial F.2).

preform thickness was identified from the results obtained during trials F.1 and F.2. These trials were identical other than the amount of yarn twist that was applied when winding the bobbins, which was reduced from 10 twists per metre (t/m) to 7 t/m when bobbins were reloaded with material between F.1 and F.2. During deposition, braid angle was stabilised at the target value of 45° ± 3° over the initial cylindrical mandrel section and then maintained over the conical section by increasing the traverse speed; deposition was in the forward direction only.

Final thickness measurements for the as-deposited preforms, averaged over an 800 mm length of the conical mandrel section, are presented in Table 6.3. These results show a statistically significant reduction in preform thickness with the reduction in yarn twist, which suggests that, either, the individual layer thicknesses were lower, or the extent of nesting between layers was increased as a result of the change.

Table 6.3: Mean final preform thickness measurements for trials F.1 and F.2, calculated over a 800 mm length of preform (100 mm $\leq X \leq$ 900 mm).

Trial	Yarn twists per metre	Thickness ± 1 σ (mm)
F.1	10	4.08 ± 0.26
F.2	7	3.66 ± 0.20

It was proposed that the reduced twist enabled greater spread of the yarns during deposition and

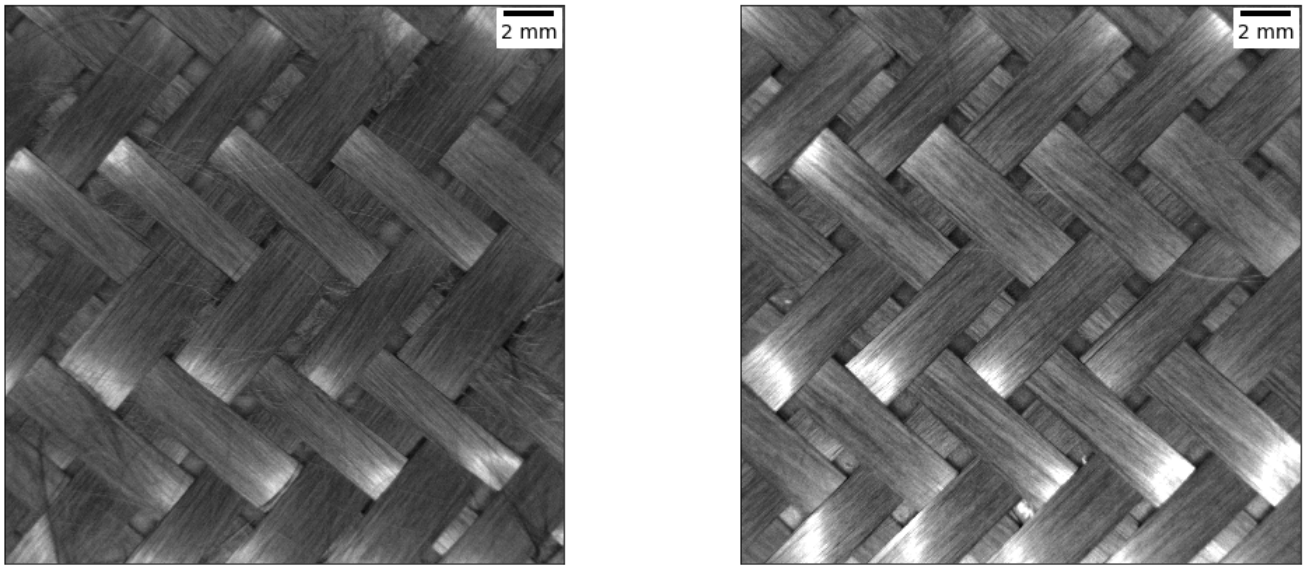

Figure 6.5: Example images from layer 1 of trial F.1 (left) and trial F.2 (right), illustrating the difference in yarn width variability between 10 t/m and 7 t/m, respectively.

a corresponding reduction of the layer thickness. This hypothesis was tested by comparing manual measurements of yarn widths from images acquired by the measurement system. Measurements were made for layers 1 and 4 of trials F.1 and F.2 from images acquired over the 100 mm section of cylindrical mandrel immediately adjacent to the conical mandrel section, five images per layer. Braid angle measurements were stable at the target angle of 45° ± 1° over this section, whilst perspective distortion due to mandrel surface gradient along the braiding axis was avoided. The widths of yarns in both orientations were measured using the length tool in ImageJ [272], one measurement per yarn and no less than 17 measurements per image. The width in pixels was divided by the known image scale in pixels/mm.

A normalised histogram of measured yarn widths for the two trials is presented in Figure 6.4, which shows a distinct difference in yarn width distributions as a function of yarn twist. For trial F.1, with 10 t/m, widths were found to range between 1.3 mm and 3.1 mm with a relatively shallow distribution. For trial F.2, in which yarn twist was reduced to 7 t/m, widths ranged between 1.9 mm and 2.9 mm, with a much narrower distribution. The corresponding coefficient of variation in yarn width reduced from 15 % to 7 %, in line with that reported in previous studies using untwisted yarns [23, 283].

These results indicate that yarn widths were more consistent, and had a higher peak value at between 2.4 mm - 2.5 mm, when fewer twists were applied. The lower peak value of between 2.2 mm - 2.3 mm observed with 10 t/m is consistent with a more tightly bundled yarn as might be expected, which in turn would result in thicker preform layers. However, the broad distribution

of widths suggests that yarn cross-section geometry was not consistent along a length of yarn or between yarns. Instead, it is likely that the twist was unevenly distributed, with some sections bundled more tightly than others, resulting in some narrower yarn sections and some wider, flatter yarn sections.

The importance of deposited preform thickness in ensuring a satisfactory manufacturing outcome was highlighted during the subsequent infusion of the preform produced in trial E, which was conducted as a vacuum bag infusion on the mandrel. End sections of the preform were cut away to leave an 800 mm length of preform, around which vacuum bagging was wrapped and sealed. Once the vacuum was applied, the preform was found to compact, causing excess length in each of the layers to manifest as wrinkles along the length of the preform. The technician carrying out the infusion carefully adjusted the vacuum and manipulated the preform in order to align the wrinkles at one location around the mandrel circumference prior to infusion, as shown in Figure 6.6. This was done to mitigate the influence of wrinkles on flow front measurements acquired from the opposite side of the mandrel during the infusion.

Both pre- and post-infusion measurements of thickness, made by the infusion operator using calipers and the CT-scan analyst, respectively, gave an average thickness of 5.6 mm across the non-wrinkled section of the laminate. Preform compaction from 6.9 mm to 5.6 mm on a 200 mm diameter mandrel corresponds to an excess length of 8.2 mm in the outer layer; the resultant wrinkle height was measured from the CT scan image presented in Figure 6.7 as 3.4 mm above the laminate surface.

6.1.3 Discussion

Braid angle measurements acquired during this project using the in-process measurement capability were collected in order to characterise preform quality and partially validate assumptions pertaining to preform structure made in corresponding simulation activities. The measurements revealed considerable variation in both the initial braid angle and the length of braid that was deposited before an acceptable, stable braid angle was obtained; a significant potion of the deposited braid (i.e. a complete layer in one case) had to be discarded as a consequence. Although such behaviour was anticipated to some extent[3], the length of the unstable region in some instances was unexpectedly large, as was the inconsistency between layers of the same preform, deposited by the same operator.

These findings illustrate both the importance of, and challenges associated with, establishing the initial conditions for each braid layer, since a significant portion of the braid can be lost if the initial stages of deposition, i.e. braid initiation, cannot be not managed effectively. They also indicate that braid initiation based on manual adjustment of the initial braid angle alone, as performed

[3]It is common to include an initial, sacrificial run-in length in the mandrel design to allow for stabilisation of the braid.

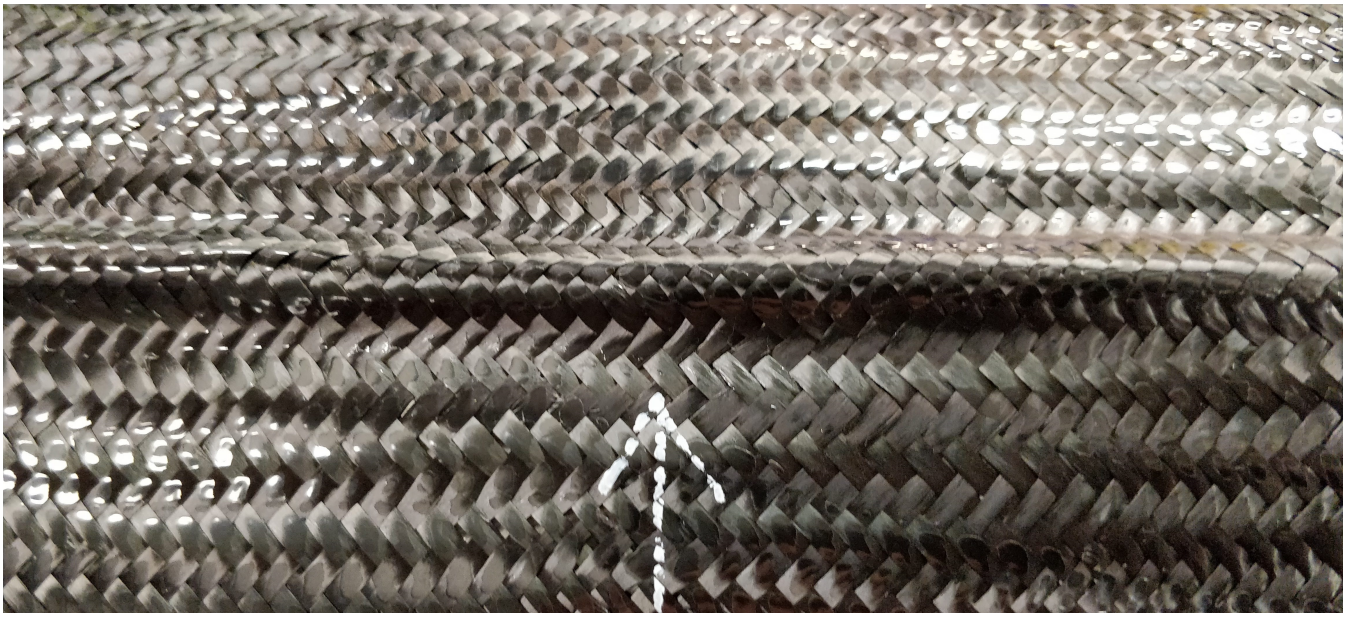

Figure 6.6: Image showing the aligned wrinkle produced during infusion of the trial E preform.

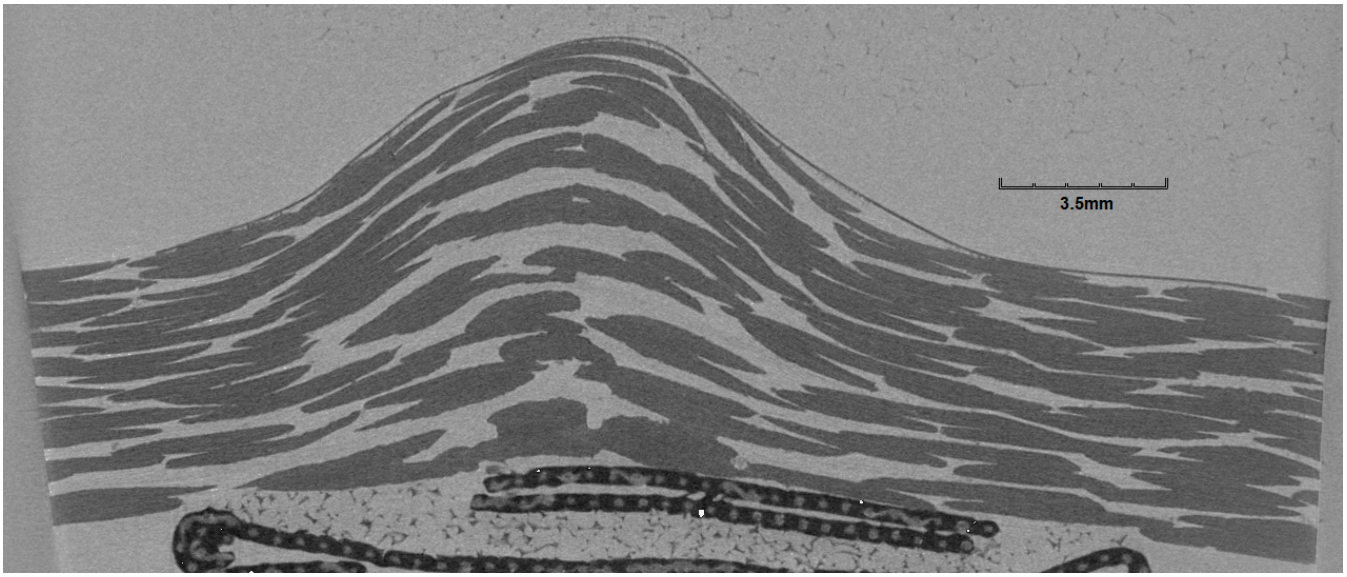

Figure 6.7: CT image of wrinkled section taken from the infused and cured preform from trial E.

during this project, cannot be regarded as a reliable process; some additional level of control is necessary to optimise the initial setup for each deposition operation. It was proposed that the shape of the convergence region, i.e. the shape formed by the interlacing yarns as they travel between the guide ring[4], or the resultant convergence length that is established prior to commencing the braid programme might offer this additional control. However, the target steady-state for these variables is not typically known when over-braiding using a relatively large number of yarns as in this work. This is due to the curvature introduced to yarn paths in the convergence region as a result of frictional interactions between crossing yarns, which, in turn, results in a reduction of the convergence length relative to the idealised scenario where convergence cone angle, and hence convergence length, is directly proportional to braid angle. Section 6.2 presents an exploratory study into the relationship between the shape of the convergence region and braid angle stability, which was undertaken on the basis of this hypothesis. aiming to enable improved control of initial conditions during braid deposition.

It should be noted that this was discernible thanks to the relatively high measurement coverage, i.e. every 20 mm along the length of the preform, enabled by the measurement capability than would otherwise have been performed with manual measurements.

Thickness measurements, again generated using the in-process measurement capability, provided insight into the deposited preform architecture, revealing a suspected sensitivity of preform thickness to yarn twist. For otherwise identical manufacturing trials, a reduction in yarn twist from 10 t/m to 7 t/m was found to correlate to a 10 % reduction in as-deposited preform thickness for a four layer preform. Upon further investigation of corresponding images (acquired primarily for the purpose of braid angle measurement, but labelled and stored to enable re-use), an associated variation in yarn width distributions was identified. Yarn width measurements showed a more uniform deposited yarn width at 7 t/m than at 10 t/m, with a greater mean value, likely resulting in thinner preform layers. Although unproven in this work, it might be expected that the resultant reduction in final preform thickness would have resulted in less severe wrinkle formation under vacuum compaction, prior to infusion, due to the lower excess material length from deposition.

The amount of yarn twist is a variable that is set prior to the braid operation itself, during the spool winding process, when the material is wound from the large spool on which it is delivered onto the spools used by the over-braider. It is typically determined by the process operator, based on experience and guidelines, as well as the behaviour of the yarn material during the winding operation, primarily as a mean to manage the occurrence of fibre damage during processing; it is not determined on the basis of resultant preform quality. However, these results suggest that the amount of twist may prove to be a critical factor in ensuring control of preform thickness and achieving an acceptable outcome for the subsequent infusion process. On this basis, and considering

[4]Or braid ring if a guide ring is not being used.

the material and time costs associated with having to re-wind spools, re-load spools onto the braider, and re-manufacture preforms should the initial twist setting result in an unacceptable manufacturing outcome, it is suggested that greater consideration should be given to optimising this manufacturing variable.

Failure to produce a sufficiently compacted preform from the braiding process means that, either:

- the achievable fibre volume fraction will be low if the preform remains uncompacted during the infusion process, i.e. by using matched solid tooling designed for the as-braided preform thickness;
- excess length will result in the formation of wrinkles during preform compaction to achieve a desired V_{f}, which are unlikely to be acceptable for subsequent production, structural or aesthetic requirements, e.g. preventing tool closure.

Hence the ability to design, setup and operate the braiding process in order to control the level of preform compaction and resultant preform thickness that is achieved during deposition is vital to the success of the design and manufacture workflow. These results suggest that yarn twist, generally applied in order to improve the processability of yarns, may have an appreciable impact on the control of layer and preform thickness and should be investigated in further detail.

6.2 Investigating the relationship between convergence cone geometry and braid structure stability

The interaction of yarns within the convergence region during an axial over-braiding process has been cited in literature as a cause of braid instability and reduction in preform quality. Inter-yarn friction is known to affect the path of yarns from carrier to mandrel, introducing curvature as yarns approach the mandrel [284]. This yarn path curvature causes a shift in fell plane position, shortening the convergence length, H_0, which would otherwise be determined by the target braid angle, θ, and mandrel and guide ring radii, r_m and r_{gr}, respectively, according to Equation 6.1.

$$H_0 = \frac{\sqrt{r_{gr}^2 - r_m^2}}{\tan\theta} \tag{6.1}$$

Ultimately, the deposited braid angle can be affected [18], by as much as 10° on tapered geometries [17]. The specified braid pattern (i.e. number and arrangement of active carriers) and applied yarn tension, as well as wound yarn properties, will determine the number and magnitude of yarn-yarn intersections along the carrier-mandrel yarn path and are therefore expected to influence the magnitude of these friction-induced effects. This phenomenon has been the subject of numerous research activities [20, 284–287], many attempting to incorporate the effects of yarn-yarn friction into process models in order to better predict the position of the fell plane during the process.

For tubular mandrels with a constant cross-section braided under steady state conditions, this phenomenon does not tend to affect the quality of the deposited braid, since the convergence length and position of the fell plane is not critical. It may, however, affect the initial stages of deposition, prior to reaching the steady state. For more complex mandrel geometries, where variations in the ratio of mandrel and carrier rotational speeds may be required to achieve the desired braid structure, the position of the fell plane relative to the mandrel is much more critical to braid quality. This is because dynamic machine speed profiles will need to be aligned with the mandrel location at which yarns are being deposited.

It was proposed that the variability in initial braid angle stability identified in Section 6.1 was, in part, due to instability in the convergence region caused by frictional interactions between yarns. In order to investigate this hypothesis, braiding trials were conducted in which a video camera was positioned perpendicular to the braiding axis, focused on the convergence region. This arrangement enabled video footage of the convergence region captured during the trials to be analysed alongside braid angle measurements from the in-process measurement system.

Initial development of the image analysis routine used to analyse the convergence region video footage was carried out by a year-in-industry undergraduate student from the University of Bristol, Amin Farjadi, whilst on placement at NCC. Subsequent refinements to its function and performance

were performed by the author.

6.2.1 Method

Results from three manufacturing trials are presented and discussed in this section; relevant details of the setup for each are presented in Table 6.1. In the first trial, B.1, two machine operators each produced a three-layer, biaxial preform, braided over a 200 mm OD cylindrical mandrel, using 144 yarns and with a constant target braid angle of 45° for all layers. Results were used to investigate variability in starting conditions between layers and the impact on braid structure stability during the initial stage of deposition.[5]

In the second trial, B.2, a transient, biaxial braid layer was deposited over a three-layer preform produced in B.1, again using 144 yarns. The braid angle transition was achieved via a step change in traverse speed to increase the target angle from 26° to 60°, causing a gradual increase in deposited braid angle over a length of approximately 600 mm. Results from this trial were used to investigate the relationship between convergence region shape and deposited braid angle.[6]

Finally, results are presented from trial F.2, conducted as part of the research discussed in Section 6.1. In this trial, a four layer preform with constant target braid angle of 45° was produced over a mandrel with cylindrical (200 mm OD) and conical (200 mm → 294 mm OD) sections; braid angle was maintained over the conical section by increasing the traverse speed proportionally to the radius increase. Results for the conical section were used to analyse the effect of mandrel radius to guide ring radius ratio on the convergence region. Also, since this trial used 288 yarns, the effect of number of yarns was investigated by comparison of steady-state results from the cylindrical mandrel section with those from B.1.

Side video footage was obtained using a Nikon DSLR camera mounted on a tripod and positioned perpendicular to, and centred on, the front guide ring. Videos were acquired during braid deposition at a frame rate of 25 frames per second. The footage was post-processed using a custom Python script, developed using the OpenCV computer vision [264] and SciKit-learn machine learning [278] libraries, to extract and process individual video frames. After converting images to grayscale, the script enabled the user to crop the image to the area of interest (AOI), i.e. the convergence region on the upper side of the mandrel; this is illustrated in Figure 6.8. Care was taken to align the right-hand edge of the crop window with the centre of the guide ring to facilitate convergence length measurements relative to the window. User selection of the AOI was performed for the first frame of each video clip only, with the same crop window applied to all subsequent frames.

Once cropped, the following sequence of image processing steps was applied to each image in order to extract the upper boundary of the cone formed by yarns in the convergence region (see

[5]Some of the braid angle measurements for operator 1 were previously presented in Section 5.1.1.
[6]Braid angle measurements trial B.2 were previously presented in Section 5.1.2.

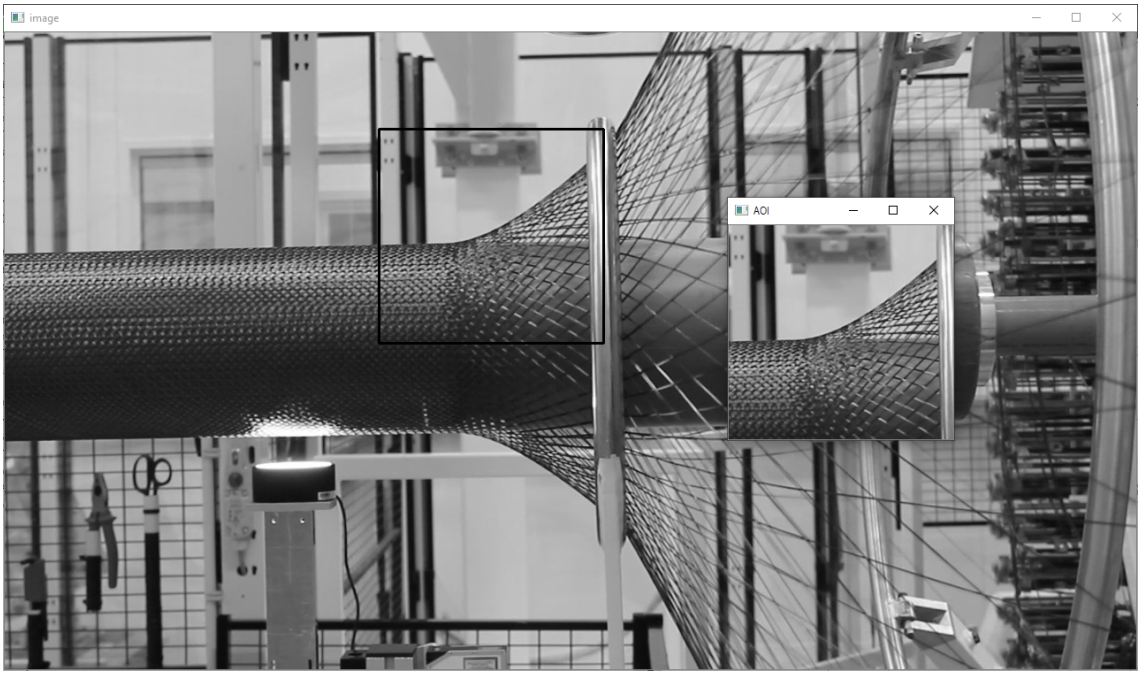

Figure 6.8: Frame from side camera video footage captured during braid deposition, illustrating the area-of-interest (AOI) that was cropped for subsequent convergence region detection.

Figure 6.9 for illustration):

- the cropped image was blurred using a median blur filter (OpenCV *medianBlur*, kernel size = 15) to retain step edge details;
- pixel intensities were inverted to generate a negative of the blurred image;
- a 3 × 3 pixel Scharr filter (OpenCV *Sobel*, ddepth = -1) was applied to the negative image (Y derivative only) to detect edge features with a strong horizontal component;
- a pixel intensity threshold (OpenCV *threshold*), set at the 98$^{\text{th}}$ %ile, was applied to the Scharr-filtered image to remove lower intensity edge features;
- horizontal (left → right) and vertical (bottom → top) pixel scanning routines were applied to determine the co-ordinates of the first edge pixel to be encountered in each row and column;
- outlier filtering was conducted using a hierarchical agglomerative clustering method (SciKit-learn *cluster.AgglomerativeClustering*) to leave only the co-ordinates of pixels coinciding with the boundary of the convergence region.

Finally, the convergence region itself, i.e. the region falling between the guide ring plane and the fell plane, was extracted, depicted in red in Figure 6.10. This was determined iteratively on the basis of gradient between neighbouring pixels, starting from the right-hand edge of the image and stepping left and down the curve. The end of the convergence region, corresponding with the position of the fell point, was determined as the point on the curve at which the gradient became

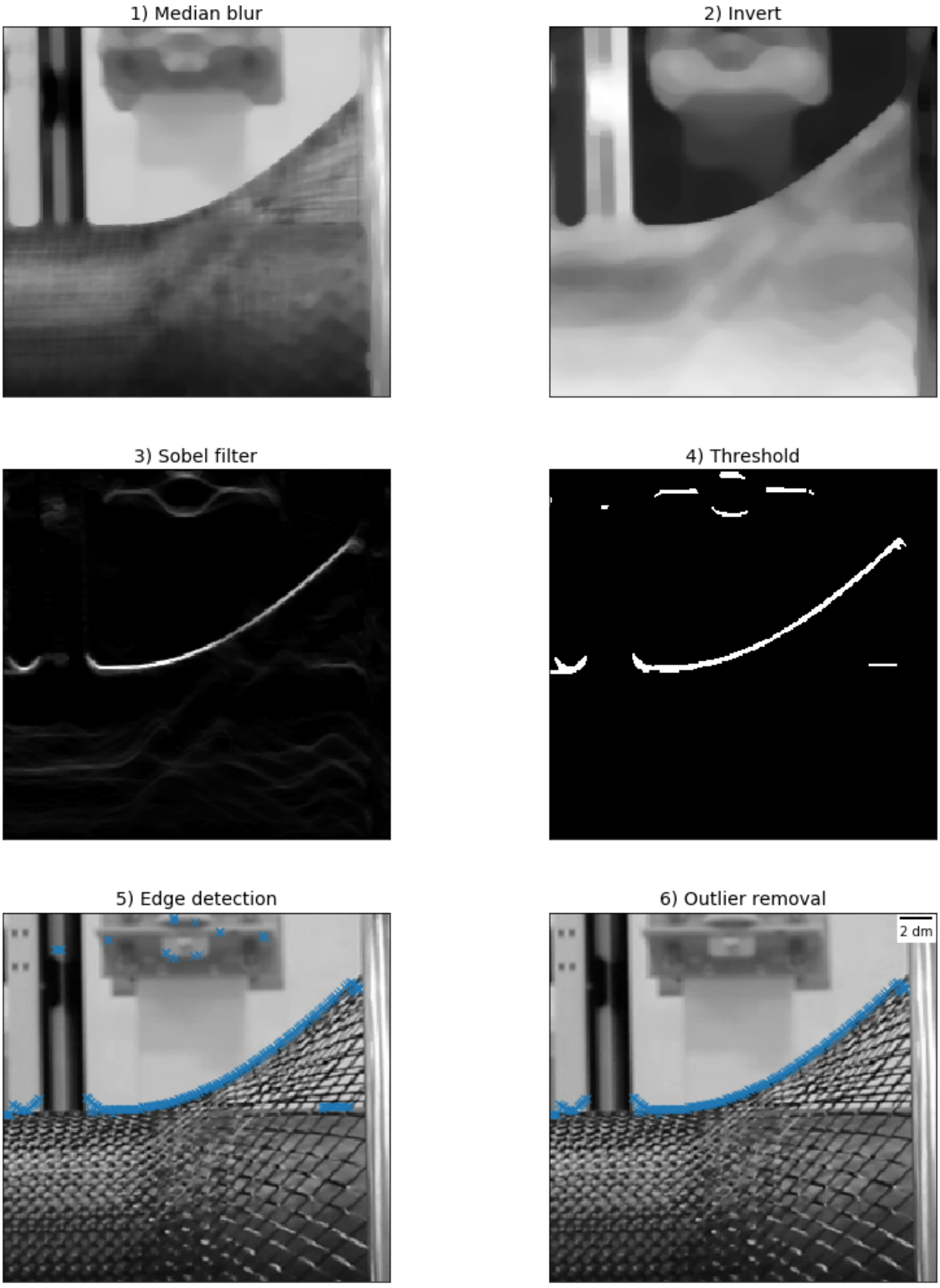

Figure 6.9: Sequence of image processing steps used in the detection of the convergence region.

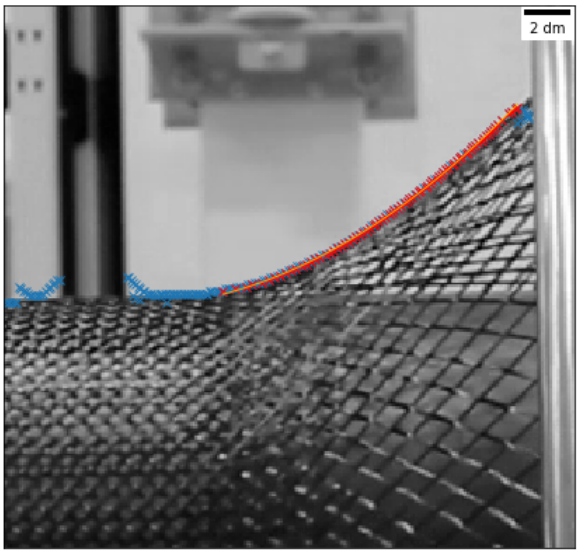

Figure 6.10: Convergence region between guide ring and fell plane, with the fitted 2nd order polynomial shown in red.

less than or equal to 0.1. The convergence length was then estimated from the distance, in pixels, between the fell point X co-ordinate and the right-hand edge of the cropped AOI, divided by the image scale in pixels per mm. A 2nd order polynomial was fitted to the convergence region to describe the shape. This enabled a location-independent approximation of the curvature of the convergence region to be determined from the 2nd derivative of the fitted polynomial. The inverse curvature is presented in the following results. This process was conducted for all frames, giving 25 data points per second of footage. Unless stated otherwise, the results presented have been averaged over 5 frames (i.e. every 0.2 seconds of footage).

Braid angle measurements were acquired during each of the trials using the in-process measurement capability. The sensor assembly was mounted such that the camera was positioned beyond the expected range of fell plane positions, meaning braid angle measurements could not be assumed to correspond with measurements from side camera footage acquired at the same time. Rather, they were expected to correspond to footage acquired some seconds earlier, depending on the offset between measurement system camera and fell plane positions and the mandrel speed. It was, therefore, necessary to align convergence length and curvature measurements with braid angle measurements according to mandrel location in order to draw correlations between the two data sets. This was achieved by fitting a generalised logistic function to convergence length measurements in order to obtain a description of convergence length as a function of time (Figure 6.11). Using this function, the distance between fell plane and measurement system camera position was estimated for each frame, from which the position of the fell plane along the mandrel was estimated. Mandrel

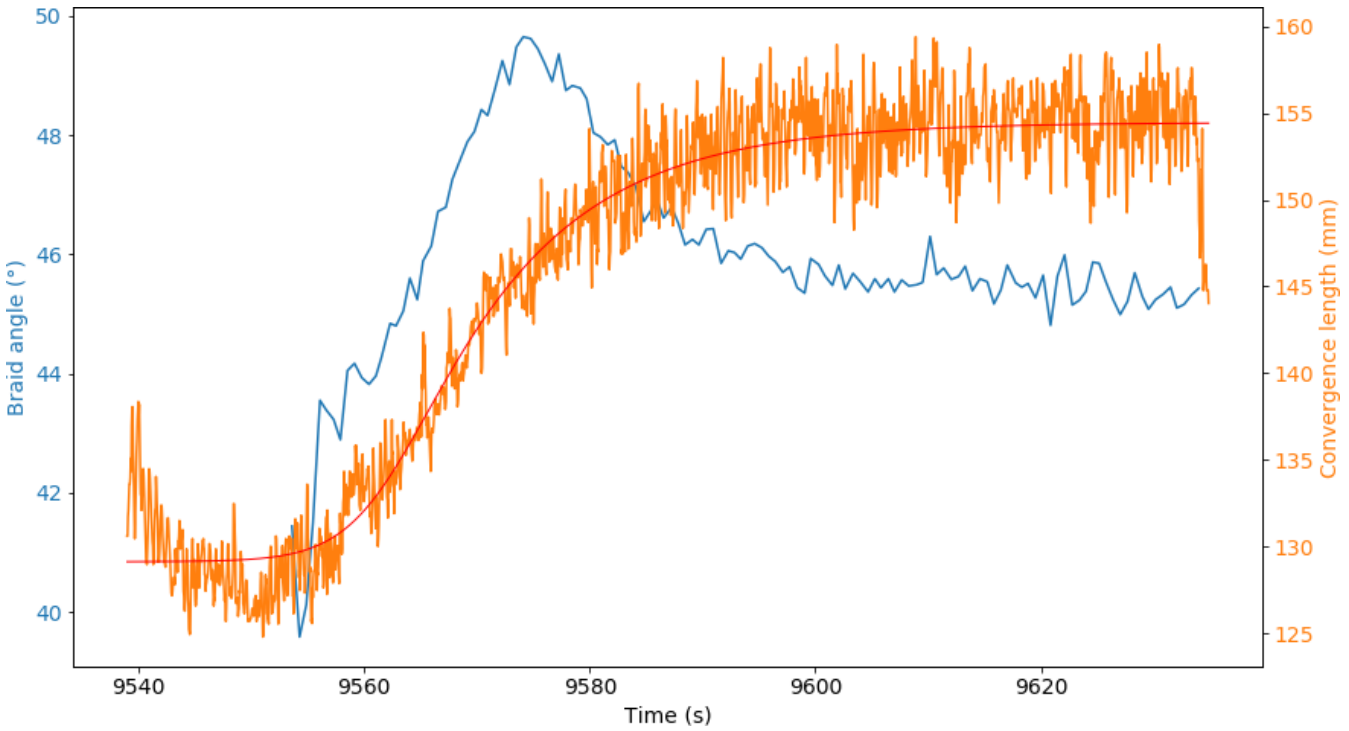

Figure 6.11: Braid angle (blue) and convergence length (orange) measurements for trial B1, operator 1, layer 1; the fitted generalised logistic function used in alignment of the data sets is plotted in red.

position for braid angle images was recorded by the in-process measurement system.

6.2.2 Results

Braid angle measurements for the two, three-layer preforms from trial B.1 are presented in Figure 6.12. The target angle of 45° is shown as a dashed green line, along with thresholds corresponding to ± 1° (orange) and ± 3° (red). *Convergence length* and *inverse cone curvature* measurements for layers braided by operator 1 are presented in Figures 6.13 and 6.14, respectively.

The results show that the initial braid angle (i.e. close to X = 0 mm) achieved for all layers fell below the target angle and outside of the wider ± 3° tolerance threshold. The spread of initial angles was greater than 10°, although all but the final layer were within a range of 7°. This variability illustrates the difficulty in establishing consistent starting conditions for each layer, even for the same operator. For the first layer deposited by each operator, braid angle increased to approximately 50° by around X = 400 mm, 2° outside the ± 3° threshold, despite initial values of ∼ 40°. θ then decreased to within ± 1° of the target angle soon after X = 600 mm. All subsequent layers remained within ± 3° once they reached the lower threshold, whilst the distance to stabilise within ± 1° ranged between X = 200 mm (operator 1, layer 2) and X = 550 mm (operator 2, layer 3).

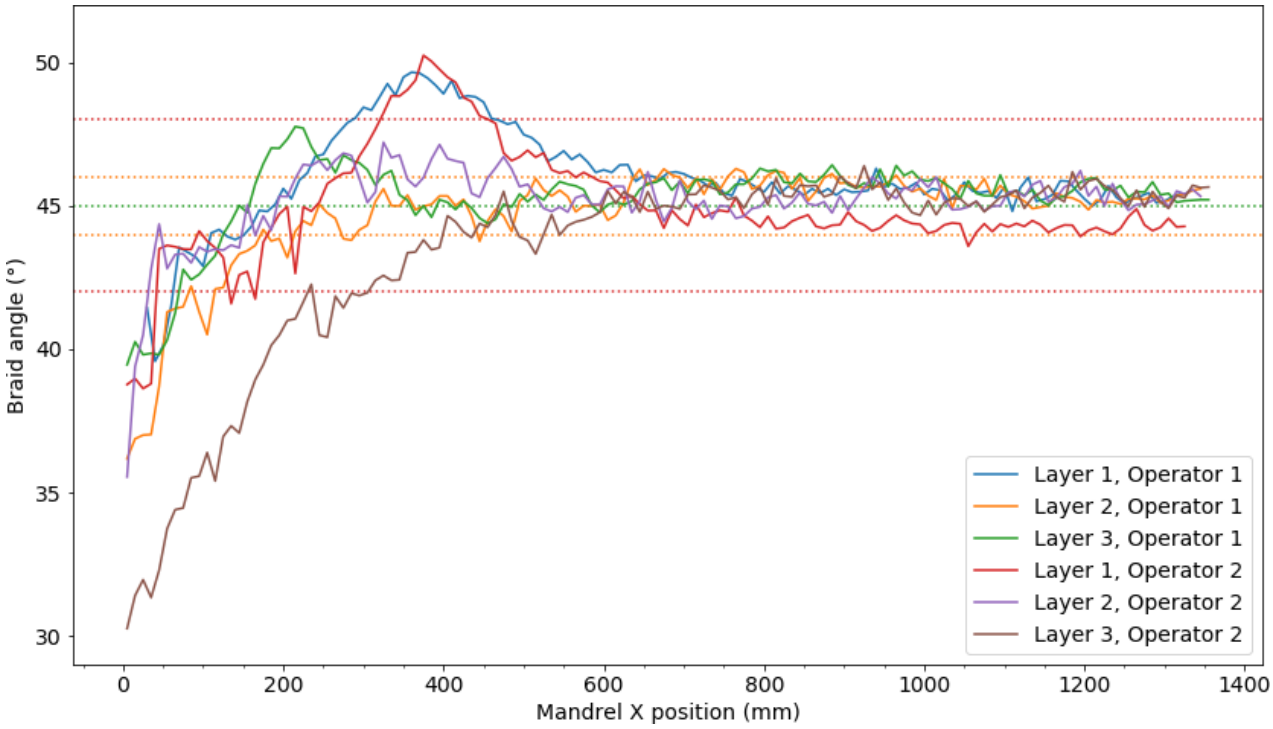

Figure 6.12: Braid angle measurements for the 2 × 3 layer preforms from trial B.1; target angle 45°.

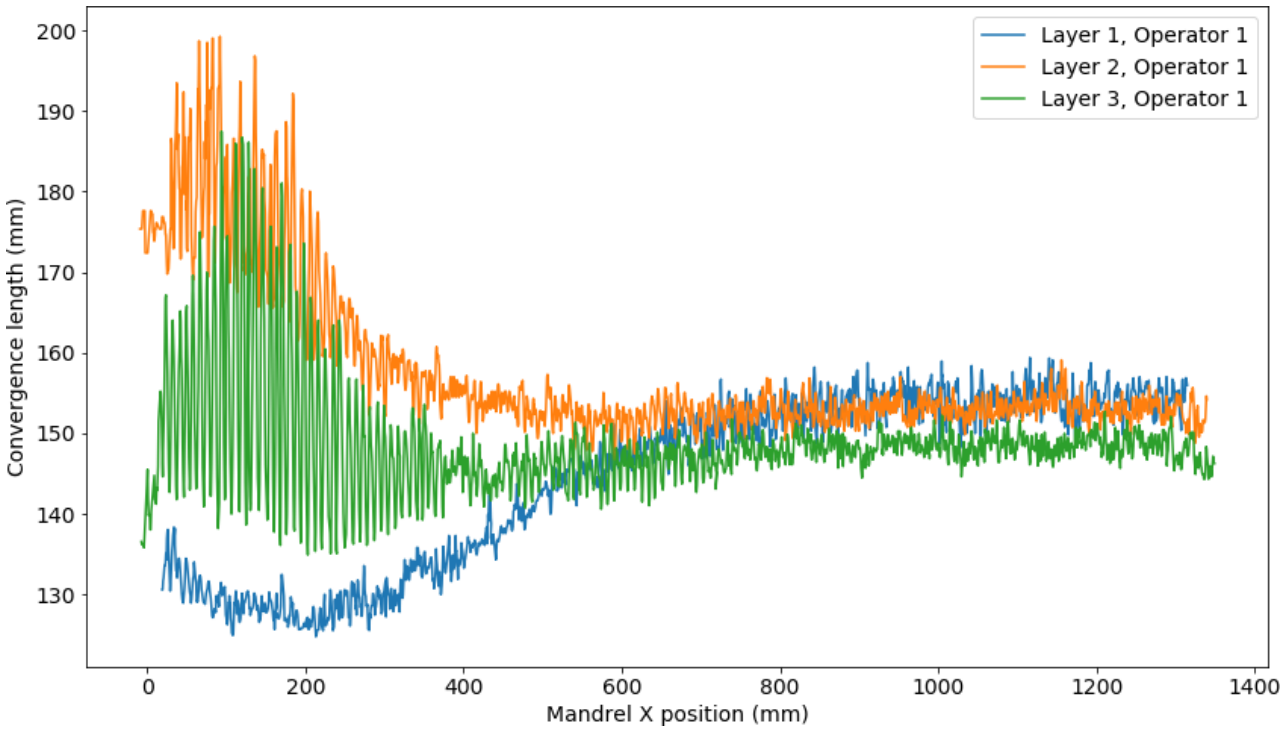

Figure 6.13: *Convergence length* measurements for the 3 layer preform produced by operator 1 (trial B.1); target angle 45°.

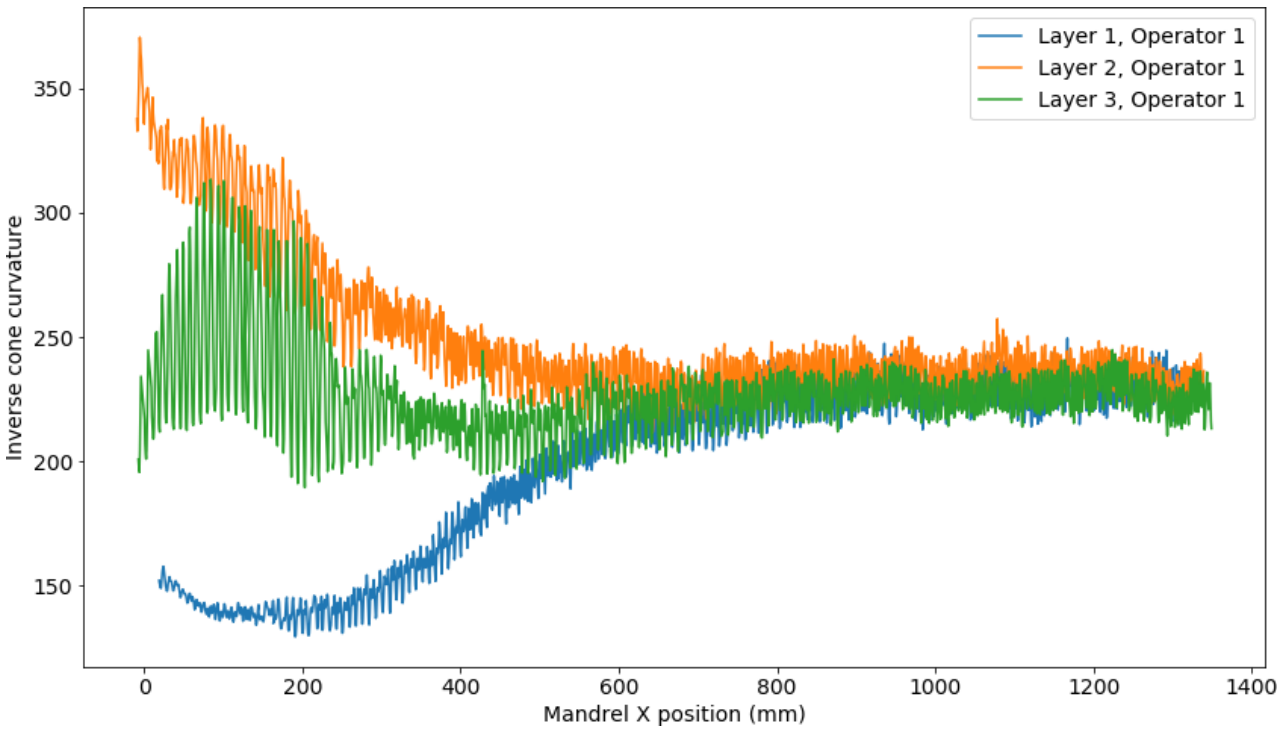

Figure 6.14: *Inverse cone curvature* measurements for the 3 layer preform produced by operator 1 (trial B.1); target angle 45°.

An apparent explanation for the difference in braid angle stability observed for both first layer depositions relative to subsequent layers is the difference in frictional properties of the substrate material. Layer 1 was deposited onto a relatively smooth, plastic mandrel surface, whilst subsequent layers were deposited onto a comparatively rough, undulating surface formed by deposited yarns. Hence, greater mobility of yarns in the layer being deposited relative to the substrate surface would be expected for first layer deposition. This was confirmed by visual inspection of the side camera footage, in which significant oscillatory motion of the depositing layer around the braiding axis was evident up until the convergence plane coincided approximately with X = 400 mm for both first layers. Oscillatory motion for subsequent layers was seen to cease earlier in the deposition, between X = 200 mm and 300 mm.

Convergence length (Figure 6.13) and inverse curvature (Figure 6.14) measurements for operator 1 exhibit similar disparity between layers to that evident in braid angle measurements. For layer 1, both sets of measurements started relatively low, reducing further over the first 200 mm, then gradually increased to a stable value by around X = 800 mm. This trend is consistent with the observation of high layer mobility, with the oscillatory motion causing an effective shortening of the convergence region and corresponding increase in braid angle seen in Figure 6.12.

As observable oscillatory motion reduced, both convergence length and inverse curvature increased, which in turn brought the braid angle back down towards the target value. Measurements

for layers 2 and 3 started at, or increased to, values greater than the eventual stable value, before reducing to the stable value by approximately X = 600 mm (layer 2) and X = 300 mm (layer 3). The large fluctuations evident whilst X < 300 mm, particularly for layer 3, were due to oscillatory motion of the depositing layer around the braiding axis. Unlike layer 1, this motion affected the convergence region due to some asymmetry in the cone geometry as a result of the way yarns were secured to the mandrel shaft prior to layer deposition, producing oscillations in convergence cone shape. These results illustrate the dependence of braid angle stability on the frictional interaction between depositing yarns and the mandrel surface, although the behaviour was exacerbated in this trial by the use of a diamond (1/1) braid pattern and relatively lower cover factor.

Figure 6.15 shows the strong linear correlation identified between convergence length and inverse cone curvature for all three layers deposited by operator 1 in trial B.1 (note that measurements were averaged over 25 frames in this plot). This relationship suggests that these two metrics are equally informative with regards to the convergence region. However, *inverse curvature* measurements in Figure 6.14 were found to converge to a common stable value of around 230 across all three layers, whilst the steady state *convergence length* for layer 3 in Figure 6.13 appeared to be lower than for the other two layers, by approximately 5 mm. This difference is expected to be an artefact of the measurement procedure, being dependent upon the manual positioning of the area of interest selected during analysis. The implication is that the cone curvature measurement was a more reliable metric associated with the convergence region, especially considering that convergence length measurement accuracy is dependent upon spatial calibration of side camera footage whereas the cone curvature is independent of scale.

The relationship between *inverse cone curvature* and deposited braid angle for all three layers deposited by operator 1 in trial B.1 is shown in Figure 6.16; again, *inverse curvature* measurements were averaged over 25 frames. From this plot, it is evident that the only layer which did not significantly exceed the target braid angle of 45° was layer 2, for which the initial braid angle was the lowest of all three layers, and the initial inverse curvature was the highest. Referring back to Figure 6.12, the distance taken to reach a stable braid angle within ± 1° of the target angle was also shortest for layer 2. It is therefore proposed that commencing braid deposition with an inverse cone curvature and convergence length above the steady state values for the target braid angle may enable the distance required to reach a stable deposited braid structure to be minimised. However, it is not possible from these results to determine what the optimal initial values would be.

Access to in-process convergence region measurements, along with prior knowledge of the expected stable values, would hence be advantageous in driving process optimisation and establishing greater control over initial conditions. In turn, this would enable optimisation of mandrel designs through minimisation of run-in sections which allow for braid stabilisation, with the amount of sacrificial yarn material that is deposited over such sections reduced accordingly.

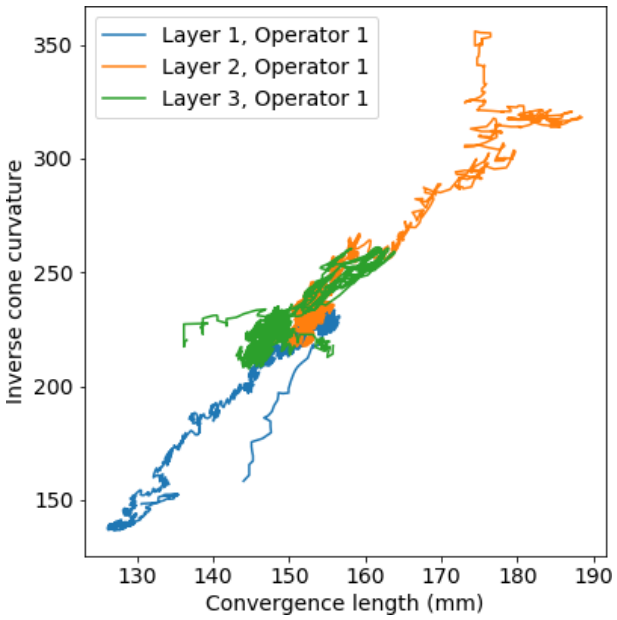

Figure 6.15: Inverse cone curvature vs convergence length measurements acquired during constant braid angle deposition (trial B.1); target angle 45°.

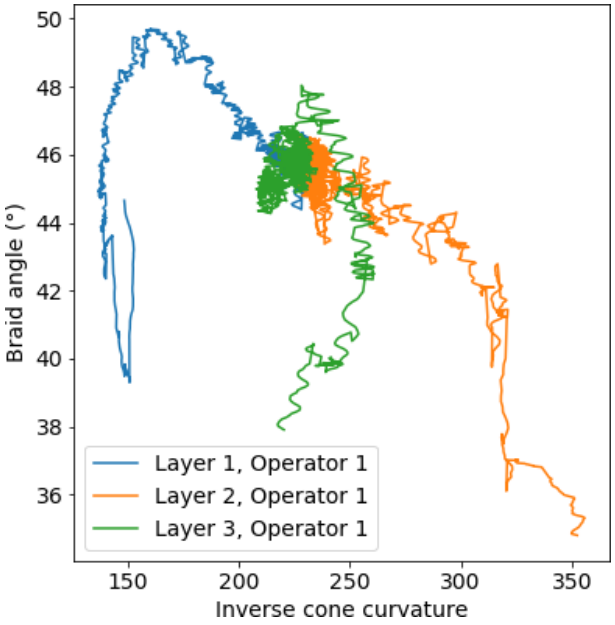

Figure 6.16: Braid angle vs *inverse cone curvature* measurements acquired during constant braid angle deposition (trial B.1); target angle 45°.

Braid angle and corresponding *convergence length* measurements for the transient braid layer produced in trial B.2 are presented in Figure 6.17, in which a further limitation of the convergence length measurement routine is evident. Sparse data points and large fluctuations between approximately X = 500 mm and X = 600 mm were the result of the fell plane coinciding with a black vertical structure in the image background. The effect of this occurrence on convergence region detection can be seen in Figure 6.10, wherein the detected edge is interrupted by the background structure.

Inverse cone curvature measurement, on the other hand, appeared to be less affected by this issue, as evident in Figure 6.18. The relationship with deposited braid angle is presented Figure 6.19; again, *inverse curvature* measurements were averaged over 25 frames in this plot. A strong linear correlation is evident, indicating that the expected cone curvature is predictable for a given target braid angle and process setup; the deviation from linearity between 45° and 50° is believed to be due to braid angle measurements errors discussed in Section 5.1.2. This finding further highlights the potential value to be gained by having cone curvature measurements available during deposition as a real-time indicator of the braid angle being deposited. The current braid angle measurement capability described in Chapter 4 provides a direct measurement once the preform structure has been deposited on the mandrel and hence enables only delayed or retrospective action to be taken. *Inverse cone curvature* would appear to provide a proxy to braid angle at the instant the preform

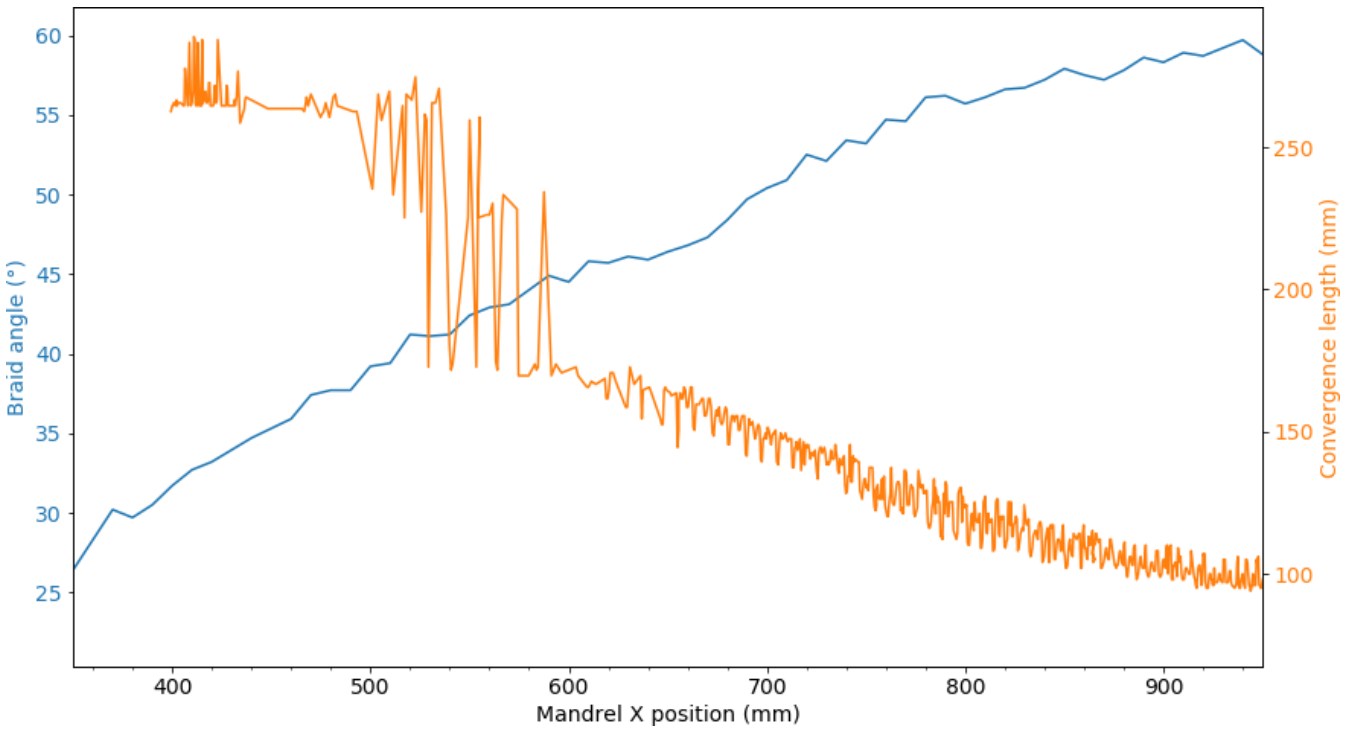

Figure 6.17: Braid angle and corresponding *convergence length* measurements acquired during transient braid angle deposition (trial B.2); target angle increasing from 26° to 60°.

is being formed and hence may enable adjustments or necessary corrections to control variables to be made in near real-time.

The final data set in this investigation was provided by trial F.2, carried out as part of the research project introduced in Section 6.1. In this trial, the preform was produced with a constant target braid angle over a conical mandrel section, making it possible to analyse the effect of varying mandrel diameter on convergence region curvature. Figure 6.20 shows the relationship between the ratio of mandrel radius to guide ring radius and *inverse cone curvature*, which were found to exhibit a strong linear correlation. These results demonstrate that the expected cone curvature for a given mandrel diameter is predictable for a given process setup and target braid angle.

The lowest radius ratio of 0.5, corresponding to the cylindrical mandrel section, is equivalent to that employed in trials B.1 and B.2 discussed previously in this section. However, the *inverse curvature* value at a radius ratio of 0.5 was approximately a quarter of the stable value seen in Figure 6.13. This is due to an increase in the number of yarns used, from 144 to 288, which increased the number of yarn intersections in the convergence region, increasing the curvature of the convergence region and shortening the *convergence length* accordingly. This comparison suggests that there may be an inverse square relationship between number of yarns and *inverse cone curvature* for a given process setup and target braid angle. If this were confirmed, it would further enhance the ability to empirically predict expected cone curvature for a given target angle.

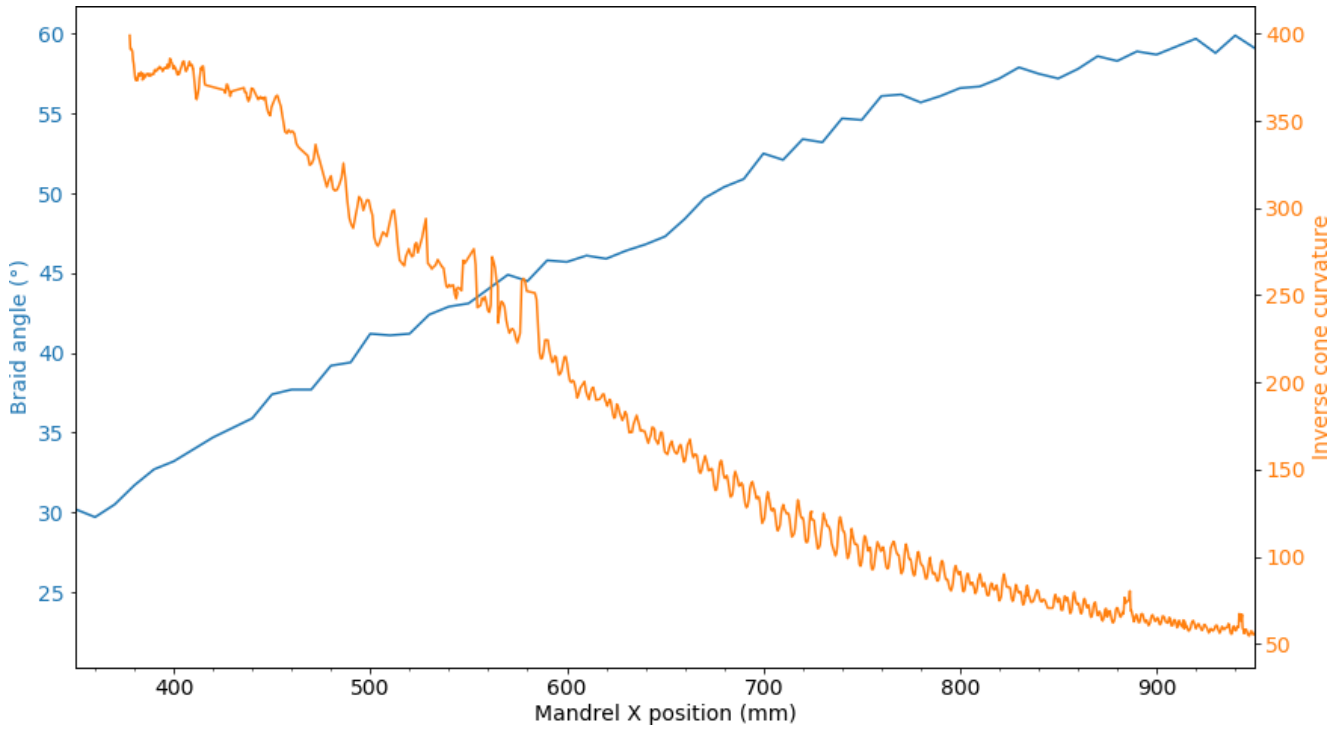

Figure 6.18: Braid angle and corresponding *inverse cone curvature* measurements acquired during transient braid angle deposition (trial B.2); target angle increasing from 26° to 60°.

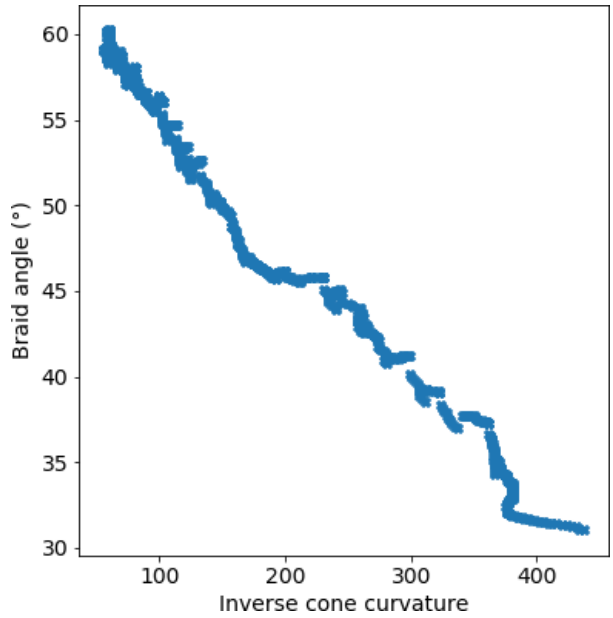

Figure 6.19: Braid angle vs *inverse cone curvature* measurements acquired during transient braid angle deposition (trial B.2); target angle increasing from 26° to 60°.

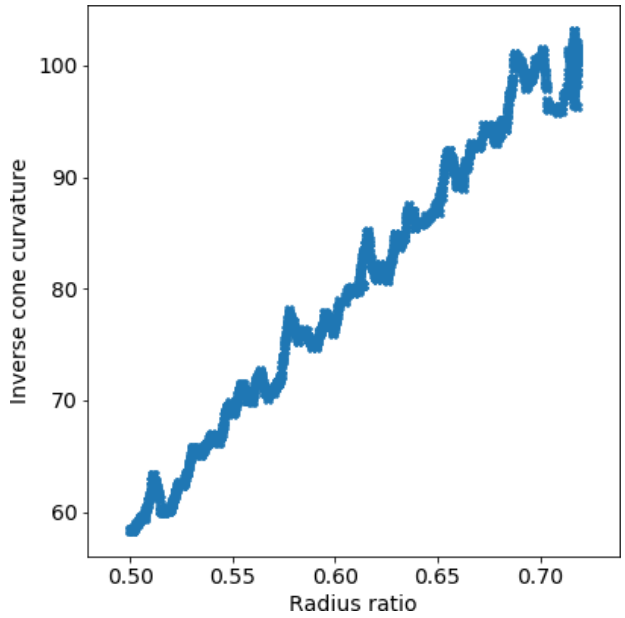

Figure 6.20: *Inverse cone curvature* vs mandrel-to-guide ring radii ratio for measurements acquired during constant braid angle deposition over a conical mandrel (trial F.2).

6.2.3 Discussion

In this section, the effect of frictional forces arising from yarn-yarn interactions in the convergence region, as yarns travel between bobbins and mandrel, on the shape of the convergence region and the stability of the deposited preform structure was investigated. This was achieved through the acquisition and analysis of video footage of the convergence region, captured perpendicular to the braiding axis during braid deposition. Frequent, timestamped, and positionally referenced braid angle measurements acquired by the in-process measurement system introduced in Chapter 4 were key to generating the results presented in this section. They enabled convergence length and cone curvature measurements to be aligned with braid angle measurements corresponding to the position of the fell plane on the mandrel.

A strong linear correlation between convergence length and inverse cone curvature measurements was demonstrated, suggesting that both offer equal insight into the effect of yarn-yarn interactions of the convergence region. However, convergence length measurements were shown to be susceptible to uncertainty in guide ring plane identification, as well as the inherent uncertainty in the fell plane identification. Values are also sensitive to spatial calibration, as well as the presence of features in the image background which interfered with the convergence region detection procedure.

Cone curvature measurements, on the other hand, proved to be a more reliable metric, being independent of image scale and not reliant on end-point plane determination. They were also found to be less sensitive to extraneous background features provided enough of the convergence region was successfully detected. As such, inverse cone curvature measurements were predominantly used for analysis. The following strong linear correlations were identified:

- between inverse cone curvature and deposited braid angle for a constant mandrel cross-section and given process setup;
- between inverse cone curvature and the ratio of mandrel radius to guide ring radius for a constant braid angle and given process setup.

Given the strength of these relationships, it seems plausible that an empirical approach to prediction of steady-state convergence length could be a viable alternative to the simulation methods presented in the scientific literature. Further research would be required to expand and confirm the validity of such an approach, since its proposal is based on a limited set of manufacturing trials. Nonetheless, the relationships identified demonstrate the potential value to be gained by acquiring curvature measurements for the convergence region in-process, as they are likely to enable optimisation of starting conditions for each layer deposition. In addition, they would appear to provide a proxy measurement for braid angle at the instant the preform is being formed and hence may enable any adjustments or necessary corrections to control variables to be made in near real-time.

Chapter 7

General discussion

At its core, this thesis is concerned with the ability to extract maximum benefit from data relating to manufacturing processes by ensuring its re-usability in future research activities. This has been explored through the development of an in-process measurement capability for the over-braiding manufacturing facility at the National Composites Centre. The measurement system that was designed and implemented during the course of the project automates the measurement of two properties of the dry fibre preform product that are commonly used to assess preform quality, namely braid angle and preform thickness. In doing so, the accuracy, repeatability and reliability of these measurements have been improved relative to pre-existing manual methods, whilst simultaneously reducing non-productive time committed to data acquisition for both the process equipment and the operator.

Had the measurement capability been destined for use in a conventional production environment, this discussion would likely have focused on the value, or return on investment, that had been generated as a result of its deployment. For example, the increase in productivity due to reduced inspection time, or the reduction in material waste generated as a result of early detection and remediation of non-conforming products might have been considered. Depending on the scale of production, analysis of the generated measurement data alongside other material and process data may also have enabled some degree of process optimisation or adaptive control to be implemented for the specific production scenario [288].

However, the capability was developed for the benefit of product engineering R&D activities within a sector-agnostic research organisation, where manufacturing capabilities are intended to be flexible and adaptable for use in a wide range of applications. In this context, the value of in-process measurement data is not as readily determined due to the transient nature of project-lead R&D. Since each project will tend to define its own objectives and quality criteria, the data required to achieve these will vary accordingly. Also, the contribution of acquired data sets to the project outcome and any subsequent developments is typically hard to quantify. For these reason,

the justification for development of persistent, standardised measurement capabilities to meet the requirements of a particular project is often not viable due to the cost and timescales associated with implementation; temporary measurement solutions are often employed instead, resulting in a lack of consistency in data acquisition between projects, both in terms of what those data are and how they are acquired.

The breadth of associated contextual information, i.e. metadata, that is captured will also typically depend on the scope of the project, with much of it stored in an unstructured manner, e.g. written project reports and presentations, such that it is not readily accessible from beyond the project. This makes the prospect of conducting research activities based on historical data sets generated across multiple previous projects unfeasible, since it may not be apparent what data are available, where they are stored, under what conditions they were acquired, etc. The time, effort and cost required to collate and prepare a suitable data set for any potential data-centric research activity can therefore be prohibitively large, with no guarantee of a successful outcome.

An inability to conduct such cross-cutting research, focused not on project requirements but rather on process-specific developments, represents a missed opportunity for research organisations. This is especially true with regards to the composite product engineering discipline, which is inherently complex due to the wide range of possible material and process combinations available, and which is all too often reliant on engineering or design experience and precedent. Variability between projects inevitably means that a significant portion of the design and manufacture envelope for a given manufacturing capability may be explored over time, as the number of projects which utilise the capability increases. By enabling consistency in data acquisition and management between projects, one would expect the ability to extract insight from the resulting data sets to also increase.

7.1 Ensuring the informational value of measurement data

The research presented within the preceding chapters was motivated by the intent to maximise the informational, or potential research value of generated data sets. This section discusses the overarching relationships between the topics of those chapters, as summarised in Figure 7.1.

Data availability

Development of the in-process measurement capability presented in Chapter 4 was driven as much by the usability of the system and the contextualisation of measurement data as it was by measurement performance. Existing measurement methods for the key quality metrics of braid angle and preform thickness were reliant on manual data collection and analysis operations, hence the

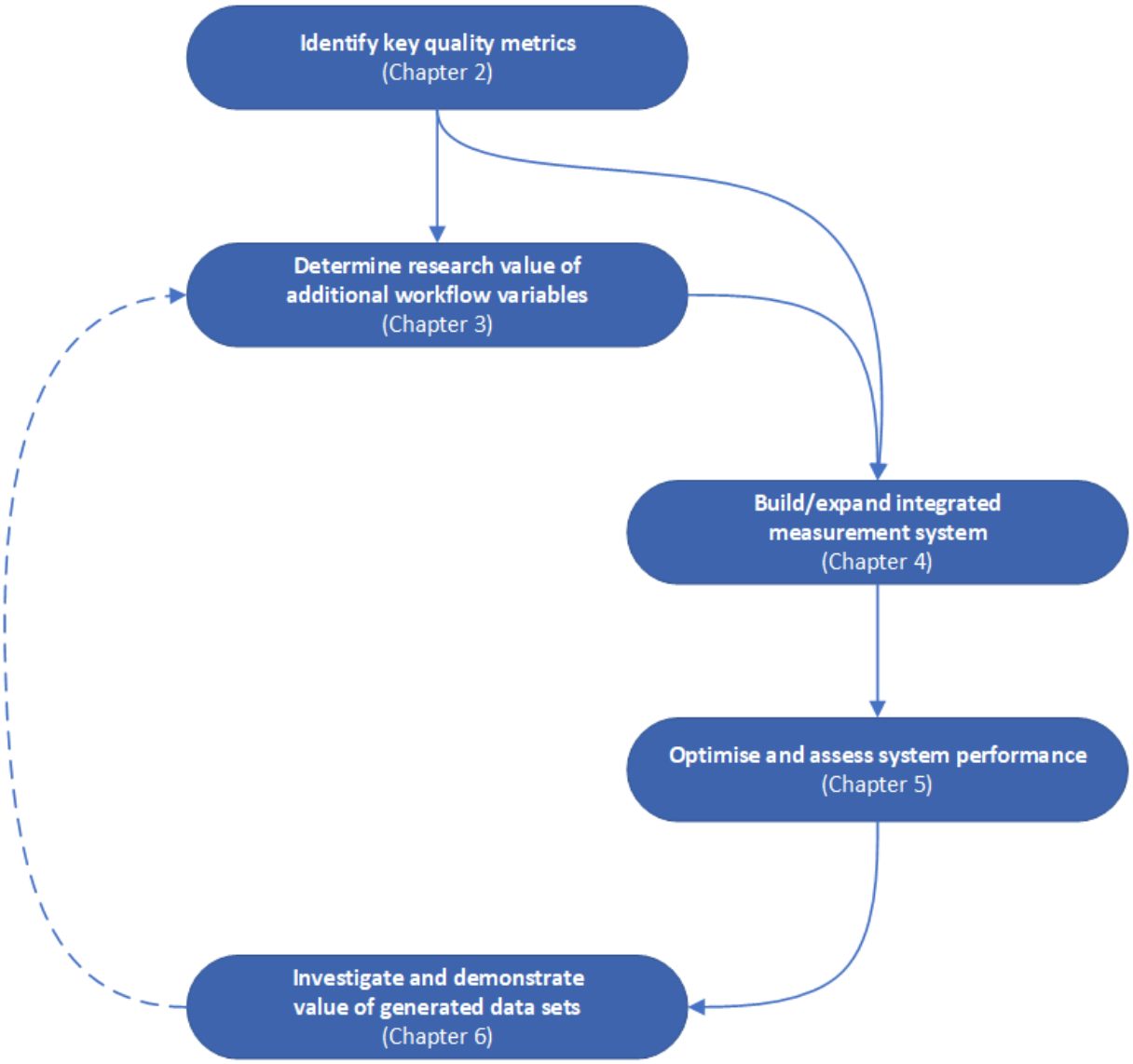

Figure 7.1: Overview of the relationships between the topics covered within the chapters of this thesis.

availability of comparable data over time and between projects could not be guaranteed. Although there are limitations to its operating envelope, the system was designed with a small footprint in order to minimise encroachment on the operators' workspace and, thus, disruption to the manufacturing process itself, whilst also requiring a minimal number of actions to operate it. Hence, it was envisaged to provide a standardised means of data acquisition for the common quality-critical properties of braid angle and preform thickness, being viable for a wide range of over-braiding projects as required for the creation of comprehensive, cross-project manufacturing data sets.

Data quality

The accuracy and reliability of measurement data are undoubtedly important to any engineering activities seeking to make use of them, hence the thorough assessment of measurement performance and uncertainty that is presented in Chapter 5. Here, the consequences of system design choices on resultant measurements were explored alongside those impacts arising from material and process factors. The greatest challenge posed by the braid angle measurement procedure was shown to be the introduction of uncertainty resulting from transformation of the acquired image to account for perspective projection of the imaged surface. This transformation was introduced in lieu of a more sophisticated camera control system to enable positioning of the camera normal to the surface, which would, in turn, require additional programming operations prior to use and increase the opportunities of misuse. The increase in measurement uncertainty, from a maximum of 0.44° to as high as 0.72°, was the price paid to minimise the barrier to system utilisation and thus maximise the opportunities to acquire reliable measurement data. Although greater than the measurement accuracy requirement specified for this system of ± 0.5°, this level of uncertainty is expected to be sufficient for many research projects. Since the source of this increase is the in-process surface gradient measurements used in the transformation, it is anticipated that the impact of this design decision may be reduced during future system developments, through improvement of the gradient measurement method or procedure.

The impact of surface gradient uncertainty on preform thickness measurements was also considered. In this case, however, it was found to be less significant than the uncertainties resulting from the material characteristics and the mechanics of the braiding machinery, both estimated to be in the region of ± 0.4 mm at a confidence interval of 95 %. Braid surface characteristics are expected to generate a distribution of thickness measurements, to a lesser or greater extent depending on the measurement technique, due to the inconsistent structure of both individual yarns and braided textiles. On the other hand, uncertainty arising from oscillation of the mandrel surface during braid deposition was a direct result of the decision to generate measurements relative to a previously acquired baseline scan. Any technique utilising this type of relative measurement would be similarly impaired. It may be questioned, therefore, whether an *in situ*, in process measurement solution of

this nature is appropriate if the underlying machine mechanics cannot be sufficiently well controlled to minimise this source of uncertainty. Nevertheless, under many scenarios, measurements averaged over a length of preform would be expected to mitigate this uncertainty whilst still providing greater coverage than typically attained using manual methods. Thus the measurement data is still expected to yield valuable information.

Data re-usability

Besides such considerations regarding the quality of acquired data, ensuring the usefulness of those data to current and future research activities is equally important for the successful implementation of data-driven product engineering practices. That means ensuring (within reason) that the acquired data have broad relevance to likely future research topics, and that they are recorded along with a wealth of metadata with which to contextualise and query data sets. These factors will strongly influence the ability to gain insight from measurement data sets, ultimately determining their potential future research value.

Being the first generation of in-process measurement capability for the NCC over-braider, the target measurands of braid angle and deposited preform thickness were selected on the basis of their direct relevance to product and process quality. Beyond these more obvious targets, however, the value of other in-process data is not so readily determined, especially when considering the possible range of future research objectives. This challenge was the motivation behind development of the variable dependency assessment method presented in Chapter 3.

The proposed method provides a means by which to evaluate the likely informational value of data relating to dependent and independent variables on the basis of the number and strength of relationships with other engineering workflow variables. Interpretation of the resulting dependency matrix may be somewhat subjective, and is by no means proposed as a definitive 'tool' for in-process measurement down-selection; for instance, it does not assess the accessibility of data, e.g. the disruption that may be caused to the manufacturing process in order to obtain it, which will inevitably warrant additional consideration. Nonetheless, the knowledge-based implementation that was conducted for the over-braiding capability did highlight a number of variables that may be of interest for a subsequent iteration of measurement system development. One of these, namely 'bias yarn path' as described by the geometry of the convergence cone, was investigated further in Chapter 6, utilising braid angle measurements acquired with the measurement capability over a number of manufacturing trials.

The systematic approach to process variable identification and the consideration given to inter-variable dependencies also highlighted a relatively large number of process and material setup variables, determined prior to the manufacturing operation itself, which are influential to the outcome of the process. By nature, these variables remain constant throughout a braiding operation

and therefore constitute metadata for any in-process measurement data. In many research scenarios, the assignment of many of these will be left to the discretion of the process operator, for example the yarn winding parameters or guide ring position, being documented and reported as part of the process description, but not directly associated with measurement and verification data. It was decided that the ability to record these variables in a structured manner within the in-process measurement system, thus creating that association between data and metadata, should be prioritised ahead of any expansion of the system's measurement capabilities. This manual data entry functionality was built into the user interface for the system, and included fields for project, tooling, material and machine programme identifiers to enable links to corresponding data sources to be created. In doing so, the measurement capability was further aligned with a number of the FAIR guiding principles that where introduced in Chapter 1. For instance, enabling the *findability* and *re-usability* of data via the availability of "rich metadata ... with a plurality of accurate and relevant attributes" [principles F2 and R1], and ensuring *interoperability* with the formatting of metadata into "a formal, accessible, shared, and broadly applicable language for knowledge representation", namely XML [principle I1]. Whilst these principles were initially proposed for the scientific research community, they are equally applicable to engineering R&D disciplines seeking to curate and extract value from historic data sets and may yet prove an invaluable tool in the enablement of data-driven practices within such fields. It is advisable, therefore, to consider these, or similar, principles in the development of data acquisition and management systems.

Value proposition

What is lacking from this work is a demonstration of a data-driven engineering activity, using data acquired from the data acquisition capability that has been developed, with which to exemplify the possible benefits of a data-centric approach to product engineering R&D. The principal reason for this was the relatively low utilisation of, and hence slow rate of data set generation for, the chosen manufacturing capability over the time period between the measurement system becoming operational and the conclusion of this work. It could forseeably take a number of years, depending on range and regularity of upcoming research projects, to generate a sufficiently large and varied data set with which to conduct a suitable demonstration. This process may, however, be expedited by the undertaking of manufacturing trials to investigate the sensitivity to, or of, particular process variables; suitable candidate variables might be identified from the variable dependency matrix (Chapter 3). A targeted, systematic investigation of this nature, recorded using the measurement capability, would enhance the diversity of the available data sets for the over-braiding design and manufacture capability and increase the opportunities for data-driven research. In the work presented in Chapter 6, the intention was to illustrate the sorts of insight that might be gained through such systematic investigations from the resultant data sets.

The first example capitalised on unintentional variability in material setup within a project, the occurrence of which was readily identified from the setup parameters recorded using the measurement system interface. Despite the limitations of the thickness measurement procedure (i.e. the relatively large uncertainty in individual measurements), it was possible in this instance to identify a significant difference in mean preform thickness as a result of the applied yarn twist. Analysis of yarn width distributions in the acquired images indicated a corresponding difference in both the mean, and distribution of, widths. This material behaviour and its impact upon the thickness of the preform can have significant implications for the quality of the resulting composite product. Hence these findings have led to a subsequent, ongoing investigation into the relationship between yarn twist and deposited yarn geometry, over a range of mandrel diameters, again utilising the data sets generated with the measurement capability.

Observations from this first example, regarding variability in the initial braid stability of a given preform layer, prompted the second study documented in Chapter 6. Here, the primary objective was to examine the relationship between braid stability, as indicated by braid angle, and the geometry of yarns in the convergence region. The reproducibility of a multi-layered preform by different machine operators was investigated, along with the effects of mandrel:guide ring radii ratio and the deposited braid angle itself. Contextualisation of braid angle measurements acquired by the measurement system enabled alignment of the data with those from an experimental technique for convergence cone geometry measurement, via transformation between the temporal and spatial domains. A strong correlation between braid angle and cone curvature was subsequently identified, which may yet be exploited in the development a closed-loop control system.

In actual fact, data used to investigate the relationship between convergence cone curvature and the ratio of guide ring:mandrel radii in the second example was acquired during the study from the first, and was subsequently re-processed and re-analysed to expand the braid stability investigation.

An additional insight derived from the combined braid angle and convergence cone measurements was the apparent dependence of braid stability on the underlying surface (i.e. the mandrel or a layer of braid), with a greater region of instability during 1^{st} layer depositions, i.e. directly onto the mandrel surface. This would appear to indicate a dependency of convergence region geometry on yarn-mandrel/substrate frictional interaction (grouped under 'bias yarn path' and 'yarn friction' variable groups, respectively, in Chapter 3).

Although limited in scope, the insights gained in these examples, into material and process behaviours and interactions, show how research and development activities can benefit from efforts to ensure the availability and re-usability of contextualised measurement data.

7.2 Enabling data-driven practices within an R&D organisation

Presented herein is an exploration of one piece of the puzzle that is required in order to realise the potential of data-driven R&D within composite product engineering. It represents a pragmatic approach by which to increase the availability of consistent, contextualised data sets pertaining to the output quality of a manufacturing capability within a project-led research environment that is not without its challenges and risks. Firstly, it is preformed in the absence of a cohesive infrastructure for the management of disparate engineering data sets. It also requires an appreciation of the host manufacturing process, its associated operations and constraints during the design and implementation of a measurement system solution to ensure that the resulting capability is suitable for adoption as part of standard operating procedures. Some foresight of likely research topics and challenges along the engineering workflow, i.e. design, manufacture, inspection, testing, is necessary in order to maximise the breadth of useful and usable metadata collected alongside measurement data. The limitations of constituent measurement capabilities must be acknowledged in order to maintain integrity of data sets that are generated; if measurement data not relevant to a project is collected without due consideration of the validity and/or accuracy of those measurements, the integrity of the corresponding data sets may be compromised, to the detriment of future activities seeking to make use of them.

Regardless of the success of measurement system implementation, the benefit that can be realised from the resulting manufacturing data sets alone is limited. Greater opportunities lie in the ability to maintain and act upon links to additional data sources, such as material and preform characterisation data, data acquired during the subsequent impregnation and product inspection processes, and outputs from the preceding design and process simulation activities. However, management of the links between these various data sources can be unreliable within a research organisation where engineering capabilities determine data storage and management practices to suit their immediate requirements, with limited oversight and alignment between capabilities. The case for an organisation-wide data management infrastructure that supports the varied and flexible requirements of evolving engineering research capabilities is not an easy one to make. Firstly, it requires the vision to perceive what the potential benefits could be and convey these effectively to the rest of the organisation and stakeholders. Secondly, it requires significant investment to either procure and implement a supported, off-the-shelf solution, many of which will be better suited to commercial engineering organisations, or to develop and maintain a bespoke infrastructure in-house.

An additional challenge relevant to RTOs such as NCC, who work with a range of companies and sectors, is ensuring the appropriate protection of customer's intellectual property. The fundamental principle discussed throughout this work is the exploitation of comprehensive, cross-project data

sets for the benefit of research and development activities, but there will inevitably be limits to what customers will be willing to share with the wider research community, some of whom may be direct competitors. Therefore, it will also be necessary to develop and implement appropriate policies and procedures that would enable, for instance, advances made through data set exploration to be publicised and shared, maintaining traceability to the founding data sets whilst restricting access to the specific data and metadata as required. This in turn will require a capable data management infrastructure, as well as trust in those infrastructure and procedures by stakeholders and customers.

The result is a "chicken and egg" scenario. To fully enable and exploit the opportunities presented by data-driven tools, techniques and practices within an engineering R&D organisation requires an appropriate infrastructure with supporting policies and procedures to allow for effective, efficient management of varied data sets. Establishing such an infrastructure requires a significant level of investment, which may otherwise be dedicated to the engineering capabilities themselves and is therefore difficult to justify without some tangible benefits. For this reason, it would seem shrewd to generate some choice, demonstrative data sets with which these benefits may begin to be explored, in a manner such that they are suitable for, and will be enhanced by, integration with additional data sources at such time as an overarching management infrastructure becomes available. The contribution made by this work towards the enablement of data-driven R&D within a resource-constrained environment is a demonstration of the generation of such data sets in a targeted fashion, based on assessment of the expected value of data to future activities, and consideration of the consistency and contextualisation of data.

Chapter 8

Conclusions and recommendations for future work

Opportunities to exploit data-driven tools and techniques for the advancement of research and development activites within industrial sectors such as FRP composite product engineering are often hampered by the inability of research organisations to generate and utilise the prerequisite data sets. Although the varied nature of R&D presents opportunities to explore the design and manufacture envelope of a given manufacturing capability, inconsistency and poor accessibility of data between projects typically limit the value of those data to any such activities. The approach outlined in this thesis sought to partially address this predicament through the methodical development of an in-process measurement capability for a manufacturing process, with which to enable the acquisition of consistent, reliable and re-usable data sets. The production of FRP components via over-braiding and subsequent LCM processes was chosen as the subject of this work.

In order to achieve the stated aim, it was necessary to identify measurands within the manufacturing workflow that would be relevant and informative to a broad range of product engineering projects, and that could be practically and unobtrusively measured *in situ* during the chosen process. Factors contributing to five themes that are typically used to assess the manufacturing quality of FRP components were reviewed, along with the availability of technologies with which quantify corresponding variables. The greatest opportunities to generate broad, useful, quality-oriented data sets were deemed to be presented by integration of measurement capability into the over-braiding process. Measurements accessible during this preforming process have direct relevance to two of the five quality themes considered, namely fibre content and orientation, whilst indirectly contributing to a further two, void content and stress-induced defect development. Based on the availability and applicability of measurement solutions, braid angle and preform thickness were identified as the principal measurands for an in-process measurement capability that was developed for the 2D axial over-braiding facility at the National Composites Centre.

In order to inform the design of the measurement capability around these chosen quality metrics, a method was developed with which to evaluate the potential research value of data relating to other over-braiding design and manufacture workflow variables, either as contextual or complementary information to the principal measurands. The method is based around assessment of the level of understanding and expected sensitivity of relationships between pairs of workflow variables, i.e. inter-variable dependencies. It is suitable for use with novel and established processes alike, with assessment conducted using available evidence and experience. The output, in the form of a matrix, was designed such that it could be iteratively updated and thus maintained as a live resource to support a given manufacturing capability.

A knowledge-based implementation of this method was conducted for the over-braiding capability at NCC, in which inter-variable dependency ratings were aggregated from a panel of three subject-matter experts to populate a variable dependency matrix. This highlighted a considerable number of process parameters determined during process setup that are expected to impact upon the quality of the manufactured component, but for which there was no suitable data collection mechanism. The recording of these parameters to ensure availability of this contextual information alongside any measurement data was prioritised accordingly, ahead of any other dependent variables that might be measured in-process. Observations made during this initial method demonstration regarding the consistency and reliability of the output were documented, along with recommendations to address these in any future development.

An in-process measurement capability for the 2D axial over-braiding facility at NCC was subsequently developed and implemented, which automates the data acquisition for, and measurement of, braid angle and preform thickness during braid deposition. The measurement system was designed for use with axisymmetric mandrels, and for production of single- or multi-layer, bi- or triaxial preforms. Braid angle measurements are based on 2D Fourier transform analysis of high resolution images, whilst preform thickness measurements rely on laser profilometry of the preform surface. Measurements are triggered at defined intervals along the braiding axis, and positionally referenced against a chosen datum feature. The facility to record information about workflow variables (i.e. material and process setup) is provided via the software user interface to enable contextualisation of measurement data as required for data-driven research. Requirements for system operation and obstruction of the braiding process itself were minimised through design considerations, in order to maximise usability. This includes the use of transformations to account misalignment between mandrel surface and measurement sensor assembly due to mandrel surface gradients.

Regarding braid angle measurements:

- Application of a median blur filter to images prior to Fourier analysis was shown to mitigate the effect of individual fibre orientations on measurement output, as required in the event that twist is applied to yarns during spool winding.

- Use of a polarising filter in the camera assembly and an edge intensity threshold limit in the analysis routine were shown to reduce the impact of yarn surface reflections on the measurement procedure, thus enabling reliable measurements under non-optimal lighting conditions.
- Measurement uncertainty in the absence of any mandrel surface gradient was determined to fall in the range of 0.22° - 0.44° at the 95 % confidence interval, meeting the design requirement providing measurement to ± 0.5°; however, uncertainty increased significantly to as much as 0.72° when surface gradient was present.

Regarding preform thickness measurements:

- A 2-stage polynomial fitting procedure was developed to estimate the outermost preform surface from an curved, undulating, noisy surface profile; it was optimised to minimise both measurement error and uncertainty in subsequent preform thickness measurements, on the basis of simulated surface profiles.
- Despite the challenging optical properties of structured dry fibre preform surfaces, the measurement procedure was ultimately limited by instability in the mandrel traverse mechanism and hence uncertainty in the mandrel surface location for a given measurement.
- Uncertainty in any single measurement was determined to be as great as 0.55 mm at the 95 % confidence interval; averaging over multiple adjacent measurements is therefore necessary to reduce uncertainty to an acceptable level, i.e. ± 0.1 mm as per system requirements.

Corrections to account for the effects of mandrel surface gradient relative to sensor orientations on braid angle and preform thickness measurements were shown to contribute to measurement uncertainty as a result of uncertainty in in-process surface gradient measurements. This limitation should be addressed as a priority in future system developments as improvements should yield significant reductions in overall measurement uncertainty. Validation of system performance over a greater range of yarn materials and mandrel designs should also be prioritised to further increase confidence in the acquired measurement data.

Over the duration of this project, it was not possible to generate data sets sufficient for the deployment of data-driven research tools and techniques. Instead, insights generated during two individual over-braiding research activities owing to the in-process measurement capability were presented, as a means to illustrate the added value that may be realised through the availability and use of an integrated data acquisition capability. For instance, the high spatial frequency of braid angle measurements facilitated by the measurement system provided visibility of trends in braid instability at the start of layer deposition, which include: deposition of a significant length of braid prior to reaching an acceptable stable state (typically in the range 200 mm - 600 mm of

wasted material per layer); variations in initial braid instability depending on substrate surface (i.e. mandrel or previous braided layer), with greater preform mobility evident for first layer depositions onto smooth plastics mandrels; a greater region of braid instability for reverse braided layers, likely to be due to the difficulty in establishing initial conditions for the deposition due to operator access constraints.

A discrepancy in multi-layer preform thicknesses resulting from nominally identical braiding operations was traced to a difference in applied yarn twist, thanks to the contextual information that was recorded alongside the measurement data. This was subsequently supported by analysis of yarn width distributions for the preforms, using high resolution images acquired for braid angle measurements, in which a difference in both the mean and dispersion of widths was identified.

A strong correlation between braid angle and convergence cone curvature was identified from analysis of automated braid angle measurements alongside video footage of the convergence region. Alignment of the data sets required temporal to spatial transformation of the video footage, which was enabled by the timestamped and positionally-referenced braid angle measurements. Measurement of the convergence region, specifically a measure of inverse convergence cone curvature, was demonstrated as a robust proxy for braid angle that can be made at the point of braid deposition. Once automated, such a measurement could enable the implementation of an adaptive control mechanism based on braid angle optimisation due to the minimal response time that could be achieved.

This body of work was focused on improving the availability of data for a single manufacturing capability within a research organisation, from which the potential return-on-investment of data-driven research activities might begin to be explored. In isolation, however, this will not be sufficient to fully realise and evaluate the benefits of such practices. Further opportunities to generate exemplar manufacturing data sets should be identified and acted upon, in order to provide a range of test cases; the approach documented in this thesis would help to achieve this. Opportunities to integrate existing data management systems and data sources should be identified to enable links between them to be established and maintained that maximise the potential research value of existing data sets. Likewise, the selection and/or development of future data acquisition and management systems should ensure interoperability with existing systems and data sources. Appropriate policies and procedures should be developed that would enable advances made through data set exploration to be publicised and shared, maintaining traceability whilst also controlling access to the original data and metadata as required to protect the intellectual property of individual projects and customers. By acting upon these recommendations, a research organisation should be well positioned to generate, maintain and exploit comprehensive, consistent data sets pertaining to its core research capabilities.

Bibliography

[1] M. D. Wilkinson, M. Dumontier, I. J. Aalbersberg, G. Appleton, M. Axton, A. Baak, N. Blomberg, J.-W. Boiten, L. B. da Silva Santos, P. E. Bourne, J. Bouwman, A. J. Brookes, T. Clark, M. Crosas, I. Dillo, O. Dumon, S. Edmunds, C. T. Evelo, R. Finkers, A. Gonzalez-Beltran, A. J. Gray, P. Groth, C. Goble, J. S. Grethe, J. Heringa, P. A. 't Hoen, R. Hooft, T. Kuhn, R. Kok, J. Kok, S. J. Lusher, M. E. Martone, A. Mons, A. L. Packer, B. Persson, P. Rocca-Serra, M. Roos, R. van Schaik, S.-A. Sansone, E. Schultes, T. Sengstag, T. Slater, G. Strawn, M. A. Swertz, M. Thompson, J. van der Lei, E. van Mulligen, J. Velterop, A. Waagmeester, P. Wittenburg, K. Wolstencroft, J. Zhao, and B. Mons. The FAIR Guiding Principles for scientific data management and stewardship. *Scientific Data*, 3(1):160018, December 2016. doi: 10.1038/sdata.2016.18.

[2] GO FAIR initiative: Make your data & services FAIR, `https://www.go-fair.org/` (Accessed: March 28, 2021).

[3] FAIRsFAIR, `https://www.fairsfair.eu/` (Accessed: March 28, 2021).

[4] FAIR for Research Software (FAIR4RS) WG, April 2020, `https://www.rd-alliance.org/groups/fair-research-software-fair4rs-wg` (Accessed: March 28, 2021).

[5] How to make your data FAIR, `https://www.openaire.eu/how-to-make-your-data-fair` (Accessed: March 28, 2021).

[6] FAIR Implementation, January 2020, `https://www.pistoiaalliance.org/projects/current-projects/fair-implementation/` (Accessed: March 28, 2021).

[7] European Commission. Directorate General for Research and Innovation. Horizon 2020 projects working on the 2019 coronavirus disease (COVID-19), the severe acute respiratory syndrome coronavirus 2 (SARS-CoV-2), and related topics: Guidelines for open access to publications, data and other research outputs, April 2020, `https://ec.europa.eu/research/participants/data/ref/h2020/other/hi/oa-pilot/h2020-guidelines-oa-covid-19_en.pdf` (Accessed: March 28, 2021).

[8] Open letter: Support data sharing for COVID-19, `https://www.covid19dataportal.org/support-data-sharing-covid19` (Accessed: March 20, 2021).

[9] F. Neveu, B. Castanié, and P. Olivier. The GAP methodology: A new way to design composite structures. *Materials & Design*, 172:107755, June 2019. doi: 10.1016/j.matdes.2019.107755.

[10] J. P. Carey, editor. *Handbook of Advances in Braided Composite Materials: Theory, Production, Testing and Applications*. Number 72 in Woodhead Publishing Series in Composites Science and Engineering. Woodhead Publishing, 2017. ISBN 978-0-08-100369-5.

[11] G. W. Melenka and J. P. Carey. Braid CAM: Braided composite analytical model. *SoftwareX*, 7:23–27, January 2018. doi: 10.1016/j.softx.2017.12.004.

[12] G. W. Melenka, A. J. Hunt, J. H. van Ravenhorst, R. Akkerman, C. M. Pastore, F. K. Ko, M. Munro, and J. P. Carey. 3 - Manufacturing processes for braided composite materials. In J. P. Carey, editor, *Handbook of Advances in Braided Composite Materials*, pages 47–153. Woodhead Publishing, January 2017. ISBN 978-0-08-100369-5. doi: 10.1016/B978-0-08-100369-5.00003-9.

[13] F. K. Ko. Engineered materials handbook. Vol. 1, Composites. In *Engineered Materials Handbook. Vol. 1, Composites*, volume 1, pages 512–28. ASM International, 1987.

[14] W. Michaeli, U. Rosenbaum, and M. Jehrke. Processing strategy for braiding of complex-shaped parts based on a mathematical process description. *Composites Manufacturing*, 1(4): 243–251, December 1990. doi: 10.1016/0956-7143(90)90047-Z.

[15] G. w. Du and P. Popper. Analysis of a Circular Braiding Process for Complex Shapes. *The Journal of The Textile Institute*, 85(3):316–337, January 1994. doi: 10.1080/00405009408631277.

[16] J. Kessels and R. Akkerman. Prediction of the yarn trajectories on complex braided preforms. *Composites Part A: Applied Science and Manufacturing*, 33(8):1073–1081, August 2002. doi: 10.1016/S1359-835X(02)00075-1.

[17] J. van Ravenhorst and R. Akkerman. Circular braiding take-up speed generation using inverse kinematics. *Composites Part A: Applied Science and Manufacturing*, 64:147–158, September 2014. doi: 10.1016/j.compositesa.2014.04.020.

[18] P. Monnot, J. Lévesque, and L. Laberge Lebel. Automated braiding of a complex aircraft fuselage frame using a non-circular braiding model. *Composites Part A: Applied Science and Manufacturing*, 102:48–63, November 2017. doi: 10.1016/j.compositesa.2017.07.011.

[19] T. Hans, J. Cichosz, M. Brand, and R. Hinterhölzl. Finite element simulation of the braiding process for arbitrary mandrel shapes. *Composites Part A: Applied Science and Manufacturing*, 77:124–132, October 2015. doi: 10.1016/j.compositesa.2015.06.003.

[20] A. Pickett, A. Erber, T. von Reden, and K. Drechsler. Comparison of analytical and finite element simulation of 2D braiding. *Plastics, Rubber and Composites*, 38(9-10):387–395, December 2009. doi: 10.1179/146580109X12540995045769.

[21] A. K. Pickett, J. Sirtautas, and A. Erber. Braiding Simulation and Prediction of Mechanical Properties. *Applied Composite Materials*, 16(6):345–364, December 2009. doi: 10.1007/s10443-009-9102-x.

[22] X. Sun, L. F. Kawashita, T. Wollmann, S. Spitzer, A. Langkamp, and M. Gude. Experimental and numerical studies on the braiding of carbon fibres over structured end-fittings for the design and manufacture of high performance hybrid shafts. *Production Engineering*, 12(2):215–228, April 2018. doi: 10.1007/s11740-018-0824-1.

[23] R. Czichos, O. Bareiro, A. K. Pickett, P. Middendorf, and T. Gries. Experimental and numerical studies of process variabilities in biaxial carbon fiber braids. *International Journal of Material Forming*, January 2020. doi: 10.1007/s12289-020-01541-4.

[24] J. P. Carey. 1 - Introduction to braided composites. In J. P. Carey, editor, *Handbook of Advances in Braided Composite Materials*, pages 1–21. Woodhead Publishing, January 2017. ISBN 978-0-08-100369-5. doi: 10.1016/B978-0-08-100369-5.00001-5.

[25] R. M. Christensen. *Mechanics of Composite Materials*. Wiley, New York, 1979. ISBN 978-0-471-05167-1.

[26] T. Chou and A. Kelly. Mechanical Properties of Composites. *Annual Review of Materials Science*, 10(1):229–259, August 1980. doi: 10.1146/annurev.ms.10.080180.001305.

[27] L. V. Smith and S. R. Swanson. Strength design with 2-D triaxial braid textile composites. *Composites Science and Technology*, 56(3):359–365, January 1996. doi: 10.1016/0266-3538(95)00113-1.

[28] M. J. Fedro and K. Willden. Characterization and Manufacture of Braided Composites for Large Commercial Aircraft Structures. In *Second NASA Advanced Composites Technology Conference*, NASA CP 3154, June 1992.

[29] L. C. Bank, T. Gentry, B. P. Thompson, and J. S. Russell. A model specification for FRP composites for civil engineering structures. *Construction and Building Materials*, 17(6-7): 405–437, September 2003. doi: 10.1016/S0950-0618(03)00041-2.

[30] L. McKague, S. Gardner, and J. H. Campbell. Design and Process Integration for Low Cost Manufacturing. *Journal of Advanced Materials*, 37(1):9, 2005.

[31] J. M. Svanberg. *Predictions of Manufacturing Induced Shape Distortions: High Performance Thermoset Composites*. PhD thesis, Lulea University of Technology, Lulea, Sweden, October 2002.

[32] T. Mesogitis, A. Skordos, and A. Long. Uncertainty in the manufacturing of fibrous thermosetting composites: A review. *Composites Part A: Applied Science and Manufacturing*, 57:67–75, February 2014. doi: 10.1016/j.compositesa.2013.11.004.

[33] R. A. Naik. Analysis of Woven and Braided Fabric-Reinforced Composites. NASA Contractor Report 194930, Analytical Services & Materials, Inc., Hampton, Virginia, June 1994.

[34] Y. Cai and H. Sun. Prediction on viscoelastic properties of three-dimensionally braided composites by multi-scale model. *Journal of Materials Science*, 48(19):6499–6508, October 2013. doi: 10.1007/s10853-013-7524-1.

[35] P. J. Falzon and I. Herszberg. Mechanical performance of 2-D braided carbon/epoxy composites. *Composites Science and Technology*, 58(2):253–265, January 1998. doi: 10.1016/S0266-3538(97)00133-4.

[36] K. M. Charlebois, R. Boukhili, O. Zebdi, F. Trochu, and A. Gasmi. Evaluation of the Physical and Mechanical Properties of Braided Fabrics and their Composites. *Journal of Reinforced Plastics and Composites*, 24(14):1539–1554, September 2005. doi: 10.1177/0731684405050391.

[37] F. Heieck, F. Hermann, P. Middendorf, and K. Schladitz. Influence of the cover factor of 2D biaxial and triaxial braided carbon composites on their in-plane mechanical properties. *Composite Structures*, 163:114–122, March 2017. doi: 10.1016/j.compstruct.2016.12.025.

[38] Y. Chai, Y. Wang, Z. Yousaf, M. Storm, N. T. Vo, K. Wanelik, T. L. Burnett, P. Potluri, and P. J. Withers. Following the effect of braid architecture on performance and damage of carbon fibre/epoxy composite tubes during torsional straining. *Composites Science and Technology*, 200:108451, November 2020. doi: 10.1016/j.compscitech.2020.108451.

[39] M. Y. Matveev. *Effects of Variabilities on Mechanical Properties of Textile Composites*. PhD thesis, University of Nottingham, Nottingham, UK, February 2015.

[40] S. van Oosterom, T. Allen, M. Battley, and S. Bickerton. An objective comparison of common vacuum assisted resin infusion processes. *Composites Part A: Applied Science and Manufacturing*, 125:105528, October 2019. doi: 10.1016/j.compositesa.2019.105528.

[41] C. C. Wong and A. C. Long. Modelling variation of textile fabric permeability at mesoscopic scale. *Plastics, Rubber and Composites*, 35(3):101–111, April 2006. doi: 10.1179/174328906X103088.

[42] Z.-R. Chen, Lin Ye, and Meng Lu. Permeability Predictions for Woven Fabric Preforms. *Journal of Composite Materials*, 44(13):1569–1586, June 2010. doi: 10.1177/0021998309355888.

[43] Carbon fibre laminates — Determination of the fibre, resin and void contents. Technical Report BS EN 2564:2018, British Standards Institution, London, 2018.

[44] Standard Test Methods for Constituent Content of Composite Materials. Technical Report ASTM D3171 - 15, ASTM International, West Conshohocken, PA, 2015.

[45] Standard Test Method for Ignition Loss of Cured Reinforced Resins. Technical Report ASTM D2584 - 18, ASTM International, West Conshohocken, PA,, 2018.

[46] Standard Test Methods for Density and Specific Gravity (Relative Density) of Plastics by Displacement. Technical Report ASTM D792 - 20, ASTM International, West Conshohocken, PA,, 2020.

[47] M. Mohsin, L. Iannucci, and E. Greenhalgh. Fibre-volume-fraction measurement of carbon fibre reinforced thermoplastic composites using thermogravimetric analysis. *Heliyon*, 5(1), January 2019. doi: 10.1016/j.heliyon.2019.e01132.

[48] C. Garschke, C. Weimer, P. P. Parlevliet, and B. L. Fox. Out-of-autoclave cure cycle study of a resin film infusion process using in situ process monitoring. *Composites Part A: Applied Science and Manufacturing*, 43(6):935–944, June 2012. doi: 10.1016/j.compositesa.2012.01.003.

[49] H.-w. He, W. Huang, and F. Gao. Comparison of four methods for determining fiber content of carbon fiber/epoxy composites. *International Journal of Polymer Analysis and Characterization*, 21(3):251–258, April 2016. doi: 10.1080/1023666X.2016.1139395.

[50] G. W. Melenka and C. Ayranci. Advanced measurement techniques for braided composite structures: A review of current and upcoming trends. *Journal of Composite Materials*, 54 (25):3895–3917, October 2020. doi: 10.1177/0021998320903105.

[51] N. Liebers, M. Buggisch, M. Kleineberg, and M. Wiedemann. Autoclave infusion of aerospace ribs based on process monitoring and control by ultrasound sensors. In *20th International Conference on Composite Materials*, Copenhagen, July 2015.

[52] B. Yenilmez, M. Senan, and E. Murat Sozer. Variation of part thickness and compaction pressure in vacuum infusion process. *Composites Science and Technology*, 69(11-12):1710–1719, September 2009. doi: 10.1016/j.compscitech.2008.05.009.

[53] C. Williams, S. Grove, and J. Summerscales. The compression response of fibre-reinforced plastic plates during manufacture by the resin infusion under flexible tooling method. *Composites Part A: Applied Science and Manufacturing*, 29(1-2):111–114, January 1998. doi: 10.1016/S1359-835X(97)00038-9.

[54] K. D. Tackitt and S. M. Walsh. Experimental Study of Thickness Gradient Formation in the VARTM Process. *Materials and Manufacturing Processes*, 20(4):607–627, July 2005. doi: 10.1081/AMP-200041896.

[55] B. Yenilmez, T. Akyol, B. Caglar, and E. M. Sozer. Minimizing Thickness Variation in the Vacuum Infusion (VI) Process. *Advanced Composites Letters*, 20(6), November 2011. doi: 10.1177/096369351102000603.

[56] Q. Govignon, S. Bickerton, J. Morris, and P. Kelly. Full field monitoring of the resin flow and laminate properties during the resin infusion process. *Composites Part A: Applied Science and Manufacturing*, 39(9):1412–1426, September 2008. doi: 10.1016/j.compositesa.2008.05.005.

[57] J. Timms, S. Bickerton, and P. Kelly. Laminate thickness and resin pressure evolution during axisymmetric liquid composite moulding with flexible tooling. *Composites Part A: Applied Science and Manufacturing*, 43(4):621–630, April 2012. doi: 10.1016/j.compositesa.2011.12.012.

[58] S. Kazmi, Q. Govignon, and S. Bickerton. Control of laminate quality for parts manufactured using the resin infusion process. *Journal of Composite Materials*, 53(3):327–343, February 2019. doi: 10.1177/0021998318783308.

[59] J. Vilà, C. González, and J. LLorca. A level set approach for the analysis of flow and compaction during resin infusion in composite materials. *Composites Part A: Applied Science and Manufacturing*, 67:299–307, December 2014. doi: 10.1016/j.compositesa.2014.09.002.

[60] B. Caglar, M. Hancioglu, and E. M. Sozer. Monitoring and modeling of part thickness evolution in vacuum infusion process. *Journal of Composite Materials*, 55(8):1053–1072, October 2020. doi: 10.1177/0021998320963173.

[61] S. S. Roy and P. Potluri. Braid-winding for optimum tubular preforming. In *Texcomp-12*, page 8, Raleigh, NC, USA, May 2015.

[62] K. Birkefeld, M. Röder, T. von Reden, M. Bulat, and K. Drechsler. Characterization of Biaxial and Triaxial Braids: Fiber Architecture and Mechanical Properties. *Applied Composite Materials*, 19(3-4):259–273, June 2012. doi: 10.1007/s10443-011-9190-2.

[63] R. Schmitt, C. Niggemann, and C. Mersmann. Laser light-section sensor automating the production of textile-reinforced composites. In *Proceedings of SPIE*, volume 7356, Prague, Czech Republic, May 2009. doi: 10.1117/12.820584.

[64] D. Brabandt and G. Lanza. Data Processing for an Inline Measurement of Preforms in the CFRP-Production. *Procedia CIRP*, 33:269–274, 2015. doi: 10.1016/j.procir.2015.06.048.

[65] N. Miesen, J. Sinke, R. M. Groves, and R. Benedictus. Simulation and detection of flaws in pre-cured CFRP using laser displacement sensing. *International Journal of Advanced Manufacturing Technology*, 82:341–349, January 2016. doi: 10.1007/s00170-015-7305-x.

[66] J. Carey, M. Munro, and A. Fahim. Longitudinal Elastic Modulus Prediction of a 2-D Braided Fiber Composite. *Journal of Reinforced Plastics and Composites*, 22(9):813–831, June 2003. doi: 10.1177/0731684403022009003.

[67] C. Ayranci and J. P. Carey. Predicting the longitudinal elastic modulus of braided tubular composites using a curved unit-cell geometry. *Composites Part B: Engineering*, 41(3):229–235, April 2010. doi: 10.1016/j.compositesb.2009.10.006.

[68] J. S. Tate, A. D. Kelkar, and J. D. Whitcomb. Effect of braid angle on fatigue performance of biaxial braided composites. *International Journal of Fatigue*, 28(10):1239–1247, October 2006. doi: 10.1016/j.ijfatigue.2006.02.009.

[69] C. Ayranci and J. Carey. 2D braided composites: A review for stiffness critical applications. *Composite Structures*, 85(1):43–58, September 2008. doi: 10.1016/j.compstruct.2007.10.004.

[70] A. Rawal, H. Saraswat, and A. Sibal. Tensile response of braided structures: A review. *Textile Research Journal*, 85(19):2083–2096, November 2015. doi: 10.1177/0040517515576331.

[71] R. A. Naik, P. G. Ifju, and J. E. Masters. Effect of Fiber Architecture Parameters on Mechanical Performance of Braided Composites. In *Proceedings of the 4th NASA/DOD Advanced Composites Technology Conference*, volume 1 of *NASA CP 3229*, pages 525–554, Salt Lake City, UT, USA, June 1993.

[72] A.-M. Harte and N. A. Fleck. On the mechanics of braided composites in tension. *European Journal of Mechanics - A/Solids*, 19(2):259–275, March 2000. doi: 10.1016/S0997-7538(99)00164-3.

[73] O. Zebdi, R. Boukhili, and F. Trochu. An Inverse Approach Based on Laminate Theory to Calculate the Mechanical Properties of Braided Composites. *Journal of Reinforced Plastics and Composites*, 28(23):2911–2930, December 2009. doi: 10.1177/0731684408094063.

[74] M. Dadkhah, J. Flintoff, T. Kniveton, and B. Cox. Simple models for triaxially braided composites. *Composites*, 26(8):561–577, August 1995. doi: 10.1016/0010-4361(95)92621-I.

[75] F. Guo-dong, L. Jun, W. Yu, and W. Bao-lai. The effect of yarn distortion on the mechanical properties of 3D four-directional braided composites. *Composites Part A: Applied Science and Manufacturing*, 40(4):343–350, April 2009. doi: 10.1016/j.compositesa.2008.12.007.

[76] I. Mertová, E. Moučková, B. Neckář, and M. Vyšanská. Influence of Twist on Selected Properties of Multifilament Yarn. *AUTEX Research Journal*, 18(2):110–120, June 2018. doi: 10.1515/aut-2017-0018.

[77] B. K. Cheung and J. P. Carey. Improving two-dimensional braided composite tensile properties by including low angle yarn twist: Production, experimental verification, and modeling. *Journal of Engineered Fibers and Fabrics*, 15, January 2020. doi: 10.1177/1558925020946449.

[78] K. Potter, B. Khan, M. Wisnom, T. Bell, and J. Stevens. Variability, fibre waviness and misalignment in the determination of the properties of composite materials and structures. *Composites Part A: Applied Science and Manufacturing*, 39(9):1343–1354, September 2008. doi: 10.1016/j.compositesa.2008.04.016.

[79] A. Endruweit, A. C. Long, F. Robitaille, and C. D. Rudd. Influence of stochastic fibre angle variations on the permeability of bi-directional textile fabrics. *Composites Part A: Applied Science and Manufacturing*, 37(1):122–132, January 2006. doi: 10.1016/j.compositesa.2005.04.014.

[80] A. Long. Process modelling for liquid moulding of braided preforms. *Composites Part A: Applied Science and Manufacturing*, 32(7):941–953, July 2001. doi: 10.1016/S1359-835X(00)00153-6.

[81] A. Endruweit and A. Long. A model for the in-plane permeability of triaxially braided reinforcements. *Composites Part A: Applied Science and Manufacturing*, 42(2):165–172, February 2011. doi: 10.1016/j.compositesa.2010.11.003.

[82] R. Blanc, C. Germain, J. D. costa, P. Baylou, and M. Cataldi. Fiber orientation measurements in composite materials. *Composites Part A: Applied Science and Manufacturing*, 37(2):197–206, February 2006. doi: 10.1016/j.compositesa.2005.04.021.

[83] N. Sharp, J. Goodsell, and A. Favaloro. Measuring Fiber Orientation of Elliptical Fibers from Optical Microscopy. *Journal of Composites Science*, 3(1):23, March 2019. doi: 10.3390/jcs3010023.

[84] M. Krause, J. M. Hausherr, B. Burgeth, C. Herrmann, and W. Krenkel. Determination of the fibre orientation in composites using the structure tensor and local X-ray transform. *Journal of Materials Science*, 45(4):888–896, February 2010. doi: 10.1007/s10853-009-4016-4.

[85] P. A. Hessman, T. Riedel, F. Welschinger, K. Hornberger, and T. Böhlke. Microstructural analysis of short glass fiber reinforced thermoplastics based on x-ray micro-computed tomography. *Composites Science and Technology*, 183:107752, October 2019. doi: 10.1016/j.compscitech.2019.107752.

[86] R. Karamov, L. M. Martulli, M. Kerschbaum, I. Sergeichev, Y. Swolfs, and S. V. Lomov. Micro-CT based structure tensor analysis of fibre orientation in random fibre composites versus high-fidelity fibre identification methods. *Composite Structures*, 235:111818, March 2020. doi: 10.1016/j.compstruct.2019.111818.

[87] D. Wilhelmsson and L. Asp. A high resolution method for characterisation of fibre misalignment angles in composites. *Composites Science and Technology*, 165:214–221, September 2018. doi: 10.1016/j.compscitech.2018.07.002.

[88] C. Creighton, M. Sutcliffe, and T. Clyne. A multiple field image analysis procedure for characterisation of fibre alignment in composites. *Composites Part A: Applied Science and Manufacturing*, 32(2):221–229, February 2001. doi: 10.1016/S1359-835X(00)00115-9.

[89] M. Sutcliffe, S. Lemanski, and A. Scott. Measurement of fibre waviness in industrial composite components. *Composites Science and Technology*, 72(16):2016–2023, November 2012. doi: 10.1016/j.compscitech.2012.09.001.

[90] K. Kratmann, M. Sutcliffe, L. Lilleheden, R. Pyrz, and O. Thomsen. A novel image analysis procedure for measuring fibre misalignment in unidirectional fibre composites. *Composites*

Science and Technology, 69(2):228–238, February 2009. doi: 10.1016/j.compscitech.2008.10.020.

[91] O. Wirjadi, K. Schladitz, P. Easwaran, and J. Ohser. Estimating fibre direction distributions of reinforced composites from tomographic images. *Image Analysis & Stereology*, 35(3):167, December 2016. doi: 10.5566/ias.1489.

[92] R. A. Smith. *Use of 3D Ultrasound Data Sets to Map the Localised Properties of Fibre-Reinforced Composites*. PhD thesis, University of Nottingham, Nottingham, UK, July 2010.

[93] L. Nelson and R. Smith. Fibre direction and stacking sequence measurement in carbon fibre composites using Radon transforms of ultrasonic data. *Composites Part A: Applied Science and Manufacturing*, 118:1–8, March 2019. doi: 10.1016/j.compositesa.2018.12.009.

[94] L. Nelson, R. Smith, and M. Mienczakowski. Ply-orientation measurements in composites using structure-tensor analysis of volumetric ultrasonic data. *Composites Part A: Applied Science and Manufacturing*, 104:108–119, January 2018. doi: 10.1016/j.compositesa.2017.10.027.

[95] I. Pelivanov, T. Buma, J. Xia, C.-W. Wei, and M. O'Donnell. NDT of fiber-reinforced composites with a new fiber-optic pump–probe laser-ultrasound system. *Photoacoustics*, 2 (2):63–74, June 2014. doi: 10.1016/j.pacs.2014.01.001.

[96] I. Pelivanov, Ł. Ambroziński, A. Khomenko, E. G. Koricho, G. L. Cloud, M. Haq, and M. O'Donnell. High resolution imaging of impacted CFRP composites with a fiber-optic laser-ultrasound scanner. *Photoacoustics*, 4(2):55–64, June 2016. doi: 10.1016/j.pacs.2016.05.002.

[97] L. Ambrozinski, J. Mrowka, M. O'Donnell, and I. Pelivanov. Detection and imaging of local ply angle in carbon fiber reinforced plastics using laser ultrasound and tilt filter processing. *Composites Part A: Applied Science and Manufacturing*, 126:105581, November 2019. doi: 10.1016/j.compositesa.2019.105581.

[98] H. Heuer, M. Schulze, M. Pooch, S. Gäbler, A. Nocke, G. Bardl, C. Cherif, M. Klein, R. Kupke, R. Vetter, F. Lenz, M. Kliem, C. Bülow, J. Goyvaerts, T. Mayer, and S. Petrenz. Review on quality assurance along the CFRP value chain – Non-destructive testing of fabrics, preforms and CFRP by HF radio wave techniques. *Composites Part B: Engineering*, 77:494–501, August 2015. doi: 10.1016/j.compositesb.2015.03.022.

[99] J. Mersch, G. Bardl, A. Nocke, C. Cherif, M. H. Schulze, and H. Heuer. Development of a method for the non-destructive evaluation of fiber orientation in multilayer 3D carbon fiber

preforms and CFRP with robot-guided high- frequency eddy current testing technology. In *10th International Symposium on NDT in Aerospace*, Dresden, Germany, October 2018.

[100] G. Bardl, A. Nocke, M. Hübner, T. Gereke, M. Pooch, M. Schulze, H. Heuer, M. Schiller, R. Kupke, M. Klein, and C. Cherif. Analysis of the 3D draping behavior of carbon fiber non-crimp fabrics with eddy current technique. *Composites Part B: Engineering*, 132:49–60, January 2018. doi: 10.1016/j.compositesb.2017.08.007.

[101] K. Mizukami and K. Ogi. Non-contact visualization of fiber waviness distribution in carbon fiber composites using eddy current testing. *Advanced Composite Materials*, 27(2):135–146, March 2018. doi: 10.1080/09243046.2017.1344917.

[102] Y. Kyosev and M. Aurich. Investigations about the braiding angle and the cover factor of the braided fabrics using Image processing and symbolic math toolbox of matlab. In Y. Kyosev, editor, *Advances in Braiding Technology: Specialized Techniques and Applications*, Woodhead Publishing Series in Textiles, pages 549–69. Woodhead Publishing, Oxford, 2016. ISBN 978-0-08-100926-0.

[103] B. Lian, L. Jiang, J. McGrath, and J. Jaranson. Quantitative determination of morphological features of triaxially braided composites by the use of machine vision. *Composites Science and Technology*, 60(2):159–166, February 2000. doi: 10.1016/S0266-3538(99)00115-3.

[104] R. Schmitt, C. Mersmann, and A. Schoenberg. Machine vision industrialising the textile-based FRP production. In *Proceedings of 6th International Symposium on Image and Signal Processing and Analysis*, pages 260–264, Salzburg, Austria, September 2009. ISBN 978-953-184-135-1. doi: 10.1109/ISPA.2009.5297720.

[105] A. J. Hunt and J. P. Carey. A machine vision system for the braid angle measurement of tubular braided structures. *Textile Research Journal*, 89(14):2919–2937, July 2019. doi: 10.1177/0040517518803792.

[106] S. Zambal, W. Palfinger, M. Stöger, and C. Eitzinger. Accurate fibre orientation measurement for carbon fibre surfaces. *Pattern Recognition*, 48(11):3324–3332, November 2015. doi: 10.1016/j.patcog.2014.11.009.

[107] M. Schöberl, K. Kasnakli, and A. Nowak. Measuring Strand Orientation in Carbon Fiber Reinforced Plastics (CFRP) with Polarization. In *19th World Conference on Non-Destructive Testing*, Munich, Germany, June 2016.

[108] V. Michaud. A Review of Non-saturated Resin Flow in Liquid Composite Moulding processes. *Transport in Porous Media*, 115(3):581–601, December 2016. doi: 10.1007/s11242-016-0629-7.

[109] M. Mehdikhani, L. Gorbatikh, I. Verpoest, and S. V. Lomov. Voids in fiber-reinforced polymer composites: A review on their formation, characteristics, and effects on mechanical performance. *Journal of Composite Materials*, 53(12):1579–1669, May 2019. doi: 10.1177/0021998318772152.

[110] H. Zhu, B. Wu, D. Li, D. Zhang, and Y. Chen. Influence of Voids on the Tensile Performance of Carbon/epoxy Fabric Laminates. *Journal of Materials Science & Technology*, 27(1):69–73, January 2011. doi: 10.1016/S1005-0302(11)60028-5.

[111] K. Xu and X. Qian. An FEM Analysis with Consideration of Random Void Defects for Predicting the Mechanical Properties of 3D Braided Composites. *Advances in Materials Science and Engineering*, 2014:1–12, 2014. doi: 10.1155/2014/439819.

[112] X. Gao, L. Yuan, Y. Fu, X. Yao, and H. Yang. Prediction of mechanical properties on 3D braided composites with void defects. *Composites Part B: Engineering*, 197:108164, September 2020. doi: 10.1016/j.compositesb.2020.108164.

[113] Standard Test Methods for Void Content of Reinforced Plastics. Technical Report ASTM D2734-16, ASTM International, West Conshohocken, PA,, 2016.

[114] D. Stone and B. Clarke. Ultrasonic attenuation as a measure of void content in carbon-fibre reinforced plastics. *Non-Destructive Testing*, 8(3):137–145, June 1975. doi: 10.1016/0029-1021(75)90023-7.

[115] T. Okahara, S. Biwa, and A. Kuraishi. Nondestructive Evaluation of Porosity Content in the Curved Corner Section of Composite Laminates Using Focused Ultrasonic Waves. *Journal of Nondestructive Evaluation, Diagnostics and Prognostics of Engineering Systems*, 1(1):011009, February 2018. doi: 10.1115/1.4037546.

[116] Y. G. Sokolovskaya, N. B. Podymova, and A. A. Karabutov. Application of Laser-Ultrasonic Technique of Acoustic Impedance Measurement with Signals Detection by Backward-Mode Scheme for Porosity Content Evaluation in CFRP Laminates. *Journal of Nondestructive Evaluation*, 39(3):55, September 2020. doi: 10.1007/s10921-020-00700-6.

[117] G. W. Melenka, E. Lepp, B. K. Cheung, and J. P. Carey. Micro-computed tomography analysis of tubular braided composites. *Composite Structures*, 131:384–396, November 2015. doi: 10.1016/j.compstruct.2015.05.057.

[118] J. Vilà, F. Sket, F. Wilde, G. Requena, C. González, and J. LLorca. An in situ investigation of microscopic infusion and void transport during vacuum-assisted infiltration by means of X-

ray computed tomography. *Composites Science and Technology*, 119:12–19, November 2015. doi: 10.1016/j.compscitech.2015.09.016.

[119] J. Hemmer, C. Burtin, S. Comas-Cardona, C. Binetruy, T. Savart, and A. Babeau. Unloading during the infusion process: Direct measurement of the dual-scale fibrous microstructure evolution with X-ray computed tomography. *Composites Part A: Applied Science and Manufacturing*, 115:147–156, December 2018. doi: 10.1016/j.compositesa.2018.09.013.

[120] J. Castro, L. Helfen, C. González, and F. Sket. An in situ investigation of void generation and transport during resin transfer moulding by means of synchrotron X-ray laminography. In *18th European Conference on Composite Materials*, Athens, Greece, June 2018.

[121] B. de Parscau du Plessix, P. Lefébure, N. Boyard, S. L. Corre, N. Lefèvre, F. Jacquemin, V. Sobotka, and S. Rolland du Roscoat. In situ real-time 3D observation of porosity growth during composite part curing by ultra-fast synchrotron X-ray microtomography. *Journal of Composite Materials*, 53(28-30):4105–4116, December 2019. doi: 10.1177/0021998319846260.

[122] J. Kratz, P. Galvez-Hernandez, L. R. Pickard, J. Belnoue, and K. Potter. Lab-based in-situ micro-CT observation of gaps in prepreg laminates during consolidation and cure. *Composites Part A: Applied Science and Manufacturing*, 140:106180, January 2021. doi: 10.1016/j.compositesa.2020.106180.

[123] K. Naresh, K. Khan, R. Umer, and W. Cantwell. The use of X-ray computed tomography for design and process modeling of aerospace composites: A review. *Materials & Design*, 190: 108553, May 2020. doi: 10.1016/j.matdes.2020.108553.

[124] A. Endruweit, P. Glover, K. Head, and A. C. Long. Mapping of the fluid distribution in impregnated reinforcement textiles using Magnetic Resonance Imaging: Methods and issues. *Composites Part A: Applied Science and Manufacturing*, 42(3):265–273, March 2011. doi: 10.1016/j.compositesa.2010.11.012.

[125] A. Endruweit, P. Glover, K. Head, and A. C. Long. Mapping of the fluid distribution in impregnated reinforcement textiles using Magnetic Resonance Imaging: Application and discussion. *Composites Part A: Applied Science and Manufacturing*, 42(10):1369–1379, October 2011. doi: 10.1016/j.compositesa.2011.05.020.

[126] F. LeBel, É. Ruiz, and F. Trochu. Experimental study of saturation by visible light transmission in dual-scale fibrous reinforcements during composite manufacturing. *Journal of Reinforced Plastics and Composites*, 36(23):1693–1711, December 2017. doi: 10.1177/0731684417725187.

[127] F. LeBel, É. Ruiz, and F. Trochu. Void content analysis and processing issues to minimize defects in liquid composite molding. *Polymer Composites*, 40(1):109–120, January 2019. doi: 10.1002/pc.24609.

[128] M. Nordlund and V. Michaud. Dynamic saturation curve measurement for resin flow in glass fibre reinforcement. *Composites Part A: Applied Science and Manufacturing*, 43(3):333–343, March 2012. doi: 10.1016/j.compositesa.2011.12.001.

[129] F. LeBel, A. E. Fanaei, E. Ruiz, and F. Trochu. Experimental characterization by fluorescence of capillary flows in dual-scale engineering fabrics. *Textile Research Journal*, 83(15):1634–1659, September 2013. doi: 10.1177/0040517512471742.

[130] P. A. Burton. *In Situ Analysis of Void Formation at the Flow Front in RTM*. Masters Dissertation, Brigham Young University, School of Technology, 2018.

[131] C. Lystrup, A. George, B. Zobell, K. Boster, C. Childs, H. Girod, and D. Fullwood. Optical measurement of voids in situ during infusion of carbon reinforcements. *Journal of Composite Materials*, 55(6):775–786, March 2021. doi: 10.1177/0021998320959820.

[132] L. Labat, M. Grisel, J. Breard, and G. Bouquet. Original use of electrical conductivity for void detection due to injection conditions of composite materials. *Comptes Rendus de l'Académie des Sciences - Series IIB - Mechanics*, 329(7):529–534, July 2001. doi: 10.1016/S1620-7742(01)01363-0.

[133] S. Guéroult, L. Bizet, and J. Bréard. Experimental determination of void formation and transport in the RTM process. In *FPCM-11*, pages 111–118, Auckland, New Zealand, July 2012.

[134] P. Carlone, F. Rubino, V. Paradiso, and F. Tucci. Multi-scale modeling and online monitoring of resin flow through dual-scale textiles in liquid composite molding processes. *International Journal of Advanced Manufacturing Technology*, 96(5-8):2215–2230, May 2018. doi: 10.1007/s00170-018-1703-9.

[135] M. Villière, S. Guéroult, V. Sobotka, N. Boyard, J. Bréard, and D. Delaunay. Dynamic saturation curve measurement in liquid composite molding by heat transfer analysis. *Composites Part A: Applied Science and Manufacturing*, 69:255–265, February 2015. doi: 10.1016/j.compositesa.2014.11.024.

[136] M. K. Saraswat, D. Heider, and Y. S. Song. A Qualitative Study of the Void Formation using Ultrasounds During the VARTM Process. In *SAMPE 2007*, Baltimore, MD, USA, June 2007.

[137] N. Samet, P. Maréchal, and H. Duflo. Ultrasound monitoring of bubble size and velocity in a fluid model using phased array transducer. *NDT & E International*, 44(7):621–627, November 2011. doi: 10.1016/j.ndteint.2011.06.005.

[138] H. L. Liu, X.-C. Tu, J. O. Lee, H.-B. Kim, and W. R. Hwang. Visualization of resin impregnation through opaque reinforcement textiles during the vacuum-assisted resin transfer molding process using ultrasound. *Journal of Composite Materials*, 48(9):1113–1120, April 2014. doi: 10.1177/0021998313482157.

[139] A. A. Skordos, P. I. Karkanas, and I. K. Partridge. A dielectric sensor for measuring flow in resin transfer moulding. *Measurement Science and Technology*, 11(1):25, 2000. doi: 10.1088/0957-0233/11/1/304.

[140] A. Pouchias, P. R. Cunningham, J. Stein, and M. Kazilas. Development of a Flexible Dielectric Sensor for Flow Monitoring of the Liquid Resin Infusion Process. *Sensors*, 19(23):5292, December 2019. doi: 10.3390/s19235292.

[141] X. Qing, X. Liu, J. Zhu, and Y. Wang. In-situ monitoring of liquid composite molding process using piezoelectric sensor network. *Structural Health Monitoring*, September 2020. doi: 10.1177/1475921720958082.

[142] T. Mesogitis, G. Maistros, M. Asareh, C. Lira, and A. Skordos. Optimisation of an in-process lineal dielectric sensor for liquid moulding of carbon fibre composites. *Composites Part A: Applied Science and Manufacturing*, 140:106190, January 2021. doi: 10.1016/j.compositesa.2020.106190.

[143] R. Matsuzaki, S. Kobayashi, A. Todoroki, and Y. Mizutani. Full-field monitoring of resin flow using an area-sensor array in a VaRTM process. *Composites Part A: Applied Science and Manufacturing*, 42(5):550–559, May 2011. doi: 10.1016/j.compositesa.2011.01.014.

[144] M. Murata, R. Matsuzaki, A. Todoroki, Y. Mizutani, and Y. Suzuki. Three-dimensional reconstruction of resin flow using capacitance sensor data assimilation during a liquid composite molding process: A numerical study. *Composites Part A: Applied Science and Manufacturing*, 73:1–10, June 2015. doi: 10.1016/j.compositesa.2015.01.031.

[145] T. Luthy and P. Ermanni. Flow monitoring in liquid composite molding based on linear direct current sensing technique. *Polymer Composites*, 24(2):249–262, April 2003. doi: 10.1002/pc.10026.

[146] J. Sánchez del Río, C. Pascual-González, V. Martínez, J. L. Jiménez, and C. González. 3D-printed resistive carbon-fiber-reinforced sensors for monitoring the resin frontal flow during composite manufacturing. *Sensors and Actuators A: Physical*, 317:112422, January 2021. doi: 10.1016/j.sna.2020.112422.

[147] A. Dominauskas, D. Heider, and J. W. Gillespie. Electric time-domain reflectometry distributed flow sensor. *Composites Part A: Applied Science and Manufacturing*, 38(1):138–146, January 2007. doi: 10.1016/j.compositesa.2006.01.019.

[148] G. Pandey, H. Deffor, E. T. Thostenson, and D. Heider. Smart tooling with integrated time domain reflectometry sensing line for non-invasive flow and cure monitoring during composites manufacturing. *Composites Part A: Applied Science and Manufacturing*, 47:102–108, April 2013. doi: 10.1016/j.compositesa.2012.11.017.

[149] C. Buchmann, J. Filsinger, and E. Ladstätter. Investigation of Electrical Time Domain Reflectometry for infusion and cure monitoring in combination with electrically conductive fibers and tooling materials. *Composites Part B: Engineering*, 94:389–398, June 2016. doi: 10.1016/j.compositesb.2016.02.060.

[150] T. Stöven, F. Weyrauch, P. Mitschang, and M. Neitzel. Continuous monitoring of three-dimensional resin flow through a fibre preform. *Composites Part A: Applied Science and Manufacturing*, 34(6):475–480, June 2003. doi: 10.1016/S1359-835X(03)00059-9.

[151] V. Antonucci, M. Giordano, L. Nicolais, A. Calabrò, A. Cusano, A. Cutolo, and S. Inserra. Resin flow monitoring in resin film infusion process. *Journal of Materials Processing Technology*, 143–144:687–692, December 2003. doi: 10.1016/S0924-0136(03)00338-8.

[152] G. Bektaş, T. Boz, C. J. Keulen, M. Yıldız, C. Öztürk, Y. Z. Menceloğlu, and A. Suleman. Fiber Bragg grating and etched optic sensors for flow and cure monitoring of resin transfer molded composite structures. In *18th International Conference on Composite Materials*, Jeju, Korea, Auhust 2011.

[153] S. Konstantopoulos, E. Fauster, and R. Schledjewski. Monitoring the production of FRP composites: A review of in-line sensing methods. *Express Polymer Letters*, 8(11):823–840, 2014. doi: 10.3144/expresspolymlett.2014.84.

[154] M. Torres. Parameters' monitoring and in-situ instrumentation for resin transfer moulding: A review. *Composites Part A: Applied Science and Manufacturing*, 124:105500, September 2019. doi: 10.1016/j.compositesa.2019.105500.

[155] F. A. L. Dullien. *Porous Media: Fluid Transport and Pore Structure*. Academic Press, New York, 1979. ISBN 978-0-12-223650-1.

[156] N. Patel, V. Rohatgi, and L. J. Lee. Micro scale flow behavior and void formation mechanism during impregnation through a unidirectional stitched fiberglass mat. *Polymer Engineering and Science*, 35(10):837–851, May 1995. doi: 10.1002/pen.760351006.

[157] C. Lira, M. Stojkovic, J. Simpson, K. Potter, and G. Maistros. In-line monitoring and numerical verification of resin transfer moulding process with CYCOM 890 RTM resin system. In *20th International Conference on Composite Materials*, Copenhagen, July 2015.

[158] A. Dimassi, M. G. Vargas Gleason, M. Hübner, A. S. Herrmann, and W. Lang. Using piezoresistive pressure sensors for resin flow monitoring in wind turbine blades. *Materials Today: Proceedings*, 34:140–148, January 2021. doi: 10.1016/j.matpr.2020.01.493.

[159] DC dielectric sensors for industrial composites production, `https://www.compositesworld.com/articles/dc-dielectric-sensors-for-industrial-composites-production` (Accessed: December 31, 2020).

[160] E. Chehura, S. W. James, S. Staines, C. Groenendijk, D. Cartie, S. Portet, M. Hugon, and R. P. Tatam. Production process monitoring and post-production strain measurement on a full-size carbon-fibre composite aircraft tail cone assembly using embedded optical fibre sensors. *Measurement Science and Technology*, 31(10):105204, October 2020. doi: 10.1088/1361-6501/ab8a7b.

[161] R. E. Lyon and D. L. Schumann. Determination of matrix-dominated mechanical properties of fiber composite lamina. *Polymer Composites*, 13(1):1–6, February 1992. doi: 10.1002/pc.750130102.

[162] D. Hull. Matrix-dominated properties of polymer matrix composite materials. *Materials Science and Engineering: A*, 184(2):173–183, August 1994. doi: 10.1016/0921-5093(94)91030-8.

[163] S.-Y. Lee and G. S. Springer. Effects of Cure on the Mechanical Properties of Composites. *Journal of Composite Materials*, 22(1):15–29, January 1988. doi: 10.1177/002199838802200102.

[164] J.-K. Kim and Y.-w. Mai. High strength, high fracture toughness fibre composites with interface control—A review. *Composites Science and Technology*, 41(4):333–378, January 1991. doi: 10.1016/0266-3538(91)90072-W.

[165] E. Ruiz and F. Trochu. Thermomechanical Properties during Cure of Glass-Polyester RTM Composites: Elastic and Viscoelastic Modeling. *Journal of Composite Materials*, 39(10): 881–916, May 2005. doi: 10.1177/0021998305048732.

[166] S. Alavi-Soltani, S. Sabzevari, H. Koushyar, and B. Minaie. Thermal, rheological, and mechanical properties of a polymer composite cured at different isothermal cure temperatures. *Journal of Composite Materials*, 46(5):575–587, March 2012. doi: 10.1177/0021998311415443.

[167] V. Trappe, S. Günzel, and M. Jaunich. Correlation between crack propagation rate and cure process of epoxy resins. *Polymer Testing*, 31(5):654–659, August 2012. doi: 10.1016/j.polymertesting.2012.03.007.

[168] T. D. Chang, S. H. Carr, and J. O. Brittain. Studies of epoxy resin systems: Part B: Effect of crosslinking on the physical properties of an epoxy resin. *Polymer Engineering and Science*, 22(18):1213–1220, December 1982. doi: 10.1002/pen.760221807.

[169] J. B. Enns and J. K. Gillham. Effect of the extent of cure on the modulus, glass transition, water absorptio, and density of an amine-cured epoxy. *Journal of Applied Polymer Science*, 28(9):2831–2846, September 1983. doi: 10.1002/app.1983.070280914.

[170] M. Aldridge, A. Wineman, A. Waas, and J. Kieffer. In Situ Analysis of the Relationship between Cure Kinetics and the Mechanical Modulus of an Epoxy Resin. *Macromolecules*, 47 (23):8368–8376, December 2014. doi: 10.1021/ma501441c.

[171] L. E. Nielsen. Cross-Linking–Effect on Physical Properties of Polymers. *Journal of Macromolecular Science, Part C*, 3(1):69–103, January 1969. doi: 10.1080/15583726908545897.

[172] S. L. Kim, M. D. Skibo, J. A. Manson, R. W. Hertzberg, and J. Janiszewski. Tensile, impact and fatigue behavior of an amine-cured epoxy resin. *Polymer Engineering and Science*, 18 (14):1093–1100, November 1978. doi: 10.1002/pen.760181410.

[173] E. Crawford and A. J. Lesser. The effect of network architecture on the thermal and mechanical behavior of epoxy resins. *Journal of Polymer Science Part B: Polymer Physics*, 36(8):1371–1382, 1998. doi: 10.1002/(SICI)1099-0488(199806)36:8⟨1371::AID-POLB11⟩3.0.CO;2-4.

[174] T. A. Bogetti and J. W. Gillespie. Process-Induced Stress and Deformation in Thick-Section Thermoset Composite Laminates. *Journal of Composite Materials*, 26(5):35, March 1992.

[175] A. T. DiBenedetto. Prediction of the glass transition temperature of polymers: A model based on the principle of corresponding states. *Journal of Polymer Science Part B: Polymer Physics*, 25(9):1949–1969, September 1987. doi: 10.1002/polb.1987.090250914.

[176] S. C. Chowdhury, R. M. Elder, T. W. Sirk, and J. W. Gillespie. Epoxy resin thermo-mechanics and failure modes: Effects of cure and cross-linker length. *Composites Part B: Engineering*, 186:107814, April 2020. doi: 10.1016/j.compositesb.2020.107814.

[177] Standard Test Method for Short-Beam Strength of Polymer Matrix Composite Materials and Their Laminates. Technical Report ASTM D2344 - 16, ASTM International, West Conshohocken, PA,, 2016.

[178] Fibre-reinforced plastic composites — Determination of compressive properties in the in-plane direction. Technical Report BS EN ISO 14126:1999, British Standards Institution, London, 1999.

[179] Plastics — Differential scanning calorimetry (DSC) Part 2: Determination of glass transition temperature and step height. Technical Report BS EN ISO 11357-2:2020, British Standards Institution, London, 2020.

[180] Plastics — Determination of dynamic mechanical properties Part 11: Glass transition temperature. Technical Report BS ISO 6721-11:2019, British Standards Institution, London, 2019.

[181] G. A. George, G. A. Cash, and L. Rintoul. Cure Monitoring of Aerospace Epoxy Resins and Prepregs by Fourier Transform Infrared Emission Spectroscopy. *Polymer International*, 41 (2):169–182, October 1996. doi: 10.1002/(SICI)1097-0126(199610)41:2⟨169::AID-PI606⟩3.0.CO;2-2.

[182] L. Wang, A. Tomlin, S. D. Pandita, B. D. Gupta, S. A. Malik, M. Hudson, P. T. Curtis, and G. F. Fernando. In-situ monitoring of cross-linking reactions using E-glass fibres and evanescent wave spectroscopy. *Sensors and Actuators B: Chemical*, 236:358–366, November 2016. doi: 10.1016/j.snb.2016.05.126.

[183] L. Merad, M. Cochez, S. Margueron, F. Jauchem, M. Ferriol, B. Benyoucef, and P. Bourson. In-situ monitoring of the curing of epoxy resins by Raman spectroscopy. *Polymer Testing*, 28 (1):42–45, February 2009. doi: 10.1016/j.polymertesting.2008.10.006.

[184] R. Hardis, J. L. P. Jessop, F. E. Peters, and M. R. Kessler. Cure kinetics characterization and monitoring of an epoxy resin using DSC, Raman spectroscopy, and DEA. *Composites Part*

A: Applied Science and Manufacturing, 49:100–108, June 2013. doi: 10.1016/j.compositesa.2013.01.021.

[185] N. Pantelelis, G. Nedelec, Y. Amosse, M.-P. Toitgans, A. Beigbeder, I. Harismendy, R. Mezzacasa, J. Zhang, and E. Bistekos. Industrial cure monitoring and control of the RTM production of a CFRP automotive component. In *15th European Conference on Composite Materials*, Venice, Italy, June 2012.

[186] C. Lauter, K.-P. Jaquemotte, and N. Pantelelis. Improvement of productivity and quality in the wind energy industry through the use of an advanced sensor system. In *SAMPE Europe Conference 2017*, Stuttgart, Germany, November 2017.

[187] M. Etchells, N. Pantelelis, and C. Lira. Cure monitoring of highly reactive resin during high-pressure compression resin transfer moulding. In *18th European Conference on Composite Materials*, Athens, Greece, June 2018.

[188] F. Stéphan, X. Duteurtre, and A. Fit. In-process control of epoxy composite by microdielectrometric analysis. Part II: On-line real-time dielectric measurements during a compression molding process. *Polymer Engineering & Science*, 38(9):1566–1571, September 1998. doi: 10.1002/pen.10327.

[189] M. C. Kazilas and I. K. Partridge. Exploring equivalence of information from dielectric and calorimetric measurements of thermoset cure—a model for the relationship between curing temperature, degree of cure and electrical impedance. *Polymer*, 46(16):5868–5878, July 2005. doi: 10.1016/j.polymer.2005.05.005.

[190] F. A. Martin, A. F. Koutsomitopoulou, I. K. Partridge, and A. A. Skordos. Dielectric cure monitoring of a fast curing resin system. In *20th International Conference on Composite Materials*, Copenhagen, Denmark, July 2015.

[191] G. Chiesura, A. Lamberti, Y. Yang, G. Luyckx, W. Van Paepegem, S. Vanlanduit, J. Vanfleteren, and J. Degrieck. RTM Production Monitoring of the A380 Hinge Arm Droop Nose Mechanism: A Multi-Sensor Approach. *Sensors*, 16(6):866, June 2016. doi: 10.3390/s16060866.

[192] P. A. Gibbs. Ultrasonic cure measurements during the processing of an unsaturated polyester dough moulding compound. In *Designed for Life: Composites '94*, pages 7–16, November 1994.

[193] D. D. Shepard and K. R. Smith. A new ultrasonic measurement system for the cure monitoring of thermosetting resins and composites. *Journal of thermal analysis*, 49(1):95–100, July 1997. doi: 10.1007/BF01987425.

[194] F. Lionetto and A. Maffezzoli. Monitoring the Cure State of Thermosetting Resins by Ultrasound. *Materials*, 6(9):3783–3804, September 2013. doi: 10.3390/ma6093783.

[195] A. Cusano, A. Cutolo, M. Giordano, and L. Nicolais. Optoelectronic refractive index measurements: Application to smart processing. *IEEE Sensors Journal*, 3(6):781–787, December 2003. doi: 10.1109/JSEN.2003.820319.

[196] T. Kosaka and K. Kusukawa. Monitoring and simulation of non-uniform cure process of FRP by embedded sensors. In *20th International Conference on Composite Materials*, Copenhagen, Denmark, July 2015.

[197] J. F. Oelhafen. *Cure and Viscosity Measurement of Thermosetting Epoxy Resin with Fresnel Reflectometer Sensors*. PhD thesis, Technical University of Munich, Munich, Germany, October 2019.

[198] D. J. O'Brien, P. T. Mather, and S. R. White. Viscoelastic Properties of an Epoxy Resin during Cure. *Journal of Composite Materials*, 35(10):883–904, May 2001. doi: 10.1177/002199801772662442.

[199] L. Khoun, T. Centea, and P. Hubert. Characterization Methodology of Thermoset Resins for the Processing of Composite Materials — Case Study: CYCOM 890RTM Epoxy Resin. *Journal of Composite Materials*, 44(11):1397–1415, June 2010. doi: 10.1177/0021998309353960.

[200] Y. Nawab, P. Casari, N. Boyard, and F. Jacquemin. Characterization of the cure shrinkage, reaction kinetics, bulk modulus and thermal conductivity of thermoset resin from a single experiment. *Journal of Materials Science*, 48(6):2394–2403, March 2013. doi: 10.1007/s10853-012-7026-6.

[201] I. Baran, R. Akkerman, and J. H. Hattel. Material characterization of a polyester resin system for the pultrusion process. *Composites Part B: Engineering*, 64:194–201, August 2014. doi: 10.1016/j.compositesb.2014.04.030.

[202] K. Shivakumar and L. Emmanwori. Mechanics of Failure of Composite Laminates with an Embedded Fiber Optic Sensor. *Journal of Composite Materials*, 38(8):669–680, April 2004. doi: 10.1177/0021998304042393.

[203] K. Shivakumar and A. Bhargava. Failure Mechanics of a Composite Laminate Embedded with a Fiber Optic Sensor. *Journal of Composite Materials*, 39(9):777–798, May 2005. doi: 10.1177/0021998305048156.

[204] M. Salvetti, C. Sbarufatti, A. Gilioli, M. Dziendzikowski, K. Dragan, A. Manes, and M. Giglio. On the mechanical response of CFRP composite with embedded optical fibre when subjected to low velocity impact and CAI tests. *Composite Structures*, 179:21–34, November 2017. doi: 10.1016/j.compstruct.2017.07.063.

[205] D. Griffin, A. Aktas, M. Lodeiro, T. Young, I. Hamerton, and I. Partridge. A comparison of material state monitoring techniques applied to resin transfer moulding. In *21st International Conferences on Composite Materials*, Xi'an, China, August 2017.

[206] D. Griffin, S. Wood, and I. Hamerton. Measurement of the glass transition temperature of an epoxy resin using principal components of Raman spectra. *Composites Part B: Engineering*, 200:108210, November 2020. doi: 10.1016/j.compositesb.2020.108210.

[207] M. R. Wisnom, L. G. Stringer, R. J. Hayman, and M. J. Hinton. Curing stresses in thick polymer composite components, Part I: Analysis. In *12th International Conference on Composite Materials*, Paris, France, July 1999.

[208] K. D. Potter. Understanding the origins of defects and variability in composites manufacture. In *17th International Conference on Composite Materials*, Edinburgh, UK, July 2009.

[209] D. W. Radford and T. S. Rennick. Separating Sources of Manufacturing Distortion in Laminated Composites. *Journal of Reinforced Plastics and Composites*, 19(8):621–641, May 2000. doi: 10.1177/073168440001900802.

[210] M. Wisnom, M. Gigliotti, N. Ersoy, M. Campbell, and K. Potter. Mechanisms generating residual stresses and distortion during manufacture of polymer–matrix composite structures. *Composites Part A: Applied Science and Manufacturing*, 37(4):522–529, April 2006. doi: 10.1016/j.compositesa.2005.05.019.

[211] L. G. Stringer, R. J. Hayman, M. J. Hinton, R. A. Badcock, and M. R. Wisnom. Curing stresses in thick polymer composite components, Part II : Management of residual stresses. In *12th International Conference on Composite Materials*, Paris, France, July 1999.

[212] I. Baran, K. Cinar, N. Ersoy, R. Akkerman, and J. H. Hattel. A Review on the Mechanical Modeling of Composite Manufacturing Processes. *Archives of Computational Methods in Engineering*, 24(2):365–395, April 2017. doi: 10.1007/s11831-016-9167-2.

[213] M. Abouhamzeh, J. Sinke, and R. Benedictus. Prediction Models for Distortions and Residual Stresses in Thermoset Polymer Laminates: An Overview. *Journal of Manufacturing and Materials Processing*, 3(4):87, October 2019. doi: 10.3390/jmmp3040087.

[214] N. Rabearison, C. Jochum, and J. Grandidier. A FEM coupling model for properties prediction during the curing of an epoxy matrix. *Computational Materials Science*, 45(3):715–724, May 2009. doi: 10.1016/j.commatsci.2008.11.007.

[215] A. Plepys and R. Farris. Evolution of residual stresses in three-dimensionally constrained epoxy resins. *Polymer*, 31(10):1932–1936, October 1990. doi: 10.1016/0032-3861(90)90019-U.

[216] S. Mukhopadhyay, M. I. Jones, and S. R. Hallett. Compressive failure of laminates containing an embedded wrinkle; experimental and numerical study. *Composites Part A: Applied Science and Manufacturing*, 73:132–142, June 2015. doi: 10.1016/j.compositesa.2015.03.012.

[217] S. Mukhopadhyay, M. I. Jones, and S. R. Hallett. Tensile failure of laminates containing an embedded wrinkle; numerical and experimental study. *Composites Part A: Applied Science and Manufacturing*, 77:219–228, October 2015. doi: 10.1016/j.compositesa.2015.07.007.

[218] M. Thor, U. Mandel, M. Nagler, F. Maier, J. Tauchner, M. G. R. Sause, and R. M. Hinterhölzl. Numerical and experimental investigation of out-of-plane fiber waviness on the mechanical properties of composite materials. *International Journal of Material Forming*, 14:19–37, January 2020. doi: 10.1007/s12289-020-01540-5.

[219] T. Wehrkamp-Richter, R. Hinterhölzl, and S. T. Pinho. Damage and failure of triaxial braided composites under multi-axial stress states. *Composites Science and Technology*, 150:32–44, September 2017. doi: 10.1016/j.compscitech.2017.07.002.

[220] M. R. Wisnom. The role of delamination in failure of fibre-reinforced composites. *Philosophical Transactions of the Royal Society A: Mathematical, Physical and Engineering Sciences*, 370: 1850–1870, April 2012. doi: 10.1098/rsta.2011.0441.

[221] D. S. Ivanov, F. Baudry, B. Van Den Broucke, S. V. Lomov, H. Xie, and I. Verpoest. Failure analysis of triaxial braided composite. *Composites Science and Technology*, 69(9):1372–1380, July 2009. doi: 10.1016/j.compscitech.2008.09.013.

[222] M. Naebe, M. M. Abolhasani, H. Khayyam, A. Amini, and B. Fox. Crack Damage in Polymers and Composites: A Review. *Polymer Reviews*, 56(1):31–69, January 2016. doi: 10.1080/15583724.2015.1078352.

[223] S. Gholizadeh. A review of non-destructive testing methods of composite materials. *Procedia Structural Integrity*, 1:50–57, 2016. doi: 10.1016/j.prostr.2016.02.008.

[224] B. Wang, S. Zhong, T.-L. Lee, K. S. Fancey, and J. Mi. Non-destructive testing and evaluation of composite materials/structures: A state-of-the-art review. *Advances in Mechanical Engineering*, 12(4):1–28, April 2020. doi: 10.1177/1687814020913761.

[225] A. S. Maxwell, W. R. Broughton, and M. J. Lodeiro. Review of Techniques for the Characterisation of Residual Stress in Polymer Composites. NPL Report DEPC MPR 056, National Physical Laboratory, December 2006.

[226] A. S. Maxwell, W. Broughton, M. Lodeiro, and R. Shaw. Measurement of Residual Stresses and Strains in Carbon Fibre Composites. NPL Report MN 7, National Physical Laboratory, April 2009.

[227] P. P. Parlevliet, H. E. Bersee, and A. Beukers. Residual stresses in thermoplastic composites—A study of the literature—Part II: Experimental techniques. *Composites Part A: Applied Science and Manufacturing*, 38(3):651–665, March 2007. doi: 10.1016/j.compositesa.2006.07.002.

[228] X. Yan and T. Ohsawa. Measurement of the internal local stress distribution of composite materials by means of laser imaging methods. *Composites*, 25(6):443–450, July 1994. doi: 10.1016/0010-4361(94)90101-5.

[229] B. Andersson, A. Sjögren, and L. Berglund. Micro- and meso-level residual stresses in glass-fiber/vinyl-ester composites. *Composites Science and Technology*, 60(10):2011–2028, August 2000. doi: 10.1016/S0266-3538(00)00099-3.

[230] M. W. Nielsen, J. W. Schmidt, J. H. Hattel, T. L. Andersen, and C. M. Markussen. In situ measurement using FBGs of process-induced strains during curing of thick glass/epoxy laminate plate: Experimental results and numerical modelling: *In situ* process-induced strains during curing of thick laminate. *Wind Energy*, 16:1241–1257, September 2012. doi: 10.1002/we.1550.

[231] K. Takagaki, S. Minakuchi, and N. Takeda. Process-induced strain and distortion in curved composites. Part I: Development of fiber-optic strain monitoring technique and analytical methods. *Composites Part A: Applied Science and Manufacturing*, 103:236–251, December 2017. doi: 10.1016/j.compositesa.2017.09.020.

[232] L. Moretti, P. Olivier, B. Castanié, and G. Bernhart. Experimental study and in-situ FBG monitoring of process-induced strains during autoclave co-curing, co-bonding and secondary bonding of composite laminates. *Composites Part A: Applied Science and Manufacturing*, 142:106224, March 2021. doi: 10.1016/j.compositesa.2020.106224.

[233] D. M. Sánchez, M. Gresil, and C. Soutis. Distributed internal strain measurement during composite manufacturing using optical fibre sensors. *Composites Science and Technology*, 120:49–57, December 2015. doi: 10.1016/j.compscitech.2015.09.023.

[234] J.-T. Tsai, J. S. Dustin, and J.-A. Mansson. Cure strain monitoring in composite laminates with distributed optical sensor. *Composites Part A: Applied Science and Manufacturing*, 125: 105503, October 2019. doi: 10.1016/j.compositesa.2019.105503.

[235] D. A. Drake, R. W. Sullivan, J. E. Spowart, and K. Thorp. Influence of cure parameters in polymer matrix composites using embedded optical fibers. *Journal of Composite Materials*, 54(19):2611–2621, August 2020. doi: 10.1177/0021998319899153.

[236] M. Mulle, F. Collombet, P. Olivier, and Y.-H. Grunevald. Assessment of cure residual strains through the thickness of carbon–epoxy laminates using FBGs, Part I: Elementary specimen. *Composites Part A: Applied Science and Manufacturing*, 40(1):94–104, January 2009. doi: 10.1016/j.compositesa.2008.10.008.

[237] M. Mulle, F. Collombet, P. Olivier, R. Zitoune, C. Huchette, F. Laurin, and Y.-H. Grunevald. Assessment of cure-residual strains through the thickness of carbon–epoxy laminates using FBGs Part II: Technological specimen. *Composites Part A: Applied Science and Manufacturing*, 40(10):1534–1544, October 2009. doi: 10.1016/j.compositesa.2009.06.013.

[238] L. Khoun, R. de Oliveira, V. Michaud, and P. Hubert. Investigation of process-induced strains development by fibre Bragg grating sensors in resin transfer moulded composites. *Composites Part A: Applied Science and Manufacturing*, 42(3):274–282, March 2011. doi: 10.1016/j.compositesa.2010.11.013.

[239] S. Minakuchi. In situ characterization of direction-dependent cure-induced shrinkage in thermoset composite laminates with fiber-optic sensors embedded in through-thickness and in-plane directions. *Journal of Composite Materials*, 49(9):1021–1034, April 2015. doi: 10.1177/0021998314528735.

[240] U. Thombansen, G. Buchholz, D. Frank, J. Heinisch, M. Kemper, T. Pullen, V. Reimer, G. Rotshteyn, M. Schwenzer, S. Stemmler, D. Abel, T. Gries, C. Hopmann, F. Klocke, R. Poprawe, U. Reisgen, and R. Schmitt. Design framework for model-based self-optimizing

manufacturing systems. *International Journal of Advanced Manufacturing Technology*, 97 (1-4):519–528, July 2018. doi: 10.1007/s00170-018-1951-8.

[241] T. Hartmann, A. Moawad, F. Fouquet, G. Nain, J. Klein, Y. L. Traon, and J.-M. Jezequel. Model-Driven Analytics: Connecting Data, Domain Knowledge, and Learning. *arXiv*, abs/1704.01320, April 2017.

[242] D. J. Branscomb. *A Machine Vision and Sensing System for Braid Defect Detection, Diagnosis and Prevention during Manufacture*. Masters Dissertation, Auburn University, Auburn, AL, USA, December 2007.

[243] D. Branscomb and D. G. Beale. Fault detection in braiding utilizing low-cost USB machine vision. *Journal of the Textile Institute*, 102(7):568–581, July 2011. doi: 10.1080/00405000.2010.498174.

[244] A. J. Hunt. *A Machine Vision System for the Real-Time Fiber Orientation Measurement of Tubular Braided Preforms*. Master of Science, University of Alberta, Department of Mechanical Engineering, 2017.

[245] V. Reimer, M. Persiyanov-Dubrov, J. Dawson, and T. Gries. Developing control systems for the radial over-braiding process. In *17th European Conference on Composites Materials*, Munich, Germany, June 2016.

[246] V. Reimer, A. S. Dyagilev, and T. Gries. Effect of Vibration Mechanism Operating Conditions on the Structure of a Braided Preform. *Fibre Chemistry*, 49(5):330–333, January 2018. doi: 10.1007/s10692-018-9892-4.

[247] Self-optimisation of the Radial Braiding Process. Technical report, RWTH Aachen University.

[248] T. von Reden. *Erweiterung der Systemgrenzen der Flechttechnik durch elektronisch gesteuerte Klöppel*. Number Band 9 in LCC / Technische Universität München. Verlag Dr. Hut, München, 1. auflage edition, 2015. ISBN 978-3-8439-2374-3.

[249] M. O. Braeuner. Klöppel für eine Flechtmaschine, Flechtmaschine sowie Verfahren zum Steuern und Regeln einer auf ein Flechtmaterial aufgebrachten Spannung, July 2016, `https://patents.google.com/patent/DE102014016381B4/de` (Accessed: March 2, 2020).

[250] S. Maidl, M. Sabieraj, A. Mierzwa, C. Ebel, and K. Drechsler. Investigating the unwinding behavior of technical yarns and development of a new sensor system for the braiding process. In *13th International Conference on Textile Composites (TEXCOMP-13)*, volume 406 of *IOP*

Conference Series: Materials Science and Engineering, page 012065, Milan, Italy, September 2018. doi: 10.1088/1757-899X/406/1/012065.

[251] S. Maidl, A. Mierzwa, C. Ebel, and K. Drechsler. Development of a novel type of online monitoring system for the braiding process. In *18th Europeam Conference on Composite Materials*, Athens, Greece, June 2018.

[252] S. Maidl, Á. Fernández Villalba, K. Kind, and K. Drechsler. Development of sensor integrated braiding rings for the automated detection of braiding defects. *Materials Today: Proceedings*, 34(1):74–81, January 2020. doi: 10.1016/j.matpr.2020.01.194.

[253] M. Braley and M. Dingeldein. Advancements in braided materials technology. Technical report, A&P Technology, Inc., Cincinnati, Ohio 45245, 2005.

[254] Y. Liu and Y. Kyosev. Automatic analysis the braiding angle of the braided fabrics using image processing. In *22nd International Conference STRUTEX*, pages 63–68, December 2018.

[255] W. Zhenkai and L. Jialu. Braided angle measurement technique for three-dimensional braided composite material preform using mathematical morphology and image texture. *AUTEX Research Journal*, 6(1):10, March 2006.

[256] M. Tàpias, M. Ralló, and J. Escofet. Automatic measurements of partial cover factors and yarn diameters in fabrics using image processing. *Textile Research Journal*, 81(2):173–186, January 2011. doi: 10.1177/0040517510380107.

[257] R. Schmitt, T. Pfeifer, C. Mersmann, and A. Orth. A method for the automated positioning and alignment of fibre-reinforced plastic structures based on machine vision. *CIRP Annals - Manufacturing Technology*, 57(1):501–504, 2008. doi: 10.1016/j.cirp.2008.03.128.

[258] R. Schmitt, T. Fürtjes, B. Abbas, P. Abel, W. Kimmelmann, P. Kosse, and A. Buratti. Real-Time Machine Vision System for an Automated Quality Monitoring in Mass Production of Multiaxial Non-Crimp Fabrics. *IFAC-PapersOnLine*, 48(3):2393–2398, 2015. doi: 10.1016/j.ifacol.2015.06.446.

[259] S. Thumfart, W. Palfinger, M. Stöger, and C. Eitzinger. Accurate Fibre Orientation Measurement for Carbon Fibre Surfaces. In R. Wilson, E. Hancock, A. Bors, and W. Smith, editors, *Computer Analysis of Images and Patterns*, volume 8048 of *Lecture Notes in Computer Science*, pages 75–82. Springer, Berlin, Heidelberg, 2013. ISBN 978-3-642-40246-3.

[260] L. Veldenz. *Automated Dry Fibre Placement and Infusion Process Development for Complex Geometries*. PhD thesis, University of Bristol, Bristol, UK, January 2019.

[261] S. Woodward, S. Brown, and M. McCarthy. Good practice guide for generating high-density 3D point-cloud data sets of complex freeform machined surfaces using optical scanning techniques positioned directly on the machine tool. Technical Report IND62 TIM, EURAMET.

[262] R. Schmitt, A. Orth, and C. Niggemann. A method for edge detection of textile preforms using a light-section sensor for the automated manufacturing of fibre-reinforced plastics. In *Proceedings of SPIE*, volume 661609, Munich, Germany, June 2007. doi: 10.1117/12.726177.

[263] R. Bitter, T. Mohiuddin, and M. Nawrocki. *LabView Advanced Programming Techniques*. CRC Press/Taylor & Francis Group, Boca Raton, FL, 2nd ed edition, 2007. ISBN 978-0-8493-3325-5.

[264] G. Bradski. The OpenCV Library, `http://www.drdobbs.com/open-source/the-opencv-library/184404319` (Accessed: December 4, 2020).

[265] P. Virtanen, R. Gommers, T. E. Oliphant, M. Haberland, T. Reddy, D. Cournapeau, E. Burovski, P. Peterson, W. Weckesser, J. Bright, S. J. van der Walt, M. Brett, J. Wilson, K. J. Millman, N. Mayorov, A. R. J. Nelson, E. Jones, R. Kern, E. Larson, C. J. Carey, İ. Polat, Y. Feng, E. W. Moore, J. VanderPlas, D. Laxalde, J. Perktold, R. Cimrman, I. Henriksen, E. A. Quintero, C. R. Harris, A. M. Archibald, A. H. Ribeiro, F. Pedregosa, P. van Mulbregt, SciPy 1.0 Contributors, A. Vijaykumar, A. P. Bardelli, A. Rothberg, A. Hilboll, A. Kloeckner, A. Scopatz, A. Lee, A. Rokem, C. N. Woods, C. Fulton, C. Masson, C. Häggström, C. Fitzgerald, D. A. Nicholson, D. R. Hagen, D. V. Pasechnik, E. Olivetti, E. Martin, E. Wieser, F. Silva, F. Lenders, F. Wilhelm, G. Young, G. A. Price, G.-L. Ingold, G. E. Allen, G. R. Lee, H. Audren, I. Probst, J. P. Dietrich, J. Silterra, J. T. Webber, J. Slavič, J. Nothman, J. Buchner, J. Kulick, J. L. Schönberger, J. V. de Miranda Cardoso, J. Reimer, J. Harrington, J. L. C. Rodríguez, J. Nunez-Iglesias, J. Kuczynski, K. Tritz, M. Thoma, M. Newville, M. Kümmerer, M. Bolingbroke, M. Tartre, M. Pak, N. J. Smith, N. Nowaczyk, N. Shebanov, O. Pavlyk, P. A. Brodtkorb, P. Lee, R. T. McGibbon, R. Feldbauer, S. Lewis, S. Tygier, S. Sievert, S. Vigna, S. Peterson, S. More, T. Pudlik, T. Oshima, T. J. Pingel, T. P. Robitaille, T. Spura, T. R. Jones, T. Cera, T. Leslie, T. Zito, T. Krauss, U. Upadhyay, Y. O. Halchenko, and Y. Vázquez-Baeza. SciPy 1.0: Fundamental algorithms for scientific computing in Python. *Nature Methods*, 17(3):261–272, March 2020. doi: 10.1038/s41592-019-0686-2.

[266] H. Scharr. Optimal Filters for Extended Optical Flow. In B. Jähne, R. Mester, E. Barth, and H. Scharr, editors, *Complex Motion*, volume 3417 of *Lecture Notes in Computer Science*, pages 14–29. Springer, Berlin, Heidelberg, 2007. ISBN 978-3-540-69864-7 978-3-540-69866-1. doi: 10.1007/978-3-540-69866-1_2.

[267] D.-J. Kroon. Numerical optimization of kernel based image derivatives. December 2009.

[268] J. E. Bresenham. Algorithm for computer control of a digital plotter. *IBM Systems Journal*, 4(1):25–30, 1965. doi: 10.1147/sj.41.0025.

[269] J. Fox. Robust regression. In *An R and S-Plus Companion to Applied Regression*. Sage Publications, Thousand Oaks, CA, USA, 2002. ISBN 978-0-7619-2279-7 978-0-7619-2280-3.

[270] N. K. Naik and V. Madhavan. Twisted impregnated yarns: Elastic properties. *Journal of Strain Analysis for Engineering Design*, 35(2):83–91, February 2000. doi: 10.1243/0309324001514044.

[271] D. Branscomb, D. Beale, and R. Broughton. New Directions in Braiding. *Journal of Engineered Fibers and Fabrics*, 8(2):11–24, June 2013. doi: 10.1177/155892501300800202.

[272] J. Schindelin, I. Arganda-Carreras, E. Frise, V. Kaynig, M. Longair, T. Pietzsch, S. Preibisch, C. Rueden, S. Saalfeld, B. Schmid, J.-Y. Tinevez, D. J. White, V. Hartenstein, K. Eliceiri, P. Tomancak, and A. Cardona. Fiji: An open-source platform for biological-image analysis. *Nature Methods*, 9(7):676–682, July 2012. doi: 10.1038/nmeth.2019.

[273] Hugin - Panorama photo stitcher, `http://hugin.sourceforge.net/` (Accessed: March 27, 2020).

[274] G. A. Atkinson and J. D. Ernst. High-sensitivity analysis of polarization by surface reflection. *Machine Vision and Applications*, 29(7):1171–1189, October 2018. doi: 10.1007/s00138-018-0962-7.

[275] Evaluation of measurement data — Supplement 1 to the "Guide to the expression of uncertainty in measurement" — Propagation of distributions using a Monte Carlo method. Technical Report JCGM 101:2008, JCGM, 2008.

[276] M. Matsumoto and T. Nishimura. Mersenne twister: A 623-dimensionally equidistributed uniform pseudo-random number generator. *ACM Transactions on Modeling and Computer Simulation*, 8(1):3–30, January 1998. doi: 10.1145/272991.272995.

[277] S. van der Walt, J. L. Schönberger, J. Nunez-Iglesias, F. Boulogne, J. D. Warner, N. Yager, E. Gouillart, and T. Yu. Scikit-image: Image processing in Python. *PeerJ*, 2:e453, June 2014. doi: 10.7717/peerj.453.

[278] F. Pedregosa, G. Varoquaux, A. Gramfort, V. Michel, B. Thirion, O. Grisel, M. Blondel, P. Prettenhofer, R. Weiss, V. Dubourg, J. Vanderplas, A. Passos, D. Cournapeau, M. Brucher,

M. Perrot, and É. Duchesnay. Scikit-learn: Machine Learning in Python. *Journal of Machine Learning Research*, 12:2825–2830, November 2011.

[279] Evaluation of measurement data — Guide to the expression of uncertainty in measurement. Technical Report JCGM 100:2008, JCGM, 2008.

[280] S. Lomov, A. Gusakov, G. Huysmans, A. Prodromou, and I. Verpoest. Textile geometry preprocessor for meso-mechanical models of woven composites. *Composites Science and Technology*, 60(11):2083–2095, August 2000. doi: 10.1016/S0266-3538(00)00121-4.

[281] B. Verleye, S. Lomov, A. Long, I. Verpoest, and D. Roose. Permeability prediction for the meso–macro coupling in the simulation of the impregnation stage of Resin Transfer Moulding. *Composites Part A: Applied Science and Manufacturing*, 41(1):29–35, January 2010. doi: 10.1016/j.compositesa.2009.06.011.

[282] ESI Group. PAM-RTM - Resin Molding Software Module for PAM-COMPOSITES, `https://www.esi-group.com/products/composites` (Accessed: June 27, 2021).

[283] J. Cichosz. *Experimental Characterization and Numerical Modeling of the Mechanical Response for Biaxial Braided Composites*. PhD thesis, Technical University of Munich, Faculty of Mechanical Engineering, January 2016.

[284] Q. Zhang, D. Beale, and R. M. Broughton. Analysis of Circular Braiding Process, Part 1: Theoretical Investigation of Kinematics of the Circular Braiding Process. *Journal of Manufacturing Science and Engineering*, 121(3):345–350, August 1999. doi: 10.1115/1.2832687.

[285] Q. Zhang, D. Beale, R. M. Broughton, and S. Adanur. Analysis of Circular Braiding Process, Part 2: Mechanics Analysis of the Circular Braiding Process and Experiment. *Journal of Manufacturing Science and Engineering*, 121(3):351–359, August 1999. doi: 10.1115/1.2832688.

[286] A. Mazzawi. *The Steady State and Transient Behaviour of Two-Dimensional Braiding.* PhD thesis, University of Ottawa, Ottowa, Canada, December 2001.

[287] J. van Ravenhorst and R. Akkerman. A yarn interaction model for circular braiding. *Composites Part A: Applied Science and Manufacturing*, 81:254–263, February 2016. doi: 10.1016/j.compositesa.2015.11.026.

[288] R. Leach. Mapping metrology intelligently. *Materials World*, 28(9):50–52, September 2020.

Appendix A

Published journal article: Measurement of the glass transition temperature of an epoxy resin using principal components of Raman spectra

Composites Part B 200 (2020) 108210

Contents lists available at ScienceDirect

Composites Part B

journal homepage: www.elsevier.com/locate/compositesb

Measurement of the glass transition temperature of an epoxy resin using principal components of Raman spectra

Daniel Griffin [a,b,*], Sebastian Wood [a], Ian Hamerton [b]

[a] National Physical Laboratory, Hampton Road, Teddington, Middlesex, TW11 0LW, UK
[b] Bristol Composites Institute (ACCIS), Department of Aerospace Engineering, School of Civil, Aerospace, and Mechanical Engineering, Queen's Building, University Walk, University of Bristol, Bristol, BS8 1TR, UK

ARTICLE INFO

Keywords:
Thermosetting resin
Thermal properties
Analytical modelling
Cure Raman spectroscopy

ABSTRACT

Many fibre reinforced polymer (FRP) composite manufacturing processes benefit from the ability to monitor the polymerisation of the resin constituent, either for process control or quality assurance purposes. Whilst most available resin monitoring systems achieve this by measuring the percentage conversion of reactants, measurement of the corresponding glass transition temperature, *Tg*, is often more informative. The ability to measure *Tg* directly from spectra acquired by Raman spectroscopy, using principal components analysis, has been demonstrated here for an amine-cured epoxy resin system.

A regression model was generated using principal components identified from spectra acquired of cured resin samples produced at a range of isothermal conditions, regressed against corresponding *Tg* values measured by dynamic scanning calorimetry (DSC). Spectra acquired during the cool-down period following completion of one trial were incorporated into the calibration dataset to ensure effects of sample temperature were accounted for in the principal components analysis (PCA). Measurements obtained with the resultant model, generated using 5 principal components accounting for 97% of the variance in the calibration dataset, were shown to agree well with final sample DSC measurements from *in situ* cure trials, differing by $\leq$ 0.6 °C, and exhibiting negligible sensitivity to sample temperature.

The results demonstrate the potential of Raman spectroscopy coupled with PCA as a non-contact cure monitoring technique, able to directly measure *Tg* of a thermosetting epoxy resin system typical of those used in FRP composites manufacture, independent of sample temperature.

1. Introduction

The performance of fibre-reinforced polymer (FRP) composite materials often employed in aerospace, marine and, increasingly, automotive and wind energy structures, is partly dependent on the physical and chemical properties of the polymeric matrix constituent. For the most part, matrices are produced from thermosetting resins, concurrent with the form of the structure itself, via thermal activation. A specific thermal profile is applied during the manufacture process to ensure that the polymerisation reaction proceeds to an extent such that the required properties in the resultant cross-linked polymer are achieved.

A number of techniques that enable the formation of the matrix from thermosetting resins to be monitored *in situ* during the manufacture process, typically measured as the degree of cure, α, or conversion of reactants to products, have been developed and demonstrated. Established examples include dielectric analysis (DEA) [1–4], electrical resistivity [5–7], and ultrasound [8–10], which monitor the evolution of a physical property, i.e. electrical or acoustic impedance respectively.

Since the physical properties measured depend on sample temperature, concurrent temperature measurements are required in order to thermally calibrate the sensor signal. These techniques also tend to require physical contact with the material under test, i.e. the composite product, which is not always feasible or desirable.

Whilst α can be valuable information for the process operator, to ensure that the polymerisation has proceeded as desired before progressing to subsequent production stages, greater value lies in the determination of the glass transition temperature, T_g, of the polymer product, as it is this material property which is critical to the products

* Corresponding author. Bristol Composites Institute (ACCIS), Department of Aerospace Engineering, School of Civil, Aerospace, and Mechanical Engineering, Queen's Building, University Walk, University of Bristol, Bristol, BS8 1TR, UK.
E-mail address: daniel.griffin@bristol.ac.uk (D. Griffin).

https://doi.org/10.1016/j.compositesb.2020.108210
Received 18 February 2020; Received in revised form 21 May 2020; Accepted 3 June 2020
Available online 10 August 2020
1359-8368/

mechanical performance. Determination of T_g from the measurement system usually requires a model describing the relationship between α and T_g, often captured in the form of the DiBenedetto equation [11–13], and thus involves additional material characterisation and uncertainty propagation.

An alternative set of techniques that has been less extensively researched in the context of FRP composites manufacture applications, but which offers the potential advantages of non-contact measurement and reduced thermal sensitivity, is vibrational spectroscopy [14–18]. Of these, Raman spectroscopy is particularly well-suited to in-process applications given the lack of prerequisite sample preparation [19] and the flexibility of optical configuration, as illustrated by its widespread deployment in process analytical technology (PAT) applications across a range of industries [20,21].

The majority of studies conducted into monitoring the production of thermoset polymers with Raman spectroscopy have looked to correlate changes in individual spectral peaks with established methods for measurement of α. Merad et al. [22] and Hardis et al. [23] compared α measurements for amine-cured epoxy resins under isothermal conditions calculated from the reduction in epoxide peak area with those obtained using dynamic scanning calorimetry (DSC), and both DSC and DEA respectively. Both reported good correlation between the methods, despite the differing physical phenomena measured by each, although the strength of correlation was found to exibit some temperature dependence. Cruz and Osswald [24] utilised the depletion of a less prominent, epoxide-associated CH_2 group to monitor reaction rates of a different amine-cured epoxy resin system under elevated pressures. They, as well as Skrifvars et al. [25], achieved similar results for unsaturated polyester and vinyl ester resins via the depletion of peaks attributed to reactive C=C groups, although neither made comparison with alternative methods.

In each of these studies, a spectral peak attributed to either a reactive or emergent functional group was identified, whose concentration and therefore peak intensity varied through the reaction. The ratio of this peak area against that of an internal reference peak, i.e. a spectral peak which remained constant over the course of the reaction, was then correlated with α. This univariate approach relies on an understanding of the underlying reaction chemistry to identify a suitable, unimpeded reactant or product peak to monitor; it also discards the remainder of the spectral data, which is likely to hold further value in reducing measurement uncertainty.

Other studies have implemented principal components analysis (PCA), a multivariate analysis method that has been shown to enable prediction of a range of polymer material properties [26–28], to develop regression models for α measurement from Raman spectra of thermosetting resin. Aust [29] generated models for amine-cured epoxy resins utilising single principal components (PC) of the acquired spectral datasets, shown to account for > 95% of sample variance. Calibrations were conducted against heat of reaction measurements made by DSC to enable determination of α. The models were subsequently applied to bulk and industrial samples with a quoted uncertainty of ± 0.54% and ± 0.82% cure respectively. However, the measurements did not account for the potential influence of temperature gradients on % cure evolution, given that calibration samples were collected under isothermal conditions but were applied to bulk samples produced at different temperatures, which also experienced significant exotherms (i.e. increase of 90 °C). Cooper [30] highlighted a major benefit of utilising multivariate analysis in model generation by demonstrating the reduction in measurement scatter that can be achieved in comparison to a selection of single peak, univariate models, for which interference of overlapping spectral peaks was shown to be an issue. A regression model for a cyanate ester resin system was generated utilising a single PC, identified from spectra collected at the start and end of sample production, regressed against assumed α of 0% and 100% respectively. However, since the initial (i.e. reactants) and final (i.e. product) spectra used for model calibration were acquired at different temperatures (20 °C vs 180 °C), the model would have been unable to distinguish spectral changes due to reaction progress from those due to sample temperature variation, thus incorporating temperature sensitivity into the resultant measurements.

The studies reviewed demonstrate the capability of Raman spectroscopy as a technique to monitor the progression of polymerisation reactions for a range of thermoset polymers, and the advantages of utilising PCA to do so. This paper expands on the research to date by investigating the use of PCA, and subsequent principal components regression (PCR) modelling, to enable measurement T_g for a thermosetting epoxy resin system directly from Raman spectra collected *in situ* during the curing process, without prior determination of α. In doing so, the ability to distinguish between configurational (i.e. chemical) and conformational (i.e. physical) changes in spectra is explored, as required in order to correlate spectral changes due to reaction progress with T_g, independently of conformational changes due to thermal gradients. Thus the potential for temperature insensitive, non-contact T_g measurement is assessed.

2. Experimental methods

2.1. Model development

This study was conducted using a 2-part amine-cured epoxy resin, Gurit PRIME 20LV, with PRIME Slow hardener, the predominant reactive constituents of which are shown in Fig. 1 and Fig. 2 respectively. Resin samples for initial, isothermal model calibration were prepared in standard aluminium DSC sample pans, to enable subsequent conditioning and analysis activities to be conducted without further sample manipulation. A mixture of the two resin components was prepared at a ratio of 0.26 by weight (hardener:resin), stirred for 5 min at room temperature and degassed for a further 5 min. Aliquots of the mixture, ~25 mg ± 5 mg, were transferred to pre-weighed aluminium DSC sample pans, which were sealed with hermetic lids. The sealed sample pans were then transferred to a freezer at −18 °C within 1 h of initial mixing to inhibit reaction progress during storage.

A DSC (TA Instruments Q2000) was used to cure the resin samples under controlled, isothermal conditions. Sample pans were individually removed from the freezer, the lid removed, pan and sample weighted, and the pan loaded into the DSC cell. The sample was cured under isothermal conditions until the reaction had ceased, as indicated by a plateau in the heat flow trace. This was conducted under a nitrogen atmosphere, and the cure temperatures and times used are given in Table 1; a temperature ramp of 100 °C/min was used to reach the desired temperature in all cases. The total time between removal of sample from the freezer and commencing the DSC program did not exceed 10 min for any sample.

Following isothermal curing in the DSC, sample pans were transferred to a benchtop confocal Raman micro-spectrometer (Horiba LabRAM HR800 Evolution) for analysis. Raman spectroscopy was conducted under ambient conditions, using a 633 nm laser source (24 mW intensity at sample, 150 lines/mm grating giving 1.2 cm^{-1} spectral resolution, 50 × NA 0.45 long working-distance objective) focussed on the sample surface to obtain spectra across the range 620 cm^{-1} - 1720 cm^{-1}. The excitation wavelength was selected on the basis that the

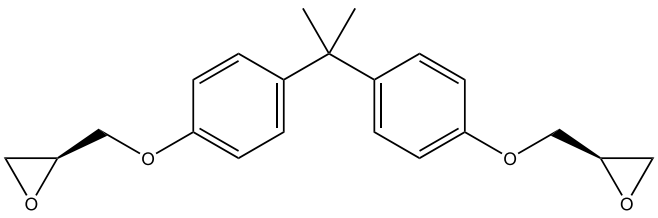

Fig. 1. Epoxide constituent of the resin system.

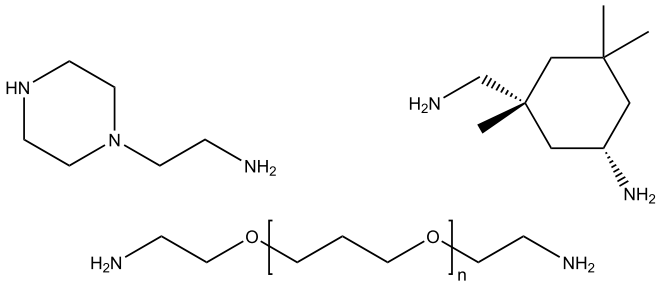

Fig. 2. Major amine constituents of the resin system.

Table 1
Isothermal cure profiles of the calibration samples.

Cure temperature (°C)	Cure time (h)
40	18
50	12
60	12
70	8
80	6
90	6

sample material was transparent to this wavelength and did not exhibit significant fluorescence; alternative wavelengths may be more optimal for other sample materials. Four spectra were collected per sample, each at different locations, and each the mean of 5 × 10 s acquisitions. Averaging of multiple spectra assisted in the removal of spikes from cosmic ray detection as well as improving the signal-to-noise ratio.

Sample pans were then returned to the DSC to measure glass transition temperature, *Tg*, and residual heat of reaction, H, using a temperature ramp of 10 °C/min between 25 °C and 300 °C. *Tg*, DSC was measured as the point of inflection in the heat flow trace; these values were assigned to the corresponding Raman spectra.

In order to incorporate the anticipated effects of sample temperature on Raman spectra, and hence mitigate model sensitivity to these effects, the initial isothermal calibration dataset was expanded to include spectra acquired during the cool-down period of an *in situ* monitoring trial, as described in the 2.2. Specifically, spectra from Trial B corresponding to sample temperatures in the range 75 °C - 30 °C at 5 °C intervals were added; all were assigned the $T_{g,\ DSC}$ for the cured sample, assuming a constant T_g over this period.

Pre-processing of Raman spectra as well as principal components analysis and regression modelling activities were conducted in MATLAB. For consistency, pre-processing was automated using parameters determined during an initial review of the spectra. The procedures and parameters applied were as follows:

- interpolation to integer wavenumbers using a cubic spline interpolation to enable direct comparison between spectral intensities;
- smoothing with a Savitzky-Golay filter (3rd order polynomial, window size = 11);
- baseline subtraction, using a robust, 2nd order polynomial, local regression method, rloess (window size = 180 and step size = 100) to fit the baseline;
- normalisation of spectral intensity to the peak area between 1560 cm^{-1} - 1640 cm^{-1}.

The region of the spectra utilised for normalisation centred around the peak at 1605 cm^{-1}, attributed to a ring stretching mode of unreactive phenyl groups [23,31], which was assumed to remain constant throughout the course of the polymerisation.

Principal components analysis was conducted on an $n \times m$ matrix containing the pre-processed calibration spectra set, with n being the number of variables, i.e. Raman shift wavenumbers per spectra, and m the number of observations, i.e. number of spectra in the dataset. The analysis produced a series of principal components, each comprising a vector of coefficients, one per wavenumber, describing the relative contribution of each wavenumber to the PC, and a corresponding vector of loadings, one per observation (i.e. spectrum), quantifying the contribution of the PC to each spectrum. Components returned by PCA are those that best explain the variance between observations, arranged in descending order of percentage variance explained.

$$\begin{bmatrix} C_{1,1} & \cdots & C_{1,p} \\ \vdots & \ddots & \vdots \\ C_{n,1} & \cdots & C_{n,p} \end{bmatrix} \cdot \begin{bmatrix} B_1 \\ \vdots \\ B_p \end{bmatrix} = \begin{bmatrix} M_1 \\ \vdots \\ M_n \end{bmatrix} \quad (1)$$

For principal components regression, the PCA-derived loadings for a chosen number, p, of PCs were regressed against the mean-centred values of sample T_g. The scalar product of the resulting regression coefficients, B, with the corresponding PC coefficients, C, produced a vector of model coefficients, one per wavenumber, as outlined in Equation (1). Mean-centring was then reversed to generate the PCR model.

In order to minimise model complexity and avoid over-fitting, whilst also maximising accuracy, Mean Squared Error of Prediction (MSEP) was used to assess the predictive accuracy of regression models generated with increasing number of principal components.

2.2. Application

For *in situ* spectroscopic monitoring of resin cure, a heated stage supplied by Synthesites and equipped with a Jumo dTRON temperature controller was used in conjunction with the benchtop Horiba Raman spectrometer. A small quantity of resin mixture, ~ 0.5 mL, was added to a reservoir on top of the heated stage, comprising a pair of stacked silicone rings washers clamped to the stage surface. The stage was positioned such that the sample reservoir was in the focal path of the spectrometer; the excitation laser was focused 100 μm below the surface of the resin sample to ensure that the con-focal detection volume remained within the sample bulk throughout the curing process despite the anticipated volumetric changes (i.e. thermal and phase changes). The spectrometer setup described in Section 2.1 was used, with the exception that each measurement was the mean of 10 × 5 s acquisitions. Measurements were collected from the same sample location every 60 s for the duration of each resin cure.

Resin cure trials were conducted according to the temperature profiles outlined in Table 2, and consisted of a dwell period, *Di*, at the initial cure temperature, *Ti*, followed by a temperature ramp at rate *R* to the post-cure temperature, T_{pc}, for a second dwell period, D_{pc}. The profiles were programmed using the temperature controller of the heated stage, with the initial controller setpoint equal to *Ti* for each profile. A new resin mixture was prepared for each trial according to the procedure described in Section 2.1, after which a sample was transferred to the heated stage with a pipette. Once the resin sample had been positioned, the heater programme was initiated, followed by the Raman acquisition. Upon completion of the programmed cure profile, the heated stage and cured sample were left to cool down to room temperature; collection of spectra continued during this period.

Table 2
Cure profiles used during *in situ* monitoring trials.

Trial	A	B	C
Ti (°C)	65	65	50
Di (min)	840	420	720
R (°C/min)	–	2	2
Tpc (°C)	–	80	80
Dpc (min)	–	180	360

$$\begin{bmatrix} I_1 \\ \vdots \\ I_n \end{bmatrix} \cdot \begin{bmatrix} M_1 \\ \vdots \\ M_n \end{bmatrix} = T_{g,\mathrm{PCR}} \quad (2)$$

Each collected spectrum was pre-processed according to the procedures and parameters outlined for the calibration spectra in Section 2.1 before the PCR model was applied to produce a Raman-derived measurement of sample glass transition temperature, *Tg*,PCR. This was achieved by evaluating the dot product of the model vector with the corresponding vector of Raman spectral intensities, as outlined in Equation (2).

Tg, DSC measurement of *in situ* cured samples was conducted following removal of the sample from the heated stage. A small piece, 13 mg ± 5 mg, was removed from the cured sample and added to a Tzero aluminium DSC pan with lid. A temperature ramp of 10 °C/min from 25 °C to 300 °C was used for the DSC analysis, with *Tg* measured as the point of inflection of the heat flow trace. A minimum of 3 measurements were performed per sample.

3. Results and discussion

3.1. Model development

The set of spectra used for model calibration are presented in Fig. 3, as collected and after pre-processing. The region of the spectra used for normalisation is indicated by dashed vertical lines. The corresponding glass transition temperatures for isothermally cured samples are shown in Fig. 4. These show an increase in *Tg* with increasing cure temperature up to 70 °C, at which temperature the *Tg* is comparable to that reported by the resin manufacturer for the recommended cure cycle (16 h at 50 °C) of 82.6 °C (DMTA - peak tan delta). Above 70 °C no further increase in *Tg* was observed; however, spectral changes in the regions of 1100 cm^{-1} and 1500 cm^{-1} were observed. These are likely to indicate undesirable chemical changes resulting from curing the resin above the manufactures recommended temperature range, 50 °C - 65 °C.

Principal components analysis of the calibration spectra set identified five principal spectral components which accounted for 97% of variance between the spectra, as plotted in Fig. 5, with all subsequent components accounting for ≤ 0.5% of the total variance per component. Using *K*-fold cross-validation ($k = 10$), the Mean Squared Error of Prediction (MSEP) for PCR models incorporating the first *p* components was estimated for *p* in range 1–10. MSEP values, also plotted in Fig. 5, exhibited a large reduction upon inclusion of the fifth PC, from 10.2

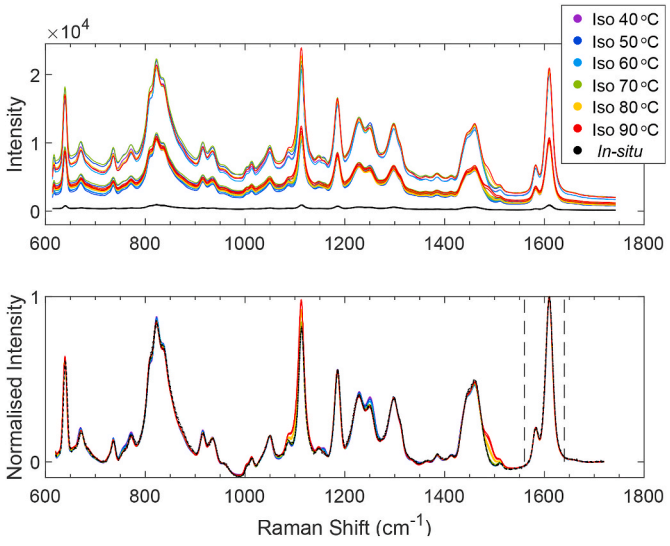

Fig. 3. Raman spectra of calibration samples: as collected (top); after pre-processing (bottom).

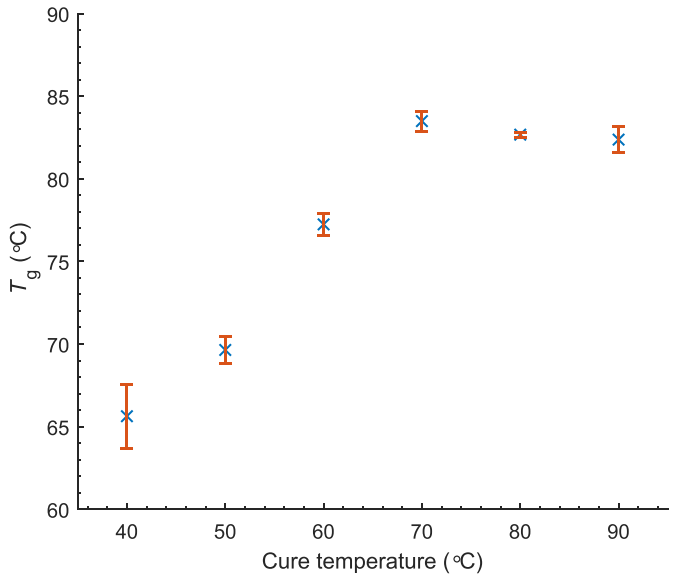

Fig. 4. *Tg* of isothermal calibration samples as measured by DSC, including standard error of the mean.

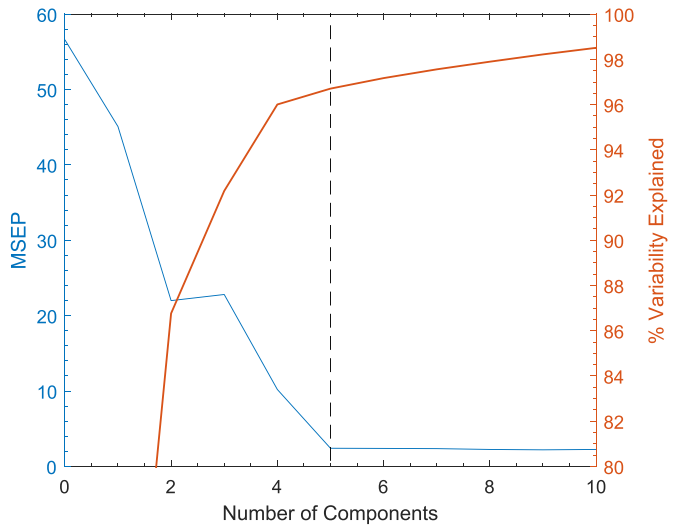

Fig. 5. MSEP and % explained variability against number of principal components (top).

°C²–2.4 °C², with negligible further reduction seen beyond that. Hence, PCR model generation using the first five principal components was judged to represent the optimal compromise between model complexity and measurement accuracy.

Application of the 5-component model to the calibration spectra set produced a strong correlation between Raman-derived, *Tg*, PCR, and *Tg*, DSC measurements, with correlation coefficient, *R2*, = 0.97 and root mean-squared error, *RMSE*, = 1.28 °C. Table 3 presents the regression coefficients calculated for the selected PCs, whilst the corresponding component coefficients are presented Fig. 6 (top), along with those of the resulting PCR model (bottom). It should be noted that the relative magnitudes of PC coefficients (Fig. 6 top) are not representative of PC contributions to the PCR model (Fig. 6 bottom); this is determined by the regression coefficients (Table 3).

A number of spectral regions dominate the five components:

Table 3
Regression coefficients for corresponding PC loadings against sample *Tg*, DSC measurements.

Principal component	Regression coefficient
PC1	10.0
PC2	−22.3
PC3	−4.63
PC4	−39.1
PC5	70.1

- multiple overlapping peaks between 700 cm^{-1} - 900 cm^{-1}, likely to correspond to C-*O*-C and C-N-C symmetric bond stretches [32,33], as well as C-C chain and aromatic ring vibrational modes;
- multiple overlapping peaks in the region 1100 cm^{-1} - 1300 cm^{-1}, again corresponding to C-C chain and aromatic ring vibrational modes, as well as a contribution at ~ 1255 cm^{-1} attributed to the symmetric stretch of the epoxide functional group [32] often utilised in univariate reaction monitoring studies;
- multiple overlapping peaks between 1400 cm^{-1} - 1550 cm^{-1} corresponding to spectral regions dominated by -CH_2 and -CH_3 vibrational modes [34];
- peaks at around 640 cm^{-1} and 1610 cm^{-1}, corresponding to aromatic ring bend and stretch modes respectively [35];
- peaks at ~ 1110 cm^{-1} and 1490 cm^{-1}, particularly prevalent in PC1, which correspond to the regions at which spectral changes were observed for the 80 °C and 90 °C isothermal calibration samples.

In general, the same regions can be seen to dominate the PCR model coefficients; whilst the large negative coefficients around 1255 cm^{-1} indicate the expected model sensitivity to reduction of the epoxide functional group, comparable coefficient magnitudes across the regions 700 cm^{-1} - 900 cm^{-1}, 1100 cm^{-1} - 1300 cm^{-1} and 1400 cm^{-1} - 1550 cm^{-1} highlight the significant predictive power of peaks within these spectral regions, many of which are attributed to non-reactive functional groups, which would otherwise be neglected by univariate methods. This suggests that the model is sensitive to conformational rearrangements resulting from the polymerisation reaction, as well as to changes in the chemical structure.

Relatively small coefficients at ~1110 cm^{-1} and 1490 cm^{-1} suggest low model sensitivity to the spectral changes observed for isothermal cures at 80 °C and 90 °C. This is a combined result of the inclusion of those samples in the calibration data set and the relatively small regression coefficient calculated for PC1. Similarly, inclusion of spectra for varying sample temperatures, i.e. those taken from the cool-down period following one of the *in-situ* cure trials presented in Section 3.2, was intended to capture thermal effects on sample spectra in the model calibration and thus reduce model sensitivity to sample temperature. A full spectral interpretation of these thermal effects is beyond the scope of this paper, but we would expect anharmonicity of Raman active modes to result in a shift of the peaks towards lower vibrational energies, as well more complex spectral changes arising from thermally-induced molecular conformational changes. It was found that omission of these spectra during PCA decreased the number of components required to explain 97% of sample variance from 5 to 3, whilst the resulting PCR model exhibited greater dominance of distinct peaks, with reduced broad-band contribution. The corresponding three component PCR model is presented in supplementary data.

3.2. Application

To evaluate model performance for *in situ* measurement of sample *Tg*, the PCR model was applied to the time series spectra collected during three cure trials with different cure profiles. The results for each of the three trials, A, B and C, are shown in Fig. 7, plotted alongside sample temperature, with the final *Tg*, DSC values indicated by dashed horizontal lines. Since model calibration was conducted with cured, glassy samples cured within the temperature range 40 °C–90 °C, *Tg*, PCR values have only been presented for $Tg \geq 40$ °C and therefore values for early stages of the trials are omitted. Model calibration would need to be extended to include samples corresponding to these early cure states in

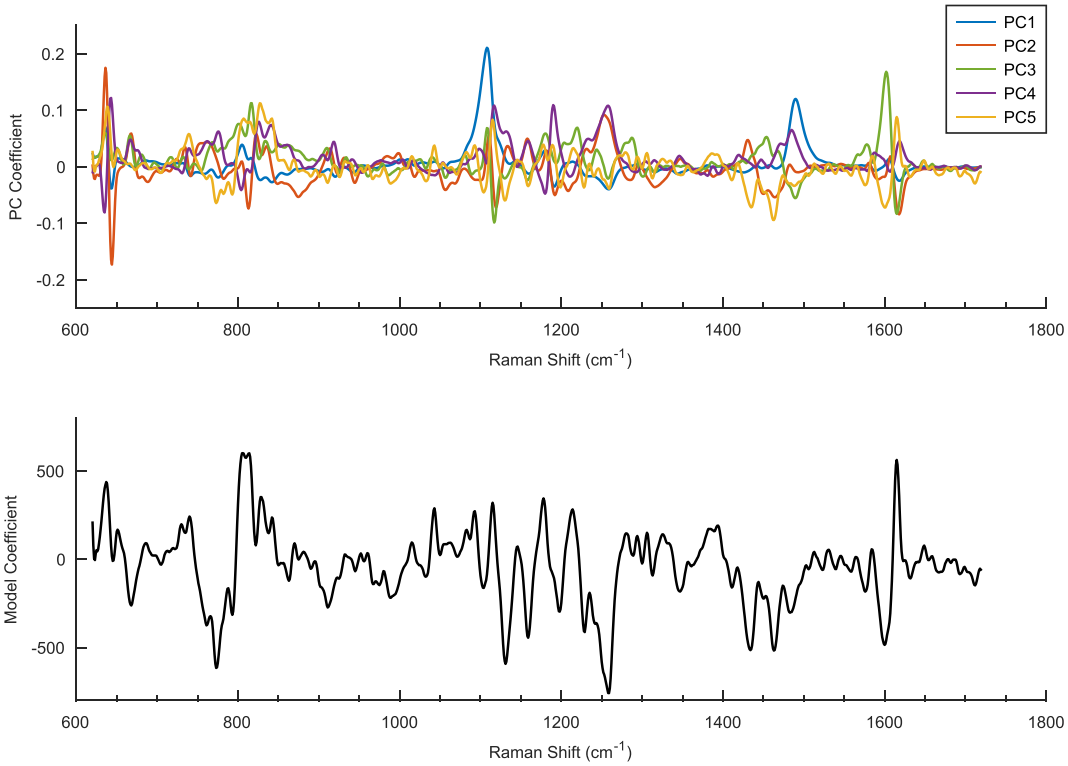

Fig. 6. Principal component coefficients for the first 5 PCs (top); model coefficients for the resulting PCR model (bottom).

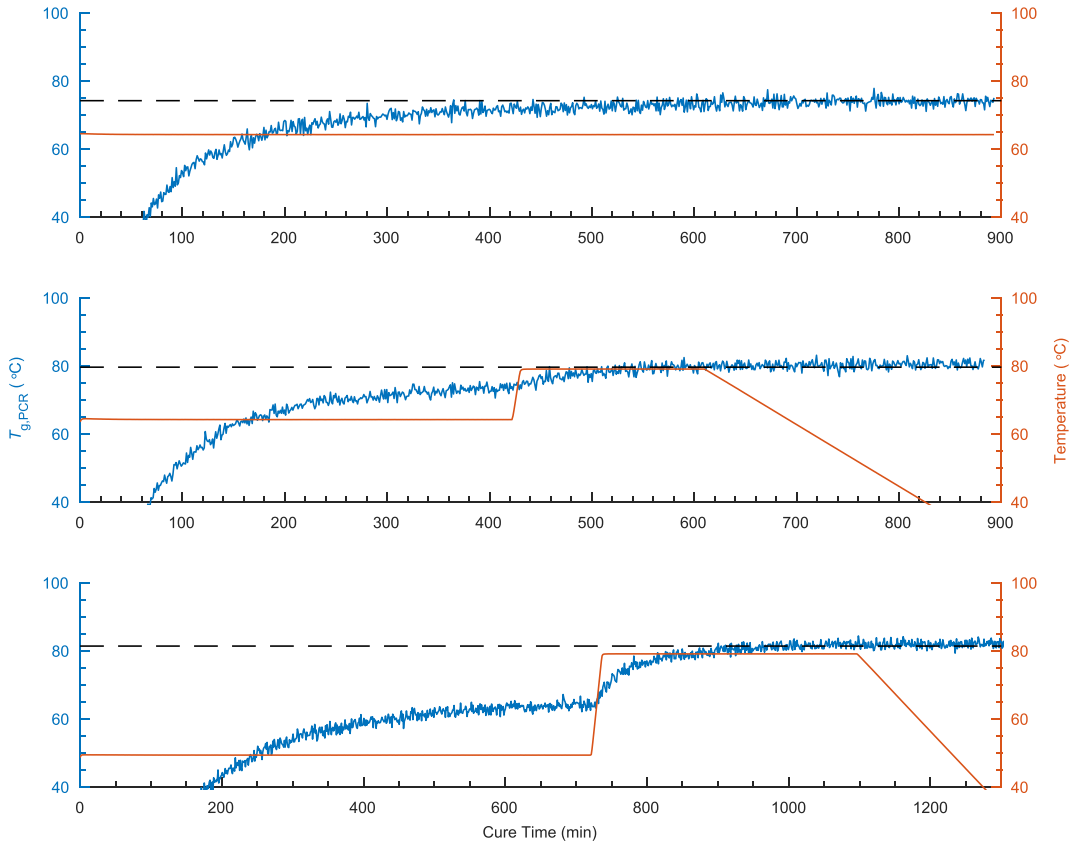

Fig. 7. Model measurements for sample *Tg* during *in situ* trials A (top), B (middle), and C(bottom).

order to evaluate the model performance during these stages.

It can be seen in Fig. 7 that all three *Tg*, PCR traces exhibited the expected trend for *Tg* evolution during thermal cure, with a relatively fast rate of evolution in the early stages, gradually decreasing to a plateau as the reaction slowed and ceased. Trials B and C exhibited further evolution in *Tg* as the ramp to the post cure dwell temperature commenced; the greater rate increase for C is consistent with a higher level of extant reactivity as a consequence of the lower initial dwell temperature.

Tg, PCR measurements towards the completion of all three cure profiles, i.e. prior to cool-down, were found to be in close agreement with the values measured by DSC, indicated by the dashed reference lines in Fig. 7. In the case of B and C, Raman-based measurements were also seen to remain stable following completion of the post cure dwell, indicating negligible model sensitivity to sample temperature. Whilst this outcome is to be expected for trial B, given the inclusion of spectra from the cool-down period of B in the calibration dataset, the measurement stability evident for trial C serves to validate this approach to model calibration. Results generated using a 3 component PCR model calibrated in the absence of spectra from trial B are presented in supplementary data, in which measurements for trials B and C both exhibit a continual increase in *Tg*, PCR during the same period.

The agreement between *Tg*, PCR and *Tg*, DSC for trials A and C, both of which used different cure profiles to trial B, demonstrates the accuracy of the Raman-based measurement technique. Table 4 presents values of *Tg*, DSC as measured for each *in situ* trial, alongside mean and standard deviation values for Raman-derived measurements, calculated from the last 50 data points acquired prior to completion of the cure profile, i.e. excluding cool-down.

Table 4
End-of-cure *Tg* values for *in situ* cure trials.

Trial	A	B	C
Tg, DSC (°C)	74.2	79.6	81.4
Tg, PCR (°C)	74.1 ± 1.1	79.6 ± 1.1	82.0 ± 0.9

Considering the inherent uncertainties associated with repeat *Tg* measurements made by DSC, arising from sample preparation and signal interpretation, the difference of ≤ 0.6 °C ± 1.1 °C between model and DSC measurements for trials A and C is remarkable. It is well within the 95% confidence interval of 2.77 °C for an epoxy glass reported in ASTM E1356-08 [36], albeit for *Tg* measured as the midpoint of the heat flow step change rather than the point of inflection.

The results presented demonstrate that *Tg* measurement of thermosetting resin directly from Raman spectra acquired *in situ* during the curing process can be achieved using principal component analysis and regression modelling of spectral components, to within the uncertainty of DSC measurements used in model calibration. It has also been shown that multivariate spectral analysis can enable non-contact measurements that exhibit negligible sensitivity to sample temperature over the sample processing temperature range.

4. Conclusion

The research presented in this paper highlights the potential for Raman spectroscopy as a non-contact monitoring system in the production of fibre reinforced plastics (FRP) composite structures, where the glass transition temperature of the polymeric matrix is a key factor in the mechanical performance of the material and structure.

Raman spectroscopy, in combination with PCA, has been demonstrated as a viable, non-contact technique able to accurately measure *Tg* of a thermosetting amine-cured epoxy polymer during the cure, without apparent sample temperature sensitivity. Multivariate model calibration utilised the full width of spectra acquired across 1100 cm^{-1} to identify and aggregate collinear trends in spectral features which were shown to correlate strongly with variations in glass transition temperature. The

PCR model generated comprised the first 5 principal components identified by the PCA, with the number of PCs selected to maximise the percentage variation explained and minimise Mean Squared Error of Prediction, whilst minimising the risk of over-fitting.

Inclusion of spectra collected over a range of sample temperatures (30 °C - 75 °C) into the calibration dataset, alongside those collected at ambient temperature over a range of glass transition temperatures (66 °C - 82 °C), enabled contributions of thermally sensitive features to the principal components to be minimised and, thus, temperature insensitive measurements to be made within the bounds of the calibration data.

When applied to time series spectra collected *in situ* over the duration of resin cure trials, model-based measurements upon completion of cure were shown to agree closely with those measured by DSC, to within 0.6 °C ± 1.1 °C. This level of uncertainty in *Tg*, DSC values is less than that associated with the DSC measurements themselves, and could be reduced further by increased averaging of the Raman spectra.

Although outside of the valid model range, predictions during the initial stages of the *in situ* cure trials appeared to follow the expected evolution of *Tg*; future work will seek to extend model validation into this region. It will also seek to determine model performance in the presence of reinforcing fibres, e.g. carbon and glass, for which it is anticipated that re-optimisation of the spectroscopy parameters or spectral pre-processing procedures would be required, for example selecting a longer excitation laser wavelength to avoid absorption from the reinforcing materials themselves The research should then be extended to investigate the use of this methodology with other resin systems of interest in FRP applications.

Potential limitations to its application do exist, such as fluorescence from optical excitation of some polymeric resins, which can obscure the Raman scattering signal, as well as optical absorption from carbon fibres resulting in an attenuated Raman scattering signal. However, it is anticipated that, with careful system design and optimisation [37], these can be overcome and the full potential of Raman spectroscopy for monitoring FRP production process realised.

Author statement

Daniel Griffin: Conceptualization of this study, Methodology, Investigation, Data curation, Formal analysis, Visualization, Writing - original draft. **SebastianWood:** Methodology, Resources, Writing - review & editing. **Ian Hamerton:** Supervision, Writing - review & editing.

Declaration of competing interest

The authors declare that they have no known competing financial interests or personal relationships that could have appeared to influence the work reported in this paper.

Acknowledgements

This work was supported by the Engineering and Physical Sciences Research Council through the EPSRC Centre for Doctoral Training in Composites Manufacture [EP/K50323X/1]; and the Department for Business, Energy and Industrial Strategy (BEIS) through the National Measurement System.

Appendix A. Supplementary data

Supplementary data to this article can be found online at https://doi.org/10.1016/j.compositesb.2020.108210.

References

[1] Stéphan F, Duteurtre X, Fit A. In-process control of epoxy composite by microdielectrometric analysis. Part II: on-line real-time dielectric measurements during a compression molding process. Polym Eng Sci 1998;38:1566–71. https://doi.org/10.1002/pen.10327.

[2] Kazilas MC, Partridge IK. Exploring equivalence of information from dielectric and calorimetric measurements of thermoset cure—a model for the relationship between curing temperature, degree of cure and electrical impedance. Polymer 2005;46:5868–78. https://doi.org/10.1016/j.polymer.2005.05.005.

[3] Martin FA, Koutsomitopoulou AF, Partridge IK, Skordos AA. Dielectric cure monitoring of a fast curing resin system. In: 20th International conference on composite materials, Copenhagen; 2015.

[4] Chiesura G, Lamberti A, Yang Y, Luyckx G, Van Paepegem W, Vanlanduit S, Vanfleteren J, Degrieck J. RTM production monitoring of the A380 hinge arm droop nose mechanism: a multi-sensor approach. Sensors 2016;16. https://doi.org/10.3390/s16060866.

[5] Pantelelis N, Nedelec G, Amosse Y, Toitgans MP, Beigbeder A, Harismendy I, Mezzacasa R, Zhang J, Bistekos E. Industrial cure monitoring and control of the RTM production of a CFRP automotive component. In: 15th European conference on composite materials, Venice, Italy; 2012.

[6] Lauter C, Jaquemotte KP, Pantelelis N. Improvement of productivity and quality in the wind energy industry through the use of an advanced sensor system. In: SAMPE Europe conference 2017, Stuttgart, Germany; 2017. p. 8.

[7] Etchells M, Pantelelis N, Lira C. Cure monitoring of highly reactive resin during high-pressure compression resin transfer moulding. In: 18th European conference on composite materials, Athens, Greece; 2018. p. 10.

[8] Gibbs PA. Ultrasonic cure measurements during the processing of an unsaturated polyester dough moulding compound. In: Designed for life: composites '94; 1994. p. 7–16.

[9] Shepard DD, Smith KR. A new ultrasonic measurement system for the cure monitoring of thermosetting resins and composites. J Therm Anal 1997;49:95–100. https://doi.org/10.1007/BF01987425.

[10] Lionetto F, Maffezzoli A. Monitoring the cure state of thermosetting resins by ultrasound. Materials 2013;6:3783–804. https://doi.org/10.3390/ma6093783.

[11] Nielsen LE. Cross-linking–effect on physical properties of polymers. J Macromol Sci, Part C 1969;3:69–103. https://doi.org/10.1080/15583726908545897.

[12] DiBenedetto AT. Prediction of the glass transition temperature of polymers: a model based on the principle of corresponding states. J Polym Sci B Polym Phys 1987;25:1949–69. https://doi.org/10.1002/polb.1987.090250914.

[13] Chowdhury SC, Elder RM, Sirk TW, Gillespie JW. Epoxy resin thermo-mechanics and failure modes: effects of cure and cross-linker length. Compos B Eng 2020;186:107814. https://doi.org/10.1016/j.compositesb.2020.107814.

[14] Lyon RE, Chike KE, Angel SM. In situ cure monitoring of epoxy resins using fiber-optic Raman spectroscopy. J Appl Polym Sci 1994;53:1805–12. https://doi.org/10.1002/app.1994.070531310.

[15] George GA, Cash GA, Rintoul L. Cure monitoring of aerospace epoxy resins and prepregs by Fourier transform infrared emission spectroscopy. Polym Int 1996;41:169–82. https://doi.org/10.1002/(SICI)1097-0126(199610)41:2<169::AID-PI606>3.0.CO;2-2.

[16] Kondyurin A, Komar L, Svistkov A. Combinatory model of curing process in epoxy composite. Compos B Eng 2012;43:616–20. https://doi.org/10.1016/j.compositesb.2011.11.019.

[17] Wang Z, Meng F, Li X, Zhang X, Hu W, Zhao G. Cure behaviors of furfuryl alcohol/epoxy/methyltetrahydrophthalic anhydride and their enhanced mechanical and anti-acid properties of basalt fiber reinforced composites. Compos B Eng 2018;154:263–71. https://doi.org/10.1016/j.compositesb.2018.08.011.

[18] Mphahlele K, Ray SS, Kolesnikov A. Cure kinetics, morphology development, and rheology of a high-performance carbon-fiber-reinforced epoxy composite. Compos B Eng 2019;176:107300. https://doi.org/10.1016/j.compositesb.2019.107300.

[19] Pomerantsev AL, Rodionova OY. Process analytical technology: a critical view of the chemometricians: PAT: a critical view of the chemometricians. J Chemometr 2012;26:299–310. https://doi.org/10.1002/cem.2445.

[20] Chew W, Sharratt P. Trends in process analytical technology. Anal. Methods 2010;2:1412. https://doi.org/10.1039/c0ay00257g.

[21] Simon LL, Pataki H, Marosi G, Meemken F, Hungerbühler K, Baiker A, Tummala S, Glennon B, Kuentz M, Steele G, Kramer HJM, Rydzak JW, Chen Z, Morris J, Kjell F, Singh R, Gani R, Gernaey KV, Louhi-Kultanen M, O'Reilly J, Sandler N, Antikainen O, Yliruusi J, Frohberg P, Ulrich J, Braatz RD, Leyssens T, von Stosch M, Oliveira R, Tan RBH, Wu H, Khan M, O'Grady D, Pandey A, Westra R, Delle-Case E, Pape D, Angelosante D, Maret Y, Steiger O, Lenner M, Abbou-Oucherif K, Nagy ZK, Litster JD, Kamaraju VK, Chiu MS. Assessment of recent process analytical technology (PAT) trends: a multiauthor review. Org Process Res Dev 2015;19:3–62. https://doi.org/10.1021/op500261y.

[22] Merad L, Cochez M, Margueron S, Jauchem F, Ferriol M, Benyoucef B, Bourson P. In-situ monitoring of the curing of epoxy resins by Raman spectroscopy. Polym Test 2009;28:42–5. https://doi.org/10.1016/j.polymertesting.2008.10.006.

[23] Hardis R, Jessop JLP, Peters FE, Kessler MR. Cure kinetics characterization and monitoring of an epoxy resin using DSC, Raman spectroscopy, and DEA. Compos Appl Sci Manuf 2013;49:100–8. https://doi.org/10.1016/j.compositesa.2013.01.021.

[24] Cruz JC, Osswald TA. Monitoring epoxy and unsaturated polyester reactions under pressure-Reaction rates and mechanical properties. Polym Eng Sci 2009;49:2099–108. https://doi.org/10.1002/pen.21448.

[25] Skrifvars M, Niemelä P, Koskinen R, Hormi O. Process cure monitoring of unsaturated polyester resins, vinyl ester resins, and gel coats by Raman spectroscopy. J Appl Polym Sci 2004;93:1285–92. https://doi.org/10.1002/app.20584.

[26] Chai CK, Dixon NM, Gerrard DL, Reed W. Rheo-Raman studies of polyethylene melts. Polymer 1995;36:661–3. https://doi.org/10.1016/0032-3861(95)91578-U.

[27] Hamerton I, Herman H, Mudhar A, Chaplin A, Shaw S. Multivariate analysis of spectra of cyanate ester/bismaleimide blends and correlations with properties. Polymer 2002;43:3381–6. https://doi.org/10.1016/S0032-3861(02)00092-7.
[28] Farquharson S, Smith W, Rose J, Shaw M. Correlations between molecular (Raman) and macroscopic (rheology) data for process monitoring of thermoset composite. JPAC (sm) Process Analytical Chemistry 2002:45–53.
[29] Aust JF, Booksh KS, Stellman CM, Parnas RS, Myrick ML. Precise determination of percent cure of epoxide polymers and composites via fiber-optic Raman spectroscopy and multivariate analysis. Appl Spectrosc 1997;51:247–52. https://doi.org/10.1366/0003702971939956.
[30] Cooper JB. Chemometric analysis of Raman spectroscopic data for process control applications. Chemometr Intell Lab Syst 1999;46:231–47. https://doi.org/10.1016/S0169-7439(98)00174-9.
[31] Vašková H, Křesálek V. Raman spectroscopy of epoxy resin crosslinking. In: Recent researches in automatic control, 13th WSEAS international conference on automatic control, modelling and simulation (ACMOS'11), Lanzarote, Spain; 2011. p. 357–61.
[32] Lin-Vien D, Colthup NB, Fateley WG, Grasselli JG. Ethers and peroxides. In: The handbook of infrared and Raman characteristic frequencies of organic molecules. Elsevier; 1991. p. 61–72. https://doi.org/10.1016/B978-0-08-057116-4.50011-0.
[33] Lin-Vien D, Colthup NB, Fateley WG, Grasselli JG. Compounds containing –NH2, –NHR, and –NR2 groups. In: The handbook of infrared and Raman characteristic frequencies of organic molecules. Elsevier; 1991. p. 155–78. https://doi.org/10.1016/B978-0-08-057116-4.50016-X.
[34] Lin-Vien D, Colthup NB, Fateley WG, Grasselli JG. Alkanes. In: The handbook of infrared and Raman characteristic frequencies of organic molecules. Elsevier; 1991. p. 9–28. https://doi.org/10.1016/B978-0-08-057116-4.50008-0.
[35] Lin-Vien D, Colthup NB, Fateley WG, Grasselli JG. Aromatic and heteroaromatic rings. In: The handbook of infrared and Raman characteristic frequencies of organic molecules. Elsevier; 1991. p. 277–306. https://doi.org/10.1016/B978-0-08-057116-4.50023-7.
[36] E37 Committee, reportTest method for assignment of the glass transition temperatures by differential scanning calorimetry. Technical Report. ASTM International. doi:10.1520/E1356-08R14.
[37] Tschudi J, O'Farrell M, Hestnes Bakke KA. Inline spectroscopy: from concept to function. Appl Spectrosc 2018;72:1298–309. https://doi.org/10.1177/0003702818788374.

Appendix B

Over-braiding workflow variables

Table B.1: List of variables identified as relating to the manufacturing quality of the over-braiding process, including logical variable groupings and categorisations.

Category	Variable group	Variable
Output	Braid angle	Braid angle
Output	Cover factor	Cover factor
Output	Thickness / compaction	Preform thickness / compaction
Output	Permeability	Permeability
Dependent	Yarn friction	Yarn-yarn friction
Dependent	Yarn friction	Yarn-guide ring friction
Dependent	Yarn friction	Yarn-mandrel friction
Dependent	Yarn tension	Bias yarn tension
Dependent	Yarn tension	Axial yarn tension
Dependent	Bias yarn path	Fall angle
Dependent	Bias yarn path	Entry / exit angle of yarn to guide ring
Dependent	Bias yarn path	Guide ring eccentricity
Dependent	Axial yarn position	Axial yarn distribution / spread
Dependent	Axial yarn position	Axial yarn stacking
Dependent	Yarn spread	Yarn spread
Dependent	Cell geometry	Deposited yarn x-section
Dependent	Cell geometry	Yarn undulation length
Dependent	Cell geometry	Crimp
Dependent	Bias carrier spool diameter / mass	Bias carrier spool diameter / mass
Dependent	Yarn damage / failure	Yarn breaks

Dependent	Yarn damage / failure	Damaged yarns
Dependent	Yarn damage / failure	Yarn fuzz balls
Dependent	Yarn damage / failure	Buckling of axial yarn
Dependent	Yarn damage / failure	Yarn end quantity
Independent	Braid layer	Number of layers
Independent	Mandrel geometry	Mandrel diameter
Independent	Mandrel geometry	Mandrel X-sectional shape
Independent	Mandrel geometry	Mandrel curvature along length
Independent	Mandrel geometry	Change of mandrel X-sectional shape along length
Independent	Mandrel geometry	Change of mandrel curvature along length
Independent	Environmental conditions	Humidity
Independent	Environmental conditions	Temperature
Independent	Braid layer	Direction of braid
Independent	Guide ring vibration	Guide ring vibration frequency / amplitude (inner / outer ring depending on direction)
Independent	Deposition rate	Deposition rate
Independent	Mandrel : carrier speed ratio	Mandrel take-up speed : machine carrier speed
Parameter	Mandrel design	Lead-in length
Parameter	Mandrel design	Lead-out length
Parameter	Mandrel design	Mandrel material
Parameter	Mandrel design	Surface finish
Parameter	Yarn selection	Yarn material
Parameter	Yarn selection	Yarn weight
Parameter	Yarn selection	Yarn sizing
Parameter	Yarn selection	Initial yarn x-section
Parameter	Material preparation	Yarn twist
Parameter	Material preparation	Bias carrier winding tension
Parameter	Braid architecture	Yarn directionality
Parameter	Braid architecture	Number of carriers
Parameter	Braid architecture	Braid pattern
Parameter	Machine tension setup	Bias yarn carrier spring tension
Parameter	Guide ring selection / setup	Guide ring cross section shape
Parameter	Guide ring selection / setup	Guide ring diameter
Parameter	Guide ring selection / setup	Guide ring surface coating

Parameter	Machine tension setup	Axial yarn brake tension
Parameter	Guide ring selection / setup	Guide ring x-position

Appendix C

Effect of light offset on edge intensity

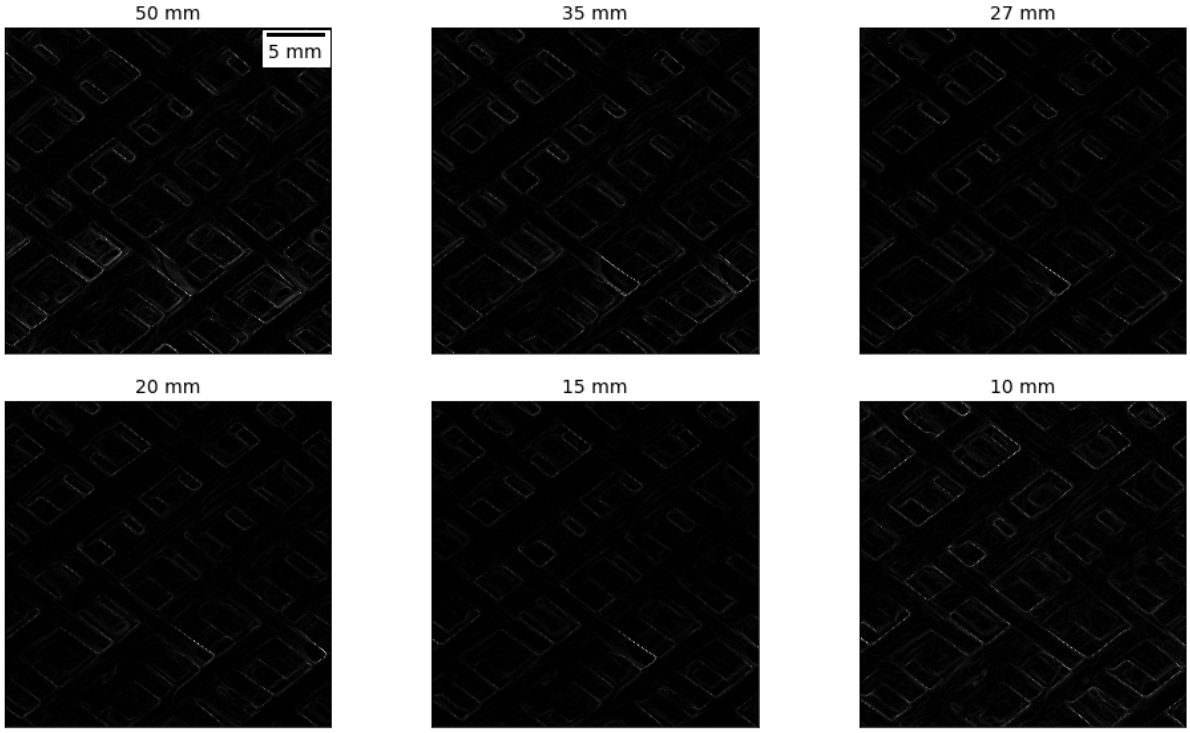

Figure C.1: Edge intensities for images at X = 130 mm with varying light offset.

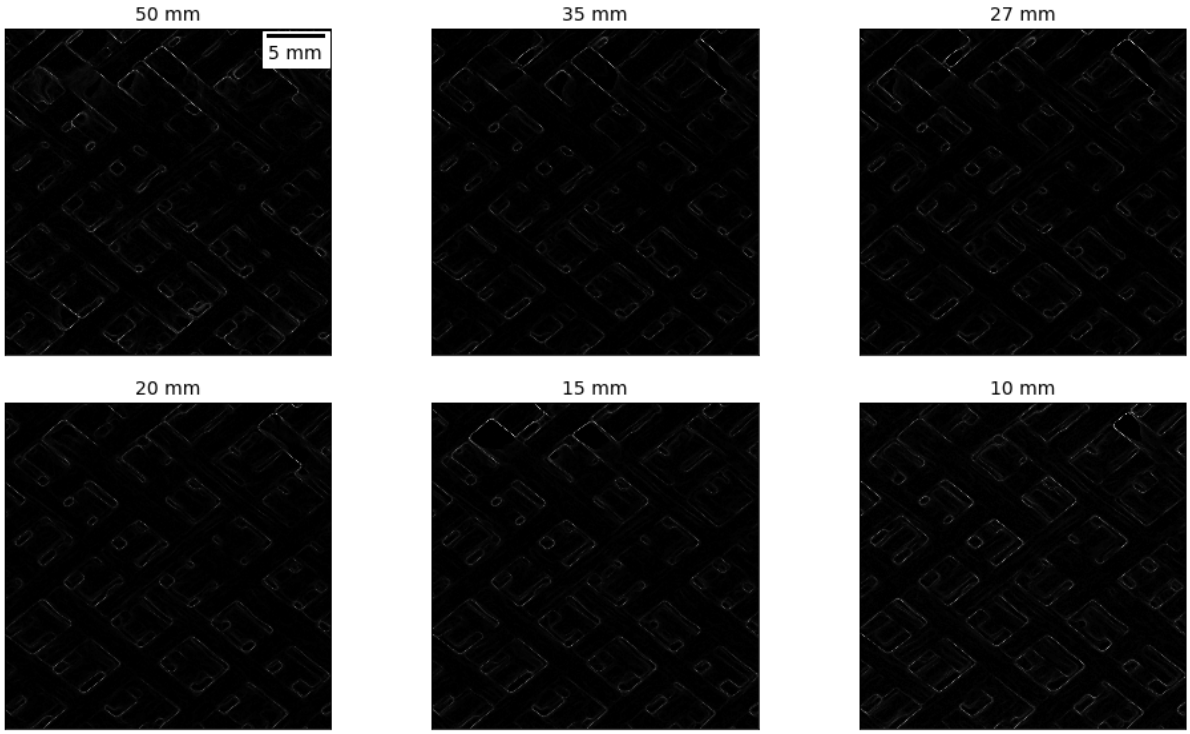

Figure C.2: Edge intensities for images at X = 580 mm with varying light offset.

Appendix D

Braided preform image simulation

Table D.1: Sequence of steps and associated distributions used to generate simulated preform images for braid angle uncertainty assessment.

Define:	- image size, Im_{xy}	3600 px
	- intensity of background	$\mathcal{N}(63, 16^2)$ or $\mathcal{N}(191, 32^2)$
	- nominal yarn width, Ψ_{nom}	2.2 mm
	- width of visible fibre detail on yarns [x2]	0.01 mm
	- image scale	87 px/mm
	- number of layers	$\mathcal{U}(1, 2)$
	- intensity of fibre details:- mid	$\mathcal{N}(63, 4^2)$
	- low	mid - $\mathcal{N}(36, 16^2)$
	- high	mid + $\mathcal{N}(36, 16^2)$
	- number of high intensity 'reflections' per yarn mask	$\mathcal{U}(1, 5)$
	- size of gaussian kernel used to represent 'reflections'	$\mathcal{N}(200, 20^2)$
	- number of 'stray fibres' per image	$\mathcal{U}(1, 2)$
For L in *number of layers*:		
⌞ Define:	- nominal braid angle, θ_{nom}	$\mathcal{U}(25, 65)^\circ$
	- yarn spacing	$\Psi_{nom} + \mathcal{U}(10, \Psi_{nom})$ px
⌞ Calculate number of visible yarns in image		
⌞ For Y in *number of yarns*:		
⌞ Define:	- actual yarn angle, θ_{act}	$\mathcal{N}(\pm\theta_{nom}, 0.5^2)^\circ$
	- angle of fibre detail	$\theta_{act} \pm \mathcal{N}(2, 1^2)^\circ$
	- actual yarn width	$\mathcal{N}(\Psi_{nom}, 0.2^2)$ mm
⌞ Generate mask image of fibre detail at defined angle, using predefined fibre detail widths and intensities		

⌞ For R in *number of reflections*:	
⌞ Define: - reflection location	$(\mathcal{U}(0, Im_{xy}),\mathcal{U}(0, Im_{xy}))$ px
⌞ Add 'reflection' of predefined size to mask image	
⌞ Generate mask of yarn area	
⌞ Extract masked yarn area from fibre detail image, add to background image	
For S in *number of stray fibres*:	
⌞ Define: - stray fibre length	$\mathcal{N}(500, 200^2)$ px
- stray fibre width	$\mathcal{N}(0.001, 0.0002^2)$ mm
- stray fibre position on image	$\mathcal{U}(0, Im_{xy})$,$\mathcal{U}(0, Im_{xy})$ px
- stray fibre angle	$\mathcal{U}(0, 359)^\circ$
- stray fibre intensity	low, mid or high
⌞ Add stray fibre to image	
Add gaussian blur	
Add gaussian noise	

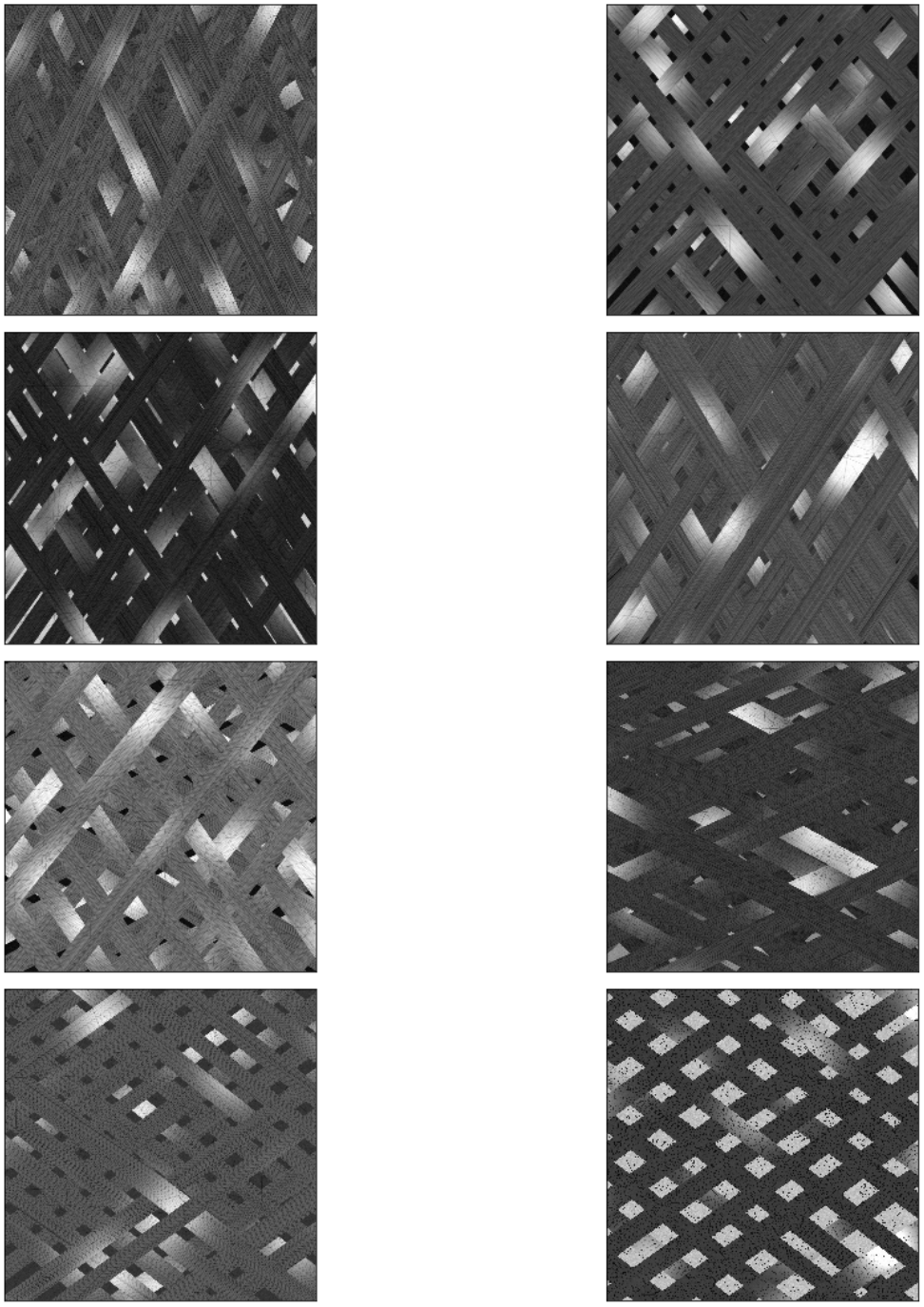

Figure D.1: Example simulated images of single and double layer preforms used for Monte Carlo evaluation of braid angle measurement uncertainty.